

AN ABSTRACT OF THE DISSERTATION OF

Chris J. Russo for the degree of Doctor of Philosophy in Oceanography presented on June 15, 2007.

Title: Mantle Melting and Heterogeneity along Mid-ocean Ridges: Insights from Basalt Geochemistry along Axial Depth and Morphologic Gradients for Intermediate Spreading Rate Systems

Abstract approved: _____

David W. Graham

This investigation focuses on gaining a better understanding of the complex relationship between melt generation, source variability and mid-ocean ridge morphology. The approach adopted here uses a variety of geochemical techniques to evaluate the ability of ‘global’ models to predict regional scale geochemical variability associated with axial depth and axial morphologic changes. Three separate regional scale studies were conducted along ridges characterized by intermediate spreading rates (where the system is very sensitive to variations in magma production).

The first study focuses on the development of the Australian-Antarctic Discordance (AAD), an anomalously deep portion of the modern global ridge system located in the eastern Indian Ocean, over the period from 28 to 14 Ma during which the eastern Indian Ocean basin was in a relatively young stage of formation. Major and trace

element results from this study suggest a more magmatically robust ridge was present during this period.

The second study investigates the link between U-series disequilibria and axial ridge depth. In this study U and Th isotopic compositions and elemental concentrations were analyzed along the Southeast Indian Ridge. The results of this study suggest that a simple relationship, such as that predicted from global MORB variations, does not exist on a regional scale in this part of the Indian Ocean. Plausible explanations of this data set require the consideration of other intrinsic variables such as residual porosity and mantle melting rates.

The third investigation focuses on the western Galapagos Spreading Center (GSC), an intermediate spreading ridge whose axial morphology is affected by the addition of heat and material from the nearby Galapagos hotspot. This study investigates the origin and nature of the transfer of this material through analysis of rare earth element concentrations in melt inclusions. The results from this study support a deep (≥ 60 km), strong lateral flow of hotspot-derived mantle toward the GSC.

Collectively these studies support a strong link between axial morphology and melt generation and verify that geochemical investigations along regional morphologic gradients provide a meaningful 'window' into the underlying mantle, while demonstrating that although 'global' models succeed in providing a valid platform from which to evaluate regional-scale observations, they do not accurately describe the complex process of melt generation on a regional scale.

©Copyright by Chris J. Russo
June 15, 2007
All Rights Reserved

Mantle Melting and Heterogeneity along Mid-ocean Ridges: Insights from Basalt
Geochemistry along Axial Depth and Morphologic Gradients for Intermediate Spreading
Rate Systems

by
Chris J. Russo

A DISSERTATION

submitted to

Oregon State University

in partial fulfillment of
the requirements for the
degree of

Doctor of Philosophy

Presented June 15, 2007
Commencement June 2008

Doctor of Philosophy dissertation of Chris J. Russo presented on June 15, 2007.

APPROVED:

Major Professor, representing Oceanography

Dean of the College of Oceanic and Atmospheric Sciences

Dean of the Graduate School

I understand that my dissertation will become part of the permanent collection of Oregon State University libraries. My signature below authorizes release of my dissertation to any reader upon request.

Chris J. Russo, Author

ACKNOWLEDGEMENTS

Without question the completion of this thesis would not have been possible without a tremendous amount of help from the family, friends and colleagues who have surrounded me during the nearly nine years I spent in Corvallis. Foremost, I would like to thank Dave Graham for his mentorship and friendship. This thesis would have never been completed were it not for Dave's patience, hard work, and intelligence. Throughout this process Dave has remained steadfastly devoted to my education and the pursuit of my interests. I am extremely grateful to him for the freedom he has given me in my exploration of mantle melting and geochemistry and for granting me unlimited access to the vault of knowledge that is his brain. All of this would mean significantly less had it not been for the fact that through it all Dave also consistently reminded me that science, much like life, should be fun. In this way, having the regular opportunity to share in Dave's love of fine food, wine, whiskey and baseball will be sorely missed.

I will also be eternally grateful to Doug Pyle for his guidance and friendship. The time spent working on this thesis certainly would have been a lot less fun without Doug's continued involvement throughout the years. I also owe a big thank you to both Doug and his wife, Kris McElwee, for opening their home to me and for their amazing hospitality during my many (long) visits to Hawaii.

I'd like to thank Gary Klinkhammer for playing a critical role in sparking my interest in analytical geochemistry and for his mentorship, friendship and endless generosity throughout the years.

Along these lines I also owe Andy Ungerer a big thank you for his patient and forgiving instruction in the lab and for always being willing to lend an ear to talk about the daily goings on in the world of sports.

I thank Sam VanLangingham and Brian Haley for their friendship, help and willingness to take a break from the daily grind now and again... and again, and again. I cannot imagine having been accompanied through this process by people any more enjoyable than them.

I thank Ken Rubin for allowing me to come to the University of Hawaii to learn from his expertise. Throughout my interaction with Ken I have found his unfailing drive towards excellence inspiring. I appreciate his patience, devotion and willingness towards working with me despite the fact I was in Oregon most of the time.

I thank the wonderful friends I have had in Corvallis. Especially Kristen and Andy (and more recently, Maggie) Hackethorn for their companionship, laughter and support throughout my time in Corvallis. I will certainly miss having you so close by.

To my Mom and Dad, I love you very much! Thank you for your support and encouragement along the way. I admire your generosity and patience and will be forever grateful for all the opportunities you have helped provide me in life.

Last but certainly not least, I thank my loving wife Candace for all that she is. I love you and look forward to many more years exploring life together.

CONTRIBUTION OF AUTHORS

The guidance and insight given to me by my major advisor, David W. Graham, played a vital role in the development and presentation of the observations, concepts and ideas expressed throughout this thesis. Additionally, Chapters 2, 3 and 4 are the products of considerable collaboration with co-authors. Specifically, Chapter 2 builds upon the previous work of Doug Pyle and Dave Christie, both of who contributed significantly to the analysis, interpretation, development and presentation of the ideas put forward in this chapter. Ken Rubin's role in the development of Chapter 3 was critical in every step of the process. His insight into the inner workings of uranium-series geochemistry and mid-ocean ridge melt generation improved the quality of both the analytical work and interpretations presented in this chapter. Similarly, Chapter 4 benefited from Adam Kent's expertise in the field of laser ablation ICP-MS improving not only the approach used, but also the quality of the melt inclusion analyses presented in this chapter.

TABLE OF CONTENTS

	<u>Page</u>
Chapter 1 General Introduction.....	1
1.1 Foreword.....	2
1.2 Background.....	4
1.2.1 MORB compositional variations, axial depth and crustal thickness	4
1.2.2 U-series disequilibria and region variations in Indian MORB melt generation	5
1.2.3 Melt inclusions as a probe of partial melt composition variability along intermediate spreading rate ridges.....	10
 Chapter 2 Development and evolution of the Australian-Antarctic Discordance: A geochemical perspective	16
2.1 Abstract.....	17
2.2 Introduction.....	17
2.3 Sample Selection, Analytical Methods and Results.....	21
2.4 Site Locations and Tectonic Settings	22
2.4.1 Group 1	23
2.4.2 Group 2	24
2.4.3 Group 3	24
2.5 Major Element Populations, Mantle Domains and the Evolution of the AAD	25
2.5.1 Changes in the Indian and Pacific MORB Populations.....	25
2.5.2 Changes in Melting Conditions.....	27
2.5.3 Changes in Parental Magma Compositions	28
2.5.4 Trace element characterization.....	29
2.6 Discussion.....	31
2.6.1 Models for the evolution of the AAD.....	31
2.7 Conclusions.....	33

TABLE OF CONTENTS (Continued)

	<u>Page</u>
Chapter 3 Mantle Heterogeneity and Melting Conditions along the Southeast Indian Ridge: A U-Series Disequilibria Perspective.....	48
3.1 Abstract.....	49
3.2 Introduction.....	49
3.3 Geologic Background.....	52
3.3.1 Along axis morphologic variation.....	52
3.3.2 Along axis geochemical variation.....	54
3.4 Results.....	56
3.4.1 Trace element concentrations Ba-Th-U.....	56
3.4.2 Sample alteration and ($^{234}\text{U}/^{238}\text{U}$).....	57
3.4.3 ($^{230}\text{Th}/^{232}\text{Th}$) and ($^{226}\text{Ra}/^{230}\text{Th}$).....	57
3.4.4 Along axis variations: A U-series perspective.....	59
3.5 Discussion.....	60
3.5.1 Global correlations at a regional scale 1: U-series as an indicator of the depth of melting.....	60
3.5.2 SEIR basalts and the 'equiline' diagram.....	62
3.5.3 U-series disequilibria and morphologic characteristics.....	66
3.5.4 Morphologic groups and the 'global' ^{230}Th vs. axial depth trend.....	68
3.5.5 Morphologic groups and the 'equiline' diagram.....	73
3.5.6 Mantle heterogeneity along the SEIR: a combined trace element, U-series and long-lived isotope perspective.....	74
3.5.7 Trace elements.....	75
3.5.8 The long-lived and primordial isotopes: Sr, Pb and He.....	78
3.5.9 The Th-Sr isotope correlation.....	80
3.5.10 Kappa (κ) versus Kappa-lead (κ_{pb}).....	82
3.5.11 A conceptual model for enrichment and subsequent depletion of the Indian Ocean mantle beneath the SEIR.....	87
3.6 Summary.....	93
3.7 Conclusions.....	95

TABLE OF CONTENTS (Continued)

	<u>Page</u>
Chapter 4 Rare earth elements in melt inclusions from the western Galapagos Spreading Center: Evidence for deep melting beneath a plume-influenced intermediate spreading rate ridge	119
4.1 Abstract.....	120
4.2 Introduction.....	121
4.3 Background.....	122
4.3.1 General tectonic overview	122
4.3.2 The Galapagos Archipelago and Plateau	123
4.3.3 The western Galapagos Spreading Center	124
4.3.4 Hydrous melting along the western GSC.....	126
4.4 Methods	128
4.5 Results	130
4.5.1 Sample description and host lava geochemistry	130
4.5.2 Trace element variation by enrichment groups	132
4.6 Discussion.....	134
4.6.1 Hydrous melting and the depth of melt initiation.....	134
4.6.2 Aggregated non-modal fractional melting of spinel lherzolite and garnet lherzolite lithologies	136
4.7 Conclusions.....	139
Chapter 5 General Conclusions.....	166
5.1 Summary.....	167
Bibliography.....	171

LIST OF FIGURES

<u>Figure</u>	<u>Page</u>
1.1 Schematic diagram from Klein and Langmuir (1988).....	12
1.2 The 'equiline' diagram.....	13
1.3 (²³⁰ Th/ ²³⁸ U) versus melting rate	14
1.4 (²³⁰ Th/ ²³⁸ U) versus melt initiation depth and melt productivity.....	15
2.1 Regional map of the Southeast Indian Ocean between 110°E and 150°E.....	35
2.2 Line drawings of the Southeast Indian Ridge from ~115°E to ~135°E.	36
2.3 Oxide-Oxide variation diagrams	37
2.4 Major element ratio diagrams	38
2.5 Fractionation corrected major element variation diagrams	39
2.6 Chondrite normalized rare earth element patterns.....	40
3.1 Satellite altimetry of the Indian Ocean basin between 40°E and 130°E	97
3.2 Geochemical tracers of source heterogeneity and melting along the SEIR between 88° and 118°E	98
3.3 Longitudinal variation in U-series activity, k and kPb along the SEIR between 88°E and 118°E.....	99
3.4 Measured (²³⁰ Th/ ²³⁸ U) for basaltic glasses from the SEIR (as regional groups) versus axial depth.....	100
3.5 'Equiline' diagram for SEIR compared to Global MORB	101
3.6 SEIR- 'Equiline' diagram	102
3.7 ²³⁰ Th-excess versus axial depth by morphologic groups	103
3.8 (²³⁰ Th/ ²³⁸ U) versus melting rate	104

LIST OF FIGURES (Continued)

<u>Figure</u>	<u>Page</u>
3.9 ($^{230}\text{Th}/^{238}\text{U}$) versus melt initiation depth and melt productivity.....	105
3.10 'Equiline' diagram and axial morphology	106
3.11 Th/U versus measured $^{176}\text{Lu}/^{177}\text{Hf}$ in SEIR basalts.....	107
3.12 ($^{230}\text{Th}/^{232}\text{Th}$), ($^{238}\text{U}/^{232}\text{Th}$) and Th/U versus $\Delta 8/4$ and $^3\text{He}/^4\text{He}$	108
3.13 ($^{230}\text{Th}/^{232}\text{Th}$) versus $^{87}\text{Sr}/^{86}\text{Sr}$	109
3.14 κ versus κ_{pb} diagram	110
3.15 Schematic diagram of enrichment/depletion evolution model.....	111
3.16 % contribution of pyroxenite source melt versus volume % of pyroxenite in the source region.....	112
3.17 Incompatibility diagrams for components of the model and SEIR lavas	113
3.18 Summary Cartoon of along-axis variation in the melt region beneath the SEIR from 88°E to 118°E.....	114
4.1 Regional map of the eastern equatorial Pacific near the Galapagos Islands.....	141
4.2 Chondrite normalized values for USGS fused glass basalt standards	142
4.3 Enrichment groups for melt inclusions from the western GSC	143
4.4 Trace element variation diagrams	144
4.5 (La/Yb) _n versus (La) _n	145
4.6 (Tb/Yb) _n versus (La/Yb) _n	146
4.7 Normalized La and Yb concentrations of western GSC melt inclusions	147

LIST OF TABLES

<u>Table</u>	<u>Page</u>
2.1 Major and trace element concentrations of ODP Leg 187 basalts	41
2.2 Selected major and trace element averages for ODP Leg 187 lavas	47
3.1 Previous results- Along axis isotopic compositions of SEIR glasses.....	115
3.2 SEIR U-series, Ba, Ra, Th and U concentrations.....	116
4.1 Trace element results for USGS standard glasses	148
4.2 Sample locations and enrichment groups	149
4.3 Trace element concentrations in GSC melt inclusions	150
4.4 Aggregated non-modal fractional melting model parameters.....	165

Chapter 1:
General Introduction

Chris J. Russo

1.1 Foreword

Melt generation beneath mid-ocean ridge spreading centers is a fundamental process that creates the Earth's ocean floor. It plays a major role in the chemical evolution of the Earth's interior, and drives hydrothermal circulation that in return is key to the existence of life in these extreme deep ocean environments. Mid-ocean ridge spreading centers bisect all the Earth's ocean basins as a nearly continuous ~65,000 km-long volcanic mountain range. Magma generated beneath these vast features has produced the oceanic crust currently covering 60% of the Earth's surface and provides the best 'view' of the geochemical diversity of the Earth's upper mantle. Research into the complexities of this process over the last few decades has certainly advanced our understanding of the ways in which melt (or magma) is produced, but a clear picture of what controls variations in melt generation, and geochemical variability in erupted mid-ocean ridge basalts (MORBs) remains elusive.

A generally accepted view is that melt is produced at depth beneath the ridge axis as the result of passive mantle upwelling and nearly adiabatic (isentropic) decompression (Stolper, 1992; Chen, 1996). As ridge axes spread laterally, upwelling material (mantle) rises. This parcel of mantle ascends isentropically across the local pressure-temperature geotherm and eventually crosses the mantle solidus, at which point melting begins. The degree of melting achieved in these passive systems is therefore dependent on the length of the melting column and the rate of melting, commonly referred to as the melt productivity (usually given in terms of %/km of ascent). Previous studies combining observations of axial depth, ridge morphology, spreading rate and MORB geochemistry have suggested that the depths at which melting initiates and/or ceases (i.e. melt column height) varies at the ocean basin scale (10,000 to 1000 km) and even along segment length scales (~100 km; e.g. Klein and Langmuir, 1987; Niu and Hekinian, 1997; Michael and Cornell, 1998).

The mantle temperature profile beneath mid-ocean ridges depends on both a conductive (linear) temperature gradient to the surface and a convective (non-linear transition to adiabatic) gradient at depth in the mantle (Shen and Forsyth, 1995; Niu and Hekinian, 1997). Variations in the initial depth of melting are then dictated by mantle temperature whereas the final depth of melting is dictated by the efficiency of a system to remove heat from above (Herzberg, 2004). The extent of crustal fracturing is believed to contribute significantly to cooling of the crust by creating pathways through which seawater, and thus, heat can be transferred (Reid and Jackson, 1981; Niu and Hekinian, 1997). A comparison of the way in which these competing forces may control the structure of the temperature profile beneath the global mid-ocean ridge spreading system is summarized in Figure 1.

Spreading rate and underlying mantle temperature are certainly variable in a global sense, but the link between the two and the potential of either to exert dominant control remains a matter of debate. In part this is due to the fact that both hotter mantle and/or faster spreading ridges are predicted to generate greater amounts of melting (and/or more continuous magma supply) leading to a more magmatically robust ridge morphology. In contrast, cooler mantle and/or slower spreading ridges are predicted to generate smaller amounts of melting (and/or less continuous supply), which leads to magmatically starved, tectonically dominated (and therefore more fractured) ridge morphology.

Emerging experimental results (Pertermann and Hirschmann, 2002,2003a,b) and state-of-the-art geochemical investigations of MORB via U-series and melt inclusion studies indicate that there are several important parameters in these systems. These include, but are not limited to: 1) mantle temperature (for example Klein and Langmuir, 1987; Bourdon et al., 1996); 2) mineralogic/lithologic heterogeneity of the mantle, either in the form of garnet pyroxenite or eclogite (e.g. Prinzhofer et al., 1989; Hirschman and Stolper, 1996); and 3) the previous history of the mantle source

region and its constituents (e.g. Hanson, 1977; Wood, 1979; Blichert-Toft et al., 2005; Graham et al., 2006).

1.2 Background

1.2.1 MORB compositional variations, axial depth and crustal thickness

In the early and mid 1980's, as ridge systems in the Atlantic, Pacific and Indian Oceans became more densely sampled, the development of an initial 'global MORB database' paved the way for the landmark paper by Klein and Langmuir (1987). Drawing on differences in major element characteristics of MORB erupted from ridge axes of different depth, Klein and Langmuir suggested that differences in axial depth, crustal thickness and MORB chemistry were all linked, and were dominantly controlled by lateral variations in mantle potential temperature (the temperature at which the mantle adiabat intersects zero pressure).

In the Klein and Langmuir model, hotter mantle intersects its solidus and begins to melt at a greater depth than cooler mantle. Because this temperature is achieved at greater depth when hotter mantle is involved, hotter mantle melts over a greater depth range, resulting in a higher degree of melting and greater magma supply to the ridge. The increased magma supply thereby results in thicker ocean crust and shallower axial depths compared to the relatively cooler mantle scenario (Figure 1). In their model, melting begins at a nominal depth of ~60 km as upwelling peridotite crosses the solidus and enters the bottom of the melt generation region. As this mantle continues to rise towards the surface it melts at a roughly constant rate of ~0.33%/km, continuing all the way to the base of the crust (typically ~6 km). In this scenario, partial melts up to 20% are achieved and the average percent melting (F) equals 10%, which translates into a 6 km thick crust. From this perspective, a change in the depth to the solidus of ± 20 km (equivalent of a change in mantle potential temperature of ~

75°C) could account for the global range of inferred crustal thickness along mid-ocean ridges away from mantle hotspots such as Iceland.

The first case study presented in this thesis (Chapter 2) focuses on the observed variations in major and trace element composition of 28 to 14 Ma basalts erupted near the eastern margin of the Australian-Antarctic Discordance (AAD). The data presented in this chapter are interpreted within the context of the Klein and Langmuir model and plate reconstructions based on the geomagnetic record, to reconstruct how morphology may have varied during early stages of mid-ocean ridge magmatism in the relatively young eastern Indian Ocean basin. The results show that the major element compositions of the 28 to 14 Ma basalts are consistent with their derivation from larger extents of melting originating from greater depths than lavas erupted within this region today.

1.2.2 U-series disequilibria and regional variations in Indian MORB melt generation

Trace elements (such as the heavy rare earth elements, HREE) and isotopic ratios can be sensitive to the presence of residual garnet in the mantle source region, and may make good indicators of the initial depth of melting because garnet is only stable in periodotite assemblages at depths ≥ 60 -80 km (Hirschmann and Stolper, 1996; Harpp and White, 2001). Uranium and thorium isotopic compositions represent one such isotopic system that is sensitive to the presence of garnet, because it is widely accepted that garnet is the primary mineral phase controlling U-Th fractionation in the Earth's mantle (La Tourrette et al., 1993; Beattie, 1993). The fractionation between Th and U can be systematically visualized on the '*equiline*' diagram (Figure 2a; Allegre, 1968; or isochron diagram as it was originally called by Kigoshi (1967)). This diagram consists of the measured ($^{230}\text{Th}/^{232}\text{Th}$) value (on the y-axis) plotted against the measured ($^{238}\text{U}/^{232}\text{Th}$) value (on the x-axis), where the parentheses denote activity

ratios, or the rate of atomic disintegration (i.e. $\lambda_i N_i$; where λ_i is the decay constant and N_i is the number of atoms present). The diagram is divided across the middle by a line of equality between the two activity ratios (the 'equiline'; solid line Figure 2a) representing secular equilibrium at any value of ($^{238}\text{U}/^{232}\text{Th}$). The condition of secular equilibrium exists in a system closed to chemical perturbation and describes a system in which the activities of all nuclides in a decay chain are equivalent (described as $\lambda_1 N_1 = \lambda_2 N_2 = \dots = \lambda_n N_n$, where λ = the decay constant of the given nuclide and N = the number of atoms of a given nuclide). The equiline divides the Th-enriched side (left side) from the U-enriched side (right side) of the diagram. Prior to a chemical fractionation event, the mantle system is located along the equiline at a ($^{238}\text{U}/^{232}\text{Th}$) value equivalent to the Th/U ratio of the source ($\text{Th}/\text{U} = 3.034 / (^{238}\text{U}/^{232}\text{Th})$, where $\lambda_{238} / \lambda_{232} \times W_{\text{Th}} / W_{\text{U}} \times \text{Ab}_{238} / \text{Ab}_{232} = 3.034$, and λ , W and Ab are the decay constant, atomic weight and abundance of an isotope, respectively). When a fractionation event occurs, such as melt initiation in the mantle, the product (melt) and residue move away from each other to opposite sides of the equiline. The direction (i.e. either left or right of the equiline) the melt moves away from the equiline is determined by the bulk partition coefficients (D 's, where D is for solid/melt) for U and Th during melting, which are controlled by the mineralogic composition and mode (relative mineral abundances) of the mantle source and the individual mineral-melt K_d 's. If the event results in an activity ratio > 1 in the melt (e.g., ($^{230}\text{Th}/^{238}\text{U}$)), then the nuclide in the numerator is said to be in excess. Such melts are displaced to the left of the equiline and will return to secular equilibrium as the unsupported (excess) ^{230}Th decays away. Conversely, if the event results in an activity ratio < 1 the nuclide in the numerator is said to be in deficit and the material moves to the right of the equiline and returns to the equiline as the deficit in ^{230}Th ingrows from decaying ^{238}U (Figure 2a). The rate at which a given parent-daughter pair returns to secular equilibrium is dictated by the nuclide with the shortest half-life (i.e. ^{230}Th in the above example). As a general

rule of thumb, an activity ratio in disequilibrium will return to a state of secular equilibrium in the time equivalent to 5 half-lives of the shorter-lived nuclide (this is a practical limit, because after this amount of time any excess or deficit still present is effectively not detectable with modern instrumentation).

Simple batch (equilibrium modal) melting moves melt and solid away from the equiline along horizontal lines, but because this is strictly an equilibrium processes significant Th-U elemental fractionation can only occur at degrees of melting that are smaller than or equivalent to the values of bulk partition coefficients (~ 0.002 to 0.005). Although simple batch melting has not been completely abandoned as an explanation of U-Th systematics in volcanic rocks (see Condomines and Sigmarsson, 2000), it is difficult to resolve the extent of ^{230}Th -excesses commonly observed in MORB with the small extents of melting required to fractionate Th from U, and with the relatively high extents of melting inferred from major element compositions ($\sim 10\%$; Klein and Langmuir, 1987; Peate and Hawkesworth, 2005). This disparity, in part, has led to the development of more complicated ‘in-growth’ models to explain the ^{230}Th -excesses typically observed in MORB. These models, commonly referred to as ‘equilibrium dynamic melting models’ were first introduced for non-radiogenic elements by Langmuir et al. (1977), and later modified by McKenzie (1985) and by Williams and Gill (1989). In these models, a small volume of melt (referred to as residual porosity) is left in contact with the melting solid as it ascends through the melting column. As long as the residual porosity is similar to the partition coefficients of the elements under consideration, some elemental fractionation occurs and it is no longer only controlled by the degree of melting. Additionally, because this parcel of melt ascends with the residual solid, radiogenic in-growth of ^{230}Th in the ascending solid continually adds to the melt provided the melting rate is sufficiently slow. In these models the melt and residual solid will follow paths similar to those depicted schematically in Figure 2b. Because these models are dependent on both melting rate

and residual porosity, there is a trade off between these parameters which is described by the factor β , such that;

$$\beta = M / (\rho_s \phi + (\rho_f (1 - \phi)))$$

where M equals the melting rate in $\text{kg m}^{-3} \text{ yr}^{-1}$, ρ_s is the density of the solid in kg m^{-3} , ρ_f is the density of the melt in kg m^{-3} , and ϕ is the residual porosity. The relationship between M and $(^{230}\text{Th}/^{238}\text{U})$ as a function of ϕ is shown graphically in Figure 3 for the case in which the bulk partition coefficient and porosity are held constant during melting.

The above parameters can then be related to the depth of melting (or length of the melting column) by the relationship:

$$M = (W F \rho_m) / h$$

(Asmerom, 1999) where M is once again melting rate in $\text{kg m}^{-3} \text{ yr}^{-1}$, W is the solid upwelling rate in km yr^{-1} , F is the melt fraction, ρ_m is the density of the melt in kg m^{-3} and h is the height of the melting column in km. For the case of mid-ocean ridge magmatism it is reasonable to assume that W is set by the spreading rate of the ridge system and ρ_m can be considered a constant (2800 kg m^{-3}). This leaves the degree of melting (F), the melting rate (M) and the length of the melting column (h) unconstrained, but inextricably linked, meaning no one variable can be changed independently. The final model parameter having a systematic effect on ^{230}Th -excess is the depth at which melting initiates. It is possible to investigate the effect of initial depth of melting on the system by using an ‘incremental dynamic melting model’ (Stracke et al., 2003). This model uses the same basic equations originally presented by McKenzie (1985), but reworked to allow for calculation of residual modal mineralogy and therefore variable bulk solid/melt partitioning at different heights in the melting column. Figure 4a is a diagram of $(^{230}\text{Th}/^{238}\text{U})$ versus the depth of initiation of melting for 4 different values of F (0.05, 0.08, 0.12 and 0.15). In these models garnet is stable at depths $> 75 \text{ km}$ and melting occurs at a constant

productivity beginning at depths between 75 and 100 km depth, continuing to a depth of 10 km. For example, if melting initiates at 90 km depth and melts to a final F of 8% then melting proceeds at a constant productivity of 0.1%/km ascent (assuming mantle porosity is held constant at 0.2% and that the bulk D 's are the same as the examples described above). As demonstrated in Figure 4a the extent of ($^{230}\text{Th}/^{238}\text{U}$) disequilibrium increases as the depth of melt initiation deepens because the proportion of melt generated in the presence of garnet increases. Lower degrees of melting ultimately produce higher ^{230}Th -excesses relative to higher degrees of melting, in part because fertile phases such as clinopyroxene and garnet are consumed to a lesser extent per melting increment at smaller degrees of melting, and in part because productivity is lower over a given depth interval when compared to higher degree melts. This latter effect is demonstrated in Figure 4b. In summary, the models presented above show that ^{230}Th -excesses will be increased by lower porosity, lower degrees of melting, lower melting rates and increased melt initiation depth.

The second case study presented in this thesis (Chapter 3) focuses on the variability in U-series measurements along the Southeast Indian Ridge, an ~2500 km long section of the global spreading system over which a gradient in axial depth tracks a regional decrease in mantle temperature. In that chapter, uranium-series (U-series) measurements have been added to an already extensive suite of major and trace element concentrations and isotopic compositions. The results support a systematic regional variation in the style of melt production and sampling of discrete compositional heterogeneity in the Indian Ocean mantle that is only partly accounted for by previous models based on a broad global sampling of MORB (Bourdon et al., 1996).

1.2.3 Melt inclusions as a probe of melt composition variability along intermediate spreading ridges

A common characteristic of MORB chemistry is the occurrence of rare earth element (REE) patterns which are positively sloped from the LREE to MREE, and relatively flat or negatively sloped from the MREE to HREE (where L, M and H designate light, middle and heavy; e.g. $(\text{La}/\text{Sm})_n < 1$ and $(\text{Sm}/\text{Yb})_n \geq 1$, where n indicates chondrite normalized values). Gast (1968), followed by numerous other investigators (Bender et al., 1984; Hoffman, 1988; White et al., 1993; Frey et al., 1993; Shen and Forsyth, 1995, to name a few) suggested that the LREE to MREE pattern resulted from partial melting of the MORB mantle prior to the most recent melting event. The MREE-HREE characteristics have been largely attributed to the presence of minor amounts of residual garnet during the melting process. REE compositions are particularly diagnostic of source residual mineralogy because their mineral/melt partition coefficients are well constrained, ranging from highly incompatible at La to relatively compatible (especially in garnet-bearing assemblages) at Yb. However, open system behavior, magma mixing and homogenization at shallow levels in the mantle and/or crust may be effective at masking the volumetrically small contributions from deeper in the melting column where garnet is present.

Melt inclusions are thought to represent near-fractional melts that experienced less mixing and homogenization than the magmas which erupt as MORB at the seafloor (Saal et al., 1998; Sobolev and Shimizu, 1993; Shimizu, 1998; Sours-Page et al., 1999; Slater et al., 2001). Analysis of melt inclusions can therefore provide insight into the nature of the melting process and source compositions that may be masked by homogenization processes that presumably occur at shallower levels in these systems.

The third case study presented in this thesis (Chapter 4) focuses on the western Galapagos Spreading Center (GSC), a section of spreading ridge with an along-axis

gradient in axial depth and change in ridge morphology that is related to thermal and material input from the nearby Galapagos hotspot. The GSC has been the subject of detailed geophysical investigation that suggests a decrease in crustal thickness from east to west coinciding with the axial depth gradient (Canales et al., 2002; Detrick et al., 2002; Sinton et al., 2003; Behn et al., 2004; Cushman et al., 2004). This fourth chapter presents REE concentration data from a suite of melt inclusions hosted in plagioclase and olivine phenocrysts taken from basalts along the Galapagos Spreading Center. The melt inclusions are similar to, but more diverse than, the MORB lavas erupted along the GSC. The regional diversity of the melt inclusions is consistent with lavas closer to the hotspot having a larger contribution of melt generated in the presence of garnet. Forward modeling of the REE concentrations suggests the degree of melting is small in the garnet stability field, consistent with experimental predictions (Hirth and Kohlstedt, 1996; Hirschmann et al., 1999; Asimow and Langmuir, 2003; Asimow et al., 2004) and the basalt glass data from the lavas (Cushman et al., 2004), supporting a component of deeper melts generated at low productivities in the most strongly hotspot influenced lavas along the GSC.

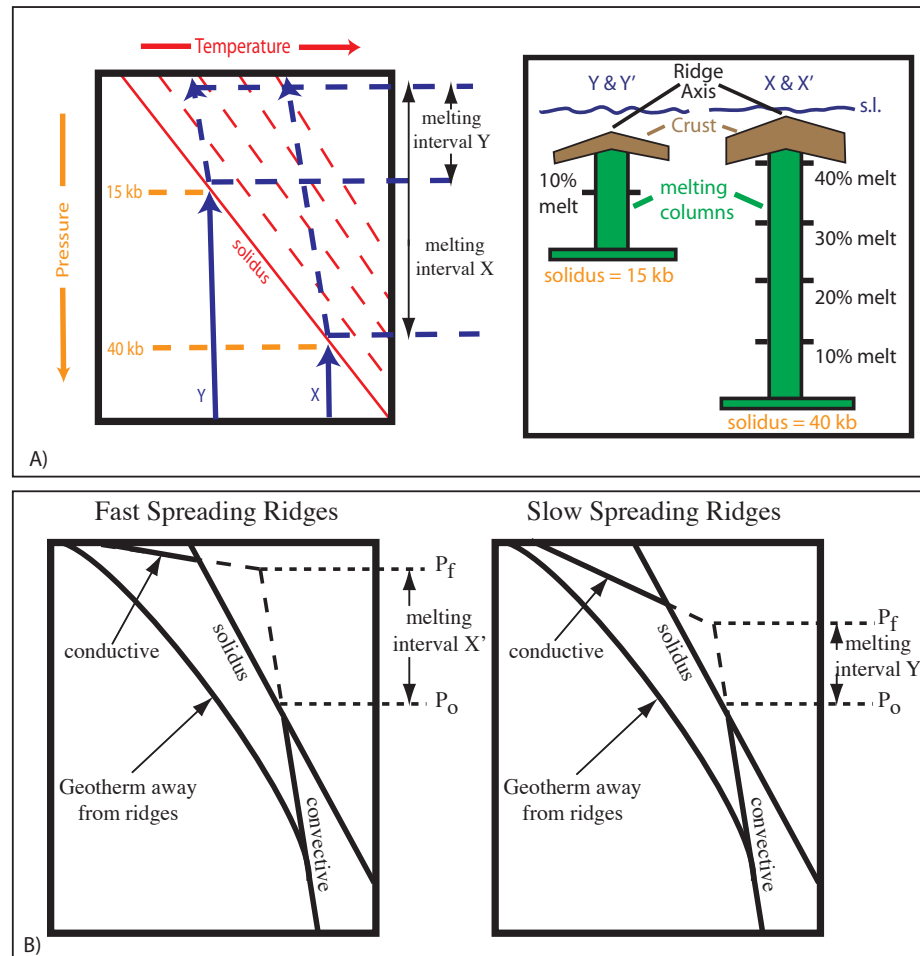


Figure 1-1. A) Schematic diagram from Klein and Langmuir (1988) of the intersection of 'hot' mantle (X) and 'cold' mantle (Y) with the solidus. Dashed lines represent increased degree of melting from 0 at the solidus to ~40% at the top of the diagram for X and ~20% at the top of the diagram for Y. Cartoon depiction of the effects of mantle temperature on the depth of melting and crustal thickness. 'Hot' mantle (X) is shown to intersect its solidus at greater depth which leads to higher degrees of melting, thicker crust and a shallower ridge axis depth when compared to relatively 'cold' mantle (Y). B) Schematic diagram demonstrating the potential effect of conductive cooling at fast versus slow spreading ridges (from Niu and Hekinian, 1997). In these schematics mantle upwelling along a similar adiabat (convective thermal gradient) will intersect the solidus at the same depth (P_o) and begin to melt. In this model, mantle beneath fast spreading ridges rises faster and is therefore able to melt to shallower depths (P_f) than mantle beneath relatively slower ridges. This leads to a greater melting interval, higher degree melts and thicker ocean crust just like in Klein and Langmuir's model, however, here the dominant control is spreading rate and not mantle temperature, which has been held constant.

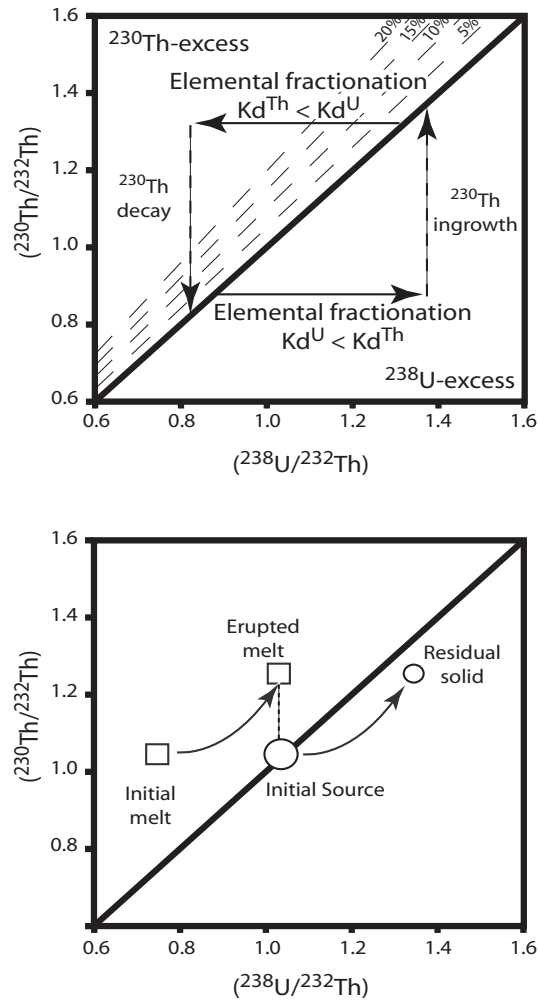


Figure 1-2. The ‘equiline’ diagram. Top) General systematics of the equiline diagram (after Elliott, 1997). The thick black line represents secular equilibrium. Relative fractionations are shown by the horizontal arrows. The vertical arrows represent the paths along which this fractionated material will return to secular equilibrium. The sub-parallel dashed lines indicate lines of equal ^{230}Th -excess with the amount of excess labeled on each line at the top of the diagram. Bottom) Schematic of the path traveled for a parcel of melt during dynamic melting in a system where $D_{\text{Th}} < D_{\text{U}}$. Initial fractionation of the source moves the first increment of melt to the left of the equiline (^{230}Th -excess), a complementary point (the residue would lie to the right of the equiline). In dynamic melting, if the melting rate is slow enough, in-growth occurs in the solid residue which supplies additional ^{230}Th the initial melt. Because fractionation has moved the residue to the right of the equiline and time has allowed it to decay back towards the equiline, the subsequent additions will plot above and to the right of the initial melt. The result of the combined effect is the curved path represented by the arrows which point to the final melt and residue, respectively.

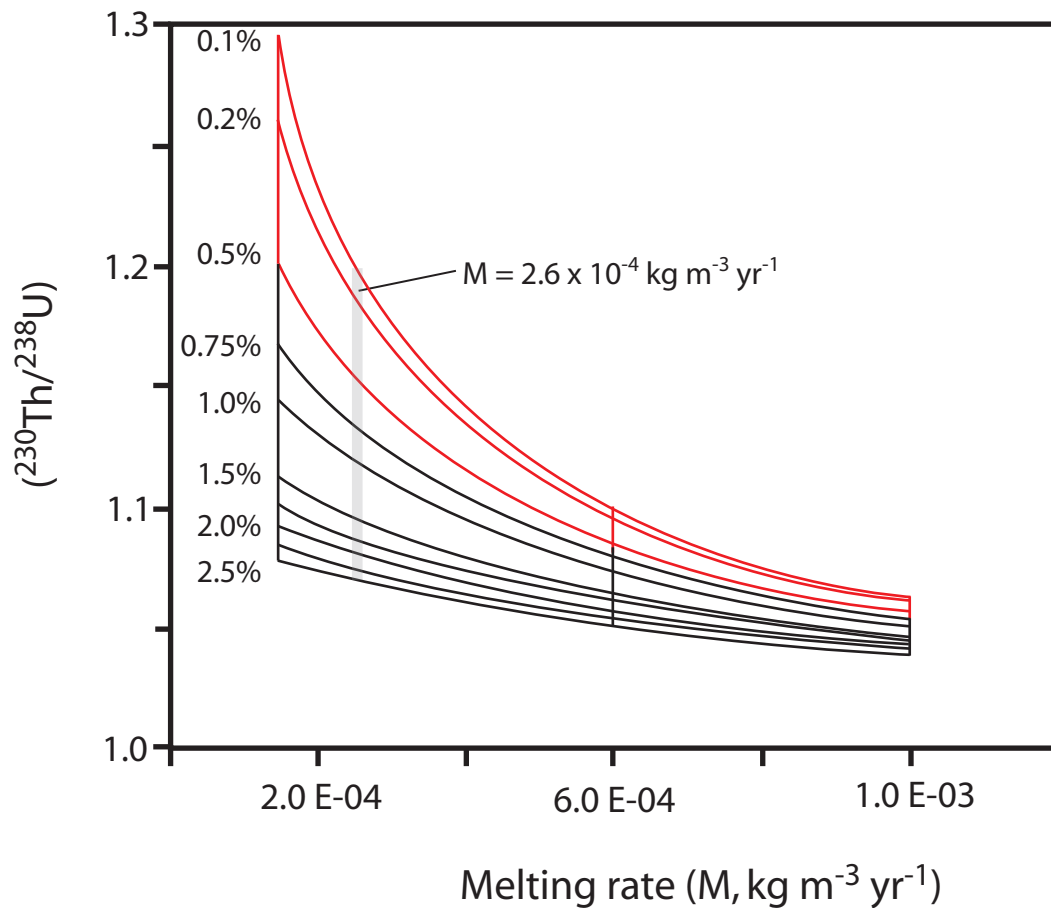


Figure 1-3. ($^{230}\text{Th}/^{238}\text{U}$) versus melting rate. ($^{230}\text{Th}/^{238}\text{U}$) values are calculated at varying mantle porosity and plotted against melting rate (after Stracke et al., 2003). ^{230}Th -excesses are calculated using the dynamic melting equations of McKenzie (1985) and Williams and Gill (1989). Bulk partition coefficients are from Salters et al. (2004) with $D_{\text{Th}} = 2.0 \times 10^{-3}$ and $D_{\text{U}} = 4.3 \times 10^{-3}$. Residual mantle porosity (ϕ) expressed as % along left hand side of curves. The model curves demonstrate the effect of melting rate and/or porosity on ^{230}Th -excesses. ^{230}Th -excesses decrease with increasing melting rate and/or porosity, all other factors being equal. The light grey vertical line demonstrates the maximum modeled melting rate capable of producing the entire range of ^{230}Th -excesses observed along the SEIR (Chapter 3) by varying only mantle porosity. The red model curves indicate constant porosity at which the melting rate variations can produce the entire range of ^{230}Th -excesses observed along the SEIR.

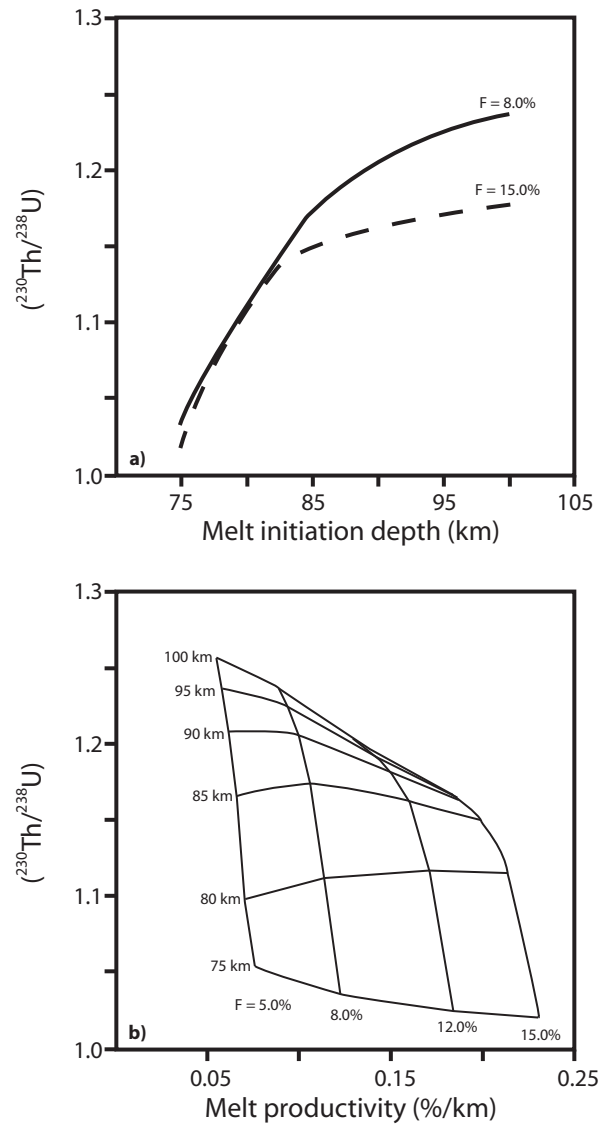


Figure 1-4. $(^{230}\text{Th}/^{238}\text{U})$ versus melt initiation depth and melt productivity. Model curves were generated using the ‘incremental dynamic melting’ equations of Stracke et al. (2003). Partition coefficients are from Salters et al. (2004) with $D_{\text{Th}} = 2.0 \times 10^{-3}$ and $D_{\text{U}} = 4.3 \times 10^{-3}$. In these models garnet is stable at depths > 75 km. a) The effect of increasing melt initiation depth on generating $(^{230}\text{Th}/^{238}\text{U})$ for two different final degrees of melting ($F = 8.0$ and 15.0%). b) $(^{230}\text{Th}/^{238}\text{U})$ versus melt productivity (%/km). Labeled horizontal lines indicate the depth of melt initiation and quasi-vertical lines indicate the maximum % of melting achieved in the melt column. Melt productivity is held constant at all heights in the melting column and melt production ceases at 10 km depth in each model. Mantle porosity for all models is 0.2% .

Chapter 2:
Development and evolution of the Australian-Antarctic Discordance:
A geochemical perspective

Chris J. Russo¹, David M. Christie¹ and Douglas G. Pyle²

¹ College of Oceanic and Atmospheric Sciences, Oregon State University, Corvallis,
OR 97331, USA

² SOEST, University of Hawaii, Honolulu, HI 96822, USA

2.1 Abstract

Ocean Drilling Program (ODP) Leg 187 sampled ~14-28 Ma oceanic crust north and east (Zone A) of the Australian-Antarctic Discordance (AAD) to evaluate the relationship between the basin-wide, seafloor depth anomaly, upper mantle melting conditions and the isotopic boundary between Indian and Pacific mid-ocean ridge basalt (MORB) mantle sources. Results of major and trace element analysis of basaltic glass recovered during this expedition are presented here. Basaltic rock compositions from ODP sites within the depth anomaly lack the high Na₂O signature that characterizes present-day AAD MORB, suggesting that mantle temperature and/or mantle upwelling beneath the AAD has declined significantly in the last 14 Ma. Consequently, contrasts between Indian and Pacific (AAD vs. Zone A) lavas in the ODP suite are muted to indistinguishable. Lavas sampled during ODP Leg 187 are the product of a more robust magma supply to the ridge axis during the period from ~14-28 Ma compared to their modern day counterparts.

2.2 Introduction

The Australian-Antarctic Discordance (AAD) located between ~118 ° E and 127 ° E along the Southeast Indian Ridge (SEIR) is centered on a regional, seafloor depression known as the Australian-Antarctic Depth Anomaly (AADA, Figure 1, Marks et al., 1992, 1999; Christie et al., 2004). The AADA spans the entire Southern ocean basin from the continental margins of Australia to Antarctica forming an arc-shaped trough that appears to record an eastward migration (~15 mm/yr) of the SEIR over a fixed, N-S oriented, cooler-than-normal, upper mantle thermal anomaly (Marks et al., 1992, 1999; Gurnis et al., 1998; Ritzwoller et al., 2003; Christie et al., 2004). Seafloor depths within the AADA are ~1 km deeper than surrounding oceanic crust

and are atypical compared to predictions of standard seafloor subsidence models (Geli et al., 2007). The AADA has existed in this region at least since the onset of seafloor spreading at 96 Ma (Cande and Mutter, 1982), and perhaps as long ago as 300 Ma, based on sedimentary basin subsidence that predates the initiation of continental rifting between Australia and Antarctica (Veevers, 1982). Seafloor spreading in this region occurred in at least two stages, beginning with a period of ultra-slow spreading from the time of initial break-up (spreading rates between 10 mm/yr and 4 mm/yr; Cande and Mutter, 1982; Veevers et al., 1990; Tikku and Cande, 1999) until about 43 Ma, followed by an abrupt increase to >60 mm/yr which has gradually increased to ~75 mm/yr at present (Vogt et al., 1984; Royer and Sandwell, 1989; Pyle et al., 1995). The AADA cuts obliquely across large transform faults and fracture zones that presently define the axial segments of the eastern AAD. In fact, magnetic anomaly lineations indicate that the crenulated, “discordant” offset spreading segments within the AAD have developed only over the past 25 Ma (Vogt et al., 1984; Marks et al., 1992, 1999). Therefore, configuration of the AADA appears to be decoupled from the spreading history in the region.

In the modern ocean basins, the AAD is truly unique. It is one of the deepest spreading centers in the global mid-ocean ridge system with an average depth of ~4500 m. The ridge segments within the AAD (also known as Zone B) are characterized by axial valley morphology, unusually low gravity signals, high upper mantle seismic velocities, chaotic off-axis topography, and large transform offsets (Weissel and Hayes, 1971, 1972, 1974; Forsyth et al., 1987; Marks et al., 1990; Sempéré et al., 1991; West et al., 1994, 1997), morphologic characteristics that are typically associated with slow (or ultraslow) spreading ridges (Sempere et al., 1991; Ma and Cochran, 1996; West et al., 1997, Christie et al., 1998). In contrast, the regions east of the 127°E transform (also known as Zone A) and west of the 118° E transform (also known as Zone C) are characterized by axial high ridge morphology

with smooth off-axis abyssal hills, morphologic characteristics that are typically associated with fast spreading ridges (Ma and Cochran, 1996; Sempere et al., 1997; Cochran et al., 1997). Tolstoy (1995) showed that the abrupt change in morphologic characteristics at the eastern AAD boundary coincides with a decrease in crustal thickness from ~7 km thick in Zone A to ~4 km thick within the AAD. A reduction in crustal thickness of this order, at normal mantle potential temperatures (1350° C) is predicted to be sufficient enough to change the crustal structure, from one capable of sustaining a magma lens to one more similar to a slow-spreading thermal structure having no quasi-steady state magma lens (Chen, 1996). Since spreading rate is uniform throughout this region (DeMets et al., 1990), differences in accretionary tectonics, axial morphology and crustal thickness can only be explained by a dramatic reduction in melt supply to the AAD spreading segments relative to the more robust melting beneath Zone A and C segments (Palmer et al., 1993; Sempéré et al., 1991, 1996; Christie et al., 2004).

The geochemical attributes of the AAD and Zone A lavas are equally distinctive as the physical contrasts summarized above. AAD lavas are high $\text{Na}_{8,0}$ and low $\text{Fe}_{8,0}$ MORB, and as a group are less evolved than lavas from Zone A (Klein et al., 1988; Pyle et al., 1995). MORB diversity in the AAD is dominated by partial melting effects and some high-pressure fractionation of a heterogeneous group of parental magmas. In Zone A, differentiation is dominated by low-pressure fractionation of a more limited range of parental melts. These characteristics suggest melt supply within Zone A is high enough to create and sustain a sub-axial magma system that aggregates melts, limits the range of parental magmas that erupt to the surface, and allows extensive low-pressure differentiation. The scarcity of evolved lavas (i.e., low MgO) in the AAD suggests an absence of low-pressure magma systems, and consequently, melting conditions unable to create and maintain such a system. Only high MgO (i.e. high temperature) lavas have the thermal inertia to breach the crust and erupt on the

seafloor. Furthermore, Zone A and AAD lavas are derived from upper mantle sources that are isotopically distinct, involving Pacific MORB mantle (PMM) and Indian MORB mantle (IMM), respectively (Dupre and Allegre, 1983, Klein et al., 1988; Pyle et al., 1992, 1994, 1995; Kempton et al., 2002; Hanan et al., 2004). The transition between these upper mantle domains occurs abruptly along a <25 km section of the easternmost AAD spreading center, where axial depth increases by 1 km and axial morphology transforms from an axial rise to an axial valley due to a drastic reduction in melt production between Zone A and the AAD (Pyle et al., 1992).

Given the confluence of geochemical and geophysical attributes within the AAD, ODP Leg 187 was proposed to locate the trace of the Indian/Pacific mantle isotopic boundary off-axis and determine whether the AADA and the isotopic boundary were inextricably linked, or whether or not, the isotopic boundary and AADA were migrating westward at different rates (Pyle et al., 1992, 1995; Lanyon et al., 1995) and therefore unrelated by mantle dynamics.

In recent years two arguments have been proposed for the existence and location of the AADA and the AAD ridge configuration. The first is supported by tomographic analyses and seismic wave inversions that suggest the AADA is the result of a Cretaceous age subducted oceanic slab that stagnated in the deep upper mantle, effectively cooling the shallow upper mantle beneath this portion of the ridge axis (Gurnis et al., 1998; Ritzwoller et al., 2003). An alternative explanation suggests that the mantle beneath this portion of ridge has been affected by the entrainment of lower continental material entrained during the rifting of Gondwana, an idea supported by Hf and Pb isotopic measurements made on basaltic glasses from this region (Alvarez, 1990; Hanan et al., 2004).

In this paper, we focus on MORB glass major and trace element contents of samples recovered from north of the AAD (Australian Plate) during ODP Leg 187 (Figure 1). Drilling sites penetrated Zone A and AADA crust to basement, recovering

samples with IMM and PMM source signatures (Christie et al., 2004). The isotope data show that the boundary between IMM and PMM is indeed associated with the eastern boundary (-500 m depth contour) of the AADA (Christie et al., 2004) and, by inference, likely originated with the AADA at the initiation of seafloor spreading. However, comparing major and trace element characteristics of 28-14 Ma samples recovered within the AADA to their “near-axis” (0-5 Ma) AAD counterparts demonstrates that the extent of upper mantle melting beneath the AADA has significantly declined over the last 14 Ma. All of the ODP lavas, whether from IMM or PMM sources, have major and trace element characteristics that more closely resemble modern lavas from the SEIR outside the AAD.

2.3 Sample Selection, Analytical Methods and Results

Fresh basaltic glass was recovered from 21 holes at 13 sites during ODP Leg 187. A total of 171 glass samples were mounted into 1-inch epoxy rounds for major element analysis on a Cameca SX 50 electron microprobe at Oregon State University. In addition to these analyses, 51 measurements were made on standard glass USNM 113498/1 VG-A99 during the same analytical sessions. The accuracy of these measurements $[\frac{\text{measured}-\text{accepted}}{\text{accepted}}*100]$ for the seven major element oxides (abundances greater than 1 wt.% oxide) agree to within 1.0% (relative) of the accepted values. The sole exception is sodium, which agrees to within 2.1% (relative) of the accepted value (measured= 2.60 wt.%; accepted= 2.66 wt. %, n=51). From these data, 33 distinct chemical groups were identified by their separation on multiple major element variation diagrams.

Representative glass samples from 29 of the 33 chemical groups were hand picked under binocular microscope to eliminate phenocryst and alteration phases. Glass samples were then cleaned, dissolved and analyzed for trace elements on a VG

Excell quadrupole inductively coupled mass spectrometer following the methods used at OSU (see Pyle et al., 1995 for detailed procedure).

Major element results for the 33 distinct chemical groups and trace element results for samples representative of 29 of these groups are reported in Table 1. In general, all ODP Leg 187 lavas are typical N-MORB ($(\text{La}/\text{Sm})_n < 0.9$ and $\text{K}_2\text{O}/\text{TiO}_2 < 1.5$) and have experienced a limited range of fractionation (8.84-6.81 wt.% MgO). The most evolved group was sampled at Site 1154 in ~28 Ma crust of Zone A2. The least evolved groups were sampled from Site 1160 (Hole B) in ~22 Ma crust of Zone A3 and Site 1164 (Hole B) in ~18 Ma crust of Zone B5. There is no definitive means of ensuring basalt sampled off-axis was erupted in place at the ridge axis (Humler et al., 1999; Fisk and Kelley, 2002). However, several lines of evidence suggest the lavas sampled during ODP Leg 187 were formed at or close to the ridge axis via melting processes that are commonly observed along ridge axes today. All ODP Leg 187 lavas plot within fields for 'zero-age' lavas from the region surrounding the AAD. Distinct trends for Zone A1, A2 and A3 lavas have been recognized by Pyle (manuscript in prep.) that indicate lavas erupted within Zone A3 are characterized by slightly higher $\text{CaO}/\text{Al}_2\text{O}_3$ and CaO , and lower SiO_2 , than Zone A1 or A2 lavas. The only ODP Site to sample Zone A3 crust (Site 1160) shares these characteristics. Finally, average values for $\text{CaO}/\text{Al}_2\text{O}_3$, $\text{Na}_{8.0}$, $\text{Fe}_{8.0}$, $(\text{Sm}/\text{Yb})_n$ and Zr/Y for these lavas are similar to those reported by Humler et al. (1999) as representative of typical MORB sampled globally, and perhaps more importantly, are nearly indistinguishable from the values reported by Humler et al. (1999) as representative of average MORB erupted along the EPR (Table 2).

2.4 Site Locations and Tectonic Settings

In order to place the ODP Leg 187 sites into an historical perspective we

have used the ~19 and 14 Ma reconstructions of Marks et al. (1999) to determine the locations of these drill sites at their time of eruption relative to local tectonic structures. Nine of the ODP sites were sampled from seafloor older than 19 Ma (28-19 Ma; Sites 1152-1158 and 1160-1161) and four are younger (19-14 Ma; Sites 1159 and 1162-1164). In terms of the present axial configuration of the AAD, two sites cored into B4 crust (ODP Sites 1152 and 1163), three sites cored into B5 crust (ODP Sites 1155, 1156, 1164), five sites cored into A1 crust (ODP Sites 1153, 1157, 1158, 1161, 1162), two sites cored into A2 crust (ODP Sites 1154 and 1159) and a single site cored A3 crust (ODP Site 1160). Figures 2a and 2b show the locations of ODP sites relative to the ridge axis, transform faults and pseudofault traces as depicted by Marks et al. (1999) at ~19 and ~14 Ma, respectively. In addition to their tectonic setting we have also used the isotopic characterization of ODP Leg 187 lavas from Christie et al. (2004) to divide the ODP sites into three tectonic/geochemical groups (see below).

2.4.1 Group 1

Group 1 lavas were sampled from the three easternmost sites and vary in age from ~28 Ma to ~14 Ma (ODP Sites 1154, 1159 and 1160). Two of these sites were erupted in crust equivalent to present day Zone A2 (ODP Sites 1154 and 1159), and one was erupted in crust equivalent to present day Zone A3. Isotopic analyses of lavas from this group have determined them to be PMM lavas. Group 1 lavas encompass the largest range in MgO (8.84 to 6.81 wt.%) and include the most evolved lavas (Site 1154). These lavas define typical smooth low-pressure fractional crystallization trends in MgO diagrams, and are considered to be representative of 'normal' axial lavas erupted during the period 28-14 Ma.

2.4.2 Group 2

Group 2 lavas were sampled from the four westernmost sites and vary in age from ~25 Ma to ~17 Ma (ODP Sites 1152, 1155, 1163 and 1164). Two of these sites were erupted in crust equivalent to present day Zone B5 lavas (ODP Sites 1155 and 1164) and two were erupted in crust equivalent to present day Zone B4 (ODP Sites 1152 and 1163). Isotopic analyses of lavas from this group have determined them to be IMM lavas. These lavas encompass a slightly smaller range in MgO (8.81 to 7.09 wt.%) than Group 1 lavas, but also define typical smooth low-pressure fractional crystallization trends in MgO diagrams. Group 2 lavas are considered to be representative of 'normal' axial lavas erupted during the period 28-17 Ma.

2.4.3 Group 3

Group 3 lavas were sampled from six sites in close proximity to the -500 m counter line of the AADA and vary in age from ~28 Ma to ~18 Ma. Five of these sites were erupted in crust equivalent to present day Zone A1 lavas (ODP Sites 1153, 1157, 1158, 1161 and 1162) and one site was erupted in crust equivalent to present day Zone B5 lavas (ODP Site 1156). Collectively these sites record the complex boundary between PMM and IMM sources originally recognized in 0-5 Ma basalts (Klein et al., 1988; Pyle et al., 1995) and now recognized to be closely related to the eastern boundary of the AADA since 28 Ma or earlier (Christie et al., 2004). The oldest samples in this group (ODP Site 1153) are the only samples recovered with transitional isotopic character between PMM and IMM sources. Site 1156 is in ~22 Ma crust erupted just west of the 127°E transform fault that bounds the eastern side of the AAD and has an IMM isotopic character. Sites 1157, 1158 and 1159 (~22, 20 and 19 Ma, respectively) are located just east of the 127°E transform fault. Near these

sites, a series of three propagating rifts created westward pointing (towards the AAD) pseudofault traces that are apparent in the Marks et al. reconstructions (Figure 2) and in present day seafloor bathymetry (Christie et al., 2004). At Site 1157, close to an inferred pseudofault, both IMM and PMM lavas were recovered while farther south at Site 1158, inside the pseudofault, only PMM lavas were recovered. At Site 1161 close to, but outside a second pseudofault, only IMM lavas were recovered. Together these sites record a transient (~3 m.y.) westward migration of the Pacific/Indian boundary similar to that which has been occurring along Segment B5 for the last ~5 m.y. (Pyle et al., 1992, 1995; Christie et al., 2004). The final site in this group (ODP Site 1162) is located south and east of Site 1161 and contains only IMM lavas. Lavas from this group encompass a smaller range in MgO (8.32 to 7.53 wt.%) and do not form smooth trends on MgO variation diagrams.

2.5 Major Element Populations, Mantle Domains and the Evolution of the AAD

2.5.1 Changes in the Indian and Pacific MORB Populations

A surprising result from the major element analyses of ODP Leg 187 lavas is that 28-14 Ma AADA lavas are unlike their modern equivalents within the AAD (Figure 3). In fact, AADA lavas are more similar to Zone A compositions, past and present. Most striking is the complete absence of the high Na₂O concentrations among AADA lavas, a hallmark of the modern AAD compositions (Klein et al., 1987; Pyle, 1995). One would expect seafloor lavas within the depth anomaly to be similar to AAD lavas over time if mantle melting was a major factor in creating the AADA feature. However, the majority of ODP Leg 187 major and trace element compositions, whether IMM, PMM or transitional, fall outside the near-axis AAD field and within the near-axis Zone A field. Therefore, it appears the extent of melting beneath the AADA has significantly declined since ~14 Ma without a significant

effect on the magnitude of the depth anomaly. This evolving magmatic history places important constraints on the origin and evolution of the AADA and its modern equivalent, the AAD.

Despite the significant compositional shift between ODP Leg 187 lavas and present-day AAD lavas, Leg 187 IMM and PMM lavas define nearly exclusive fields on SiO_2 , FeO and to a lesser extent, Al_2O_3 versus MgO diagrams (Figure 3). The offsets between Leg 187 PMM and IMM fields are in the same sense as those for modern AAD and Zone A lavas although the field boundaries are shifted in some cases. Within Groups 1 and 2, lavas define linear MgO variation trends that are consistent with fractional crystallization at low pressures (Figure 3). Group 2 (IMM) lavas are offset to higher values of SiO_2 , Na_2O and Al_2O_3 and lower values of FeO^* at a given MgO relative to Group 1 (PMM) lavas. Most of these characteristics are consistent with Group 2 magma production by lower degrees of melting that initiated from shallower mantle depths. However, the relatively low TiO_2 contents at a given MgO, similar rare earth element patterns (Figure 4), and their isotopic characteristics suggest these differences may reflect a lithological or compositionally distinct IMM source (Durpé and Allègre, 1983; Mahoney et al., 1989, 1992; Janney et al., 2005; Meyzen et al., 2005). Group 3 lavas encompass a smaller range in MgO (8.32 to 7.53 wt.%) while maintaining a similar range in other oxides compared to either Group 1 or 2. This is especially apparent in Al_2O_3 (16.02 to 14.38 wt.%), CaO (11.83 to 10.18 wt.%) and Na_2O (2.94 to 2.63 wt.%). Group 3 lavas cannot be related by simple low-pressure fractional crystallization. Significant variations in major oxides over a limited MgO range reflect either: 1) multiple parental magmas (i.e. variation in depth and degree of melting); 2) polybaric fractional crystallization; and/or 3) variation in mantle source compositions. This petrogenetic complexity is consistent with the isotopic variability and inferred complex tectonic boundaries in the vicinity of these sites at the time of their eruption.

The tendency for Group 3 lavas to consistently plot off the low-pressure fractional crystallization trends, to higher values of Al_2O_3 and Na_2O and lower values of CaO , mimics that of lavas erupted near propagating rift tips in Zone A and Segment B5 today (Figure 3; Pyle, 1994). Similar variations have also been discussed by Eason and Sinton (2006) for a group of lavas erupted near the 95.5° W propagating rift along the Galapagos Spreading Center (GSC). The similarity of Group 3 lavas to those erupted near other propagating rift tips is consistent with their inferred eruption during an ~22 to 19 Ma transient ridge propagation event, likely associated with the westward migration of the Pacific/Indian boundary.

2.5.2 Changes in Melting Conditions

Two key major element ratios $\text{CaO}/\text{Al}_2\text{O}_3$ (wt. % oxide ratio) and $\text{Ca}\#$ (molar $\text{CaO}/(\text{CaO}+\text{Na}_2\text{O})$ ratio) are plotted in $\text{Mg}\#$ (molar $\text{MgO}/(\text{MgO}+\text{FeO}^*)$ ratio) variation diagrams (Figure 4). In both diagrams fractionation proceeds from higher to lower values of both ratios. Lower $\text{CaO}/\text{Al}_2\text{O}_3$ at constant $\text{Mg}\#$ generally indicates an increase in the pressure of fractionation (le Roux et al., 2002) while lower $\text{Ca}\#$ indicates a decrease in the overall percent of melting (Schouten et al., 1987; Schilling et al., 1995). As in the oxide-oxide variation diagrams (Figure 3), the ODP Leg 187 lavas define trends similar to those of the near axis PMM lavas. Exceptions include a few Group 3 lavas that plot below the main trends in the $\text{Mg}\#$ vs. $\text{CaO}/\text{Al}_2\text{O}_3$ diagram; these lavas plot near the 0-5 Ma propagating rift trend, reflecting the more complex petrogenesis associated with rift propagation.

The absence of modern day AAD-type lavas (low $\text{Ca}\#$ at moderately high $\text{Mg}\#$) in the ODP Leg 187 suite is consistent with the 28-14 Ma lavas deriving from higher degree melts. The slightly lower $\text{Ca}\#$ values for Group 3 along with their wide range in $\text{CaO}/\text{Al}_2\text{O}_3$ values suggests these lavas may have been produced by slightly

lower degrees of melting, and underwent fractional crystallization at a wider range of pressures. Although there is considerable overlap, $\text{CaO}/\text{Al}_2\text{O}_3$ and Ca\# are generally higher for ODP Leg 187 PMM lavas relative to IMM lavas. However, it is difficult to resolve whether this relationship is process related or is the result of differences in source composition between PMM and IMM sources.

2.5.3 Changes in Parental Magma Compositions

In order to compare parental compositions for ODP Leg 187 lavas to those for the near-axis lavas as well as those representative of the global MORB dataset, we calculated fractionation-corrected Na_2O , SiO_2 and FeO^* values (see caption Figure 5 for calculation). The resulting fractionation corrected compositions are plotted in Figure 5 along with fields for the near-axis PMM and IMM lavas.

The normalized compositions emphasize two important differences between the ODP Leg 187 and near-axis lava populations. The first is that the distinctively high $\text{Na}_{8,0}$ lavas of the AAD were not present prior to ~17 Ma. The second is that the ODP Leg 187 PMM lavas have high $\text{Fe}_{8,0}$ relative to the ODP Leg 187 IMM lavas. Overall, the ODP Leg 187 lavas are orthogonal to the global array (gray line in Figure 5), suggesting that they represent local trends as identified by Klein et al. (1989) and Langmuir et al. (1993). These trends should represent suites of melts that are derived from different depths in the melting column and delivered to the ridge axis without significant intermingling. The coherence of the ODP Leg 187 local trend suggests we have correctly identified the LLD slopes for these populations.

Most ODP Leg 187 lavas have lower $\text{Na}_{8,0}$ than their near-axis counterparts. The only exceptions are a couple IMM lavas from Group 3 that plot at the lower end of the near-axis IMM field. The lower $\text{Na}_{8,0}$ values of ODP Leg 187 lavas are consistent with their derivation by higher degrees of melting. The majority of ODP

Leg 187 lavas also have high $Si_{8,0}$ values similar to those for near-axis PMM lavas. The exceptions are once again for Group 3 IMM lavas that have slightly higher $Si_{8,0}$. However, no ODP Leg 187 lavas have $Si_{8,0}$ values as high as those observed for the near-axis IMM lavas erupted within the modern AAD. Lower $Si_{8,0}$ is also indicative of a higher pressure and degree of melting (Langmuir et al., 1993). Maximum degrees of melting can be estimated from normalized compositions using the methods of Niu and Batiza (1991). ODP Leg 187 compositions lead to estimates of between ~16 and ~19%, comparable to estimates for the East Pacific Rise (EPR) between 8° and 14° N (Niu and Batiza, 1991). These maximum degrees of melting can then be used to calculate the average crustal thickness across the AAD region. ODP Leg 187 lava compositions when treated in this way suggest average crustal thickness of ~7 km during the period from ~28 to ~14 Ma. This corresponds well with the value determined using seismic refraction measurements (~7.2 km) for Zone A near 132° E (Tolstoy, 1995), a self-consistent result given the similarity of ODP Leg 187 lavas to those sampled from ‘zero’-age crust within Zone A. From a morphological perspective this value is also interesting, because it exceeds the threshold value (> 6 km) determined by Chen (1996) as sufficient for supporting an axial magma chamber and thus a ‘fast’ spreading morphology at the intermediate spreading rate in this region.

2.5.4 Trace element characterization

ODP Leg 187 glasses generally have trace element compositions typical of N-MORB (e.g. $Zr/Nb > 30$, $Y/Nb > 10$ and $(La/Sm)_n < 0.75$). Incompatible trace element ratios, such as Zr/Nb or $(La/Sm)_n$, can reflect subtle differences in mantle melting when melt fractions are small (e.g. 0.01 to 0.05). However, when melt fractions are larger (> ~0.10) incompatible trace element ratios are relatively insensitive to small

changes in melt fraction (Gast, 1968; Shaw, 1970; Schilling, 1973; Bender et al., 1984; Hoffman, 1988, 2003).

Considering only the ODP Leg 187 lavas, the concentration ranges for the rare earth elements (REE) are virtually indistinguishable between Groups 1, 2 and 3 and between PMM and IMM sources. The similarity in REE concentrations of the ODP Leg 187 lavas also distinguishes these lavas from their near-axis counterparts (Figure 6). All ODP Leg 187 lavas are depleted in light rare earth elements (LREE) relative to the middle and heavy rare earth elements (MREE and HREE, respectively). The ODP Leg 187 PMM lavas cover a slightly larger concentration range ($[La]_n \sim 3$ to ~ 25) than the ODP Leg 187 IMM lavas ($[La]_n \sim 7$ to ~ 20). The Group 1 lavas have more restricted Eu anomalies and cover a smaller range in normalized compositions than their near-axis counterparts, consistent with the more limited MgO range of Group 1 lavas relative to near-axis Zone A lavas. In addition, there are 2 other notable differences in the Group 2 and Group 3 lavas relative to the modern-day AAD lavas; 1) the absence of enriched (e.g. $(La/Sm)_n > 1$) lavas in Group 2 supports their derivation by higher degree melts and 2) the parallel REE patterns extending to higher normalized concentrations suggests Group 2 has experienced more fractional crystallization than their near-axis counterparts. The effect of fractional crystallization is to raise REE concentration without significantly altering REE/REE ratios (Hékinian et al., 1995). For example, assuming a bulk partition coefficient (K_D) of 0.12, a sample with $[La]_n = 12$ can be raised to $[La]_n = 20$ with $\sim 40\%$ fractional crystallization, while the $(La/Sm)_n$ would remain constant (Figure 6).

The overall similarity of Groups 1, 2 and 3 lavas to each other and to those of modern-day Zone A lavas supports the presence of a more robust ridge system operating throughout this region during the period from ~ 28 Ma to at least 17 Ma.

2.6 Discussion

2.6.1 Models for the evolution of the AAD

Plate motion reconstructions by Gurnis and co-workers (Gurnis et al., 1998, 2001; see also Ritzwoller et al., 2003) have suggested that the origin and ongoing dynamics of the AAD and the AADA can be attributed to the persistence of ancient subducted material in the lower part of the upper mantle. This material, derived from Cretaceous subduction of the Pacific plate beneath Gondwana, effectively reduces the temperature of the upper mantle, leading to reduced melt production. Further, based on simple dynamic modeling, Gurnis and co-workers (Gurnis et al., 1998, 2001) postulated that some of this subducted material has, within the last few million years, become entrained in the upwelling mantle beneath the AAD. Because this dynamic model incorporates a constant mantle viscosity with no depth dependence, its validity has been questioned by Christie et al. (2004), based in part on the early geochemical data from ODP Leg 187 and in part on earlier, variable viscosity models of West et al. (1997). More recently, Lin et al. (2002) developed a new variable viscosity model, in which, cold, viscous, deep mantle material can be entrained into the upwelling region only during the early stages of ocean basin formation. Their model shows that, for the region around the AAD, this effect would have been greatest soon after the ~45 Ma increase in spreading rate, and that the effect would diminish over approximately 20 million years. If this were true, the influence of the 'cold' anomaly would have been strongest ~40 to 20 Ma, after which time the enhanced upwelling of the anomalously cold material would have diminished due to increasing distance from the colder, thick continental margins.

If the entrained anomalous material reached the melting region, both a subduction related compositional signature and evidence of a negative thermal impact (i.e. thin crust, low volume, shallow melts) should have been present prior to ~20 Ma,

within the area covered by ODP Leg 187. However, the ODP Leg 187 lavas record no subduction signature. For example, Leg 187 lavas have $Ba/Th = 32$ to 90 and $Th/Nb = 0.06$ to 0.08 compared to lavas from the East Scotia Ridge and Lau back arc (Ba/Th up to 300 and 500 ; Th/Nb up to 0.5 and 0.9 , respectively) and the Leg 187 lavas are within values for the Southeast Indian Ridge (SEIR) between $88^\circ E$ and $114^\circ E$ ($Ba/Th = 60$ to 220 and $Th/Nb = 0.04$ - 0.09). This is consistent with the findings of Hanan et al. (2003) whose Hf isotope measurements preclude a Cretaceous parent-daughter fractionation event (which would be expected if slab material is present in the mantle beneath the AAD). Rather, the Hf isotope data require a much older Proterozoic (or older) subcontinental lithospheric component in the AAD source. More recently Janney et al. (2005) and Meyzen et al. (2005) have suggested that ancient continental lithospheric material is a common and widespread component within the western Indian Ocean mantle.

In light of our inference that a more robust magma supply existed in this region during the period from ~ 28 Ma to ~ 17 Ma, perhaps the most intriguing result of the Lin et al. model is the prediction of enhanced upwelling during time periods when the continental margin was still close to the spreading axis. In their model, the first 20 to 30 Myr of rifting is dominated by the translation of the thick continental keels of the Australian and Antarctic continents, favorably driving upwelling behind these keels or beneath the ridge axis. After about 40 Myr their model predicts this 'boost' would diminish and upwelling would return to normal oceanic spreading.

Consistent with the apparent decline in magma production beneath the developing AAD since ~ 20 Ma, we suggest a modification of the Lin et al. (2002) model. From ~ 45 Ma (when spreading rates along the SEIR sharply increased) to ~ 20 Ma, magma supply beneath the proto-AAD was enhanced by relatively rapid upwelling driven by continental separation. By about 20 Ma, the continents were sufficiently far apart that the enhanced upwelling began to fade, leading to a gradual

reduction in melt supply, and ultimately to the present-day deep axial valleys of the AAD. This change appears to coincide with two other important observations. First, magnetic anomaly interpretations by Vogt et al. (1984) show that the transform faults that define the AAD began to develop at ~25 Ma, and that persistent spreading asymmetries since that time have led to the present segmented, crenulated configuration of the AAD. Second, a recent study of the SEIR by Geli et al. (in press) reveals a significant change in subsidence rates on the flanks of the AAD at ~20 Ma.

Any model must allow for the long-term persistence of the AADA. This problem is not explicitly addressed by any of the models discussed above and a thorough examination is beyond the scope of this paper. However, it is interesting to note that Schilling et al. (1995) speculated that the long term mantle history beneath the Mid-Atlantic ridge equatorial 'coldspot' and its connection to the western boundary of the Pangean supercontinent may play a role in the existence of this 'unusual' portion of the mid-Atlantic ridge.

2.7 Conclusions

1. Major element characteristics of lavas erupted near the eastern boundary of the AADA, between 28-14 million years ago, are consistent with their derivation as higher degree melts originating from greater depths within the mantle compared to lavas erupted within the AAD since 5 Ma.
2. Lavas erupted between 25 and 17 Ma along the eastern trace of the AADA (Group 3 lavas) have low $\text{Ca}/\text{Ca}+\text{Na}$ and $\text{CaO}/\text{Al}_2\text{O}_3$, and relatively high $\text{Na}_{8,0}$, consistent with derivation from slightly lower degree melts. Group 3 lavas represent the older such identified lava-types and their location and age is consistent with the timing and location of the initial tectonic reorganization suggested by Vogt (1984) and summarized by Marks et al., (1990; 1999).

3. Trace element ratios of ODP Leg 187 lavas are consistent with their derivation from 'normal' degrees of melting and do not support a link to either a hydrous or sedimentary subducted component in the mantle source region of these basalts.
4. Following Lin et al. (2002), we favor a model in which enhanced upwelling caused by the close proximity of a thick continental keel increased the amount of melt delivered to this portion of the SEIR until circa 20 Ma. Greater degrees of melting were achieved beneath the ridge axis during this time, allowing a 'fast'-spreading morphology to be maintained. After about 20 Ma, the present day configuration of the AAD began to develop as the continents were moved further from the ridge axis by plate spreading. Mantle upwelling and the degree of melting lessened, resulting in a thinner crust and eventually to the 'slow'-spreading morphology present within the AAD today.
5. The persistence of the AADA despite these changes in melting characteristics suggests this basin-wide feature is not solely controlled by local melting systematics.

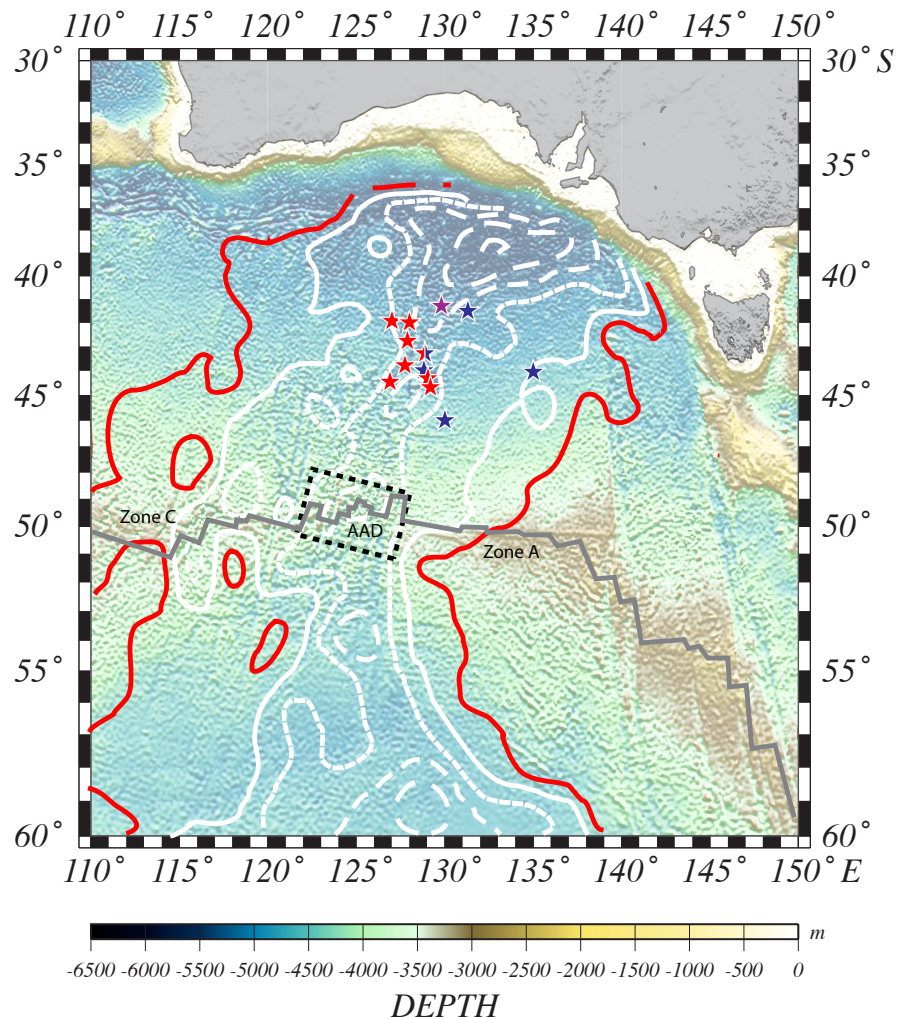


Figure 2-1. Regional map of the southeastern Indian Ocean basin between 110° E and 150° E. Ocean Drilling Program Leg 187 site locations are shown as stars colored coded by the isotopic signature of each site (Red = IMM, Blue = PMM, Purple = TMM; see text for discussion). The solid red line depicts the trace of ‘normal’ seafloor depth (i.e. depth anomaly = 0), white lines (solid and dashed) depict contour intervals (-200 m) of the basin wide Australian-Antarctic Depth Anomaly (AADA), modern-day SEIR is depicted by the solid gray line and the portion of ridge axis within the Australian-Antarctic Discordance is shown by the dashed yellow box.

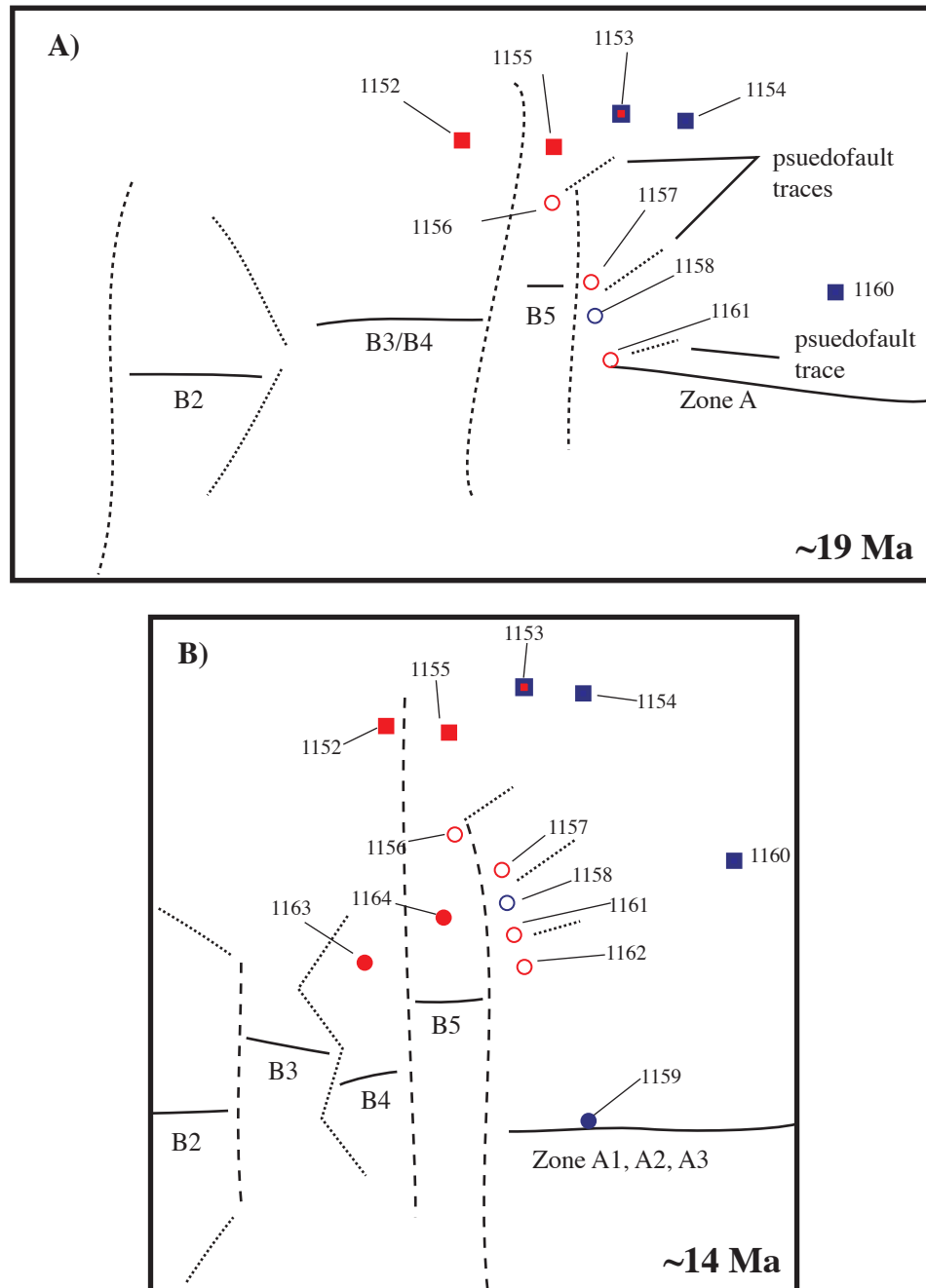


Figure 2-2. Line drawings of the Southeast Indian Ridge from $\sim 115^{\circ}\text{E}$ to $\sim 135^{\circ}\text{E}$, solid line represents the trace of the ridge axis (letter and number distinctions refer to the current ridge segment nomenclature), dotted lines represent non-transform offsets and dashed lines represent transform faults. Numbered symbols refer to drill site locations from the Ocean Drilling Program's Leg 187, symbols are color coded by mantle source (red) Indian, (blue) Pacific, (mixed) Transitional and represent tectonic groups (solid blue symbols) Group 1, (solid red symbols) Group 2, (open and mixed symbols) Group 3 (see text for explanation of groups). A) Ridge axis at ~ 19 Ma; B) Ridge axis at ~ 14 Ma (drawings adapted from Marks et al., 1999).

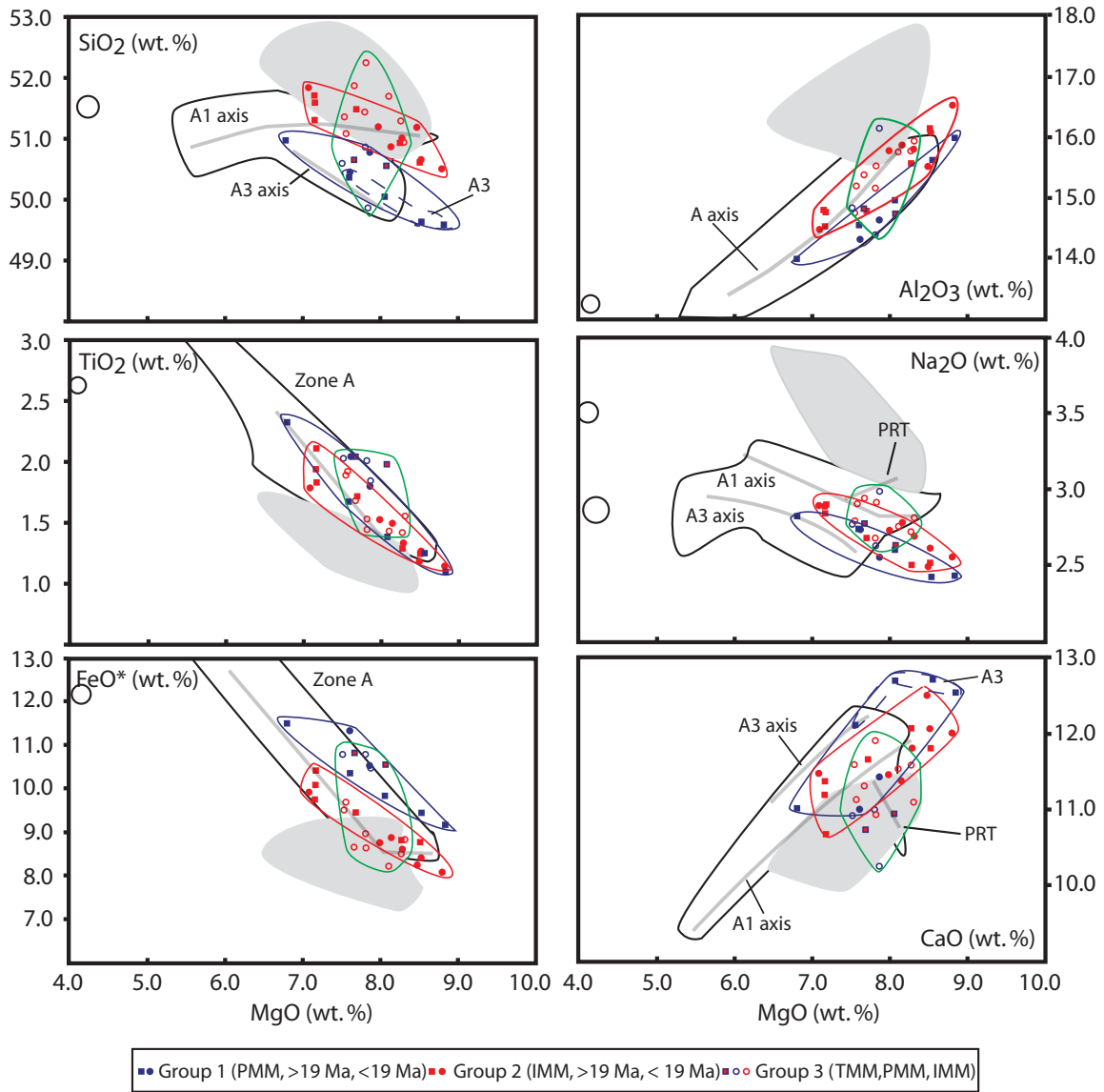


Figure 2-3. Oxide- Oxide variation diagrams. Selected major elements in oxide weight percent plotted against oxide weight percent MgO. Data points represent individual chemical groups and correspond to the tectonic groups identified in Figure 2. Trends of Groups 1, 2 and 3 are highlighted by the blue, red and green outlines, respectively. Where trends distinctive of Zone A3 are relevant they are labeled A3 and outlined by dashed, blue fields. Other data fields represent those of the near axis (0-5 Ma) lavas erupted within the AAD (gray field) and to the east of the AAD in Zone A (open field). Trend lines define the unique characteristics of Zone A segments when consistent variation is present and for propagating rift tips.

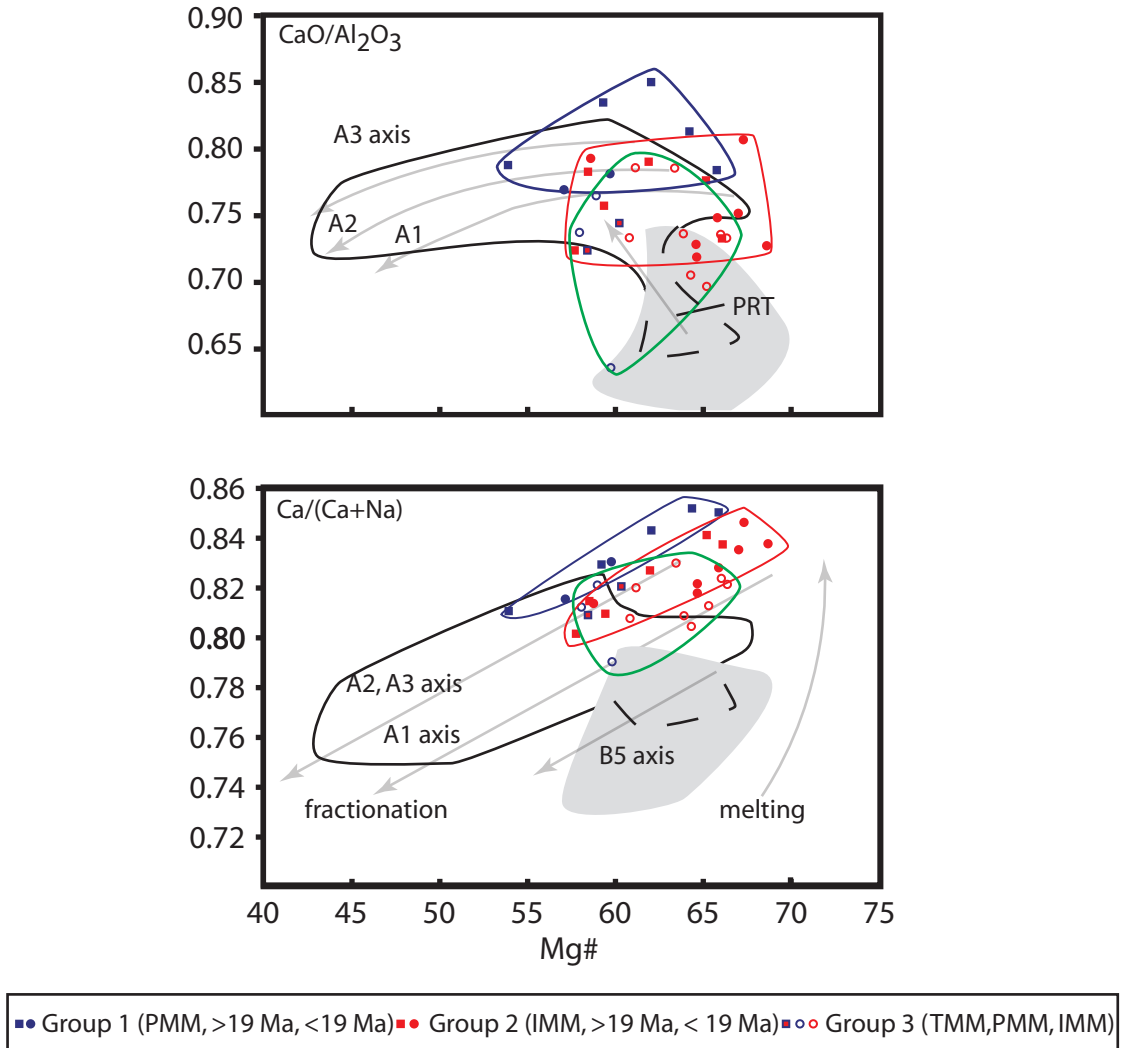


Figure 2-4. Major element ratio diagrams. A) $\text{CaO}/\text{Al}_2\text{O}_3$ vs. $\text{Mg}\#$ (molar $\text{MgO}/(\text{MgO}+\text{FeO})$, where FeO is 0.9 FeO^*). B) $\text{Ca}\#$ vs. $\text{Mg}\#$ (where $\text{Ca}\# = \text{molar CaO}/(\text{CaO}+\text{Na}_2\text{O})$). Symbols and fields are the same as in Figure 2.

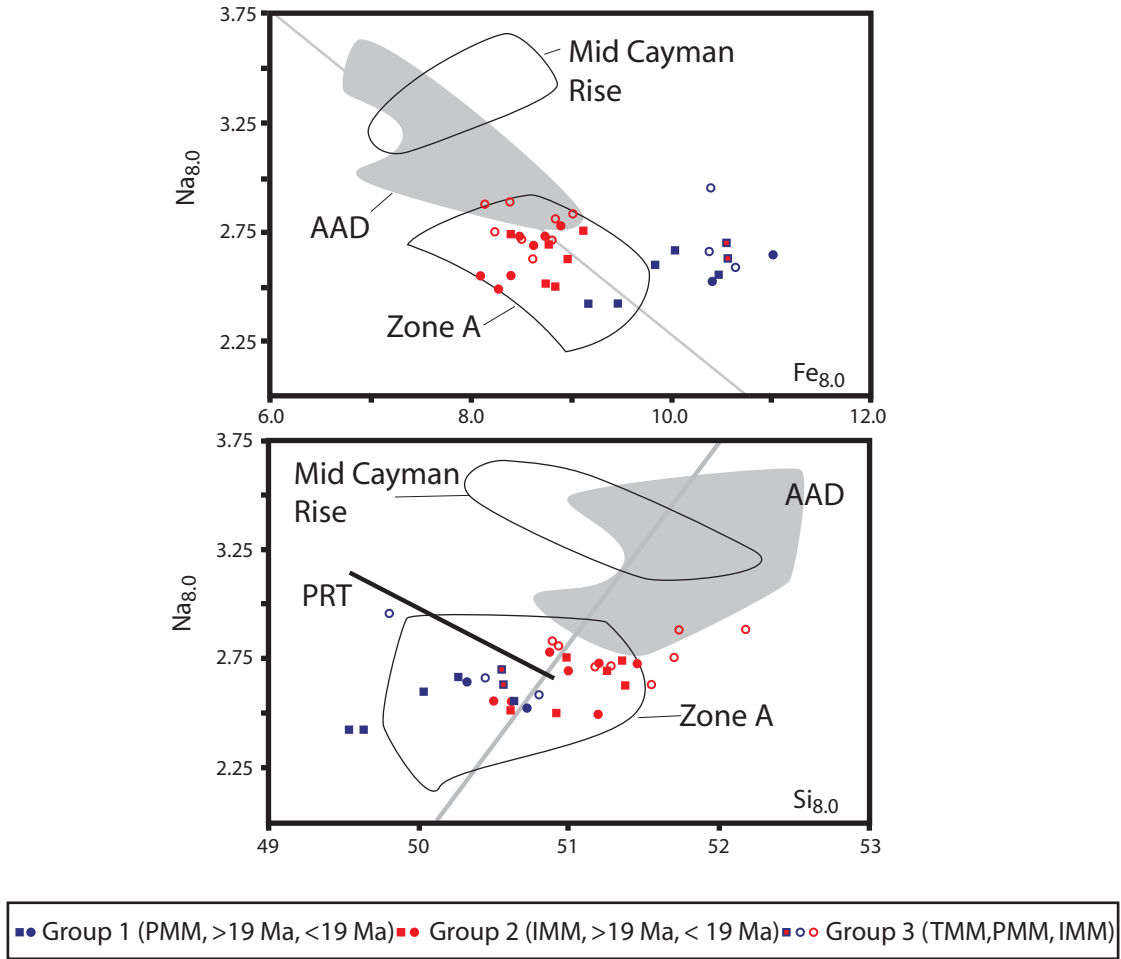


Figure 2-5. Fractionation corrected major element variation diagrams. A) $\text{Na}_{8.0}$ vs. $\text{Fe}_{8.0}$. B) $\text{Na}_{8.0}$ vs. $\text{Si}_{8.0}$. Symbols and fields are the same as in previous figures. All lavas with an MgO content less than 8.0 wt.% had their Na_2O , SiO_2 and FeO^* contents corrected using similar equations, for example $\text{Fe}_{8.0} = \text{FeO}^* + m(\text{MgO} - 8.0)$, where (m) is the slope of the LLD (Klein and Langmuir, 1987; Langmuir et al., 1992). Due to the consistent offset between lavas found to be isotopically Pacific from those found to be isotopically Indian and the likely different mantle compositions of these source regions there is a need for separate regression lines for the two mantle sources. Values of (m) used in these calculations are as follows $\text{Fe}_{8.0}$ $m = 0.874$ (PMM) and 1.602 (IMM); $\text{Na}_{8.0}$ $m = 0.226$ (PMM) and 0.177 (IMM); $\text{Si}_{8.0}$ $m = 0.293$ (PMM) and 0.405 (IMM). Only samples from Groups 1 and 2 were used to calculate the LLD because of the considerable scatter in the Group 3 data as indicated by the improved fit (higher R^2 values) of the linear regressions to our data when Group 3 lavas are omitted.

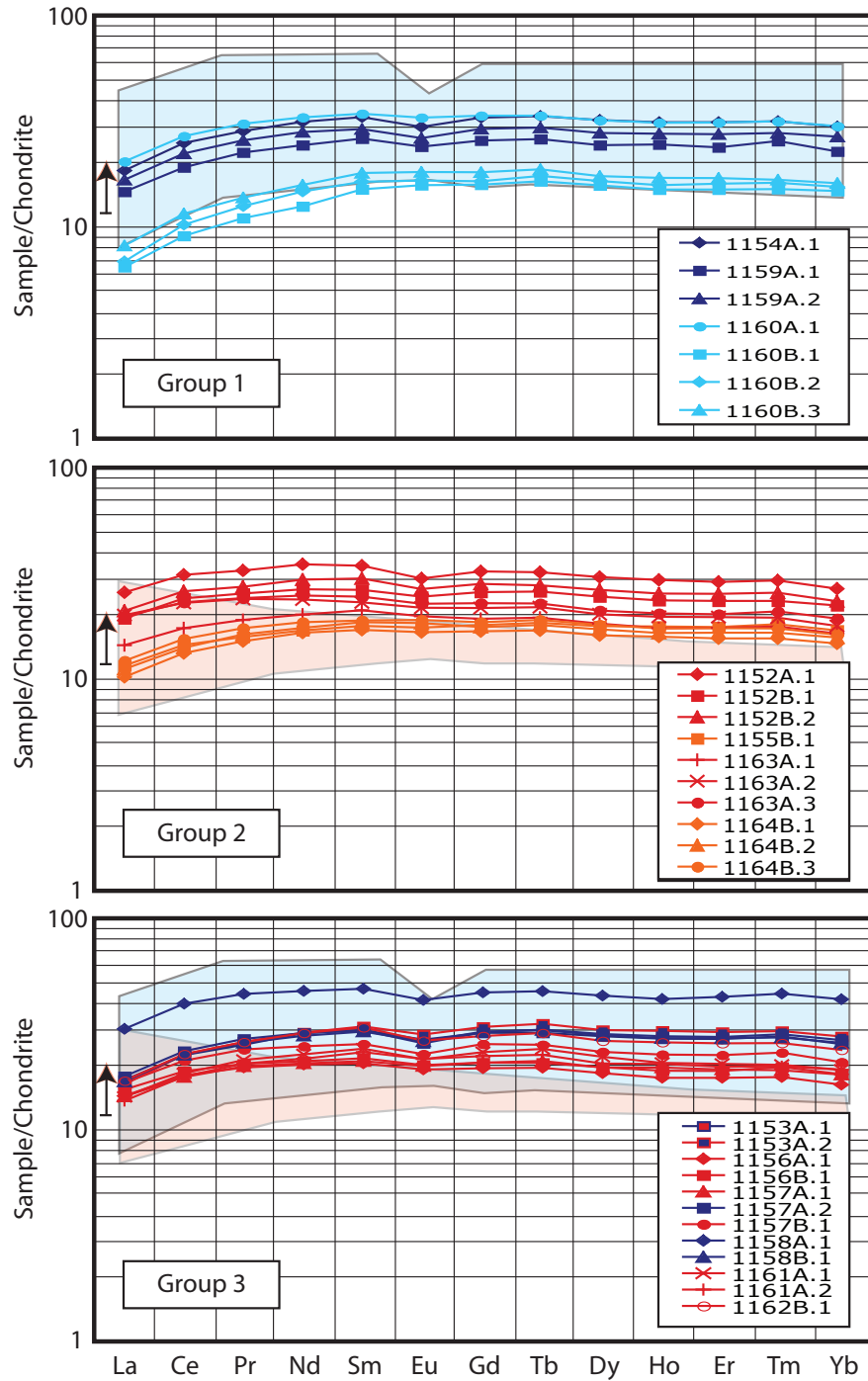


Figure 2-6. Chondrite normalized rare earth element patterns. Individual panels refer to Groups 1, 2 and 3 (see text for description of Groups) and individual patterns are color-coded according to the isotopic signature of the sample; red and orange (IMM), blues (PMM). Shaded areas represent patterns from 0-5 Ma lavas are also color-coded according to isotopic signature; red (IMM), blue (PMM) data from Pyle et al. (1995). Normalizing values are for C1 chondrite as reported by Sun and McDonough (1989).

Table 1 Averaged major element oxide data determined by electron microprobe (EMP) for the 33 flow units discussed in the text. N values refer to the number of glass samples included in each Pacific, or Transitional mantle sources, flow unit. Red, blue and black text refers to Indian, respectively, as determined by isotopic distinction. 2 σ refers to two standard deviations calculated from (n) number of samples determined to belong to a 'flow' unit. Trace elements for 29 lavas determined by ICP-MS are all as ug/g. Header on the trace element columns refers to the core interval(s) analyzed when more than one sample was analyzed within a group n and the 2 σ (calculated as two standard deviations) is reported.

	1152A.1 n=2	2s	1152B.1 n=2	2s	1152B.2 n=6	2s	1153A.2 n=1	1153A.1 n=2	2s	1154A.1 n=12	2s
SiO2	51.28	0.68	51.23	0.10	51.39	0.65	50.58	50.63	0.95	50.64	0.64
TiO2	2.10	0.02	1.70	0.06	1.83	0.04	2.04	1.97	0.05	2.30	0.08
Al2O3	14.74	0.26	14.70	0.04	14.46	0.10	14.79	14.75	0.27	13.89	0.25
FeO	10.42	0.25	9.39	0.08	10.06	0.17	10.82	10.58	0.26	11.44	0.25
MnO	0.19	0.04	0.15	0.00	0.18	0.03	0.18	0.20	0.01	0.20	0.06
MgO	7.18	0.02	7.67	0.00	7.14	0.11	7.67	8.09	0.10	6.77	0.17
CaO	10.67	0.08	11.62	0.21	11.33	0.09	10.71	10.98	0.00	10.94	0.14
Na2O	2.90	0.01	2.67	0.03	2.83	0.04	2.77	2.63	0.01	2.81	0.06
K2O	0.19	0.01	0.13	0.00	0.15	0.01	0.08	0.11	0.00	0.10	0.01
P2O5	0.23	0.04	0.17	0.01	0.18	0.03	0.18	0.17	0.01	0.20	0.04
Cr2O3	0.03	0.03	0.05	0.03	0.04	0.02	0.06	0.02	0.05	0.04	0.04
Total	99.92		99.48		99.61		99.86	100.13		99.34	

	n=2	3R-1 (2-4)	5R-1 (68-74)	7W-4 (60-65)	8R-1 (101-102)	n=2		
Sc	40.1	1.0	42.0	42.6	39.3	39.6	43.5	2.1
V	360	3	320	338	356	351	389	13
Cr	239	3	324	243	291	274	258	17
Zn	95.6	2.5	83.0	89.0	97.1	95.7	104	2
Rb	1.49	0.06	0.88	1.09	0.71	0.94	0.763	0.018
Sr	134	0.1	133	137	106	111	110	3
Y	48.6	0.6	39.8	42.2	49.3	45.6	52.4	1.4
Zr	166	2	127.2	137.7	145.8	137.8	157	6
Nb	4.31	0.05	3.01	3.31	2.11	2.63	2.41	0.06
Ba	13.0	0.1	9.00	9.76	5.39	8.04	5.34	0.18
La	6.13	0.04	4.60	5.01	3.94	4.13	4.38	0.00
Ce	19.2	0.01	14.8	16.0	14.1	14.0	15.3	0.04
Pr	3.13	0.02	2.43	2.62	2.52	2.44	2.71	0.04
Nd	16.5	0.1	12.5	13.9	13.7	13.6	14.8	0.12
Sm	5.31	0.17	4.07	4.61	4.81	4.61	5.09	0.09
Eu	1.75	0.01	1.43	1.56	1.66	1.57	1.74	0.01
Gd	6.71	0.23	5.33	5.85	6.42	6.02	6.80	0.12
Tb	1.21	0.02	0.98	1.05	1.21	1.09	1.26	0.05
Dy	7.79	0.08	6.28	6.77	7.65	7.16	8.18	0.14
Ho	1.68	0.07	1.34	1.45	1.69	1.55	1.78	0.05
Er	4.82	0.07	3.90	4.22	4.88	4.53	5.21	0.12
Tm	0.754	0.018	0.60	0.66	0.76	0.72	0.811	0.024
Yb	4.59	0.01	3.81	3.99	4.78	4.40	5.10	0.19
Lu	0.697	0.002	0.56	0.61	0.72	0.65	0.773	0.018
Hf	4.28	0.025	3.32	3.55	3.91	3.60	4.15	0.37
Ta	0.327	0.006	0.24	0.26	0.17	0.21	0.196	0.014
Pb	0.731	0.001	0.55	0.62	0.45	0.44	0.444	0.034
Th	0.293	0.022	0.21	0.22	0.13	0.17	0.146	0.001
U	0.120	0.002	0.08	0.10	0.06	0.07	0.066	0.002

Table 1 (continued)

	1155A.2 n=2	2s	1155A.1 n=1	1155B.1 n=26	2s	1156A.1 n=10	2s	1156B.1 n=9	2s	1157A.1 n=2	2s
SiO2	51.16	0.00	51.03	50.49	0.73	51.19	0.82	51.74	0.30	51.66	0.85
TiO2	1.91	0.05	1.30	1.23	0.04	1.41	0.02	1.53	0.01	1.42	0.05
Al2O3	14.62	0.22	15.59	16.10	0.20	15.73	0.21	15.15	0.09	15.73	0.10
FeO	9.63	0.21	8.86	8.73	0.32	8.50	0.23	8.99	0.10	8.23	0.19
MnO	0.19	0.04	0.20	0.16	0.05	0.16	0.03	0.15	0.00	0.15	0.01
MgO	7.09	0.02	8.30	8.50	0.13	8.26	0.17	7.79	0.01	8.11	0.02
CaO	11.07	0.35	12.10	11.78	0.22	11.57	0.27	11.83	0.29	11.53	0.08
Na2O	2.86	0.02	2.51	2.51	0.06	2.71	0.10	2.68	0.02	2.75	0.03
K2O	0.20	0.00	0.15	0.09	0.01	0.12	0.01	0.14	0.01	0.13	0.00
P2O5	0.20	0.02	0.14	0.11	0.03	0.14	0.04	0.16	0.01	0.15	0.01
Cr2O3	0.02	0.02	0.05	0.05	0.03	0.04	0.02	0.05	0.02	0.05	0.05
Total	98.96		100.22	99.77		99.82		100.20		99.91	
					n=5		n=2		n=2		1W-CC (13-17)
Sc				37.8	1.7	35.9	0.5	38.3	0.9	36.0	
V				239	9	259	3	279	2	260	
Cr				357	13	330	1	352	15	375	
Zn				66.6	3.3	70.7	1.0	74.0	1.3	70.0	
Rb				0.628	0.18	0.60	0.07	0.753	0.007	0.92	
Sr				117	4	132	3	133	6	125	
Y				30.7	1.4	31.8	0.5	33.6	0.5	33.2	
Zr				83.3	5.1	97.9	1.3	106	3	104	
Nb				1.77	0.10	2.15	0.03	2.61	0.18	2.49	
Ba				5.84	0.29	6.89	0.24	8.02	0.75	9.35	
La				2.73	0.14	3.46	0.07	3.72	0.26	3.45	
Ce				8.89	0.35	11.2	0.30	11.7	0.73	11.0	
Pr				1.50	0.07	1.90	0.02	1.98	0.07	1.92	
Nd				7.95	0.44	9.64	0.25	10.0	0.5	9.77	
Sm				2.73	0.11	3.20	0.05	3.39	0.08	3.28	
Eu				1.02	0.05	1.13	0.02	1.19	0.05	1.18	
Gd				3.72	0.19	4.07	0.29	4.33	0.11	4.34	
Tb				0.693	0.03	0.746	0.017	0.787	0.024	0.80	
Dy				4.54	0.32	4.78	0.21	5.09	0.21	5.07	
Ho				1.01	0.04	1.01	0.04	1.09	0.02	1.13	
Er				2.93	0.17	2.95	0.09	3.18	0.01	3.23	
Tm				0.464	0.03	0.459	0.033	0.513	0.015	0.49	
Yb				2.89	0.13	2.81	0.04	3.16	0.12	3.14	
Lu				0.449	0.02	0.426	0.018	0.493	0.007	0.46	
Hf				2.14	0.10	2.36	0.07	2.73	0.01	2.73	
Ta				0.137	0.015	0.157	0.013	0.199	0.018	0.19	
Pb				0.293	0.050	0.369	0.014	0.420	0.093	0.45	
Th				0.119	0.011	0.133	0.005	0.164	0.006	0.16	
U				0.046	0.002	0.057	0.006	0.069	0.008	0.06	

Table 1 (continued)

	1157A.2 n=2	2s	1157B.1 n=13	2s	1158A.1 n=1	1158B.1 n=2	2s	1159A.2 n=2	2s	1159A.1 n=7	2s
SiO2	50.84	0.32	51.59	0.97	49.49	50.60	0.20	50.49	0.02	50.41	1.17
TiO2	2.01	0.08	1.67	0.06	1.83	2.03	0.16	2.05	0.07	1.79	0.05
Al2O3	14.38	0.14	15.28	0.25	16.02	14.83	0.13	14.32	0.12	14.52	0.28
FeO	10.80	0.12	8.61	0.20	10.43	10.81	0.37	11.36	0.17	10.46	0.30
MnO	0.16	0.07	0.17	0.05	0.19	0.18	0.05	0.18	0.10	0.17	0.05
MgO	7.81	0.19	7.63	0.13	7.82	7.53	0.01	7.63	0.19	7.82	0.15
CaO	11.00	0.00	11.26	0.10	10.18	10.93	0.40	11.02	0.13	11.34	0.11
Na2O	2.63	0.06	2.93	0.06	2.97	2.77	0.03	2.73	0.11	2.54	0.05
K2O	0.09	0.01	0.11	0.01	0.12	0.10	0.00	0.09	0.01	0.08	0.01
P2O5	0.20	0.04	0.16	0.05	0.20	0.20	0.01	0.19	0.01	0.16	0.03
Cr2O3	0.05	0.03	0.05	0.04	0.05	0.05	0.03	0.05	0.01	0.03	0.03
Total	99.98		99.46		99.29	100.03		100.11		99.32	
	3R-1 (25-29)		n=2		3R-1 (0-3)	4R-1 (34-38)		1W-CC (10-13)		6R-2 (55-57)	
Sc	41.9		38.0	1.5	60.4	39.7		42.7		40.5	
V	355		292	15	465	340		372		330	
Cr	269		351	11	507	284		243		268	
Zn	99.8		76.8	3.8	138.3	94.9		99.5		90.3	
Rb	0.66		1.20	0.04	1.60	0.70		0.59		0.61	
Sr	108		129	3	226	111		110		105	
Y	47.9		39.1	0.6	71.7	46.1		46.9		41.0	
Zr	149		124	1	226	141		144		119	
Nb	2.38		2.27	0.04	4.07	2.28		2.26		1.92	
Ba	4.91		10.4	0.1	15.2	6.37		5.27		5.01	
La	4.30		4.01	0.31	7.24	4.06		3.96		3.47	
Ce	14.6		13.2	0.7	24.6	14.0		13.6		11.7	
Pr	2.60		2.32	0.15	4.27	2.49		2.45		2.14	
Nd	13.6		11.8	0.2	21.7	13.2		13.2		11.4	
Sm	4.60		3.95	0.09	7.26	4.54		4.47		4.02	
Eu	1.51		1.34	0.01	2.43	1.54		1.53		1.39	
Gd	6.06		5.32	0.34	9.37	6.10		6.02		5.28	
Tb	1.14		0.961	0.049	1.73	1.13		1.11		0.98	
Dy	7.33		6.03	0.22	11.2	7.24		7.11		6.20	
Ho	1.60		1.31	0.03	2.40	1.56		1.57		1.39	
Er	4.63		3.80	0.14	7.19	4.57		4.57		3.95	
Tm	0.73		0.600	0.010	1.15	0.71		0.71		0.65	
Yb	4.59		3.60	0.09	7.18	4.45		4.57		3.87	
Lu	0.72		0.563	0.028	1.14	0.68		0.69		0.60	
Hf	3.98		3.16	0.11	5.78	3.74		3.59		3.19	
Ta	0.19		0.175	0.004	0.31	0.18		0.18		0.16	
Pb	0.45		0.459	0.016	0.82	0.43		0.46		0.41	
Th	0.15		0.149	0.024	0.26	0.14		0.14		0.12	
U	0.07		0.057	0.003	0.11	0.06		0.07		0.05	

Table 1 (continued)										
	1160A.1 n=1	1160B.3 n=3	2s	1160B.1 n=1	1160B.2 n=9	2s	1161A.2 n=2	2s	1161A.1 n=1	1161B.1 n=1
SiO2	50.63	49.64	1.01	49.78	49.79	0.72	52.67	0.06	51.14	51.29
TiO2	1.69	1.36	0.10	1.10	1.24	0.05	1.46	0.02	1.56	1.89
Al2O3	14.62	14.83	0.49	16.08	15.65	0.29	15.65	0.10	16.00	14.73
FeO	10.43	9.77	0.17	9.21	9.51	0.22	8.73	0.01	8.88	9.52
MnO	0.22	0.18	0.04	0.15	0.18	0.04	0.14	0.08	0.17	0.18
MgO	7.65	8.01	0.12	8.88	8.58	0.21	7.90	0.15	8.35	7.55
CaO	12.20	12.61	0.36	12.62	12.75	0.16	11.04	0.21	11.15	11.58
Na2O	2.77	2.58	0.04	2.44	2.43	0.16	2.94	0.06	2.82	2.79
K2O	0.07	0.06	0.01	0.04	0.03	0.04	0.10	0.02	0.10	0.11
P2O5	0.16	0.11	0.02	0.11	0.08	0.04	0.13	0.01	0.17	0.16
Cr2O3	0.07	0.05	0.02	0.08	0.05	0.04	0.06	0.03	0.07	0.08
Total	100.50	99.22		100.48	100.31		100.81		100.41	99.88
	3R-1 (19-21)		n=2	1W-1 (8-14)		n=2	3R-1 (68-69)		3R-2 (30-32)	
Sc	67.1	40.5	0.8	37.8	40.6	0.6	35.8		34.4	
V	448	257	6	239	253	17	269		269	
Cr	373	354	8	382	363	29	303		335	
Zn	120.4	73.0	0.4	66.7	73.2	11.1	75.2		79.2	
Rb	0.60	0.284	0.340	0.21	0.265	0.000	1.27		1.23	
Sr	193	111	3	95.4	108	66	121		114	
Y	52.8	29.1	0.3	25.4	27.3	1.5	35.6		36.5	
Zr	163	72.9	2.1	57.4	69.9	23.0	108		111	
Nb	2.56	0.884	0.021	0.78	0.691	0.953	1.86		1.80	
Ba	5.42	2.56	0.02	2.28	1.71	2.39	12.1		10.8	
La	4.84	1.91	0.11	1.51	1.61	1.47	3.29		3.43	
Ce	16.5	7.03	0.23	5.50	6.23	3.59	11.1		11.5	
Pr	2.94	1.30	0.09	1.04	1.19	0.46	1.98		2.07	
Nd	15.5	7.36	0.20	5.81	6.84	1.31	10.3		10.8	
Sm	5.29	2.75	0.18	2.30	2.50	0.10	3.62		3.76	
Eu	1.92	1.05	0.03	0.91	0.959	0.033	1.27		1.27	
Gd	6.96	3.73	0.01	3.25	3.38	0.29	4.66		4.86	
Tb	1.27	0.701	0.027	0.61	0.652	0.050	0.86		0.92	
Dy	8.17	4.41	0.13	3.99	4.18	0.15	5.30		5.71	
Ho	1.77	0.966	0.033	0.85	0.891	0.013	1.18		1.19	
Er	5.19	2.81	0.02	2.48	2.65	0.05	3.33		3.45	
Tm	0.81	0.425	0.007	0.38	0.412	0.017	0.52		0.53	
Yb	5.12	2.73	0.16	2.51	2.63	0.05	3.31		3.32	
Lu	0.77	0.407	0.007	0.38	0.404	0.016	0.49		0.53	
Hf	4.12	2.00	0.02	1.69	1.84	0.20	2.77		2.78	
Ta	0.21	0.081	0.014	0.06	0.059	0.066	0.14		0.13	
Pb	0.55	0.253	0.024	0.17	0.202	0.187	0.43		0.79	
Th	0.15	0.064	0.007	0.06	0.056	0.051	0.14		0.12	
U	0.08	0.027	0.001	0.02	0.021	0.019	0.04		0.05	

Table 1 (continued)										
	1162B.1 n=4	2s	1163A.1 n=4	2s	1163A.2 n=1	1163A.3 n=23	2s	1164A.1 n=1	1164B.3 n=3	2s
SiO2	50.75	0.92	51.10	0.81	50.97	51.07	0.86	51.98	50.88	0.60
TiO2	1.90	0.04	1.17	0.02	1.50	1.53	0.06	1.79	1.33	0.04
Al2O3	15.09	0.27	15.48	0.16	15.89	15.72	0.30	14.52	15.75	0.20
FeO	9.64	0.22	8.26	0.13	8.92	8.72	0.23	9.97	8.61	0.19
MnO	0.17	0.01	0.14	0.03	0.15	0.16	0.04	0.21	0.16	0.02
MgO	7.53	0.06	8.48	0.01	8.18	7.98	0.13	7.11	8.28	0.16
CaO	11.07	0.21	12.50	0.11	11.42	11.44	0.21	11.52	11.79	0.21
Na2O	2.89	0.08	2.49	0.04	2.79	2.72	0.08	2.90	2.69	0.08
K2O	0.11	0.01	0.06	0.01	0.20	0.18	0.02	0.13	0.10	0.02
P2O5	0.18	0.05	0.10	0.04	0.15	0.17	0.03	0.14	0.13	0.04
Cr2O3	0.04	0.03	0.04	0.04	0.03	0.05	0.02	0.02	0.06	0.01
Total	99.39		99.82		100.19	99.74		100.30	99.78	
	8R-1 (80-82)	n=2			3R-1 (135-142)	n=3		1W-CC (23-25)		
Sc	37.0	36.1	1.6	35.9	36.6	0.5	36.2			
V	312	248	37	257	268	5	249			
Cr	309	372	73	356	347	9	369			
Zn	87.1	75.9	10.3	72.6	74.7	1.7	67.1			
Rb	1.24	0.739	0.620	1.00	0.909	0.036	0.47			
Sr	118	133	66	167	160	2	126			
Y	44.5	30.3	11.2	33.5	35.2	1.0	29.6			
Zr	140	92.4	68.2	118	120	3	84.8			
Nb	2.25	2.12	2.76	3.41	3.24	0.13	1.73			
Ba	11.6	7.51	9.01	11.8	11.4	2.3	5.70			
La	4.10	3.43	3.80	4.78	4.70	0.17	2.88			
Ce	14.2	10.7	10.44	14.1	14.2	0.8	9.49			
Pr	2.51	1.82	1.44	2.29	2.31	0.09	1.66			
Nd	13.6	9.48	6.35	11.2	11.7	0.4	8.71			
Sm	4.76	3.25	1.52	3.56	3.78	0.27	2.91			
Eu	1.56	1.15	0.45	1.27	1.32	0.08	1.11			
Gd	5.80	3.98	1.89	4.47	4.73	0.09	3.83			
Tb	1.09	0.733	0.342	0.82	0.857	0.023	0.71			
Dy	6.80	4.66	2.25	5.17	5.39	0.29	4.60			
Ho	1.49	0.987	0.397	1.12	1.16	0.01	0.99			
Er	4.31	2.90	1.16	3.27	3.37	0.20	2.88			
Tm	0.67	0.453	0.167	0.50	0.534	0.005	0.44			
Yb	4.12	2.80	1.05	3.05	3.30	0.05	2.76			
Lu	0.61	0.416	0.172	0.46	0.495	0.018	0.40			
Hf	3.49	2.32	1.54	2.86	2.95	0.11	2.25			
Ta	0.17	0.162	0.206	0.25	0.238	0.010	0.13			
Pb	0.48	0.493	0.023	0.61	0.547	0.081	0.31			
Th	0.14	0.137	0.177	0.22	0.205	0.023	0.11			
U	0.06	0.058	0.076	0.09	0.086	0.008	0.04			

Table 1 (continued)				
	1164B.2 n=14	2s	1164B.1 n=2	2s
SiO2	50.91	0.91	51.04	0.51
TiO2	1.22	0.05	1.15	0.04
Al2O3	16.19	0.65	16.69	0.01
FeO	8.45	0.27	8.18	0.19
MnO	0.15	0.00	0.13	0.06
MgO	8.67	0.11	8.90	0.07
CaO	12.16	0.38	12.14	0.02
Na2O	2.57	0.12	2.58	0.01
K2O	0.09	0.01	0.09	0.00
P2O5	0.13	0.01	0.12	0.03
Cr2O3	0.04	0.02	0.05	0.02
Total	100.58		101.07	
			4R-2 (66-70) n=2	
Sc	35.2	0.5	34.0	
V	237	2	223	
Cr	375	13	370	
Zn	66.6	1.3	64.4	
Rb	0.385	0.089	0.34	
Sr	124	1	125	
Y	28.5	0.1	27.0	
Zr	80.9	1.9	75.7	
Nb	1.57	0.01	1.41	
Ba	4.89	0.01	4.68	
La	2.63	0.02	2.41	
Ce	8.62	0.03	8.10	
Pr	1.55	0.01	1.44	
Nd	8.17	0.12	7.76	
Sm	2.85	0.03	2.62	
Eu	1.07	0.03	0.97	
Gd	3.63	0.06	3.46	
Tb	0.676	0.022	0.64	
Dy	4.37	0.17	4.10	
Ho	0.936	0.020	0.90	
Er	2.75	0.02	2.58	
Tm	0.424	0.021	0.40	
Yb	2.68	0.02	2.50	
Lu	0.397	0.014	0.36	
Hf	2.15	0.04	1.98	
Ta	0.114	0.020	0.11	
Pb	0.294	0.142	0.27	
Th	0.107	0.008	0.10	
U	0.044	0.000	0.04	

	Selected major and trace element averages for ODP Leg 187 lavas compared to average values for MORB and EPR as reported in Humler et al. (1999). Values for σ are 1 standard deviation of the mean and (n) refers to the number of samples used in determining these values.								
	ODP Leg 187	σ	n	EPR	σ	n	MORB	σ	n
Na _{8,0}	2.67	0.13	33	2.61	0.23	295	2.56	0.40	100
Fe _{8,0}	9.21	0.90	33	9.87	0.59	295	9.61	0.96	100
CaO/Al ₂ O ₃	0.76	0.04	33	0.79	0.04	295	0.76	0.06	84
(Sm/Yb) _n	1.18	0.08	29	1.11	0.10	70	n/r		
Zr/Y	3.02	0.26	29	3.15	0.43	60	n/r		

Chapter 3:
Mantle Heterogeneity and Melting Conditions along the Southeast Indian Ridge:
A U-Series Disequilibria Perspective

Chris J. Russo¹, Ken H. Rubin² and David W. Graham¹

¹ College of Oceanic and Atmospheric Sciences, Oregon State University, Corvallis,
OR

² School of Ocean Engineering Science and Technology,
University of Hawaii, Honolulu, HI

3.1 Abstract

Uranium and Th isotopes and U, Th, Ra and Ba concentrations have been analyzed on 16 fresh basalt glasses from along the Southeast Indian Ridge between 88° and 118°E. These new data are added to an already extensive suite of major and trace element analyses and measurements of He, Sr, Nd, Pb and Hf isotopes to form one of the most complete data sets for any portion of the global mid ocean ridge system. The new U-series measurements range in ($^{230}\text{Th}/^{232}\text{Th}$) and ($^{238}\text{U}/^{232}\text{Th}$) values equivalent to ~70% of the range observed globally in MORB, and reveal a systematic along axis relationship that responds on a regional scale to the presence of a mantle thermal gradient. The systematic variation in ^{230}Th -excess is very sensitive to changes in axial morphology and is best described by excessive melting in the warmer western region that is supplied to the ridge axis by higher mantle porosity and/or higher melting rates. Moving east along the regional temperature gradient, melt supply decreases as mantle source enrichment increases, revealed by the increase in trace elements and Th/U ratio. These higher Th/U ratios also correlate with higher $\Delta 8/4\text{Pb}$ and lower $^3\text{He}/^4\text{He}$ (R/R_A) values. Notably, this increase in Th/U ratio is accompanied by a convergence between measured $^{232}\text{Th}/^{238}\text{U}$ (κ) and $^{232}\text{Th}/^{238}\text{U}$ inferred from Pb isotopes (κ_{pb}). A model of intra-mantle differentiation involving ancient melt infiltration into the subcontinental lithosphere, followed by dispersal in the upper mantle during the breakup of Gondwana, reproduces the spatial pattern of the trace element and isotopic systematics observed today.

3.2 Introduction

The global mid-ocean ridge spreading system is approximately 65,000 km long, produces about 20 km³ of new oceanic crust each year and is ultimately

responsible for having created material now covering more than two-thirds of the Earth's surface (Chen, 1996a and b). Consequently, melt production along this system plays a major role in the geochemical evolution of the planet and, as a result of its widespread occurrence, is the best window into the chemical heterogeneity of the Earth's upper mantle.

In general, as hot material rises from depth beneath the ridge-axis, decompression occurs and melting ensues because this change in pressure occurs more rapidly than the loss of heat. In this view, the total amount of melt generated is determined by the difference between the depth at which melting begins and the depth at which melting ceases, and the rate of melt production over that interval. However, it is also known that none of these variables are constant along the global mid-ocean ridge system. For instance, the initial depth of melting has been shown to vary with mantle temperature (Klein and Langmuir, 1987; Bourdon et al., 1998a), the depth of melt cessation appears to be largely, but not exclusively, controlled by spreading rate and the depth of the conductive lithospheric lid (Niu and Hekinian, 1987; Shen and Forsyth, 1995; Herzberg, 2004), and melting rate has been suggested to vary with mineralogical make-up of the mantle and spreading rate (Hirschman and Stolper, 1996; Stracke et al., 1999; Lundstrom et al., 1998b; Pertermann and Hirschmann, 2003a,b; Kogiso et al., 2004).

An ideal location to test the geochemical response to variations in the melting regime is the Southeast Indian Ridge (SEIR) between 88°E and 118°E. This ~2300 km long section of mid-ocean ridge is characterized by a west to east gradient in axial ridge depth from ~2300 m to >4500 m, which occurs at a near constant spreading rate (72-76 mm/yr full rate) and in the absence of any large transform offsets (Cochran et al., 1997).

Coinciding with the increase in axial ridge depth is a morphologic transition from an axial high to an axial valley, implying that melt production and crustal

thickness decrease to the east (Sempere et al., 1997). Major element analyses on more than 3,000 mid-ocean ridge basalt glasses (MORB) sampled along this portion of the SEIR suggest a gradient in mantle temperature of ~80-150° C from the hottest mantle, west of the study area, underlying the Amsterdam-St. Paul plateau (ASP) to the coldest mantle, east of the study area, beneath the Australian-Antarctic Discordance (AAD, Klein et al., 1991; Pyle, 1994; Douglas Priebe, 1998; Sours-Page, 2000). There is also a broad covariation between $^3\text{He}/^4\text{He}$ ratios and fractionation corrected iron contents ($\text{Fe}_{8,0}$), which suggests that isotopic compositions, in this case higher $^3\text{He}/^4\text{He}$ ratios, may be associated with higher mean pressures of melting (Klein and Langmuir, 1987; Graham et al., 2001). All samples erupted along this portion of the SEIR are truly 'Indian'-type MORB with elevated $\Delta^{208}\text{Pb}/^{204}\text{Pb}$ values (where $\Delta^{208}\text{Pb}/^{204}\text{Pb}$ is the vertical deviation of the measured $^{208}\text{Pb}/^{204}\text{Pb}$ on a $^{208}\text{Pb}/^{204}\text{Pb}$ vs. $^{206}\text{Pb}/^{204}\text{Pb}$ diagram from the Pacific and Atlantic MORB array known as the Northern Hemisphere Reference Line NHRL; Hart 1984) and there is a tendency for the most strongly 'Indian'-type mantle to be associated with greater axial depths and by inference lower degrees of melting (Mahoney et al., 2002).

These relationships suggest that a heterogeneous mantle source may be systematically sampled in response to variations in the melting regime along the SEIR. Whether this results from the sampling of a chemically layered mantle or through the preferential sampling of heterogeneous 'blobs' within the melting regime is unknown. Measurements of uranium-series (U-series) disequilibria provide a sensitive indicator of U and Th fractionation during melting. Furthermore, these measurements add insight into the style, extent, rate and depth of melting (McKenzie, 1985; Williams and Gill, 1989; Spiegleman and Elliott, 1993; Bourdon et al., 1996 a, b; Stracke et al., 1999). In this study, U-series measurements were conducted on 16 samples from along this portion of the SEIR. These results add to an already extensive compilation of He, Sr, Nd, Hf and Pb isotope data (Graham et al., 2001; Mahoney et al., 2002;

Graham et al., 2006) plus major and trace elements. Previous chemical and isotopic results for these 16 samples are given in Table 1. These new U-series measurements are used to test how depth, style and rate of melting control the regional sampling of geochemical heterogeneity along the SEIR.

3.3 Geologic Background

3.3.1 *Along axis morphologic variation*

The present day Southern Ocean formed via rifting of Gondwana beginning at the western end of Australia around 100 Ma and propagating east at a rate of ~ 2 cm/yr (West et al., 1997). The modern southeast Indian Ridge (SEIR, Figure 1) stretches from the Rodrigues triple junction (25.6°S , 70.1°E) to the Macquarie triple junction (62°S , 151°E) and marks the plate boundary separating the Australian and Antarctic plates. Between 76°E and 78°E the SEIR crosses a bathymetric high associated with relatively hot mantle upwelling beneath Amsterdam and St. Paul islands (Graham et al., 1999; Scheirer et al., 2000). Between 120°E and 127°E the SEIR crosses the Australian-Antarctic Discordance, an unusually deep, magma starved portion of the ridge overlying relatively cold mantle (Klein et al., 1991; Sempere et al., 1991; Pyle, 1994). There is only a small variation in full spreading rate along the SEIR, from ~ 68 mm/yr across the Amsterdam-St. Paul plateau to a maximum of ~ 76 mm/yr near 50°S , 114°E (Demets et al., 1990). Between 88°E and 118°E the spreading rate is nearly constant at ~ 72 - 76 mm/yr (Cochran et al., 1997).

A detailed geophysical survey carried out during the Austral summer 1994/1995 revealed three distinct ‘zones’ of axial morphology between 88°E and 118°E (Westward expedition, Leg 9 of the R/V Melville; Small and Sandwell, 1994; Ma and Cochran, 1996; Cochran et al., 1997; Sempere et al., 1997; Goff et al., 1997; Ma et al., 1997; Figure 1). In general, the western zone (86 to 100°E segments C17-

C13) is characterized by an axial-high morphology similar in dimension and shape to the axial segments along the fast-spreading East Pacific Rise (EPR; Cochran et al., 1997; Sempere et al., 1997; Baran et al., 2005). East of segment C13, from segment C12 to segment C4 (100-114°E) the SEIR enters into a 'transitional' morphologic form typical of other intermediate-spreading ridges (Canales et al., 1997). This portion of ridge axis is characterized by two adjacent transitions from rifted axial highs in the west, to shallow axial valleys in the east. The first of these along-axis morphological transitions begins along segment C12 and transitions down through segment C9 (100 to 107°E). The second morphologic transition occurs beginning along segment C8 and transitions down to segment C4 (107 to 114°E). To the east of 114°E along segments C3 and C2 the ridge axial morphology is described as a deep axial valley, similar to what is observed along the mid-Atlantic ridge (Cochran et al., 1997).

The overall increase of >2100 m in axial depth from west to east along the SEIR has been attributed to a long wavelength decrease in mantle potential temperature. Following the 1994/1995 geophysical survey, a study of ridge flank depth and roughness was conducted (Ma and Cochran, 1997). This study revealed that despite the large increase in axial depth along the SEIR, off-axis ridge flank depth only changes by ~500 m along axis and is constant at the segment length scale except for the portion of the ridge axis east of 114°E (where the morphology transitions into a deep axial valley). This suggests that a major portion of the variation in ridge axis depth results from changes in dynamically supported axial morphology. In addition, Ma and Cochran (1997) also concluded that changes occur in off-axis bathymetric roughness where there are transitions from either axial highs or rifted axial highs to shallow axial valleys, and from shallow axial valleys to deep axial valleys. This step-like behavior suggests the presence of threshold effects. As mantle temperature and magma supply decrease along axis from west to east, a point is reached where lithospheric strength becomes very sensitive to small fluctuations in

crustal (magmatic) input (Chen, 1996). This threshold mechanism is also supported by a detailed seismic study of upper crustal structure along segments C12-C7, which reveals the presence of shallow magma lenses beneath axial highs, deeper magma lenses beneath rifted axial highs, and no magma lens beneath axial valleys (Baran et al., 2005). Baran et al. (2005) also attributed the along axis gradient in axial depth to a long wavelength change in mantle temperature, with the shorter wavelength changes in axial morphology resulting from variable magma supply along axis. One caveat is that variations in magma supply may also be connected to variations in melt production related to lateral ridge migration over the underlying mantle, as suggested by Carbotte et al. (2004).

3.3.2 *Along axis geochemical variation*

A sister expedition to the SEIR was carried out over the Austral summer 1994/1995 (Westward expedition Leg 10). The main goal of this expedition was to sample young volcanic material erupted along this ~2300 km stretch of previously un-sampled ridge-axis. Of particular interest was determining the influence, if any, that the Amsterdam-St Paul (ASP) and/or Kerguelen-Heard hotspots (located ~700 km and 1600 km to the west and southwest of segment C17, respectively) have on the geochemical and morphological variations along the SEIR (Figure 1).

Mahoney et al. (2002) determined that all lavas sampled along the SEIR are truly 'Indian'-type MORB (characterized by lower $^{206}\text{Pb}/^{204}\text{Pb}$ relative to $^{208}\text{Pb}/^{204}\text{Pb}$, lower ϵ_{Nd} , and higher $^{87}\text{Sr}/^{86}\text{Sr}$ than Pacific and North Atlantic MORB). Along-axis variations with decreasing $\text{Fe}_{8.0}$ and increasing $\text{Na}_{8.0}$ suggest a gradient in the mean pressure and extent of melting along the SEIR (Graham et al., 2001; Mahoney et al., 2002). There is also a broad correlation between $^3\text{He}/^4\text{He}$ and Fe_8 along the SEIR that suggests higher $^3\text{He}/^4\text{He}$ material is associated with greater mean depths of

melting (Graham et al., 2001). On the basis of Sr-Nd-Pb isotope measurements there is little to no support for a strong component of eastward mantle flow from either the Amsterdam-St.Paul or Kerguelen-Heard hotspots. For instance, the overall increase in $\Delta 8/4\text{Pb}$ to the east along the SEIR does not support this hypothesis. Increasing $\Delta 8/4\text{Pb}$ values to the east is opposite of what would be expected if high $\Delta 8/4\text{Pb}$ material from either hotspot is flowing eastward and mixing with depleted MORB mantle beneath the ridge axis (Mahoney et al., 2002).

One possible explanation of the $\text{Fe}_8\text{-}^3\text{He}/^4\text{He}\text{-}\Delta 8/4\text{Pb}$ co-variation is a layered upper mantle with lower $^3\text{He}/^4\text{He}$ and higher $\Delta 8/4\text{Pb}$ material concentrated in the shallower upper mantle. In this scenario, as mantle temperature decreases to the east along the axial depth gradient, melting begins at shallower depths in the mantle, which effectively increases the proportion of melting that occurs in the shallowest, low $^3\text{He}/^4\text{He}$, high $\Delta 8/4\text{Pb}$ upper mantle (Graham et al., 2001; Mahoney et al., 2002). More recently, the addition of Hf-isotope data collected on samples from along the SEIR revealed a bimodal distribution of ϵHf values along ~ 2000 km of ridge-axis (Graham et al., 2006). The existence of this bimodality in Hf isotopes and absence of such a relationship in other geochemical parameters indicates ‘memory’ of an ancient chemical fractionation that is now only apparent in time-integrated Lu/Hf ratio. However, as noted by Graham et al. (2006) and discussed by Mahoney et al. (2002), the Sr, Nd, Hf, and Pb isotopes in these lavas are correlated with their respective parent/daughter ratios and each of these correlations imply ‘ages’ of 200-400 Myr. Such ages may represent a record of small amounts of trapped melt associated with the initial stages of the breakup of Gondwana some 200-400 Myr ago (Mahoney et al., 2002). Collectively, these systematics suggest that isotopic variations along the SEIR west of the AAD are primarily controlled by variations in the depth of melting of an isotopically heterogeneous mantle (Graham et al., 2001; Mahoney et al., 2002; Burnard et al., 2004; Graham et al., 2006). A summary of these along-axis variations

is given in Figure 2 (data in Table 1).

The 16 samples analyzed in this study were selected as regionally representative of the morphologic, geographic and geochemical variations discussed above. Collectively these represent the first U-series measurements from the SEIR. The new results also provide a framework within which to investigate the regional scale variability of U-series measurements in MORB.

3.4 Results

Here we report the results for 16 samples analyzed for Th-U-Ba concentrations and U and Th isotopic compositions. In addition, ^{226}Ra concentrations were measured on a subset of 10 samples (Table 2). All samples are MORB glasses that were handpicked to be free of alteration using a binocular microscope. All isotope dilution concentrations and isotopic compositions were measured on a VG Sector 54 thermal ionization mass spectrometer (TIMS) equipped with a high abundance (WARP) filter at the University of Hawaii (see Rubin, 2001 and Pietruszka et al., 2001 for detailed descriptions of sample preparation, ion exchange separation procedures, standardization and analytical techniques). We present data from 13 ridge segments beginning in the western end of the field area with dredge 71 (90.8°E, segment C16) and ending at the eastern edge of the field area with dredge 145 (116.7°E, segment C2, Figure 1).

3.4.1 Trace element concentrations Ba-Th-U

A considerable range in Ba, Th and U concentrations and Ba/Th and Th/U are observed along the SEIR (Ba = 13.1 to 110 ug/g, Th = 130.4 to 1158 ng/g, U = 55.0 to 313 ng/g, with Ba/Th = 67 to 151 and Th/U = 2.35 to 3.78). Generally, higher

concentrations occur more frequently to the east, but both E-MORB and N-MORB compositions are distributed along this portion of the SEIR. We define E-MORB as lavas with $(\text{La}/\text{Sm})_n > 0.80$ (where n refers to the chondrite normalizing values of Sun and McDonough, 1984), consistent with the criteria used by Mahoney et al. (2002). Concentrations for Ba, Th and U are strongly correlated over a wide range of $(\text{La}/\text{Sm})_n$ values ($r^2 = 0.91, 0.94, \text{ and } 0.93$, respectively, over a $(\text{La}/\text{Sm})_n$ range of 0.64 to 1.79). Th/U and Ba/Th ratios in these lavas are not correlated with Ba, Th or U concentrations. The lack of significant correlations between Ba, Th or U and Mg# indicate these concentrations are not simply related to varying degrees of crystal fractionation from a similar parental magma.

3.4.2 *Sample alteration and $(^{234}\text{U}/^{238}\text{U})$*

These SEIR basalt glasses were all handpicked and inspected under a binocular microscope to ensure glasses were pristine and free of visible alteration. To verify the pristine nature of glasses used in this study their $(^{234}\text{U}/^{238}\text{U})$ have also been measured and are within 4‰ (0.4%) of unity. At 1.14 ± 0.03 , seawater is significantly enriched in ^{234}U making the $(^{234}\text{U}/^{238}\text{U})$ a sensitive indicator of post-eruption alteration or exchange with seawater (Thurber et al., 1967). The $(^{234}\text{U}/^{238}\text{U})$ results indicate uranium addition or exchange is insignificant, and therefore the measured U concentrations and Th/U ratios may be taken as the magmatic values at the time of eruption.

3.4.3 *$(^{230}\text{Th}/^{232}\text{Th})$ and $(^{226}\text{Ra}/^{230}\text{Th})$*

All samples analyzed in this study were dredged from, or very near, the active spreading center as guided by multibeam bathymetry. However, as with virtually all

MORB samples, and especially those sampled by dredging, it is difficult to ensure they are representative of ‘zero-age’ material. Knowledge of the ‘age’ of basalt samples is particularly important in U-series disequilibria studies, because most MORB erupt with a ^{230}Th -excess which subsequently decays at a rate of 50% every 75,000 years (in accordance with the half-life of daughter isotope ^{230}Th ; Cheng et al., 2000). In order to demonstrate the significance of this decay one can consider the location from which the sample was taken. For example, if we assume a half spreading rate of 35 mm/yr and a point source of volcanic activity at the ridge axis, a lava erupted at this location would experience a 50% reduction in its ^{230}Th -excess by the time it had been moved 2.6 km laterally from the active ridge axis by seafloor spreading. This distance is significantly shorter than the ~20 km wide volcanic high/rift zone defined by Cochran et al (1997) to be present along the SEIR.

To ensure that ^{230}Th -excesses in these lavas are primary, ^{226}Ra was measured on a subset of 10 of the samples. Because ^{226}Ra has an even shorter half-life (1600 years) than its parent ^{230}Th , any initial ^{226}Ra -excess will return to equilibrium in ~8000 years. The presence of any ^{226}Ra -excess would confirm that the ^{230}Th -excess in MORB has not been reduced by aging (Rubin and Macdougall, 1988; Volpe and Goldstein, 1993; Lundstrom et al., 1998). Nine of 10 SEIR basalts have ^{226}Ra -excesses ranging between 1.15 and 2.03 ± 0.04 , indicating that these lavas erupted within the past ~8000 years. One sample analyzed, WW10-89-4, was found to be in secular equilibrium with respect to ($^{226}\text{Ra}/^{230}\text{Th}$). However, as discussed later (see section 3.5.2 *SEIR basalts and the Equiline diagram*) this sample is believed to have experienced minimal by post-eruptive ^{230}Th -decay. Similarly, 5 of the 6 samples that were not analyzed for ^{226}Ra -excesses are believed to have ($^{230}\text{Th}/^{232}\text{Th}$) ratios that have not been significantly affected by post-eruptive decay, on the basis of their relationship to the other samples with similar geochemical characteristics (see further discussion in the following sections).

3.4.4 Along axis variations: A U-series perspective

In order to discuss the U-series results in their geographical context the data have been divided into three regional groups: 1) a Western group comprised of 5 samples from segments C16 through C13, 2) a central group comprised of 9 samples from segments C12 through C4, and 3) an Eastern group comprised of 2 samples, one each from segments C3 and C2. The regional divide between the Western and Central groups is based on the isotopic boundary identified by Mahoney et al. (2002) at 100°E (e.g. to the west and east of the transform fault separating segments C13 and C12). The Western group contains one E-MORB (WW10-89-4) and four N-MORB samples. The Central group extends from 100°E (segment C12) to ~114°E (ending with segment C4). The nine ridge segments in this group are included together because they mark the ‘transitional’ morphologic segments described by Cochran et al., 1997; Sempere et al., 1997; Goff et al., 1997. This Central group contains seven E-MORB and two N-MORB samples (WW10-113-7 and WW10-125-1). The final geographic group, the Eastern group, lies to the east of 114°E and marks the transition into a deep-axial valley morphology, which continues to the end of the field area at 118°E (segments C3 and C2). The Eastern group includes one E-MORB (WW10-145-1) and one N-MORB (WW10-141-1). A third sample analyzed by Bourdon et al. (1996a) from within the AAD is also included in the Eastern group.

Collectively these data span a very large range in Th/U ratios ($^{238}\text{U}/^{232}\text{Th}$) ranges from 1.292 ± 0.006 to 0.803 ± 0.004 , equivalent to ~70% of the range observed globally along ocean spreading centers. Additionally, all samples have ^{230}Th -excesses spanning a moderate range of ($^{230}\text{Th}/^{238}\text{U}$) between 1.210 ± 0.012 and 1.014 ± 0.010 . This range is similar to ^{230}Th -excess results recently reported for the intermediate spreading Galapagos Spreading Center (GSC) over ~800-1000 km length (Detrich et al., 2002; Kokfelt et al., 2005). The GSC is a ridge also showing an axial depth

gradient, presumably related to thermal structure in the underlying mantle produced by mantle plume-spreading ridge interaction. In general the largest ^{230}Th -excesses occur in the Central SEIR group, where $(^{230}\text{Th}/^{238}\text{U})$ ranges between 1.068 ± 0.005 to 1.210 ± 0.012 , with an average value of 1.158. The Western SEIR group spans a range of $(^{230}\text{Th}/^{238}\text{U})$ from 1.014 ± 0.01 to 1.151 ± 0.012 , with an average value of 1.076. The 2 samples from the Eastern SEIR group have similar ^{230}Th -excesses of 1.094 ± 0.011 and 1.129 ± 0.012 , with an average value of 1.112, and the additional sample from Bourdon et al. (1996a) has a reported $(^{230}\text{Th}/^{238}\text{U})$ value of 1.065.

There is a very strong along axis gradient in both Th/U (κ) and $(^{230}\text{Th}/^{232}\text{Th})$, with the highest $(^{230}\text{Th}/^{232}\text{Th})$ and lowest κ values occurring in the western portion of the SEIR, and progressing to lower and higher values, respectively in the east (Table 1, Figure 3). However, no along-axis trend is observed in $(^{230}\text{Th}/^{238}\text{U})$. Instead these data form a convex pattern along axis, with lower values associated with both the western and eastern ends of the study area. A similar convex pattern is also observed in $(^{226}\text{Ra}/^{230}\text{Th})$, with the lowest ^{226}Ra –excesses occurring in the Western and Eastern groups. Two samples from the Western group were analyzed for $(^{226}\text{Ra}/^{230}\text{Th})$ and range from 1.32 ± 0.04 to 1.00 ± 0.01 , similar to the 2 samples analyzed in the Eastern group with values of 1.32 ± 0.09 and 1.15 ± 0.04 . The six samples from the Central group show larger excesses, with $(^{226}\text{Ra}/^{230}\text{Th})$ ranging from 2.03 ± 0.04 to 1.53 ± 0.03 (Figure 3).

3.5 Discussion

3.5.1 Global correlations at a regional scale 1: U-series as an indicator of the depth of melting

Globally, segment averaged $(^{230}\text{Th}/^{238}\text{U})$ in MORB shows a weak negative correlation with axial depth (Bourdon et al., 1996a). The larger $(^{230}\text{Th}/^{238}\text{U})$ values from shallower ridges were interpreted as derived from hotter mantle, similar to the

ideas of Klein and Langmuir (1987). In regions with hotter mantle temperatures, the solidus is crossed at greater depths resulting in higher overall degrees of melting and a greater proportion of melt being generated in the garnet stability field. Because Th is more incompatible in garnet compared to U, an increase in the proportion of melting occurs in the garnet field leading to higher ($^{230}\text{Th}/^{238}\text{U}$) in the melt. Since the pioneering study of Bourdon et al. (1996a), additional data from the deep southern MAR and the shallow Reykjanes Ridge (Lundstrom et al., 1998; Peate et al., 2001; Lundstrom, 2003) have added considerably more scatter to the originally published trend, especially when the Reykjanes data are considered. Even with the addition of this more recent data, the trend is defined by ‘endmember’ samples from the shallow Azores platform and the unusually deep AAD (Figure 4; Bourdon et al., 1996a). Samples from intermediate axial depths (~3000 to 3300 m) are highly variable and span nearly the entire global range for MORB. Nevertheless, a weak negative correlation exists for the global data set (Elliott and Spiegelman, 2003), but, at the very least, these additional measurements cast doubt on the relevance of the global correlation at regional and local scales and may indicate that even at the ‘global’ scale such a relationship is not entirely valid.

The new data from the SEIR are added to the ‘global’ compilation in Figure 4. In this context no clear negative correlation is observed between the SEIR ^{230}Th -excesses and axial depth, regardless of whether these data are viewed as a complete dataset or within regional groups (as is presented in Figure 4). This is especially true in the axial depth range between ~2300 and 2700 m, where ($^{230}\text{Th}/^{238}\text{U}$) varies from 1.014 ± 0.010 to 1.203 ± 0.013 , and span the entire range observed in SEIR MORB. In particular, samples from the westernmost portion of the SEIR have lower than expected ^{230}Th -excesses for their relatively shallow axial depths.

This evaluation does not support a simple relationship between axial depth and an increased amount of melting in the presence of garnet along the SEIR, and

therefore does not support the existence of the ‘global’ trend. However, if the ‘global’ trend is real, the lack of a ^{230}Th -excess-axial depth correlation in the SEIR lavas suggests that either the range in mantle temperature in this region is not sufficient to significantly affect the depth of melt initiation, or that other variables such as melting rate and/or mantle porosity also vary with mantle temperature, and these need to be considered when evaluating ^{230}Th -excess on the regional scale. The latter possibility is investigated in more detail in section 3.5.3 (*U-series disequilibria and morphologic characteristics*).

3.5.2 SEIR basalts and the ‘equiline’ diagram

The SEIR data is compared with data from the Pacific, Atlantic and Indian oceans in Figure 5. Before discussing details of the SEIR data in terms of the equiline diagram (Figure 6), it is important to draw attention to several key characteristics of this dataset (Figure 5). First, there is a large range of $(^{238}\text{U}/^{232}\text{Th})$ in these basalts, which extends from low $(^{238}\text{U}/^{232}\text{Th})$, similar to samples from the ultra-slow spreading Southwest Indian Ridge (SWIR), to high $(^{238}\text{U}/^{232}\text{Th})$, overlapping data from the fast spreading East Pacific Rise field (EPR). A similar ‘range’ is also observed for the SWIR data but, unlike the SWIR data, the SEIR data from this study form a continuous array from enriched ($\text{Th}/\text{U} \geq 3.4$) to depleted ($\text{Th}/\text{U} \approx 2.4$) values. Second, the SEIR data encompass a similar, but greater, range in $(^{238}\text{U}/^{232}\text{Th})$ compared to data from other ridges having intermediate spreading rates, such as the Juan de Fuca and Gorda Ridges and Galapagos Spreading Center. This observation is of particular interest because the SEIR has a constant spreading rate, lacks large transform offsets and is far from any hotspot-ridge interaction. The same situation does not apply along the full extent of either the Juan de Fuca-Gorda Ridge or the Galapagos Spreading Center.

A more detailed look at the SEIR data on an equiline diagram is given in Figure 6. In terms of enrichment these data can be divided into three groups; 1) an enriched group with Th/U (κ) ≥ 3.4 , 2) an intermediate group with Th/U (κ) between 3.3 and 2.8, and 3) a depleted group with Th/U (κ) ≈ 2.4 . As previously noted there is a strong along axis gradient in ($^{230}\text{Th}/^{232}\text{Th}$) and κ (Figure 3), with depleted samples more common in the western group (red symbols) and enriched samples more common in the eastern group (blue symbols) although the intermediate group shows some overlap with both the enriched and depleted groups of the SEIR array. Thorium concentrations also overlap between the intermediate group ([Th] = 0.58- 0.17 $\mu\text{g/g}$) and the enriched group ([Th] = 1.16 -0.25 $\mu\text{g/g}$), suggesting that these groups do not simply represent different degrees of melting of a similar source. Rather, both the degree of melting and mantle source Th/U appear to vary along the SEIR. If Th concentrations and Th/U ratios were controlled by varying degrees of melting alone a strong positive correlation between these values would be expected. However when Th/U is plotted against Th concentration (not shown) no significant correlation is observed ($R^2=0.49$; with a Th/U ~ 3.5 , [Th] ranges from 280 to 943 ng/g). Samples with ^{226}Ra -excesses (samples with black dots at the center of the symbols in Figure 6) are highly correlated (slope of 0.99 with an $R^2 = 0.96$ black line). This slope is steeper than any of those reported by Lundstrom et al. (1998b) for other intermediate spreading ridges Juan de Fuca, Gorda and AAD (0.42, 0.32, 0.80, respectively) and is also greater than the slope for the super-fast spreading EPR between 20 and 27°S (0.82). A slope of 0.99 implies a slightly higher ^{230}Th -excess at the enriched end of this array compared to the depleted end ($\sim 15\%$ at ($^{238}\text{U}/^{232}\text{Th}$)= 0.8 compared to $\sim 9\%$ at ($^{238}\text{U}/^{232}\text{Th}$) = 1.3), in general agreement with the mixing model of Lundstrom et al. (1998b). According to the modeling of Lundstrom et al. (1998b) a slope of 1.0 at a solid upwelling rate similar to that of the SEIR requires dynamic melting, in which the depleted source contains lower modal garnet and clinopyroxene and it begins

melting at shallower depth than the enriched source. In their model, Lundstrom et al. (1998b) first generate positive sloping arrays on the equiline diagram ($(^{230}\text{Th}/^{232}\text{Th})$ vs. $(^{238}\text{U}/^{232}\text{Th})$) by invoking two end-member source compositions; 1) a depleted end-member with higher $(^{238}\text{U}/^{232}\text{Th})$ and 2) an enriched end-member with low $(^{238}\text{U}/^{232}\text{Th})$. The enriched end-member has higher modal abundances of clinopyroxene and garnet relative to the depleted end-member. Higher modal abundances of clinopyroxene and garnet leads to; 1) greater differences in Th and U partition coefficients, and 2) a more fertile lithology with a relative lower solidus temperature. Lowering the solidus temperature leads to melt initiation at greater depths relative to the more depleted (less fertile) end-member lithology. These characteristics lead to higher ^{230}Th -excesses in melts generated from the enriched end-member by; 1) increasing the fractionation of Th from U (due to the difference in partitioning), and 2) increasing the proportion of melting that occurs in the presence of garnet by lowering the solidus temperature of the source material, which combined leads to positive sloping arrays on the equiline diagram (i.e., higher ^{230}Th -excesses at lower $(^{238}\text{U}/^{232}\text{Th})$ values). Building on the effect predicted by their end-member source model, Lundstrom et al. (1998b) argue that, although remaining positive, the slope of the data arrays on the equiline diagram are then controlled by the solid upwelling (or spreading) rate of the ridge system and should rotate to progressively flatter arrays with decreasing solid upwelling rate. Because solid upwelling rates are lower at slow spreading ridges these systems provide more time for ingrowth to occur during melting, which leads to relatively higher ^{230}Th -excesses compared to faster spreading ridges. However, because the depleted end-member in their model melts shallower and has less garnet the amount of additional ingrowth that occurs will always be lower at the depleted end of the array relative to the enriched end-member, regardless of spreading rate. Collectively, their model suggests that as spreading rate decreases the magnitude of additional ingrowth generated from the enriched end-member is significant, but remains minor in melts

generated from the depleted source. This leads to closely stacked melts at the depleted end of the equiline diagram but increasingly larger ^{230}Th -excesses in melts generated at the enriched end as solid upwelling rates decrease, and thus flatter arrays. Since spreading rate is constant along the SEIR, source mineralogy and the initial depth of melting would have to control the generation of variable ^{230}Th -excess at the enriched and depleted ends of the array. However, in the case of the SEIR lavas, the generally higher $\text{Fe}_{8,0}$ values in the western (more depleted Th/U) region are not consistent with shallower initial depths of melting beneath that region. Furthermore, the western portion of the SEIR is characterized by the shallowest axial depth, and axial morphology indicative of an increased magma supply relative to the eastern portion of the SEIR (see section 3.3.1 *Along axis morphologic variation*). Mantle dominated by a depleted and less fertile source mineralogy would be expected to begin to melt only at very shallow depth and so appears to be unsuitable. Therefore, melting variations beneath the SEIR at the regional scale are not well explained by the upwelling/variable source model of Lundstrom et al. (1998b).

The regression discussed above is well constrained because it is generated using only samples that have a measured ^{226}Ra -excess. However, this criterion applies to only 9 of the 17 samples from the SEIR. The additional sample is from further east, within the AAD, as measured and reported by Bourdon et al. (1996 a). The remaining 7 samples either do not have measured ^{226}Ra or, in the case of sample 89-4, have $(^{226}\text{Ra} / ^{230}\text{Th}) = 1.0$. An error envelope has been calculated for the linear regression (grey curves Figure 6) in order to address the question of possible radioactive decay in these remaining samples. All of the samples with measured ^{226}Ra –excesses are either enclosed by this envelope or lie above it. If the regression does in fact describe a meaningful systematic behavior of $(^{238}\text{U}/^{232}\text{Th})$ and $(^{230}\text{Th}/^{232}\text{Th})$ in these SEIR MORB, then it is worthwhile to point out that five samples without measured ^{226}Ra that plot inside or above this envelope also appear to be representative. These five data points,

three from the intermediate (green) group and two from the western (red) group are shown on Figure 6 as solid symbols without black dots. The final two samples in this dataset, one from the study of Bourdon et al. (1996 a) and one from the western SEIR group, both plot below the error envelope suggesting these two samples may have experienced some ^{230}Th -decay. These samples are shown on Figure 6 as open symbols, where the diamond represents the work of Bourdon et al. (1996 a). If an initial ($^{230}\text{Th}/^{232}\text{Th}$) value for these samples is assumed to lie on the regression line then it is possible to calculate their ‘age’ assuming ^{230}Th -decay has led to their measured values of ($^{230}\text{Th}/^{232}\text{Th}$). This produces ‘ages’ of ~189 kyr for the western SEIR sample and ~85 kyr for the sample from Bourdon et al. (1996 a). Assuming a half-spreading rate appropriate for the SEIR and a sample age of ~189 kyr, WW10-84-7 would have to have been dredged ~7 km off-axis assuming it erupted on the ridge axis and was subsequently transported away from its original location by plate spreading. This distance is extreme for this well-defined axial-high portion of the SEIR. Nevertheless, because these ages are significant in terms of the half-life of ^{230}Th their current ($^{230}\text{Th}/^{232}\text{Th}$) values are not considered to be primary, and their positions on diagrams in the following discussion are not useful constraints on the melting history beneath the SEIR.

3.5.3 *U-series disequilibria and morphologic characteristics*

Despite a nearly constant, intermediate spreading rate, this portion of the SEIR is characterized by variable axial morphology, which likely reflects subtle differences in melt supply (Phipps-Morgan and Chen, 1993; Chen, 1996, 2000). The well-documented and systematic morphologic variations along the SEIR at constant spreading rate provide a unique opportunity to investigate the influences of ‘physical’ parameters, such as porosity, melting rate and initial depth of melting/melting

column height on U-series disequilibria. In general, the models presented in Chapter 1 (*section 1.2.2*) show that ^{230}Th -excess will be increased by lower porosity, lower degrees of melting, lower melting rate and greater initial depth of melting. Since the SEIR is spreading at a near constant rate between 88° - 118°E , it is reasonable to assume that the mantle upwelling velocity is also nearly constant throughout this region. However, along axis variations in $\text{Fe}_{8,0}$, $\text{Na}_{8,0}$, and axial morphology suggest an along axis gradient in mantle temperature from higher mantle temperatures in the west to lower mantle temperatures in the east. It is therefore reasonable to assume that the western portion of this study area, where mantle temperatures are hotter, also experiences higher degrees of melting, initiating at a greater depth, and these effects are accompanied by higher porosity than the mantle/melt region in the east.

In order to investigate potential links between melt supply and ridge morphology the SEIR data may be divided into four morphologic groups that differ slightly from the earlier 3 geographical groupings. The first group is referred to as the Axial-High group (AH) and includes five samples from segments C16 through C14 and the westernmost portion of segment C12 (samples 71-1, 75-4, 78-2, 84-7, and 96-1, respectively). These segments are similar in dimension and shape to segments along the fast-spreading EPR. A shallow axial magma lens and a thinner layer 2A was imaged beneath westernmost portion of segment C12 (Baran et al., 2005) and by inference of similar morphology this crustal structure is assumed to also be characteristic of the segments C16 to C14. The second group is referred to as the Rifted-Axial-High group (RH) and includes four samples, one each from segments C13, the eastern portion of C12, and segments C11 and C8 (samples 89-4, 100-1, 105-1 and 118-1, respectively). This group has axial morphology similar to that observed along the intermediate spreading Galapagos Spreading Center near 94.2°W . The main difference between the AH and RH groups is that the RH group is characterized by an ~ 100 - 200 m deep narrow rift on top of an otherwise axial-high morphology. Segments

C12, C11 and C8 all lie within the detailed survey area between 100°E and 111°E (Cochran et al., 1997; Sempere et al., 1997; Ma and Cochran, 1997; Baran et al., 2005). The RH group has seismically imaged magma lenses, however, the magma lens is ~1000 m deeper in the RH group when compared to the AH group. The third group is referred to as Shallow-Axial-Valley (SV) and includes 5 samples from segments C9 and C7 through C4 (samples 113-7, 125-1, 126-7, 132-1 and 141-1, respectively). It also lies within the detailed survey area between 100°E and 111°E. This group is characterized by axial morphology similar to the intermediate spreading-rate GSC west of 95°W (Detrick et al., 2002), with a poorly defined 500-800 m deep axial valley, lacking large bounding faults. No axial magma lens was imaged beneath these segments of the SEIR. The fourth group is referred to as Deep-Axial-Valley (DV) and includes three samples, one each from segment C3 and C2 and a third sample reported in Bourdon et al. (1996 a, sample D22-13) erupted further to the east within the AAD. These segments have well-defined deep axial valleys similar to the slow-spreading mid-Atlantic ridge (MAR). These segments lie outside the detailed survey area, but by inference the SV group is believed to lack an axial magma lens. It was also noted by Baran et al. (2005) that the transitions between these different modes of axial morphology occur abruptly, suggesting a threshold mechanism.

3.5.4 Morphologic groups and the 'global' ^{230}Th vs. axial depth trend

Measured ($^{230}\text{Th}/^{238}\text{U}$) values for the SEIR divided into morphologic groups are plotted against axial-depth on the global ^{230}Th -excess vs. axial depth diagram in Figure 7. Unlike the previous version of this diagram when the SEIR data was grouped geographically, the morphologic groups form discrete clusters. Three morphologic groups, the RH, SV and DV, (red, yellow, and green symbols, respectively) form an array very similar to the global trend originally discussed by Bourdon et al. (1996 a).

However, the AH group plot below the global trend to lower ^{230}Th -excess despite their similarity in axial depth to the RH group. Recently, U-series data from the 'central bulge' region of the Galapagos Spreading Center (GSC) have been reported and these have similarly low ^{230}Th -excess at even shallower axial depths (Figure 7; Kokfelt et al., 2005; Christie et al., 2005). This portion of the GSC is positioned just east of the Galapagos archipelago and is characterized as having an axial-high morphology, while further to the east the GSC transitions into an axial valley morphology (Christie et al., 2005). This transition along the GSC is believed to occur in response to an increase in mantle temperature and magma supply closer to the Galapagos hotspot (Christie and Sinton, 1981; Schilling et al., 1982; Verma et al., 1983; Ito and Lin, 1995; Canales et al., 1997; Detrick et al., 2002; Christie et al., 2005; Kokfelt et al., 2005). Although the regional features of the GSC reflect interaction of a mantle hotspot with a migrating spreading ridge, the fact that the GSC is spreading at an intermediate rate ($\sim 46\text{-}64$ mm/yr full rate) and is characterized by an along axis transition in axial morphology and depth away from the Galapagos hotspot, allows for an interesting analogy to be drawn between the eastern GSC and the SEIR. Unlike the SEIR, where the only inferred thermal inputs in the form of hotspots are hundreds to thousands of kms away, the close proximity of the GSC to the Galapagos hotspot provides a close source of additional heat and mass into the regional upper mantle. Geochemical tracers indicate that along with a thermal contribution there is also a material contribution to the GSC from the Galapagos hotspot (Schilling et al., 1982, 1991, 2003), which is a very different situation than that observed along the SEIR. However, the global correlation proposed by Bourdon et al. (1996 a) is presumed to result from variations in mantle temperature, and so the SEIR and eastern GSC provide an interesting analogy.

If axial highs at intermediate spreading rate result from an increase in magma supply and a change in the thermal regime of the lithosphere, it follows that an increase in the initial depth of melting would lead to higher total degrees of melting

and a greater melt supply to the ridge axis. In terms of global systematics, if all other parameters are fixed then an increase in the initial depth of melting should lead to a greater proportion of melting occurring in the garnet stability field, and thus an increase in ^{230}Th -excesses. Such an effect is absent along the axial high region of the SEIR and the ‘central bulge’ of the GSC, where these lavas lie along the lowermost part of the global MORB ‘trend’ (Figure 7).

An alternative possibility is that the hotter mantle beneath this western portion of the SEIR results in a higher proportion of melt being sustained in the melting region beneath the ridge axis. Such an increased proportion of melt on a fine-scale can be represented by an increase in mantle porosity, which in turn lowers ^{230}Th -excess, providing other variables such as melting rate and mineral/melt K_d 's are constant. The lower excesses in this scenario occur as a result of slightly larger degree melts remaining in contact with the residual mantle. This effect is demonstrated in Figure 8 using the dynamic melt equations of McKenzie (1985) and Williams and Gill (1989). The difference in ^{230}Th -excesses between the AH and RH groups are considerable (Figure 7), but can be accommodated by an increase in mantle porosity, from ~ 0.1 - 0.2% in the mantle beneath the RH group to a porosity of 2.5% in the mantle beneath the AH group. These increases in porosity are large and are given here as maximum values. A smaller increase in porosity would be necessary if coupled with an increase in melting rate; when these two variables change together the variation in ^{230}Th -excess can be accommodated by an increase in porosity from $\sim 0.1\%$ to $\sim 0.5\%$ provided melting rate also increases from $2.6 \times 10^{-4} \text{ (kg m}^{-3} \text{ yr}^{-1})$ beneath the RH group to $8.0 \times 10^{-4} \text{ (kg m}^{-3} \text{ yr}^{-1})$ beneath the AH group (Figure 8). However, the actual magnitude of these changes remains highly dependent on input assumptions, including the selected partition coefficients. In the following discussion, more importance is placed on the modeled changes induced by varying these parameters than on the actual values obtained from these simplified models.

Conceptually, more melt being present in the mantle underlying the most inflated portion of the ridge axis in the west might be expected, and is similar to the case presented for the difference in melting beneath hotspots compared to mid-ocean ridges (McKenzie, 2000; Stracke et al. 2006) or suggested for hotspot-influenced ridge segments (Bourdon et al., 1996b). Additionally, sustaining an increased proportion of melt within a melting region would require a coupled increase in mantle porosity and melting rate. The presence of a more sustained, but variable, supply of melt beneath these segments is also supported by the geophysical data present by Baran et al. (2005). The AH segments exhibit a relatively shallow magma lens and the RH groups are also capable of sustaining a magma lens, albeit somewhat deeper in the crust. Similar increases in the depth to the magma lens have been observed along two segments of the fast- to intermediate spreading EPR north of the Orozco transform (Chen, 2003), which were interpreted to have markedly different magmatic budgets (Carbotte et al., 1998). Thus, it appears reasonable to invoke an increase in magma supply coupled with increased melting rate and porosity beneath the AH segments relative to the RH segments. However, similar arguments are not reasonable for explaining the ^{230}Th -excess versus depth relationship for the SV and DV groups concentrated in the eastern portion of the field area, whose morphologies are indicative of progressively decreasing melt supply.

As previously mentioned, the data from the RH, SV and DV groups form a continuous, negative array on Figure 7, similar to that of the global data. The fact that these portions of the SEIR are also characterized by increasing $\text{Na}_{8,0}$, and decreasing $\text{Fe}_{8,0}$, and are consistent with a morphology indicative of a decreased melt supply, makes it more likely that there is a progressive shoaling of melt initiation depth going eastward beneath the SEIR. This results in decreased ^{230}Th -excess, as suggested by the global model of Bourdon et al. (1996a), the effects of which are demonstrated in Figure 9a and b using the incremental solutions to the dynamic melt equations

of McKenzie (1985) and Williams and Gill (1989) as reworked by Stracke et al. (2003). A variation in the depth of melt initiation of ~10 km accompanied by a 2 to 4% reduction in the overall degree of melting is sufficient to describe the entire range observed in ^{230}Th -excess from the RH group to the DV group. These results support the evidence from geophysical observations that crustal accretionary processes are particularly sensitive to melt production and supply at intermediate spreading rates. Furthermore, the SEIR U-series data, in combination with the detailed geophysical data from this region, provide plausible insight into the complexity of the crustal accretionary process. When considered in this way it should not be surprising that considerable scatter exists within the global ^{230}Th -excess versus axial depth 'trend' and highlights the importance of considering a broad range of both geochemical and geophysical observations when interpreting results of U-series disequilibria.

Thus we favor a mechanism similar to that presented by Bourdon et al. (1996a) in which mantle temperature plays a significant role in controlling the long wavelength regional variation in axial depth and ridge morphology, as previously suggested by both geophysical and other geochemical observations along the SEIR (see section 3.3.1 and 3.3.2). We also note that the U-series data gathered along the SEIR shows considerable promise in helping to decipher the complex nature of the crustal accretionary process at the segment length scale and perhaps at even finer scales. The spatial resolution of the current U-series data set does not allow a focused investigation on the ridge segment or smaller scale variations along the SEIR. The above relationships point to the morphologic transitions along segments C12 through C11 and C8 through C7 as ideal targets for a more detailed investigation in the future, in which the combination of U-Th-Pa-Ra disequilibria are ideally suited to constrain the control of porosity and melting rate on the crustal accretionary process at a scale of tens of kilometers and less.

3.5.5 Morphologic groups and the 'equiline' diagram

Lundstrom et al. (1998) used the equiline diagram to evaluate suites of data from a number of mid-ocean ridges and concluded that EMORB (i.e. higher Th/U or lower ($^{238}\text{U}/^{232}\text{Th}$)) typically have greater ^{230}Th -excesses compared to NMORB. This conclusion was drawn from the observation that slopes on the equiline diagram are typically < 1.0 , a relationship requiring relatively higher ($^{230}\text{Th}/^{232}\text{Th}$) values at lower ($^{238}\text{U}/^{232}\text{Th}$) values. The SEIR data are plotted according to their morphologic groups in Figure 10. The relationship between ^{230}Th -excess and axial depth (Figure 7) for the RH, SV and DV groups is once again apparent by the way in which the arrays formed by these groups 'stack' on the equiline diagram. This is simply a consequence of the average ^{230}Th -excess for each of these morphologic groups (average excess of 19%, 15% and 11%, respectively for the RH, SV and DV groups). In terms of enrichment the AH group extends from moderate ^{230}Th -excesses in the most depleted part of the equiline diagram to relatively low ^{230}Th -excesses at intermediate ($^{238}\text{U}/^{232}\text{Th}$). The RH group shows high ^{230}Th -excesses at a range of ($^{238}\text{U}/^{232}\text{Th}$) values from intermediate to slightly lower ($^{238}\text{U}/^{232}\text{Th}$) values. The SV group plots at a similar range of ($^{238}\text{U}/^{232}\text{Th}$) to that of the RH group but with slightly lower ^{230}Th -excesses. The DV group plots at enriched values of ($^{238}\text{U}/^{232}\text{Th}$) and even lower ^{230}Th -excesses. Least square regressions were used to calculate slopes for each of these individual morphologic data arrays. The slopes for the RH and SV groups are ≤ 1.0 , suggesting the tendency for more enriched (i.e. lower ($^{238}\text{U}/^{232}\text{Th}$)) samples to have higher ^{230}Th -excesses, whereas the AH and DV groups have steeper slopes suggesting that the more enriched samples in these groups have lower ^{230}Th -excesses. Thus, no consistent relationship is obvious between the slopes of these SEIR data arrays on the equiline diagram and enrichment. However, it is interesting to note that when only the RH, SV and DV groups are considered these slopes rotate towards steeper values as the average

^{230}Th -excess and ($^{238}\text{U}/^{232}\text{Th}$) of these groups decrease. If the decreasing ^{230}Th -excess observed between the RH, SV and DV groups actually reflects a shoaling of melt initiation depth (as discussed in the previous section), then the tendency of slopes through these data arrays to increase as average ($^{238}\text{U}/^{232}\text{Th}$) decreases supports an increased sampling of enriched material beneath the deepest ridge segments along the SEIR, and that increased sampling tends to produce lower ^{230}Th -excess. The effect of mantle heterogeneity is further addressed below beginning with section 3.5.6.

In summary, the along-axis variations observed in the U-series measurements are consistent with greater melt production beneath the western portion of this field area. In addition to this long wavelength west to east decrease in melt supply, the U-series results also track sub-regional (segment to multiple segment length scale) variations in axial morphology. Collectively, the U-series measurements and geophysical evidence support a subtle change between AH and RH segments requiring a more sustained supply of melt to the AH (western) segments. The U-series results are consistent with this enhanced supply being sustained by a coupled increase in melting rate and mantle porosity. There is a decrease in ^{230}Th -excess as the SEIR transitions into SV and DV-type morphologies. When combined with the geophysical evidence these results can be reasonably explained by a shoaling of melt initiation to the east, similar to what would be inferred from the ‘global’ model of Bourdon et al. (1996a).

3.5.6 Mantle heterogeneity along the SEIR: a combined trace element, U-series and long-lived isotope perspective

As previously stated in the results (*section 2.3.4*) the SEIR lavas show a large range in Th/U, ($^{238}\text{U}/^{232}\text{Th}$) and ($^{230}\text{Th}/^{232}\text{Th}$), spanning most of the global range for MORB in these parameters. Such variations MORB are most easily explained

by variations in Th/U of the mantle source region. Variable Th/U, ($^{238}\text{U}/^{232}\text{Th}$) and ($^{230}\text{Th}/^{232}\text{Th}$) in the source region of MORB can result from mantle heterogeneity introduced into the source region (Condomines et al., 1981; Lundstrom et al., 1998a; Hirschmann and Stolper, 1996; Stracke et al., 1999). Variable ($^{230}\text{Th}/^{232}\text{Th}$) has also been suggested to result from the progressive recent depletion of a mantle source by repeated melting events (Rubin and Macdougall, 1992; Macdougall, 1995). Several processes have been repeatedly called upon as potentially introducing heterogeneities to the mantle source region and include; 1) subduction of sediments and oceanic crust (Elliot et al., 1999), 2) contamination from mantle plumes (e.g. Schilling et al., 1982), 3) intra-mantle differentiation via partial melting (e.g. Hanson, 1977; Wood, 1979) and/or 4) crustal foundering during continental rifting (Arndt and Goldstein, 1989). In the following sections, the U-series data are combined with other geochemical tracers of mantle heterogeneity in an attempt to further constrain the geochemical variation and mantle evolution sampled by recent volcanism along the SEIR.

3.5.7 Trace elements

Incompatible trace element ratios are useful indicators of mixing and source heterogeneity in MORB because of their relatively low partition coefficients and the likely large degrees of melting involved in the generation of MORB. The combination of these two characteristics does not permit melting to generate large variations in incompatible trace element ratios because similarly incompatible elements can only be fractionated from one another at very small degrees (generally < 1%) of melting (Hofmann, 1997). In this view, enriched compositions in MORB would need to originate from very small degrees of melting, which is not supported by the major element composition of MORB and their inferred relatively large degrees of melting. Alternatively, these enrichments could come from larger degree melts derived from

relatively enriched, but volumetrically subordinate, heterogeneous veins or blobs in the mantle (Hanson, 1977; Wood, 1979; Allegre and Turcotte, 1986; Prinzhofer et al., 1989; Hirschman and Stolper, 1996).

SEIR MORB show strong linear relationships consistent with mixing on trace element ratio diagrams involving highly to moderately incompatible elements. These ratios extend from values near those of primitive mantle to values typical of NMORB. For instance, when Nb/La is plotted versus Th/La, SEIR lavas from this study range in values of Th/La from 0.12 to 0.04, equal to the range from Primitive Mantle (0.112, Sun and McDonough, 1989) to NMORB (0.048, Donnelly et al., 2004). This range is difficult to explain by melting without invoking very small degrees of melting (i.e. < 0.5%) and supports a compositionally variable mantle beneath the SEIR. Additionally, Th/La ratios in MORB are generally greater than (or equivalent to) their source ratios, thus values below that of the Primitive Mantle could indicate a previous depletion event (e.g. partial melt removal). Near constant Ce/Pb and Nb/U ratios for these SEIR basalts (23.1 ± 2.7 and 44.8 ± 3.6 , respectively) similar to the average global values of MORB and OIB (26.9 ± 2.1 and 47 ± 10 , respectively; Hofmann et al., 1986), are consistent with the entire upper mantle beneath the SEIR having experienced depletion during continental crust extraction, (Hofmann, 1997), here referred to as the ‘first continental differentiation event’.

The relationship between middle (Tb) and heavy (Yb) REE as expressed in the normalized ratio $(Tb/Yb)_n$ is believed to be a good indicator of garnet in the source region of basalt because Tb is moderately incompatible and Yb highly compatible in garnet (bulk $D \approx 1$ versus 5 for Tb and Yb, respectively). In section 3.5.4 the SEIR data were evaluated in terms of their ^{230}Th -excess and axial depth. When divided into morphologic groups the RH, SV and DV were found to overlap reasonably well with the ‘global’ trend. Recalling that the premise behind the global trend is increased melting in the garnet stability field leading to greater ^{230}Th -excess, it would then be

expected that the RH group, which has the highest ^{230}Th -excess and follows the trend defined by the global data set, would also have the highest $(\text{Tb}/\text{Yb})_n$ values and the DV group, with the lowest ^{230}Th -excess would have the lowest $(\text{Tb}/\text{Yb})_n$ values. However, this is not the case. The average $(\text{Tb}/\text{Yb})_n$ values for the RH, SV and DV groups are $1.19 (\pm 0.05)$, $1.25 (\pm 0.04)$ and $1.28 (\pm 0.06)$, respectively, suggesting increased involvement of garnet beneath the deepest portion of the SEIR. Admittedly, these differences are minor and given their uncertainty are statistically indistinguishable; nevertheless, the trend towards higher $(\text{Tb}/\text{Yb})_n$ values in lavas from the deepest ridge segments along the SEIR is consistent with an increased involvement of garnet in the source of these lavas.

Additionally, the relationship between $^{176}\text{Lu}/^{177}\text{Hf}$ and Th/U ratio has been proposed as a potential identifier of garnet in the source region of oceanic basalts (Lundstrom et al., 2000). The observation that Th/U and $^{176}\text{Lu}/^{177}\text{Hf}$ are negatively correlated in Pacific seamounts suggests that, like Th/U, Lu/Hf may also be an effective tracer of enriched and depleted material in the source region of ocean basalts. However, unlike Th and U, which are both highly incompatible elements and thus only able to be fractionated from one another at very small degrees of melting, experimental results for Lu and Hf suggest that Lu is highly compatible in garnet while Hf is moderately incompatible ($K_d \text{Lu} = 7.0$ and $K_d \text{Hf} = 0.4$; Salters and Stracke, 2004). This compatibility difference is large enough that in a fertile lherzolite assemblage (i.e. ~50% olivine, 20% orthopyroxene, 12% clinopyroxene, and 8% garnet) garnet has a strong enough influence on the relative bulk partition coefficients to lead to fractionation of Hf from Lu even at the relatively large degrees of melting characteristic of MORB source mantle (Salters and Hart, 1989). The negative correlation between Th/U and $^{176}\text{Lu}/^{177}\text{Hf}$ for Pacific seamounts has been interpreted to result from the melting, and subsequent mixing, of a lherzolite mantle with varying amounts of melt from mafic (garnet-bearing pyroxenite) veins (Lundstrom et al.,

2000). The SEIR lavas overlap the EPR seamounts (Figure 11) in Th/U – Lu/Hf space, and, consistent with the observed relationship between Th/U and (Tb/Yb)_n, lavas from the deepest SEIR ridge segments once again define the most enriched ‘garnet influenced’ portion of the trend.

Trace element indicators of enrichment in SEIR basalts are consistent with the mantle beneath the SEIR, between 88 and 118°E, being compositionally variable and possibly heterogeneous on a small scale. Additionally, trace element ratios such as Lu/Hf and Tb/Yb, thought to track the relative abundance of garnet in a melting region also suggest garnet plays a variable role in melt production across this region. Combined these tracers suggest that the mantle beneath the eastern portion of the study area is more enriched and either contains a greater abundance of garnet, or the abundance of garnet is relatively constant throughout the region but the overall lower melt production in the east results in less dilution by melting of depleted peridotite, thereby better preserving the garnet signature.

3.5.8 The long-lived isotope systems: Sr, Pb and He

A more robust assessment of source heterogeneity can be made through the comparison of U-series isotopes with those of long-lived isotopes. The combination of U-series and longer-lived isotopes provides a mechanism to investigate both short and long-term chemical fractionation related to melting (in the short-term) and the geochemical evolution of the Earth’s interior (in the long-term). In particular, Pb and Sr isotopes in combination with (²³⁰Th/²³²Th) measurements have been particularly insightful (Condomines et al., 1981; Allegre and Condomines, 1982; Ben Othman and Allegre, 1990; Rubin and Macdougall, 1992; Macdougall, 1995; Elliot, 1997, 1999; Condomines and Sigmarsson, 2000; Vlastelic et al., 2006). So called long-lived isotope systems (e.g. Rb-Sr, U-Th-Pb), with half-lives on the order of tens of billions

of years provide insight into ancient fractionation events and the evolution of the planet. As such, they are ideally suited as tracers of such events (or heterogeneities) in the source region of MORBs. However, because the parent-daughter pairs (e.g. Rb/Sr, U/Pb, Th/Pb) have very different partitioning behavior they are readily fractionated from one another during recent melting events, so these systems at face value do not provide direct information about the current parent-daughter ratios in a heterogeneous mantle. The U-series isotopes are similar to other isotopic systems in the sense that the parent isotopes decay with long half-lives to isotopes of lead, thereby providing a record of the long-term integrated history of source Th/U. However, unlike other isotope systems, the U-series system can provide direct information about the elemental ratio of Th/U in the source region. This is true provided; 1) the source was in secular equilibrium prior to the onset of melt extraction, 2) melt is extracted rapidly from the source region and 3) Th and U are not significantly fractionated from one another by the melting process. The first requirement is reasonable given the relatively long residence time of U, Th, and Pb in the mantle compared to the half-life of ^{230}Th (i.e. 10^8 vs. 10^4 years, Rubin and Macdougall, 1992; Galer and O’Nions, 1995). The second requirement is supported by the common excess of shorter-lived ^{226}Ra in MORB. And lastly, the third requirement is reasonable given the low bulk partition coefficients of Th and U and the relatively large degrees of melting inferred for MORB.

Uranium-series isotopes and Th/U in SEIR basalts show moderate to strong correlations with $^3\text{He}/^4\text{He}$ and the Pb-isotope parameter $\Delta 8/4$ (Figure 12). Generally speaking, the most enriched basalts have higher $\Delta 8/4$ and lower $^3\text{He}/^4\text{He}$. In all cases the low $\Delta 8/4$ and high $^3\text{He}/^4\text{He}$ ratios are defined by a cluster of lavas from west of 100°E (red symbols), an isotopic ‘boundary’ previously identified by Mahoney et al. (2002). The U-series results for the SEIR suggest that, in addition to a tendency for lower $^3\text{He}/^4\text{He}$ and higher $\Delta 8/4$ to occur in lavas with low $\text{Fe}_{8.0}$ (Mahoney et al., 2002),

there is also a tendency for these lavas to be more enriched in Th/U.

3.5.9 The Th-Sr isotope correlation

The relationship between Th and Sr isotopes was first discussed by Condomines et al. (1981), who noted a correlation between $(^{230}\text{Th}/^{232}\text{Th})$ and $^{87}\text{Sr}/^{86}\text{Sr}$ from different volcanic regions, with MORB compositions plotting at low-Sr, high-Th values and lavas from hotspot influenced ridges and OIB plotting at higher-Sr, lower-Th values. This observation is consistent with the MORB source representing a reservoir having a time-integrated history of Th/U and Rb/Sr depletion, and the OIB 'array' representing an increasingly more 'pristine' or less depleted mantle source (Figure 13a). Since this original observation, numerous investigations have led to an expanded view of the relationship between Th and Sr isotopes. Although the original observation that MORB mantle represents the low-Sr, high $(^{230}\text{Th}/^{232}\text{Th})$ end of this correlation still stands, considerable scatter in $(^{230}\text{Th}/^{232}\text{Th})$ within the MORB field over a narrow range of $^{87}\text{Sr}/^{86}\text{Sr}$ has since been observed (Condomines et al., 1988; Ben Othman and Allegre, 1990; Ruben Macdougall, 1992; Elliott, 1997; Condomines and Sigmarsson, 2000; Lundstrom, 2003; Bourdon and Sims, 2003). The existence of this scatter has led some to question the validity of using $(^{230}\text{Th}/^{232}\text{Th})$, arguing that $(^{230}\text{Th}/^{232}\text{Th})$ values simultaneously examine both the source Th/U and ^{230}Th in-grown during the melting process (Lundstrom, 2003). Instead, use of $(^{238}\text{U}/^{232}\text{Th})$, or measured Th/U, has been suggested as a more appropriate indicator of the source Th/U ratio (Elliott, 1997; Lundstrom, 2003). However, other studies have re-evaluated the Th-Sr diagram and concluded that the $(^{230}\text{Th}/^{232}\text{Th})$ is better correlated with $^{87}\text{Sr}/^{86}\text{Sr}$ (Condomines and Sigmarsson, 2000) and that the relationship between $(^{230}\text{Th}/^{232}\text{Th})$ and $^{87}\text{Sr}/^{86}\text{Sr}$ is actually hyperbolic (Bourdon and Sims, 2003). Both studies suggest that the Th-Sr array results from mixing of enriched (possibly garnet pyroxenite)

material having low ($^{230}\text{Th}/^{232}\text{Th}$) and variable, but potentially high, $^{87}\text{Sr}/^{86}\text{Sr}$ values. Additionally, the observation that the Th-Sr array is hyperbolic suggests that Th/Sr (concentration ratio) is greater in the enriched mantle component than in the depleted mantle component (Bourdon and Sims, 2003).

The most likely explanation for the scatter in ($^{230}\text{Th}/^{232}\text{Th}$) at the low $^{87}\text{Sr}/^{86}\text{Sr}$ end of the array is recent melt extraction from the melting region (Rubin and Macdougall, 1992, O’Nions and McKenzie, 1993; Condomines and Sigmarsson, 2000; Bourdon and Sims, 2003). For example, Rubin and Macdougall (1992) discussed the possibility that discrete pulses of small-degree melts from an originally homogenous source may account for the observed differences in ($^{230}\text{Th}/^{232}\text{Th}$) along adjacent segments of the fast-spreading southern EPR. The number of such events to go from a relatively enriched (low ($^{230}\text{Th}/^{232}\text{Th}$)) to a relatively depleted (high ($^{230}\text{Th}/^{232}\text{Th}$)) source is dependent on 1) the magnitude of the isotopic difference between these two end-members and 2) the amount of time between pulses. If the time between pulses is sufficiently long enough to allow for the return to secular equilibrium then fewer pulses are required. Conversely, if the pulses occur at shorter intervals then more pulse events are required.

These SEIR lavas have $^{87}\text{Sr}/^{86}\text{Sr}$ ratios ranging from 0.70274 to 0.70368 and collectively do not show a strong correlation with ($^{230}\text{Th}/^{232}\text{Th}$). As a result of the varying ($^{230}\text{Th}/^{232}\text{Th}$) values in SEIR basalts, they form two sub-parallel negative arrays on the Th-Sr diagram (Figure 13b). Samples from the central and eastern portions of the SEIR form the lower ($^{230}\text{Th}/^{232}\text{Th}$) array, extending from values observed in enriched samples from 33°S on the MAR to values observed in the Hawaiian islands. Samples from the western portion of the SEIR, with their higher ($^{230}\text{Th}/^{232}\text{Th}$) values, form the upper array extending from values similar to the EPR at the depleted end to more enriched values similar to high ($^{230}\text{Th}/^{232}\text{Th}$) lavas from the Azores Platform and Iceland. The similar $^{87}\text{Sr}/^{86}\text{Sr}$ range of these two arrays suggests

their sources record a similar long-term integrated history of Rb/Sr. The higher ($^{230}\text{Th}/^{232}\text{Th}$) values in the western SEIR are consistent with the mantle beneath this portion of the SEIR recording more recent melting and fractionation of Th and U.

3.5.10 *Kappa* (κ) versus *Kappa-lead* (κ_{pb})

Contrasts between the modern Th/U and the long-term integrated history of Th/U can be investigated through the comparison of κ (kappa; measured atomic $^{232}\text{Th}/^{238}\text{U}$) and κ_{pb} (kappa lead; inferred Th/U from measured $^{208}\text{Pb}/^{204}\text{Pb}$ and $^{206}\text{Pb}/^{204}\text{Pb}$, see equations 3 and 4, this section). If the Earth had remained a closed system during its entire evolution these two values would be equal. It is not surprising that this is not the case and it has been well documented that a common feature in MORB is nearly homogenous κ_{pb} values (3.8 ± 0.2) at lower and much more variable values of κ (Tatsumoto, 1978; Galer and O’Nions, 1985; Allegre et al., 1986). This disparity, the ‘kappa conundrum’, was the focus of Elliott et al. (1999) who proposed the post-Archean Uranium Recycling (PURE) model to account for this difference in modern MORB. The PURE model stems from the idea that Earth’s atmosphere became significantly more oxygen rich between 2.0 and 2.25 Ga after accretion. In oxidizing environments uranium switches from a U^{4+} oxidation state to U^{6+} , a form highly soluble in aqueous solutions. However, thorium only has a single oxidation state Th^{4+} . When both U and Th are in the 4+ oxidation state, such as is believed to be the case in the mantle beneath mid-ocean ridges, they behave similarly. However, oxidized, readily soluble U^{6+} is much more mobile than Th during continental weathering, thereby fractionating U from Th and allowing U to become concentrated relative to Th in the oceanic environment. Alteration and hydrothermal circulation leads to the exchange of U from seawater into the oceanic crust, thereby enriching it in U over

Th. Plate tectonics and subduction then recycles the U-enriched ocean crust (and sediments) into the upper mantle, significantly lowering the Th/U.

Assuming that Pb isotope evolution of the mantle can be approximated to have occurred in two stages; 1) a period of early continental growth prior to the development of an oxygen rich atmosphere and 2) a second stage of continuous U-recycling (i.e. the PURE model; Elliott et al., 1999), a useful diagram to visually represent such an evolution is that of κ versus κ_{pb} (Figure 14). By selecting reasonable values of μ (e.g. $^{238}\text{U}/^{204}\text{Pb} = 9.0$; White, 1993) and κ (e.g. $^{232}\text{Th}/^{238}\text{U} = \kappa = 4.0$; Paul et al., 2003) a simple two-stage evolution model can be used to generate ‘isochrons’ representative of the time at which the second stage fractionation occurred (Gast, 1969; Chase, 1981; O’Nions and McKenzie, 1993). The present-day $^{208}\text{Pb}/^{204}\text{Pb}$ and $^{206}\text{Pb}/^{204}\text{Pb}$ can be calculated for a two-stage evolution using the following equations:

$$\{^{208}\text{Pb}/^{204}\text{Pb}\}_o = \{^{208}\text{Pb}/^{204}\text{Pb}\}_i + \kappa_1\mu_1(\exp(\lambda_{232}T) - \exp(\lambda_{232}t)) + \kappa_2\mu_2(\exp(\lambda_{232}t) - 1) \quad (1)$$

and

$$\{^{206}\text{Pb}/^{204}\text{Pb}\}_o = \{^{206}\text{Pb}/^{204}\text{Pb}\}_i + \mu_1(\exp(\lambda_{238}T) - \exp(\lambda_{238}t)) + \mu_2(\exp(\lambda_{238}t) - 1) \quad (2)$$

For a single stage model, $^{208}\text{Pb}^*/^{206}\text{Pb}^*$ can be calculated as:

$$^{208}\text{Pb}^*/^{206}\text{Pb}^* = (^{208}\text{Pb}/^{204}\text{Pb}_o - ^{208}\text{Pb}/^{204}\text{Pb}_i) / (^{206}\text{Pb}_o - ^{206}\text{Pb}/^{204}\text{Pb}_i) \quad (3)$$

which can be used to calculate κ_{pb} using:

$$\kappa_{pb} = (^{208}\text{Pb}^*/^{206}\text{Pb}^*) ((\exp(\lambda_{232}T) - 1) / (\exp(\lambda_{232}t) - 1)) \quad (4)$$

These ‘ages’ (t in equations 1 and 2) are represented on the κ versus κ_{pb} diagram as a series of lines originating from a common point on the geochron at a value equal to the BSE value ($\kappa = \kappa_{pb} = 4.0$) and fan out between horizontal and equivalent to the geochron, the two extreme results of the model (inset Figure 14).

In this simple model a horizontal array indicates a continuous closed system evolution of the U-Th-Pb system until some time in the recent past when this reservoir was fractionated to form two complimentary reservoirs 1) a depleted mantle (represented by the low κ end of the line) and 2) an enriched reservoir ‘Primitive mantle’ which could be represented by the point at which this array meets the geochron. The complimentary reservoir to the depleted mantle would likely be continental crust and plot to the right of the geochron. Had the Earth evolved simply in this ‘instantaneous’ two-stage manner the oceanic array would be expected to lay along this horizontal trend, representing varying mixtures of depleted and primitive mantle (\pm continental crust). Because the fractionation happened at some significant time in the past, and continuously over geologic time, samples actually lie along a positively sloped trend in this diagram. The other extreme would be a closed-system throughout the Earth’s history, in which case all samples would plot along the Geochron. The two end-member cases are of course unrealistic but facilitate a clear view of the significance of the remaining lines on the diagram, each potentially representing the time of formation of two (or more) complementary reservoirs. Subsequent mixing between these two reservoirs would then produce a data array whose slope records an age of separation (Vlastelic et al., 2006).

A significant west-to-east along-axis gradient from low κ (and lower κ_{pb}) to high κ (and higher κ_{pb}) is observed along this portion of the SEIR (Figure 3). Given that the SEIR data encompasses most of the global MORB array on the equiline diagram it is perhaps not surprising that these data also encompass a significant portion of the global range of MORB in κ and κ_{pb} (2.43 – 3.91 and 3.79 – 4.02,

respectively). The presence of the coupled along axis gradient in these two parameters also leads to a convergence where $\kappa \ll \kappa_{pb}$ in the west to $\kappa \approx \kappa_{pb}$ in the east (Figure 3; Figure 14). Additionally, the SEIR data plot along a trend slightly oblique to and at higher values of κ_{pb} for a given value of κ compared to Pacific or Atlantic MORB, while intersecting the 4.55 Ga geochron at a value of 4.0, the bulk silicate Earth value (BSE). Values plotting near the geochron could suggest that the mantle beneath the eastern portion of the SEIR has existed in relative isolation over much of the course of Earth history. However, this scenario is highly unlikely, and in fact Ce/Pb and Nb/U ratios are fairly invariable across the entire region (23.1 ± 2.7 and 44.8 ± 3.6 , respectively) and are very similar to the average global values of MORB and OIB (26.9 ± 2.1 and 47 ± 10 , respectively; Hofmann et al., 1986), suggesting that this entire region has been affected by the first continental differentiation event. An alternative explanation for the SEIR data array in Figure 14 is that it represents a mixture of depleted upper mantle (that experienced a two-stage (or more) evolution during which its Th/U ratio was lowered) with material isolated since the first stage of evolution (that did not experience significant Th/U fractionation). In this case, the slope of the SEIR data array in Figure 14 suggests an approximate ‘age’ of 550 Ma. This could be viewed as a maximum age that these separate evolutions ceased, when the two reservoirs became open to mixing with one another.

This age is interesting in that it is roughly similar to ages previously determined for SEIR basalts from Pb, Nd, Sr and Hf isotope systems. For instance, a poorly defined ^{207}Pb - ^{206}Pb ‘age’ of 815 ± 245 Ma was reported by Mahoney et al. (2002) and Graham et al. report ages for these isotopic systems between 200-400 Myr as minimum ‘ages’ for these systems given the uncertain effect that recent melting had on their parent/daughter ratios. Additionally, Donnelly et al. (2004) report congruent, ‘melt corrected’-ages of 307 Ma for the Sr and Nd isotope systems, assuming recent melt extraction (melt fraction of 14%) and using the data of Mahoney et al. (2002).

However, what these ‘ages’ mean is a matter of debate. The ‘age’, determined by Mahoney et al. (2002), based on the relationship between $^{207}\text{Pb}/^{204}\text{Pb}$ and $^{206}\text{Pb}/^{204}\text{Pb}$ is less than the ‘age’ for the same isotopic pair, interpreted by White (1993), as common to the upper mantle and indicative of a complex, open-system, several-billion-year history. In fact, Mahoney et al. (2002) point out that the inferred isochron ages bracket the long period of continental stretching and rifting of East Gondwana that preceded the initiation of seafloor spreading, which was fully developed in the western portion of this region by ~160-170 Ma. A similar mechanism was also proposed by Arndt and Goldstein (1989), who suggested that enriched mafic material from beneath Gondwana was responsible for the enriched isotopic and trace element composition of the upper mantle in southern Atlantic and Indian Ocean basalts. This idea has recently re-gained attention and further support by Janney et al. (2005). Their analysis of SWIR basalts from 13°E to 47°E led to the conclusion that the distinct Indian Ocean upper mantle signature sampled today was derived by the destabilization and foundering of lithospheric mantle beneath Proterozoic orogenic belts bordering the Indian Ocean, a process that was intermittently active during the period 0.5 to 1.5 Ga (Pan-African orogeny). A similar conclusion was reached by Meyzen et al. (2005) for the source of the ‘Indian’-mantle signature in basalts from the 39-41° E section of the SWIR.

However, Mahoney et al. (2002) also mention that similar ‘ages’ have been determined for portions of the global ridge system with no relation to continental breakup, suggesting an alternative explanation for these common ‘ages’ is that they represent the turnover, replenishment or mixing time of the upper mantle (Zindler et al., 1984; Allegre and Lewin, 1995; Albarede and van de Hilst, 2002). And in fact, Donnelly et al. (2004) used a two-box model to demonstrate that these ‘ages’ do not reflect the timing of discrete events but rather continuous formation (in the mantle wedge of subduction zones) and destruction (beneath mid-ocean ridges by partial

melting) of E-MORB mantle sources, and that these ‘ages’ reflect the amount of time required for enriched mantle sources to be created and destroyed.

Regardless of the exact mechanism(s) by which these heterogeneities are formed and introduced into the mantle feeding mid-ocean ridge systems, this enriched material is preferentially removed from the system relative to normal depleted upper mantle during partial melting beneath ridges. Because melting is ultimately what samples this signal, the technique of combining U-series, trace element and long-lived isotopes offers a unique perspective on the mechanisms and timescales at which mantle heterogeneities are sampled by mid-ocean ridge volcanism along the SEIR.

3.5.11 A conceptual model for enrichment and subsequent depletion of the Indian Ocean mantle beneath the SEIR

A striking result observed in the SEIR basalts is the west to east convergence of the present day and long-term integrated record of the Th/U ratio as recorded by κ and κ_{pb} . This relationship becomes even more striking when considering the range of κ and κ_{pb} values (equivalent to the global range thus far observed in MORB) over which this correlation occurs, and the fact that a least squares linear regression through these data on a κ vs. κ_{pb} diagram ($R^2 = 0.77$) intersects the Geochron at $\kappa = \kappa_{pb} = 4.0$, the bulk silicate Earth value. As discussed above these $\kappa \approx \kappa_{pb}$ lavas also have Th/La and Ba/Zr ratios (0.12 and 0.8, respectively) similar to values for the Primitive Mantle (PM values of 0.12 and 0.65, Sun and McDonough, 1989). In contrast, samples with $\kappa \ll \kappa_{pb}$ have values similar to NMORB (0.04 and 0.2, respectively). The SEIR basalts with $\kappa \approx \kappa_{pb}$, combined with some Primitive Mantle-like trace element ratios are intriguing because these characteristics are consistent with a quasi-closed, long-term evolution of the material responsible for this signature in the source. However, the very similar Ce/Pb and Nb/U ratios of all these basalts (which are different from

Primitive Mantle values), and their Sr and Nd isotope compositions clearly reveal that they have seen a previous history of source depletion, typically thought to represent the initial formation of the depleted upper mantle through the formation of continental crust (Hofmann, 1997). In this sense the lavas from the western portion of the field area with incompatible trace elements typical of NMORB seem best explained as derived from a ‘typical’ depleted upper mantle source.

However, the relationship on the κ vs. κ_{pb} diagram suggests a relatively ancient link between these more depleted western lavas and the eastern lavas, which are characterized by more ‘primitive-like’ incompatible trace element ratios and $\kappa \approx \kappa_{pb}$. To further explore the potential genetic link between the depleted, normal MORB-like, western lavas and the enriched, primitive-like, eastern lavas we have devised a three-stage mantle evolution model. The three stages in the model are: 1) the formation of an initial depleted mantle following the formation of continental crust, envisioned in this setting to be the formation of Gondwana at some point prior to 1.0 Ga before present. This first stage obviously ignores a significant portion of Earth history and is simply meant to represent a depleted mantle residue following the formation of continents; 2) The second stage was a period of intra-mantle fractionation during which enriched, small-degree melts were separated from the convecting mantle and infiltrated the base of the lithospheric mantle, forming an ‘enriched boundary layer’. This stage is envisioned to have occurred sufficiently long ago in the past to allow for significant radioactive decay, producing enrichment in the Rb-Sr and U-Th-Pb isotope systems; 3) The third stage was a period of ocean basin formation. This stage is envisioned to have occurred along with the break-up of Gondwana as depleted upper mantle (asthenosphere) filled the shallow mantle void produced by the rifting of the thick continental lithosphere. During this stage the ‘enriched boundary layer’ formed by melt impregnation/freezing became entrained into the mantle beneath the SEIR (as in the Arndt and Goldstein, 1989 model). The stages of this model are summarized

schematically in Figure 15 and the details of each stage are explained in greater detail below.

Stage 1: Initial mantle depletion

This stage is modeled in the same manner used by Hofmann (1988) to form two complementary reservoirs, an incompatible element-enriched crust and an incompatible element-depleted upper mantle source of oceanic basalts. Crust extraction was modeled by 2% modal equilibrium batch melting using the equation:

$$[i]_{cc} = [i]_{PM} / (D_i + F(1-D_i)) \quad (5)$$

where $[i]_{cc}$ is the concentration of element (i) in the continental crust, $[i]_{PM}$ is the concentration of element (i) in the Primitive Mantle, F is the fraction of melt and D_i is the bulk partition coefficient of element (i) in the mantle source. The model assumes a fertile garnet lherzolite assemblage consisting of 50% olivine, 30% orthopyroxene, 12% clinopyroxene and 8% garnet, and utilizes the 3 GPa K_d 's from Salters and Stracke (2004). Some partition coefficient values were modified slightly to eliminate unusual anomalies in normalized concentration diagrams (the values determined are reported in Appendix 2). The residual source composition can then be calculated from the following equation:

$$[i]_{DM=2} = D_i [i]_{cc} \quad (6)$$

where the notation is the same as in equation (5). The final step in this stage is some partial melt retention. This step is necessary in order to buffer the depletion of the most incompatible elements in the residual mantle. This is achieved by assuming a

1% retention of the partial melt. As a check of this simple model the composition of our extracted continental crust is compared to that of Hofmann's TM1 composition (1988). Most elements agree to better than 5% of TM1 compositions with the notable exceptions of Th, Sm, Hf with our calculated values equal to 3.86, 3.89, and 3.26, respectively, compared to TM1 values of 3.5, 3.5, and 3, respectively (differences of 10.3%, 11.2% and 8.9%, respectively). The concept of *Stage 1* is shown schematically in Figure 15A.

Stage 2: Intra-mantle differentiation and the formation of the 'Enriched Boundary Layer'

This stage is modeled by the removal of three, small-degree, melt batches beginning with the residual composition produced in *Stage 1*. Each of the three 'events' is modeled as a 1.25% equilibrium batch melt using equation (4), along with 0.625% retention of the melt into the residual mantle (i.e., 50% by volume of the melt produced). Although seemingly arbitrary these values were determined, by trial and error, as appropriate/capable of producing three important outcomes. First, small degree melt fractions are needed to fractionate the Th/U ratio, in order for the residual mantle to achieve a value similar to the depleted mantle end-member of our data array. Second, enough 'melt' needs to be produced to establish a significant volume in the 'Enriched Boundary Layer' (EBL). The only way capable of achieving both of these goals is by pulsing the melt events. These pulsed events are effective in reducing the Th/U ratio in a step-like fashion, allowing for smaller fractionations between the EBL and the residual mantle. The only other alternative is fractionation driven by very small degrees of melting (i.e. < 1.0%), but this results in 1) over-enrichment in the EBL, 2) excessively large depletion in the residual mantle, and 3) a very low total of melt production by volume.

As depicted in Figure 15B, this process is envisioned to occur over a 400 km depth interval. In the Figure this is shown as the depth range between 200 km and 600 km, above which is envisioned to be the crust of Gondwana and the underlying non-convecting (lithospheric) mantle. Although these depths are arbitrary they are similar to depths beneath old continental bodies (sometimes referred to as the ‘tectosphere’) and what is commonly referred to as the upper mantle (Brown and Mussett, 1993). Assuming these dimensions, three melting events of 1.25% with 50% retention (by volume) leads to the production of an ~7.5 km thick EBL layer, whose composition is a mixture of the melts produced by the three events. The buffered residual mantle composition then represents the composition of the ambient depleted mantle now present beneath the SEIR. The composition of the calculated depleted mantle is compared to the composition determined by Salters and Stracke (2004) in Appendix 2. In general, the compositions of the calculated depleted mantle are within 25% of those determined by Salters and Stracke (2004) within their reported typical range of uncertainty. The results of this stage and the compositions produced for the EBL and depleted mantle ($DM_{t=2}$) in terms of the equiline diagram are shown schematically in Figure 15B.

Stage 3: Basin Formation

The final stage in the model represents the entrainment of the EBL as veined pyroxenite into the rising ambient depleted mantle ($DM_{t=2}$). Conceptually, this stage is envisioned to occur as the continents of Gondwana begin to rift apart and form the eastern Indian Ocean basin. Assuming the material representative of the EBL is entrained into the upper 200 km of mantle beneath the newly forming ocean basin, this veined material would occur as a maximum of 3.75% of the material now in the upper 200 km of mantle feeding the mid-ocean ridge system. Similar values of 2-5%

for the volume of mafic veins are observed in ophiolites and alpine massifs (Mukasa et al., 1991). We have modeled the EBL material as a garnet pyroxenite consisting of 45% orthopyroxene, 45% clinopyroxene and 10% garnet, a mineralogy similar to that proposed by Hirschmann and Stolper (1996) as representative of melt trapped within the mantle. Melt initiation in garnet pyroxenite is known to begin at lower temperatures than that of ambient lherzolite (Pertermann and Hirschmann, 2003), therefore beginning prior to the onset of melting in the surrounding lherzolite. The surrounding, more depleted peridotite is volumetrically dominant so the lherzolite assemblage melting at shallow depths is expected to dilute the garnet signature in the initial melt. Because melt production rate in pyroxenite is greater than in peridotite (up to 3.9%/km compared to 0.33%/km; Hirschmann and Stolper, 1996) pyroxenite, when present, is expected to melt to a very high degree thereby contributing disproportionately to the aggregated lherzolite-pyroxenite melt relative to its volumetric presence in the mantle (Figure 16). In order to simulate the high productivity of the pyroxenite lithology we have modeled these melts as very large degree ($F = 65\%$) melts, and because the style of melting has diminished effects at these degrees we use simple equilibrium batch melting (equation 5).

The depleted mantle ($DM_{t=2}$) is modeled as a spinel lherzolite consisting of 50% olivine, 30% orthopyroxene, 15% clinopyroxene and 5% spinel and melting of this lithology is modeled as non-modal aggregated fractional melt using the equation of Shaw (1970):

$$[i]_{liq} = ([i]_{DM_{t=2}}/F) (1 - (1 - P_i (F/D_i)))^{(1/P_i)} \quad (7)$$

where, $[i]_{liq}$ is the concentration of element (i) in the melt, $[DM]_{t=2}$ is the concentration in the depleted mantle calculated in *Stage 2*, and D_i and P_i are the bulk partition coefficient and mineral melt coefficient of element (i), respectively. A summary

of calculated compositions for the pyroxenite melt, NMORB ($F = 10\%$) and two pyroxenite-NMORB mixtures are presented on an incompatibility diagram and are discussed further in the next section (spider diagram, Figure 17).

3.6 Summary

The model presented above, despite being simple in its approach, succeeds in producing trace element compositions that mimic, remarkably well, both normal-depleted MORB and enriched MORB sampled along this portion of the SEIR (Figure 17 b). The proportions of garnet pyroxenite produced during *Stage 2* are appropriate, given natural observations (Mukasa et al., 1991) and adequate to produce the observed trace element concentration ranges and appropriate ‘shapes’ of trace element patterns observed along the SEIR. In addition, simple mixing calculations using the calculated compositions of NMORB and pyroxenite melt along with reasonable $^{87}\text{Sr}/^{86}\text{Sr}$ values for these ‘end-member’ components (0.70271 and 0.7040, respectively, equivalent to the lowest value observed by Mahoney et al., 2002 and an average value for the Reunion hotspot, Vlastelic et al., 2006) return mixing proportions similar to those required by the observed trace element concentrations for samples from the geographically central and eastern groups.

However, there are a few discrepancies between these modeled results and measured values along the SEIR. In particular the model calculations fail to produce Th/U ratios as low as values observed in the westernmost portion of the study area (model value Th/U = 2.65, WW10-84-7 Th/U = 2.37), despite the model having appropriate concentrations of Th and U. Resolving the westernmost samples become further complicated when combined with the Sr-isotopes of the western group. The samples from the westernmost portion of the field area plot at intermediate values of $^{87}\text{Sr}/^{86}\text{Sr}$ despite having among the lowest Th and U concentrations, a characteristic

that is difficult, if not impossible to produce by mixing a high $^{87}\text{Sr}/^{86}\text{Sr}$, Th- and U-enriched melt with a low $^{87}\text{Sr}/^{86}\text{Sr}$, Th- and U-depleted melt. One possible solution to this discrepancy is that we have failed to identify the true depleted end-member component. For instance, allowing for one more extraction ‘event’ in *Stage 2* could produce adequately low Th/U ratios, but this DM source would then have a considerably lower trace element budget than the composition presented by Salters and Stracke (2004). This alone does not preclude the existence of such a depleted reservoir but would make it impossible to produce the most depleted lavas from the SEIR without involving some contribution from the trace element enriched pyroxenite generated melt. One possibility that could resolve this discrepancy, and is also supported by the elevated ($^{230}\text{Th}/^{232}\text{Th}$) values at intermediate values of $^{87}\text{Sr}/^{86}\text{Sr}$ for these westernmost lavas, is that the latest depletion is a more recent phenomenon that affects the shorter lived isotope ^{230}Th without effecting the longer lived Sr isotope record (Rubin and Macdougall, 1991).

Although highly speculative, this most recent event may then be sampling material with a memory of the history of this intermingled two-component system, while simultaneously recording the most recent fractionation of Th and U in ($^{230}\text{Th}/^{232}\text{Th}$). This speculation becomes increasingly interesting when combined with the independent observation drawn from the relationship between ^{230}Th -excess vs. axial depth in *Section 3.5.4*, where lavas erupted in the western region have lower ^{230}Th -excesses as a result of higher mantle porosity. This idea is intriguing considering the suggestion that the removal of enriched veins in the mantle by pyroxene dissolution and olivine precipitation may lead to the development of replacement dunites representative of high porosity conduits for melt removal (Keleman et al., 1995, 1997). Regardless of these more speculative points, samples from along the SEIR are characterized by a west to east decrease in trace element enrichment, ($^{230}\text{Th}/^{232}\text{Th}$) and inferred mantle porosity and/or melting rate reflecting systematic variations in the

way melt is generated and heterogeneities are sampled along this regional temperature gradient (schematically summarized in Figure 18).

3.7 Conclusions

- Measured U-series isotopes on 16 samples from a ~2600 km long section of the SEIR (88°E to 118°E) cover a remarkable range in ($^{230}\text{Th}/^{232}\text{Th}$) and ($^{238}\text{U}/^{232}\text{Th}$), from 1.42 to 0.88 and from 1.29 to 0.80, respectively. This range is equivalent to ~70% of the entire range observed globally in MORB.
- Along the SEIR there is no simple west to east decrease in ^{230}Th -excess vs. axial depth, as would be expected in terms of the ‘global’ trend suggested by Bourdon et al. (1996a). However, when these data are systematically grouped according to the morphologic expression of the segments from which they erupted, these data form distinct groups on the ($^{230}\text{Th}/^{238}\text{U}$) vs. axial depth diagram. These groupings are consistent with the most magmatically robust (AH group) segments representing melt generation in excess of what is typical for the intermediate spreading rate of the SEIR, and are consistent with these lavas being produced in an environment with higher mantle porosity, possibly accompanied by higher melting rates. The remainder of the SEIR lavas from the RH, SV and DV groups can then be explained by generation and transport through a melting region with lower porosity and progressively shallower melt initiation depths, similar to the model proposed by Bourdon et al. (1996a).
- Values of ($^{230}\text{Th}/^{232}\text{Th}$) and ($^{238}\text{U}/^{232}\text{Th}$) are strongly correlated in SEIR basalts ($R^2 = 0.96$, including only samples with measured ^{226}Ra , and $R^2 = 0.91$ when all data are considered). The slope through this trend is considerably steeper than slopes through data arrays from other intermediate spreading ridges. In fact, the SEIR slope is most similar to the data array from the fast-spreading

southern EPR (Lundstrom et al., 1998; Lundstrom, 2003). The addition of these data to this global compilation verifies the large range observed in the slopes through these data arrays from intermediate spreading ridges. This suggests that melt generation and delivery to intermediate spreading rate ridges is widely variable, and that transitions in morphology along these ridges are likely to respond to small variations in temperature and upwelling rate in a threshold fashion, as supported by geophysical observations (Chen, 1996, 2000; Baran et al., 2005).

- Measured $^{232}\text{Th}/^{238}\text{U}$ (κ) values converge from west to east with $^{232}\text{Th}/^{238}\text{U}$ values inferred from Pb isotopes (κ_{pb}). This observation suggests a recent introduction of old mantle heterogeneity that experienced less Th and U fractionation throughout its history compared to the depleted upper mantle. A model of intra-mantle enrichment and depletion associated with continental rifting and crustal/lithospheric foundering is one possible explanation for κ - κ_{pb} convergence. Such a model is also capable of producing the wide range observed in ($^{230}\text{Th}/^{232}\text{Th}$) and ($^{238}\text{U}/^{232}\text{Th}$) observed along axis of the SEIR, as well as the trace element patterns.
- Basalts from the westernmost portion of the SEIR plot at similar values of $^{87}\text{Sr}/^{86}\text{Sr}$ but at considerably higher values of ($^{230}\text{Th}/^{232}\text{Th}$) than their central and eastern counterparts. This can be explained within the context of the intra-mantle differentiation model if this portion of the mantle beneath the SEIR also experienced a recent Th and U fractionation. Although speculative, such an event may be facilitated by the replacement of pyroxenite veins with high porosity melt conduits during the most recent melting event responsible for the formation of these SEIR basalts.

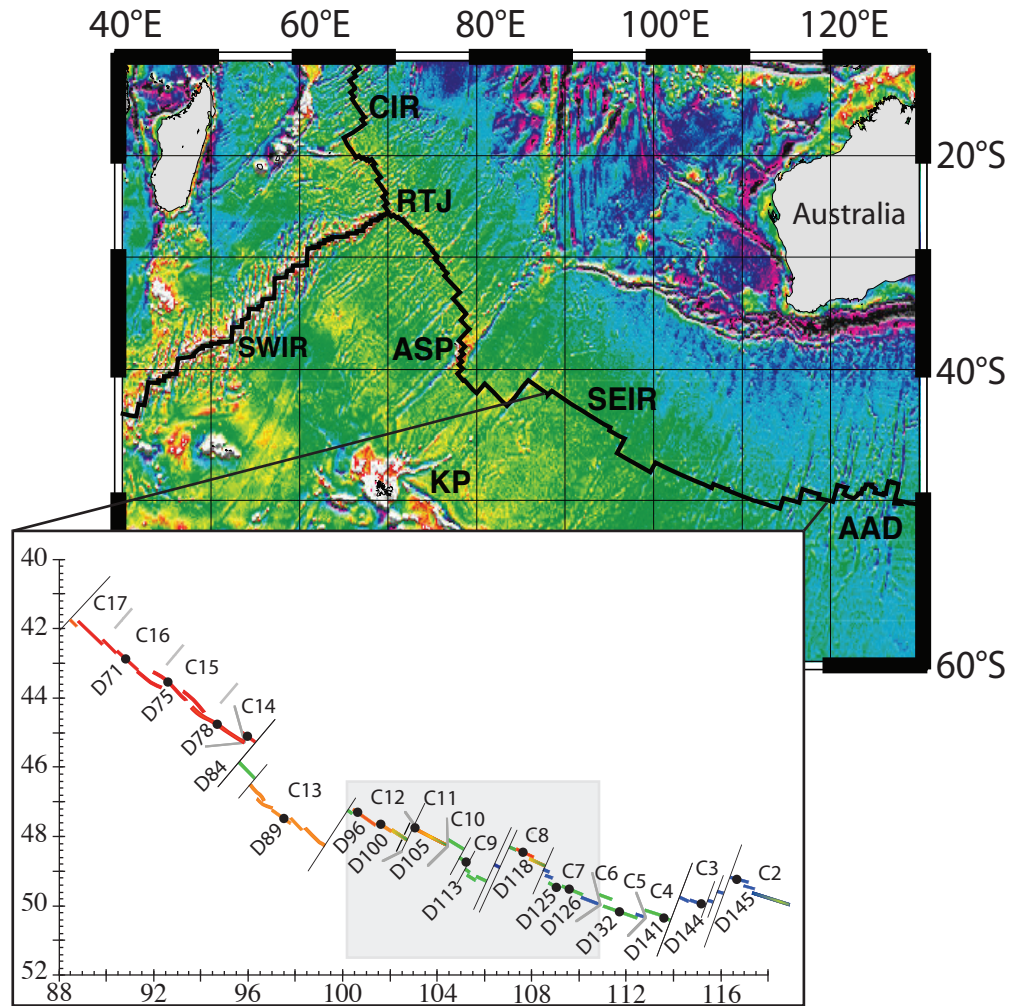


Figure 3-1. Satellite altimetry of the Indian Ocean basin between 40°E and 130°E. Labeled features include: the Southwest Indian Ridge (SWIR), Central Indian Ridge (CIR), Rodrigues Triple Junction (RTJ), Amsterdam-St. Paul Plateau (ASP), Kerguelen Plateau (KP), Southeast Indian Ridge (SEIR), and the Australian-Antarctic Discordance (AAD). Enlarged panel defines ridge-axis trace of the SEIR from 40°S to 52°S and from 88°E to 118°E. Individual ridge segments are identified above the axial trace (C17 through C2), dredge locations for samples in this study are shown by black dots along the ridge-axis and are labeled below the axial trace (D71 through D145).

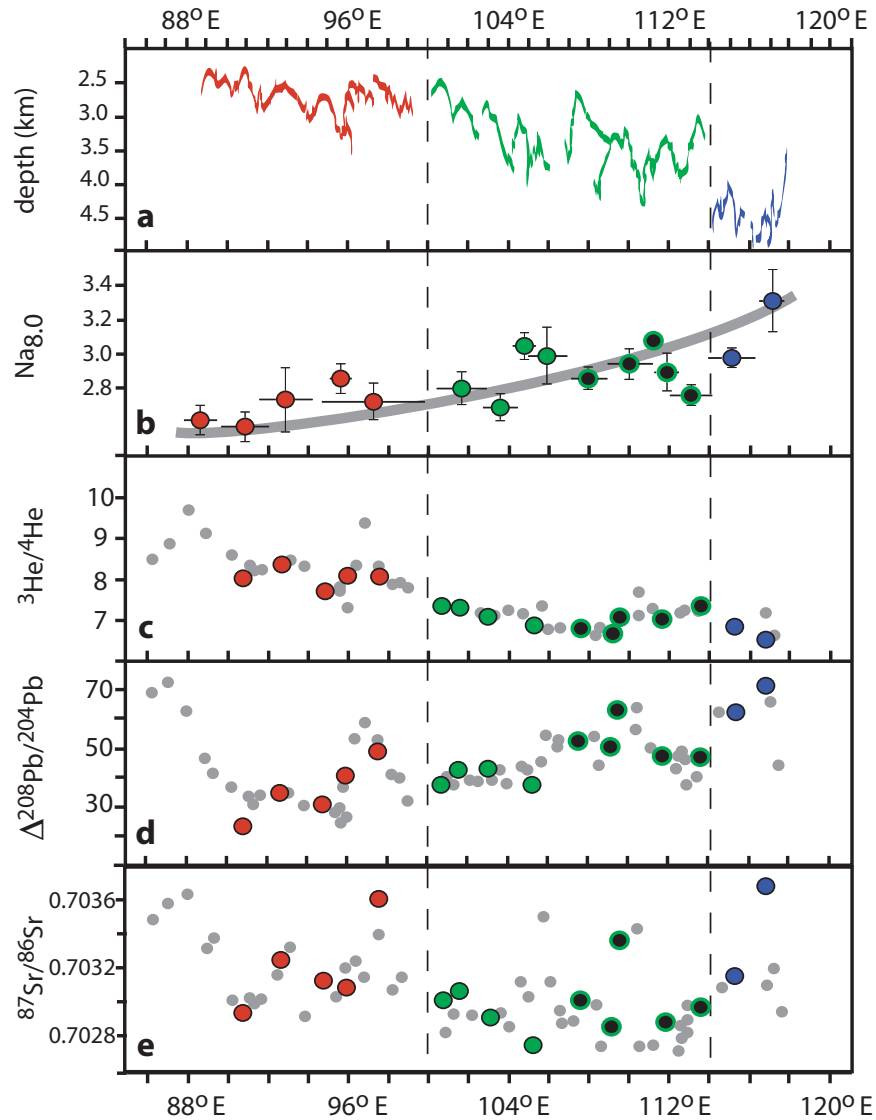


Figure 3-2. Geochemical tracers of source heterogeneity and melting along the SEIR between 88° and 118°E. Along-axis variation in (a) axial depth (Sempere et al, 1997), (b) segment averaged $\text{Na}_{8.0}$ (Sours-Page, 2000) (grey line represents a best-fit polynomial through predicted $\text{Na}_{8.0}$ values for average segment depth calculated using the relationship described by Klein and Langmuir (1987), horizontal black lines on these data points represent segment length and vertical error-bars represent ± 1 standard deviation of the mean for the segment averages) (c) $^3\text{He}/^4\text{He}$ (Graham et al., 2001; R/RA), (d) and (e) $\Delta^{208}\text{Pb}/^{204}\text{Pb}$ and $^{87}\text{Sr}/^{86}\text{Sr}$ (Mahoney et al., 2002). Samples for this U-series study are divided into three regional groups as described in the text. Red symbols are west of 100°E. Green symbols are the intermediate group (100°E to 114°E) with solid green symbols representing the western axial-high to axial-valley transition and the green symbols with black centers representing the eastern axial-high to axial-valley transition. Blue symbols are east of 114°E. Grey symbols in panels c, d and e show the full data set for SEIR basalt glasses.

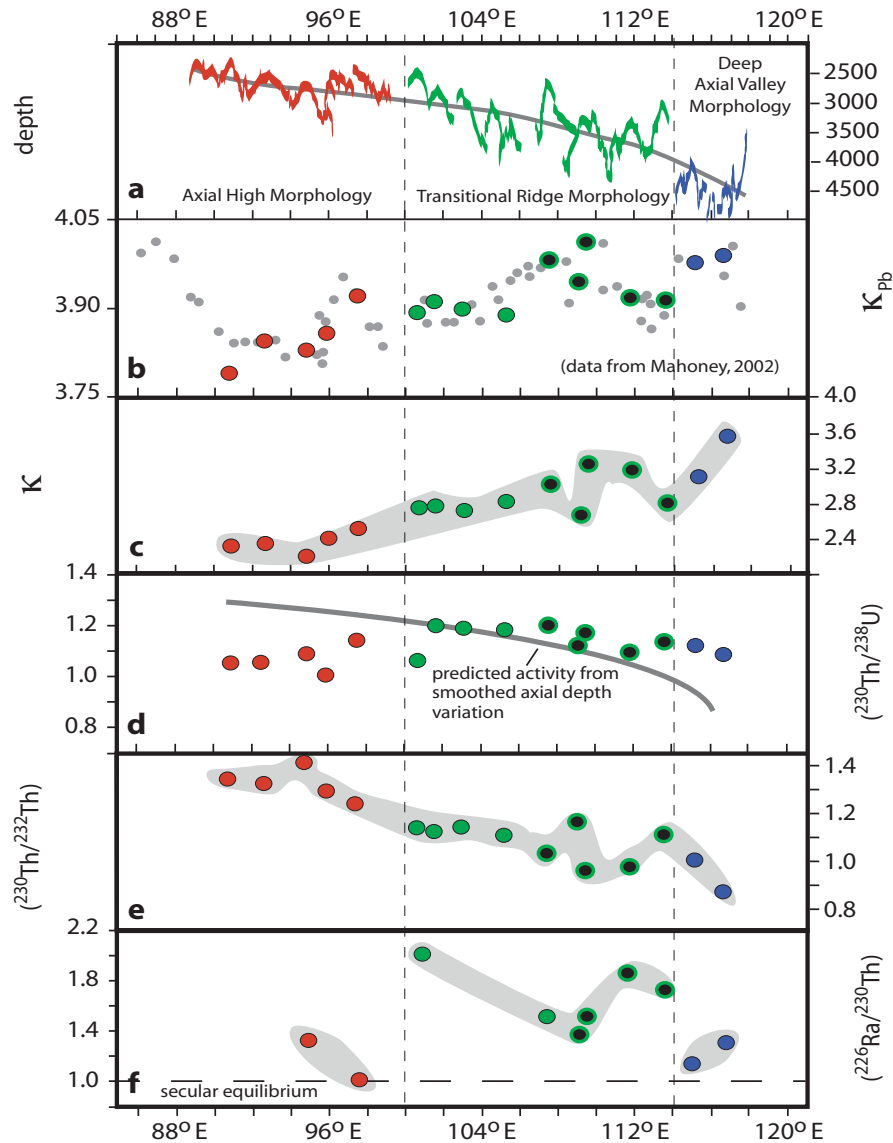


Figure 3-3. Longitudinal variation in U-series activity ratios, κ and κ_{pb} along the SEIR between 88°E and 118°E . (a) Axial-depth profile and smoothed axial depth curve (grey line) from Sempere et al. (1997). (b) κ_{pb} values are $^{232}\text{Th}/^{238}\text{U}$ atomic values calculated from the data of Mahoney et al. (2002) assuming a closed system evolution over 4.56 Ga from initial $^{206}\text{Pb}/^{204}\text{Pb}$ and $^{208}\text{Pb}/^{204}\text{Pb}$ values equal to Canyon Diablo (Tatsumoto et al., 1968) and $^{232}\lambda = 4.9475 \times 10^{-11} \text{ yr}^{-1}$ and $^{238}\lambda = 1.55125 \times 10^{-10} \text{ yr}^{-1}$. (c) Measured $^{232}\text{Th}/^{238}\text{U}$ atomic (κ) for SEIR basalt glasses. (d) Measured $(^{230}\text{Th}/^{238}\text{U})$ for SEIR basalt glasses, grey curve is predicted ^{230}Th -excess for these glasses using the smoothed axial depth in panel (a) and the ‘global’ $(^{230}\text{Th}/^{238}\text{U})$ -axial depth relationship of Bourdon et al. (1996a). (e) and (f) Measured $(^{230}\text{Th}/^{232}\text{Th})$ and $(^{226}\text{Ra}/^{230}\text{Th})$ activity ratios for these basalt glasses. All symbols are the same as in Figure 2.

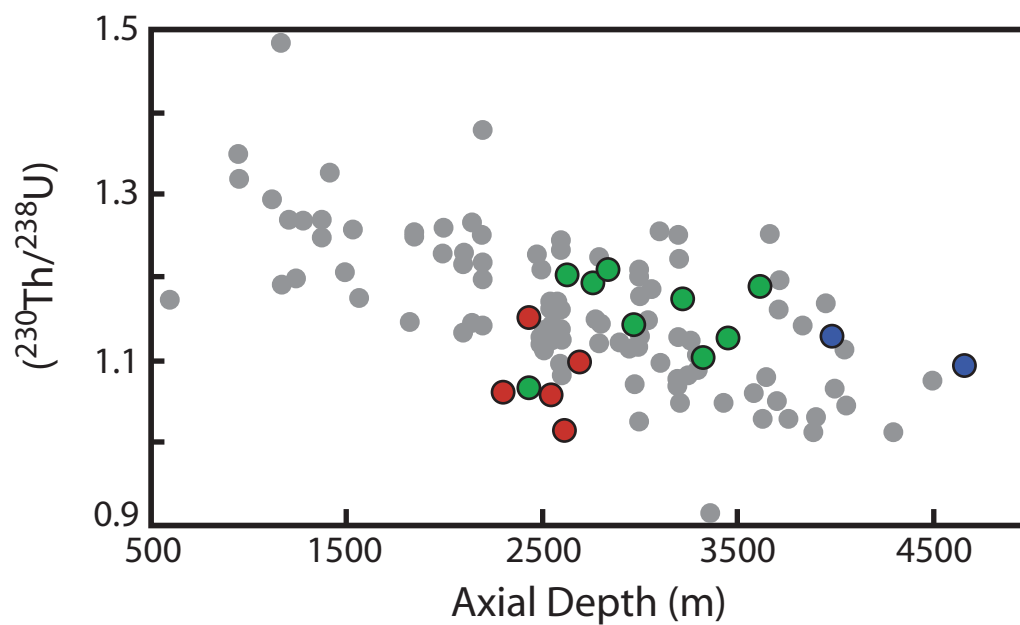


Figure 3-4. $(^{230}\text{Th}/^{238}\text{U})$ versus axial depth. Measured $(^{230}\text{Th}/^{238}\text{U})$ for basaltic glasses from the SEIR plotted, as regional groups, versus dredge depths. Symbols for the SEIR basalts are the same as in Figure 2. Grey symbols are the 'global' dataset updated by Lundstrom (2003) from Bourdon et al. (1996a).

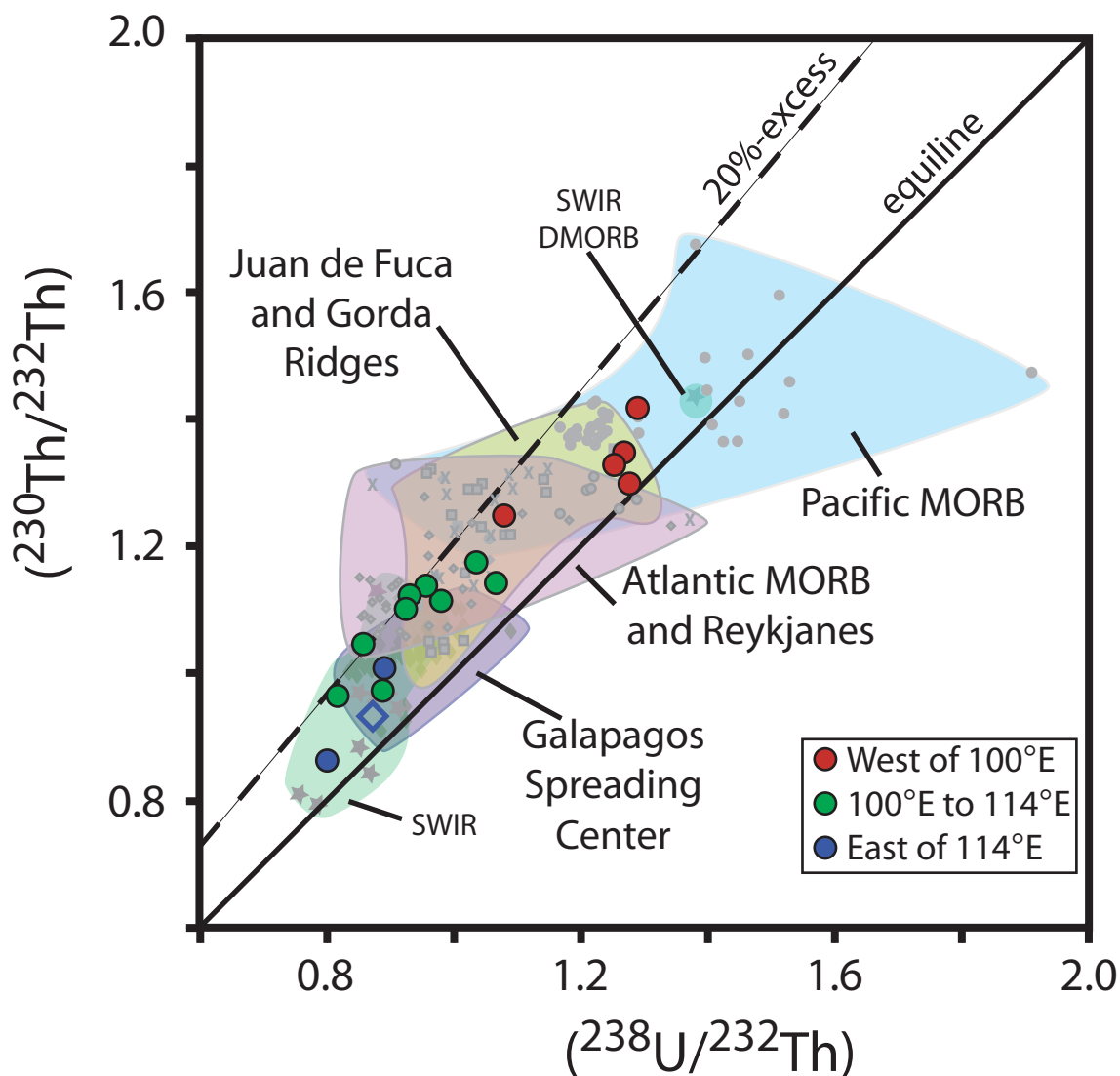


Figure 3-5. ‘Equiline’ diagram for Global MORB. A majority of the global MORB data plot to the left of the equiline with ^{230}Th -excesses of less than 20%, however, analyses with greater excesses (and even ^{230}Th -deficits) also exist. SEIR MORB are plotted using the same symbols as in Figure 2 with the addition of a single AAD sample (open blue diamond) from Bourdon et al. SEIR MORB have ranges in $(^{230}\text{Th}/^{232}\text{Th})$ and $(^{238}\text{U}/^{232}\text{Th})$ spanning $\sim 70\%$ of the range observed globally. Only one sample from the SWIR plots at a lower value and only a few of the most depleted samples from the EPR and one from the SWIR plot at higher values. Global data are from Ben Othman et al., 1990; Bourdon et al., 1996a, b; Goldstein et al., 1991, 1993; Kokfelt et al., 2005; Lundstrom et al., 1998a; Peate et al., 2001; Sims et al., 1995, 2002; Standish, 2005; Sturm et al., 2000; Tepley et al., 2004.

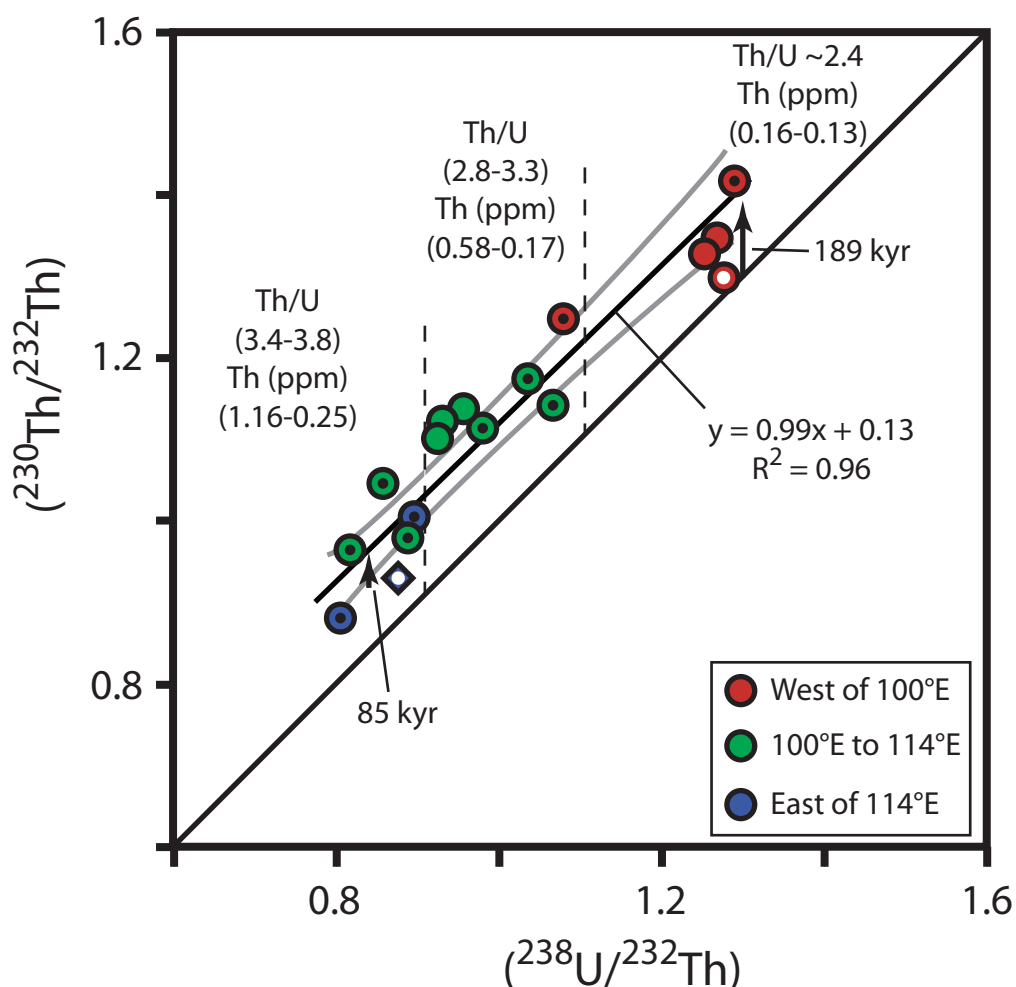


Figure 3-6. SEIR- ‘Equiline’ diagram. SEIR MORB plotted as regional groups on the equiline diagram. Symbols are the same as in Figure 2, the blue diamond is from the AAD (Bourdon et al., 1996a). Symbols with black dots have measured ^{226}Ra and thus age control, as discussed in the text. Regional groups are further divided into enrichment groups as designated by the dashed vertical lines. The solid black line is a least-squares regression through the samples having measured ^{226}Ra , following Lundstrom et al. (1998b). The slope ($m = 0.99$) suggests slightly higher ^{230}Th -excesses ($\sim 15\%$) at lower $(^{238}\text{U}/^{232}\text{Th})$ compared to slightly lower ^{230}Th -excesses ($\sim 9\%$) at higher $(^{238}\text{U}/^{232}\text{Th})$ values. Curved gray lines are a calculated ± 2 standard error envelope on the linear regression for this dataset. The 2 samples that fall below the 2 standard error envelope possibly suffered some ^{230}Th -decay since eruption, shown by the open symbols (one red circle and the blue diamond). In these cases ‘decay-ages’ have been calculated assuming the initial $(^{230}\text{Th}/^{232}\text{Th})$ values for these samples placed them on the linear regression. The ‘ages’ are shown in kyr and the decays suffered are shown by vertical black arrows. In general, higher Th (and U) concentrations occur at lower $(^{238}\text{U}/^{232}\text{Th})$, or higher Th/U values, although some overlap between concentrations and these enrichment groups occurs.

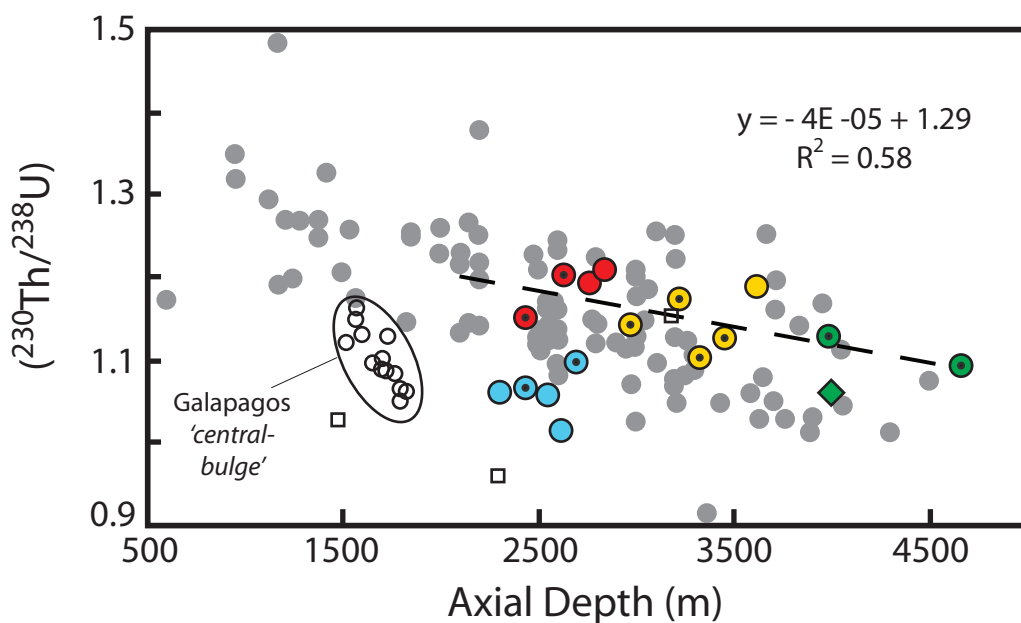


Figure 3-7. ^{230}Th -excess versus axial depth by morphologic groups. SEIR MORB ($^{230}\text{Th}/^{238}\text{U}$) are again plotted against axial depth, this time divided into four morphologic groups; an axial high group (AH; light blue circles), a rifted-axial high group (RH; red circles), a shallow-axial valley group (SV; yellow circles) and a deep-axial valley group (DV; green circles, green diamond is AAD sample from Bourdon et al., 1996a). Grey circles are the global dataset as presented by Lundstrom (2003), other data include samples with measured ^{226}Ra –excesses from the Galapagos Spreading Center (open circles; Kokfelt et al., 2005) and the SWIR (open squares; Standish, 2005). SEIR samples from the axial high group clearly plot below the global trend, which is mimicked by the other three morphologic groups. Samples from the axial high portion of the eastern GSC also plot similarly below the global trend but at shallower axial depths.

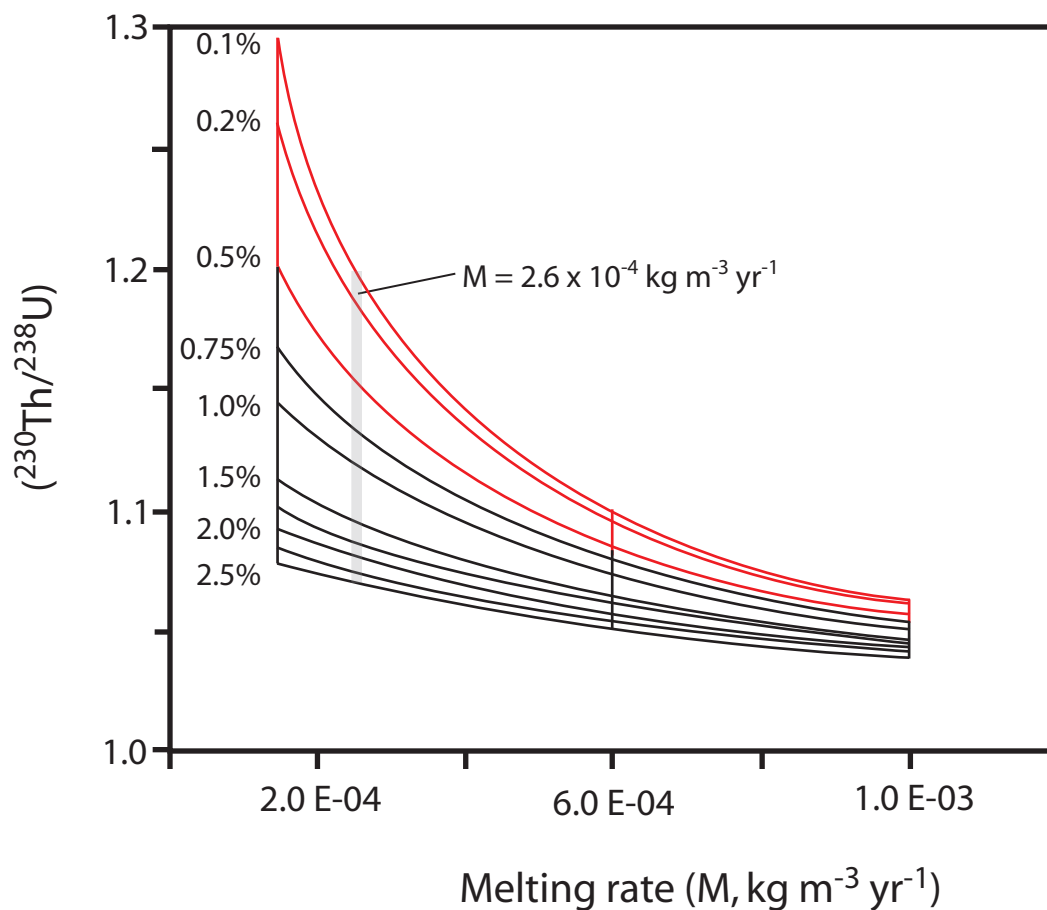


Figure 3-8. $(^{230}\text{Th}/^{238}\text{U})$ versus melting rate. $(^{230}\text{Th}/^{238}\text{U})$ values are calculated at varying mantle porosity and plotted against melting rate. ^{230}Th -excesses are calculated using the dynamic melting equations of McKenzie (1985) and Williams and Gill (1989). Bulk partition coefficients are from Salters et al. (2004) with $D_{\text{Th}} = 2.0 \times 10^{-3}$ and $D_{\text{U}} = 4.3 \times 10^{-3}$. The model curves demonstrate the effect of melting rate and/or porosity on ^{230}Th -excesses. Excesses decrease with increasing melting rate and/or porosity, all other factors being equal. The light grey vertical line demonstrates the maximum modeled melting rate capable of producing the entire range of ^{230}Th -excesses observed along the SEIR by varying only mantle porosity. The red model curves indicate constant porosity at which varying melting rate can produce the entire range of ^{230}Th -excesses observed along the SEIR.

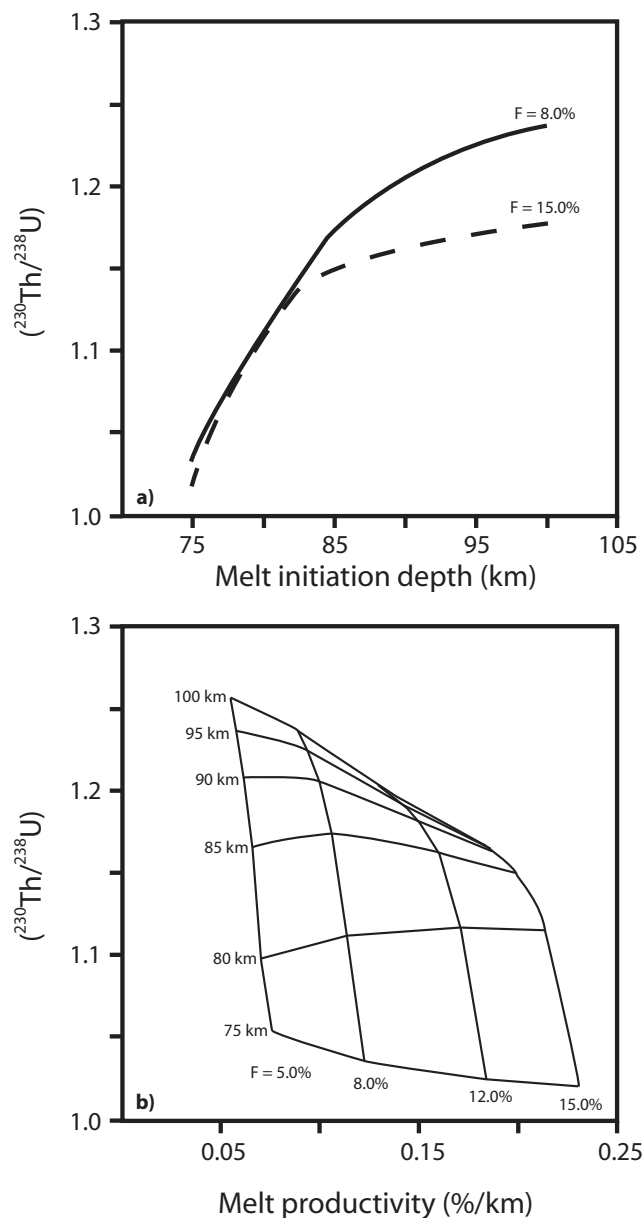


Figure 3-9. $(^{230}\text{Th}/^{238}\text{U})$ versus melt initiation depth and melt productivity. Model curves generated using the ‘incremental dynamic melting’ equations of Stracke et al. (2003). Partition coefficients are from Salters et al. (2004) with $D_{\text{Th}} = 2.0 \times 10^{-3}$ and $D_{\text{U}} = 4.3 \times 10^{-3}$. In these models garnet is stable at depths > 75 km. a) The effect of increasing melt initiation depth on generating $(^{230}\text{Th}/^{238}\text{U})$ for two different final (maximum) degrees of melting ($F = 8.0$ and 15.0%). b) $(^{230}\text{Th}/^{238}\text{U})$ versus melt productivity (%/km). Labeled horizontal lines indicate the depth of melt initiation and quasi-vertical lines indicate the maximum % of melting achieved in the melt column. Melt productivity is held constant at all heights in the melting column and melt production ceases at 10 km depth in each model. Mantle porosity for all models is 0.2%.

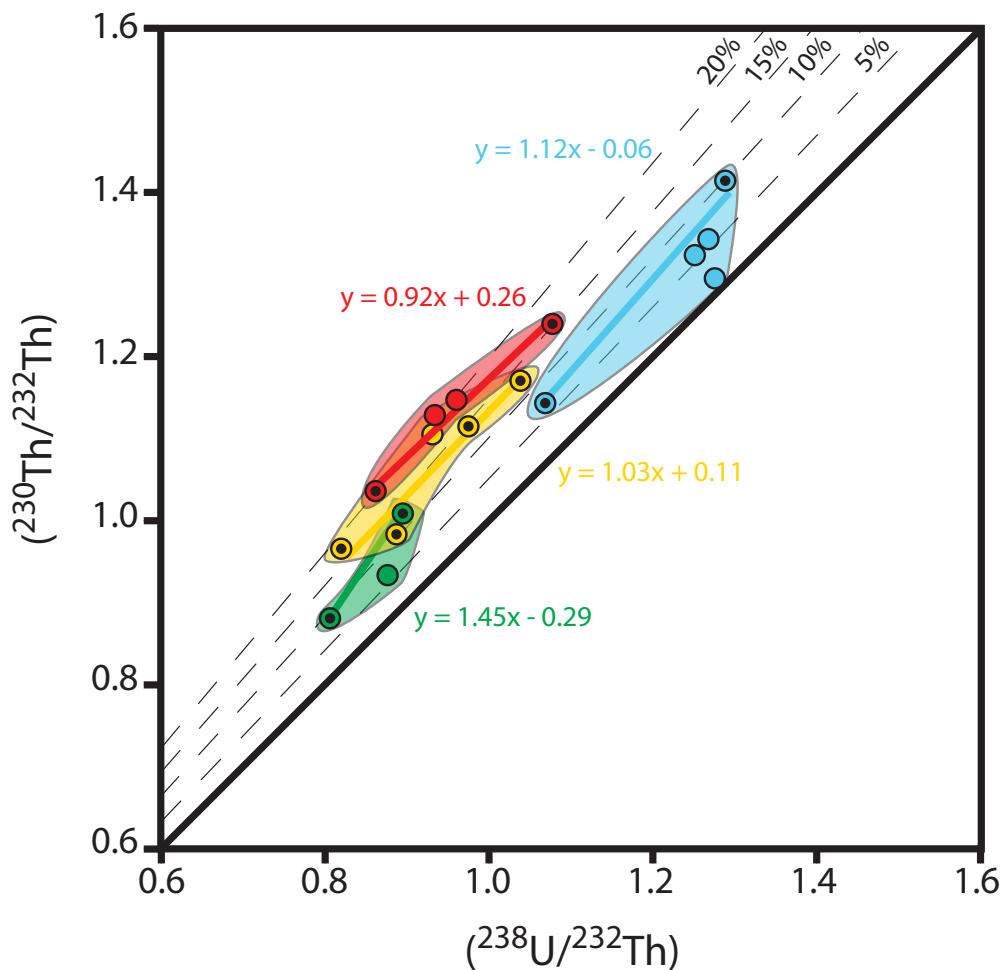


Figure 3-10. ‘Equiline’ diagram and axial morphology. SEIR MORB plotted on a $(^{230}\text{Th}/^{232}\text{Th})$ versus $(^{238}\text{U}/^{232}\text{Th})$ equiline diagram grouped by axial morphology, the groupings and color distinctions are the same as in Figure 7. As in the previous equiline diagrams the solid black line represents secular equilibrium and the dashed lines radiating out from the origin represent progressively higher ^{230}Th -excesses. Data points with black dots have measured ^{226}Ra . The colored lines within the morphologic groups represent least squares regressions through the data for each morphologic group (the 2 data points discussed in Figure 7, likely to have suffered ^{230}Th -decay, are excluded from these regressions). The generally lower ^{230}Th -excesses for the axial high group (light blue circles) are also apparent on this diagram, as are the progressively lower ^{230}Th -excesses for the rifted-axial high (RH, red circles), shallow-axial valley (SV, yellow circles) and deep-axial valley (DV, green circles) groups. Additionally, when the data are divided into these groups a progressive rotation to steeper slopes is observed from the rifted-axial high to the deep-axial valley group. This is in contrast to Figure 7 (and the global model of Lundstrom et al., 1998b), which suggest more enriched (i.e. lower $(^{238}\text{U}/^{232}\text{Th})$ MORB have greater ^{230}Th -excesses. This suggests that more enriched mantle lithologies beneath the SEIR do not necessarily result in greater Th-U fractionation. See text for further discussion.

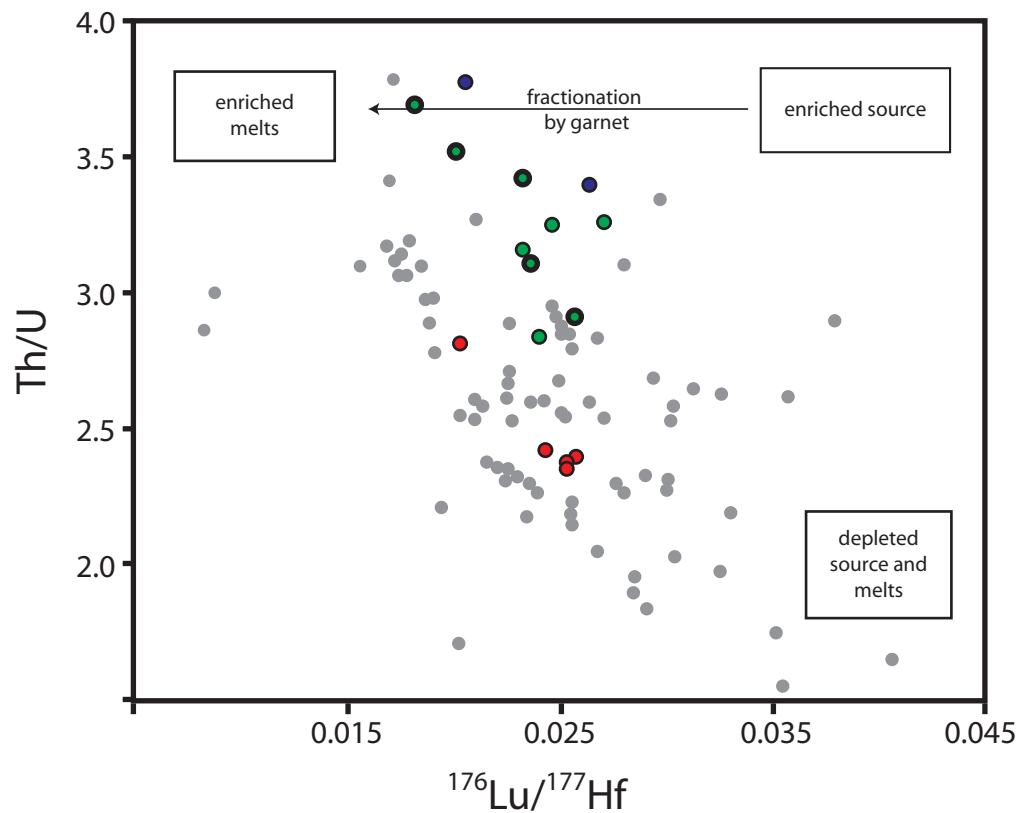


Figure 3-11. Th/U versus measured $^{176}\text{Lu}/^{177}\text{Hf}$ in SEIR basalts. Measured trace elements in SEIR basalts plotted along with data for EPR seamounts (data from Niu and Batiza, 1992). The trend of high Th/U ratios having lower $^{176}\text{Lu}/^{177}\text{Hf}$ values is interpreted to result from an increased proportion of garnet in the source region. Symbols are the same as in Figure 2 (diagram modified from Lundstrom et al., 1998).

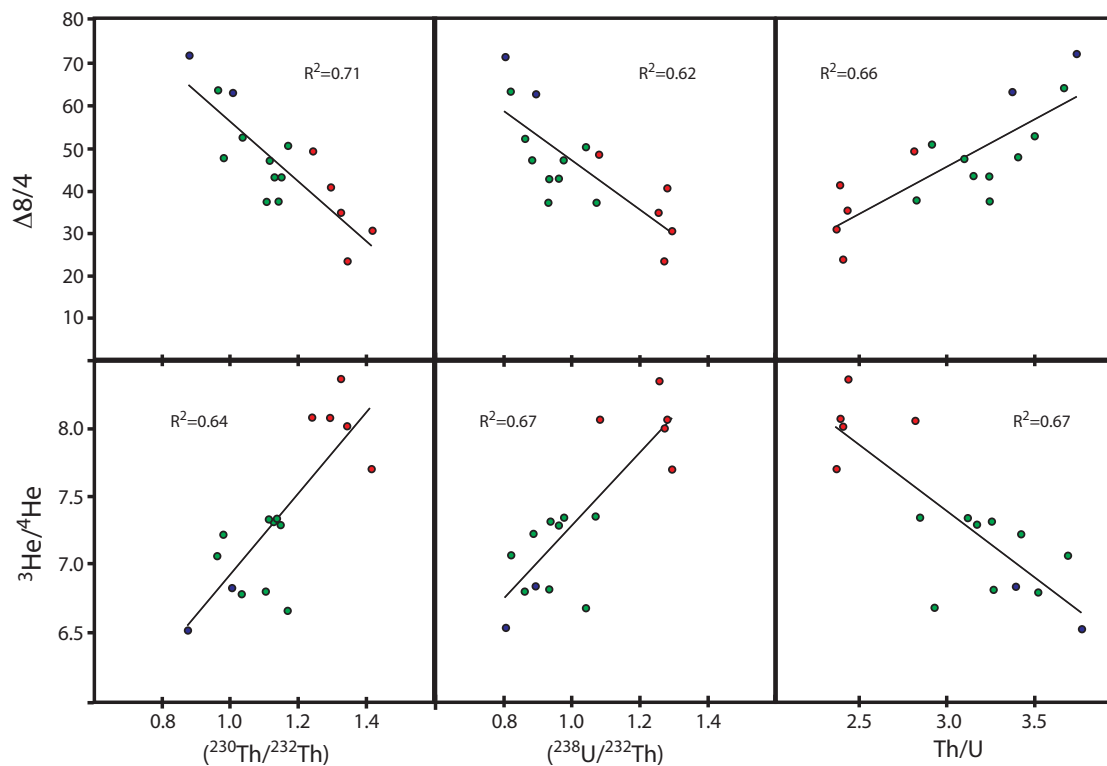


Figure 3-12. $(^{230}\text{Th}/^{232}\text{Th})$, $(^{238}\text{U}/^{232}\text{Th})$ and Th/U vs. $\Delta 8/4$ and $^3\text{He}/^4\text{He}$. U-series measurements plotted against isotopic tracers indicative of ‘Indian Ocean’ mantle. $\Delta 8/4$ data are from Mahoney et al., 2002 and $^3\text{He}/^4\text{He}$ (R/R_A) data are from Graham et al., 2001. The trends on these diagrams demonstrate the tendency for more ‘Indian-like’ lavas to be enriched in terms of the Th and U compositions. Like Figure 3, these diagrams support the increased occurrence of the most ‘Indian-like’ lavas in the eastern portion of the field area. Symbols are the same as in Figure 2.

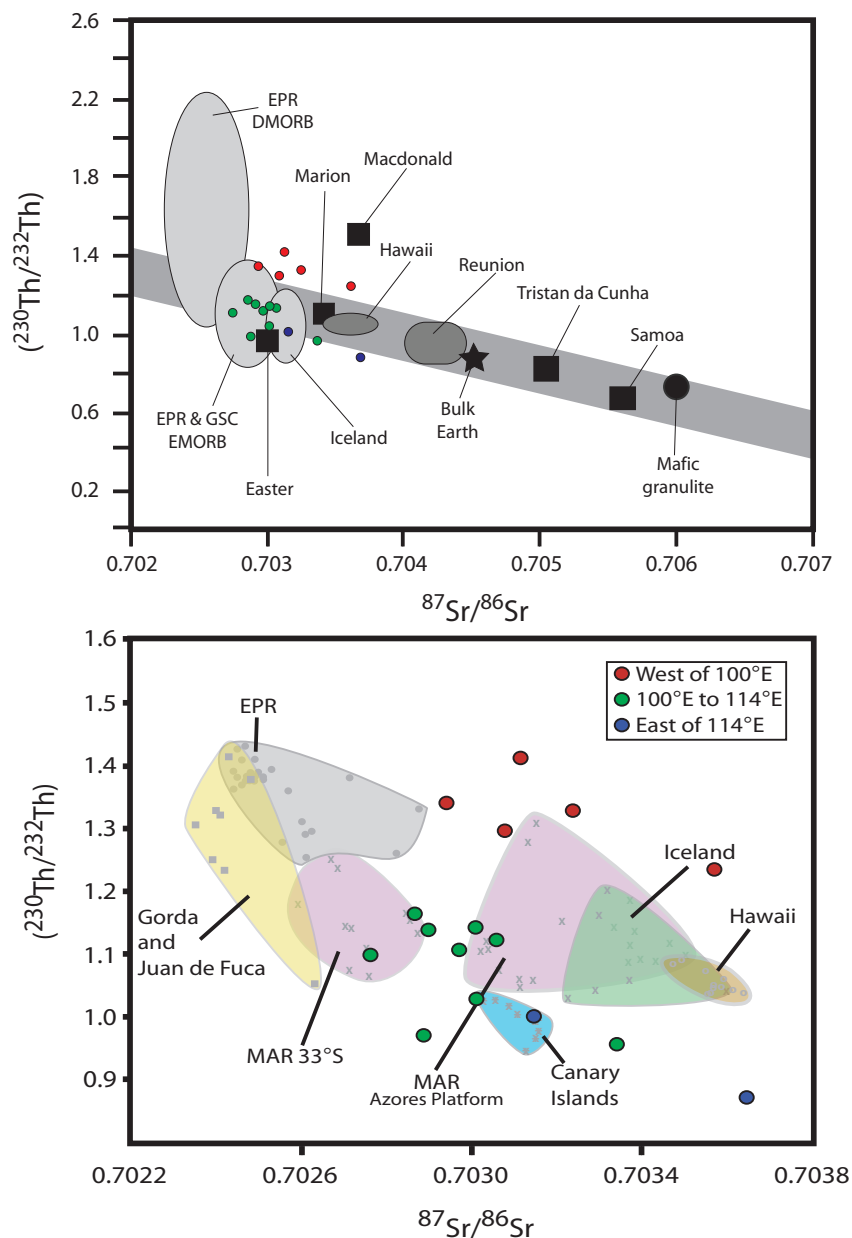


Figure 3-13. $(^{230}\text{Th}/^{232}\text{Th})$ vs. $^{87}\text{Sr}/^{86}\text{Sr}$. A) Global Th-Sr correlation originally discussed by Condomines et al. (1981) as presented by Rubin and Macdougall, (1991). The grey band extending from high values of $(^{230}\text{Th}/^{232}\text{Th})$ at low values of $^{87}\text{Sr}/^{86}\text{Sr}$ to lower values of $(^{230}\text{Th}/^{232}\text{Th})$ at high values of $^{87}\text{Sr}/^{86}\text{Sr}$ represents the global trend, which is largely controlled by the distribution of OIB. The high $(^{230}\text{Th}/^{232}\text{Th})$ end of this array is characterized by MORB with highly variable $(^{230}\text{Th}/^{232}\text{Th})$ values at low and nearly constant $^{87}\text{Sr}/^{86}\text{Sr}$ values. Colored symbols are the SEIR basalts from this study. B) Enlarged view of the low $^{87}\text{Sr}/^{86}\text{Sr}$ end of the mantle array showing the similarity between SEIR lavas from the western portion of the field area to depleted lavas from the Azores platform, EPR and Iceland. Data from Lundstrom et al., 1998; Sims et al., 1995, 2000; Bourdon et al., 1996a and b; Ben Othman et al., 1990; Sigmarrson et al., 2000.

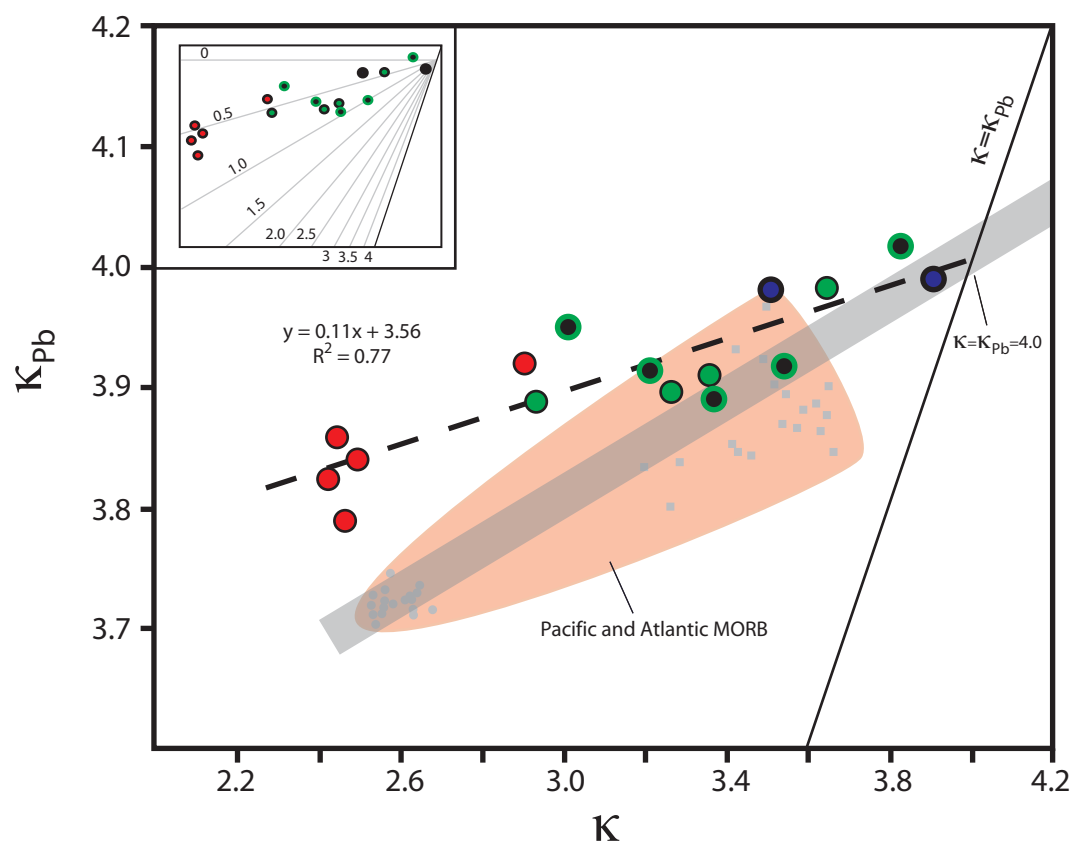


Figure 3-14. κ vs. κ_{Pb} . Measured $^{232}\text{Th}/^{238}\text{U}$ atomic value (κ) plotted against the long-term integrated $^{232}\text{Th}/^{238}\text{U}$, atomic value from measured $^{208}\text{Pb}/^{204}\text{Pb}$ and $^{206}\text{Pb}/^{204}\text{Pb}$ (κ_{Pb}). $\kappa = \kappa_{Pb}$ is for a closed system (single stage) evolution beginning with $^{208}\text{Pb}/^{204}\text{Pb}$ and $^{206}\text{Pb}/^{204}\text{Pb}$ equal to values for Canyon Diablo (Tatsumoto et al., 1968), $\kappa_1 = 4.0$ and $\mu_1 = 9.0$. SEIR data are colored symbols as in Figure 2. Grey band represents the global data trend reported by Vlastelic et al. (2006) through MORB and numerous OIB. Orange field represents the array of data with from the EPR and MAR with published U-series and Pb-isotope data (MAR from Bourdon et al., 1996b; EPR data from Sims et al., 2002). Inset shows the SEIR data plotted along with isochron ages calculated for a variety of two-stage mantle evolution models assuming $T = 4.55$ Ga, $\mu_1 = \mu_2 = 9.0$, $\kappa_1 = 4.0$, and $\kappa_2 = 2.35$. The age at which the fractionation event occurred (t) is shown by the numbers at the ends of the thin grey lines, and range from 4.0 Ga to 0. See text for discussion.

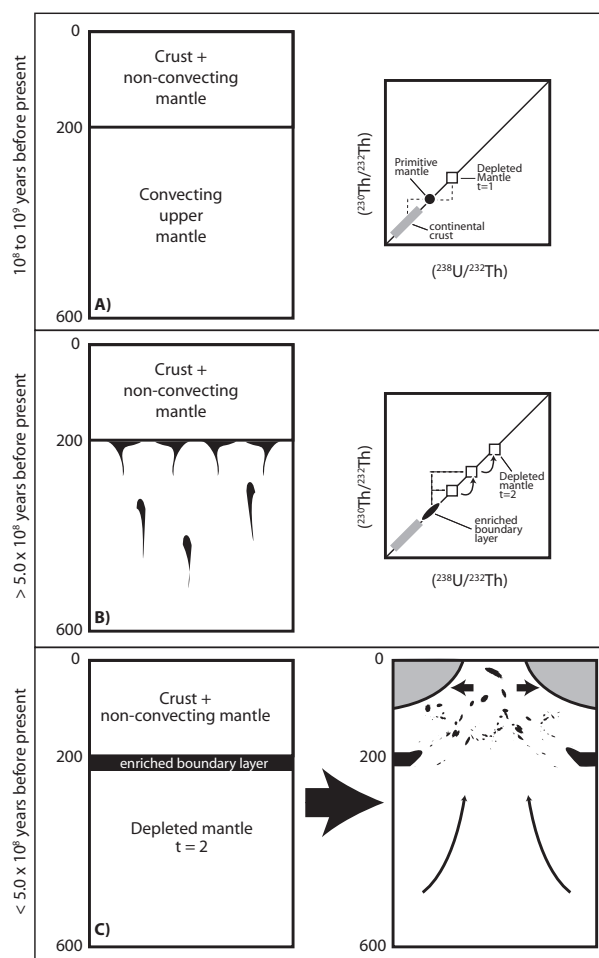


Figure 3-15. Schematic diagram of enrichment/depletion evolution model. A) Stage 1 represents the original depletion of the upper mantle into a depleted mantle reservoir ($DM_{t=1}$) and continental crust. Equiline diagram on the right shows schematically the fraction and recovery associated with $(^{230}\text{Th}/^{232}\text{Th})$ and $(^{238}\text{U}/^{232}\text{Th})$ during this stage resulting in two reservoirs, the continental crust enriched relative to the PM Th/U value and the $DM_{t=1}$ depleted relative to the PM value (PM Th/U \sim 4.0, Sun and McDonough, 1989). B) Stage 2 Intra-mantle differentiation. Schematic diagram on the left shows the production of small degree melts ($F=1.25\%$) and subsequent removal of these melts from the convecting mantle. The equiline diagram on the right shows schematically how these melting ‘events’ result in further fractionation of the $DM_{t=1}$ mantle into a $DM_{t=2}$ mantle and a homogenized ‘enriched boundary layer’ (EBL), further lowering the $(^{230}\text{Th}/^{232}\text{Th})$ and $(^{238}\text{U}/^{232}\text{Th})$ of the DM while producing an EBL with a composition similar to that of the PM. C) Stage 3 Basin Formation. Schematic on the left shows the end result of Stage 2 and the panel on the right shows the envisioned entrainment of the EBL into the upper 200 km of the upper mantle beneath the eastern Indian Ocean basin. As the continents of Gondwanaland rift and move apart to form the ocean basin $DM_{t=2}$ asthenosphere fills the void left by the translation of the massive continental keel entraining the EBL. All stages are schematic and not to scale.

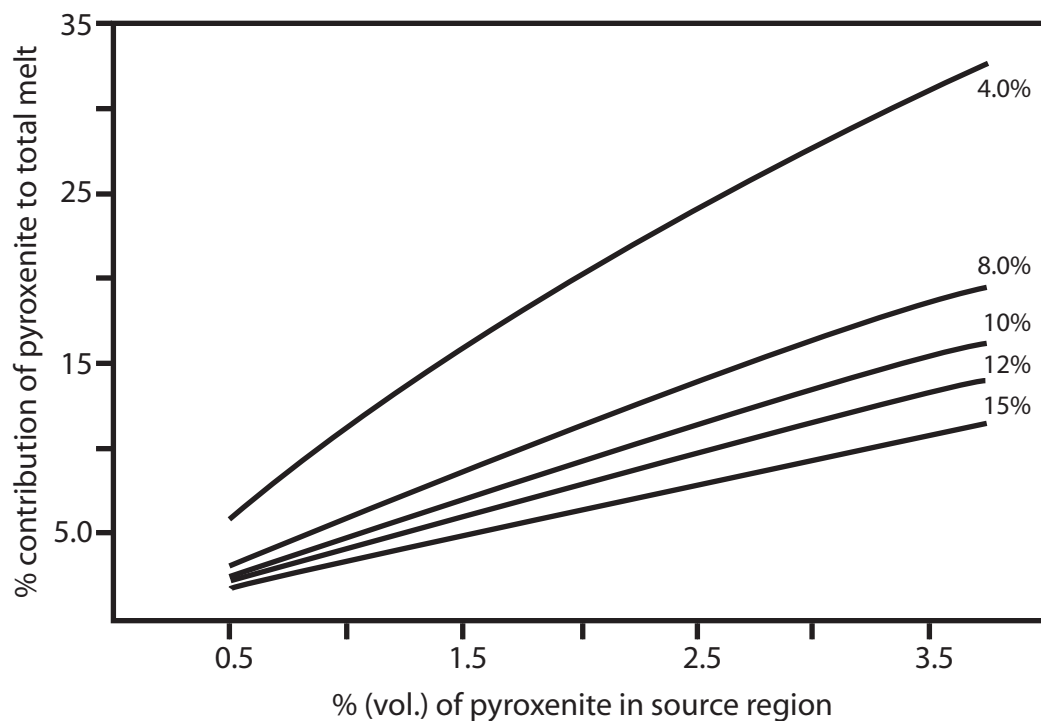


Figure 3-16. % contribution of pyroxenite to the melt vs. volume % of pyroxenite in the source. Diagram shows how very high melt production rates inferred for pyroxenite assemblages lead to a greater contribution to the melt than their volume presence in the source region. Calculations made for pyroxenite veins between 0.5 and 3.75%. All cases assume that pyroxenite veins melt to a very high degree ($F=65\%$) and are mixed with different degrees of melting of a peridotite source. Peridotite melt percentages are shown at the far right side of the diagram.

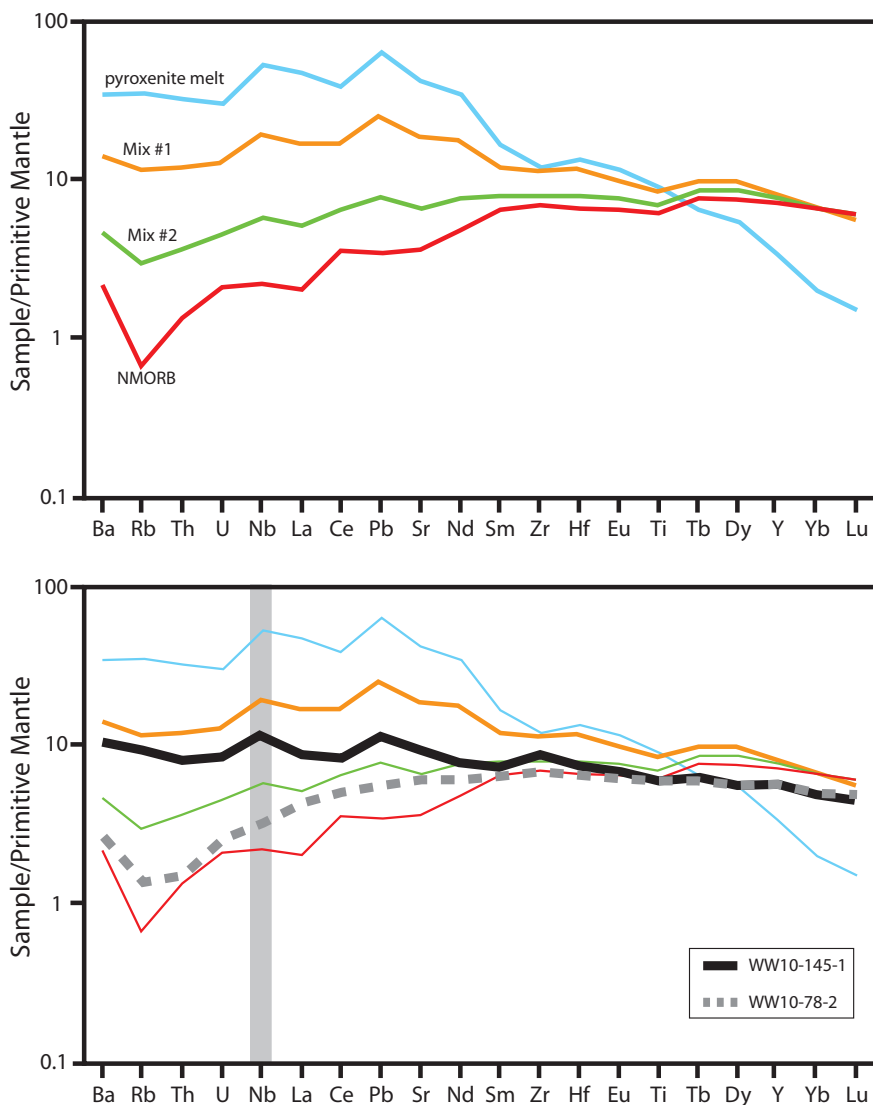


Figure 3-17. Incompatibility diagrams for components of the model and SEIR lavas. A) Results of the model calculations on an incompatibility diagram where element incompatibility decreases to the right. Light blue line is the resulting melt from the EBL assuming a high degree of melting ($F=65\%$). Red line is a non-modal aggregated fractional melt of a spinel lherzolite assemblage with $F=10\%$. Orange line is a mixture of pyroxenite melt assuming the EBL represents 3% by volume of the source region and is mixed with a 4% non-modal aggregated spinel lherzolite melt. Green line is a mixture of pyroxenite melt assuming the EBL represents 1% by volume of the source region and is mixed with an 8% non-modal aggregated spinel lherzolite melt. B) Same as in A) but with a representative enriched MORB (solid black line) and normal MORB (dashed grey line) from the SEIR. Shaded grey box highlights Nb which tends to have a positive anomaly in enriched SEIR MORB and no anomaly in normal SEIR MORB. This anomaly is reproduced well when pyroxenite melts are mixed with peridotite melts but is absent in the purely peridotite melts.

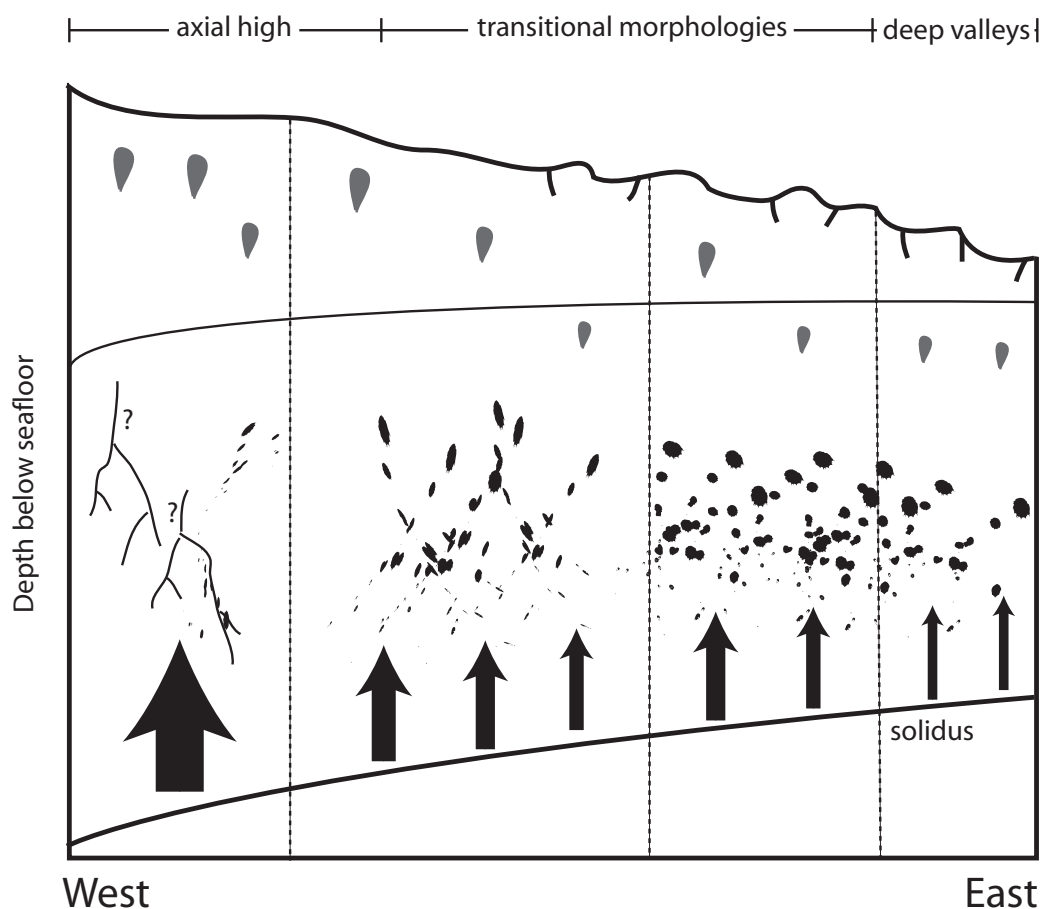


Figure 3-18. Summary schematic of along-axis variation in the melt region beneath the SEIR from 88° to 118°E. Schematic view represent the west to east change in axial morphology from axial-highs in the west to deep axial-valleys in the east. Thin black line represents a decrease in crustal thickness from west to east. Grey blobs within and just below the crust represent melt supply to the ridge axis and are scaled from larger to smaller in accordance with a decrease in melt supply from west to east. The height reached by the blobs represents the presence of shallower melt lenses beneath axial-high morphologies, the medium-sized blobs represent the presence of deeper melt lenses in the crust of rifted axial-high segments and the small melt blobs (below the lower crustal boundary) represent the absence of melt lenses in the crust of shallow and deep axial-valleys. Moving down in the diagram the abundance of black splatter represents the decrease of enriched pyroxenite veins in the mantle going from west to east. The dendritic lines with the ?'s represent the potential formation of melt conduits beneath the axial-high segments in the west (see text for discussion). The bottom-most portion of the diagram represents the inferred shoaling of the mantle solidus in response to a decrease in mantle potential temperature along the regional depth gradient and the arrows represent potential variations in melting rate along axis in this region.

Table 1 - Southeast Indian Ridge

Sample		$^3\text{He}/^4\text{He}$	$^{87}\text{Sr}/^{86}\text{Sr}$	$^{176}\text{Hf}/^{177}\text{Hf}$	$^{208}\text{Pb}/^{204}\text{Pb}$	$^{207}\text{Pb}/^{204}\text{Pb}$	$^{208}\text{Pb}/^{204}\text{Pb}$	$\Delta 8/4$	κ^*	κ_{rb}	μ	ω
WW10-71-1	W	8.02	0.70293	0.283079	17.863	15.479	37.456	23.3	2.389	3.791	8.5	21.0
WW10-75-4	W	8.37	0.70324	0.283043	17.844	15.478	37.547	34.7	2.417	3.843	8.3	20.7
WW10-78-2	W	7.71	0.70312	0.283074	17.871	15.489	37.537	30.4	2.350	3.826	8.7	21.0
WW10-84-7	W	8.08	0.70308	0.283139	17.754	15.463	37.498	40.6	2.371	3.860	7.2	17.6
WW10-89-4	W	8.08	0.70361		17.937	15.499	37.801	48.8	2.814	3.921	13.3	38.5
WW10-96-1	C	7.36	0.70301	0.283070	18.133	15.483	37.923	37.3	2.838	3.890	14.4	42.0
WW10-100-1	C	7.32	0.70306	0.283060	18.105	15.485	37.944	42.8	3.254	3.912	15.7	53.0
WW10-105-1	C	7.30**	0.70290	0.283087	17.987	15.480	37.802	42.9	3.165	3.899	9.3	30.5
WW10-113-7	C	6.82	0.70274	0.283097	18.144	15.467	37.935	37.2	3.264	3.891	12.0	40.2
WW10-118-1	C	6.80	0.70301	0.283050	18.365	15.503	38.353	52.3	3.528	3.984	17.8	64.8
WW10-125-1	C	6.68	0.70285	0.283119	18.128	15.475	38.047	50.3	2.919	3.950	9.7	29.3
WW10-126-7	C	7.07	0.70336		18.198	15.512	38.262	63.4	3.702	4.017	19.7	75.3
WW10-132-1	C	7.23**	0.70287	0.283095	17.972	15.478	37.829	47.4	3.428	3.918	9.0	31.8
WW10-141-1	C	7.35	0.70297	0.283067	17.947	15.461	37.796	47.1	3.112	3.914	14.2	44.5
WW10-144-4	E	6.84	0.70315		17.894	15.459	37.887	62.6	3.397	3.981	8.7	30.6
WW10-145-1	E	6.53	0.70368	0.283127	17.594	15.473	37.612	71.4	3.780	3.991	13.5	52.8

Western, Central and Eastern geographic zones are denoted by W, C and E, respectively

* Measured in this study

** New $^3\text{He}/^4\text{He}$ analyses from this study

all other data from Graham et al., (2001), Mahoney et al., (2002) and Graham et al., (2006)

Sample	Lat (S)	Long (E)	Depth (m)	E/N MORB	Ridge Morphology	[Th] ng/g	±
WW10-71-1	42.89	90.80	2350	N	AH	149.1	0.3
WW10-75-4	43.58	92.68	2585	N	AH	156.4	0.2
WW10-78-2	44.83	94.83	2719	N	AH	133.0	0.2
WW10-84-7	45.11	95.93	2660	N	AH	130.4	0.1
WW10-89-4	47.45	97.51	2470	E	RH	584.2	0.6
WW10-96-1	47.34	100.67	2465	E	AH	424.6	0.4
WW10-100-1	47.63	101.53	2857	E	RH	548.0	0.5
<i>WW10-100-1a</i>							
<i>WW10-100-1b</i>							
WW10-105-1	47.77	103.04	2783	E	RH	292.1	0.3
<i>WW10-105-1a</i>							
<i>WW10-105-1b</i>							
WW10-113-7	48.75	105.22	3630	N	SV	269.9	0.3
<i>WW10-113-7a</i>							
<i>WW10-113-7b</i>							
WW10-118-1	48.83	107.53	2673	E	RH	943.0	1.1
WW10-125-1	49.45	109.11	3475	N	SV	169.3	0.2
WW10-126-7	49.53	109.48	3240	E	SV	1158.3	1.3
WW10-132-1	50.21	111.78	3328	E	SV	279.7	0.3
<i>WW10-132-1a</i>							
<i>WW10-132-1b</i>							
WW10-141-1	50.35	113.62	3002	E	SV	432.3	0.6
WW10-144-4	50.01	115.21	3997	N	DV	247.3	0.3
WW10-145-1	49.27	116.72	4665	E	DV	694.4	0.7
<i>WW10-145-1a</i>							
<i>WW10-145-1b</i>							

**italics indicate replicate analyses, where replicates have been measured
normal type indicates average values of replicate analyses

Table 2 (continued)

Sample	[U] ng/g	±	(234/238)	±	232/230	±	(230/232)	±
WW10-71-1	62.4	0.3	1.003	0.003	137500	1200	1.346	0.012
WW10-75-4	64.7	0.3	1.003	0.004	139500	1300	1.327	0.012
WW10-78-2	56.6	0.3	1.003	0.003	130500	1200	1.418	0.013
WW10-84-7	55.0	0.3	1.000	0.004	142700	1300	1.297	0.012
WW10-89-4	207.56	0.9	1.001	0.003	149199.8	1400	1.240	0.012
WW10-96-1	149.63	0.7	0.999	0.004	162100	1700	1.142	0.012
WW10-100-1	168.43	0.8	1.001	0.004	164000	1400	1.129	0.010
WW10-100-1a					165200	1600	1.121	0.011
WW10-100-1b					162800	2300	1.219	0.018
WW10-105-1	92.3	0.4	1.000	0.004	161300	1100	1.148	0.008
WW10-105-1a					162800	1600	1.137	0.011
WW10-105-1b					159700	1400	1.159	0.010
WW10-113-7	82.7	0.4	1.002	0.004	167300	1200	1.106	0.008
WW10-113-7a					166700	1500	1.110	0.010
WW10-113-7b					168000	1800	1.102	0.012
WW10-118-1	267.32	1.2	1.002	0.002	178900	1700	1.035	0.010
WW10-125-1	58.0	0.3	0.998	0.003	158100	1600	1.170	0.012
WW10-126-7	312.83	1.4	1.001	0.003	192100	1700	0.963	0.009
WW10-132-1	81.601	0.4	1.003	0.004	188600	2000	0.981	0.011
WW10-132-1a					189200	2800	0.978	0.014
WW10-132-1b					188100	3000	0.984	0.015
WW10-141-1	142.38	0.6	0.998	0.004	165900	2000	1.116	0.013
WW10-144-4	72.7	0.3	1.005	0.003	183700	1800	1.007	0.010
WW10-145-1	183.72	0.8	1.002	0.003	210700	1800	0.878	0.008
WW10-145-1a					212900	2400	0.869	0.010
WW10-145-1b					208500	2700	0.888	0.011

Table 2 (continued)									
Sample	(238/232)	±	(230/238)	±	Ra fg/g	±	(226/230)	±	Ba µg/g
WW10-71-1	1.270	0.006	1.059	0.011					22.5
WW10-75-4	1.254	0.006	1.058	0.011					21.6
WW10-78-2	1.292	0.006	1.098	0.011	27.6	0.7	1.32	0.04	19.1
WW10-84-7	1.279	0.006	1.014	0.010					13.1
WW10-89-4	1.078	0.005	1.151	0.012	80.813	0.5	1.00	0.01	54.4
WW10-96-1	1.069	0.005	1.068	0.012	111	4.2	2.03	0.04	32.7
WW10-100-1	0.933	0.004	1.210	0.012					40.6
<i>WW10-100-1a</i>			1.202	0.013					
<i>WW10-100-1b</i>			1.219	0.018					
WW10-105-1	0.959	0.004	1.197	0.010					19.7
<i>WW10-105-1a</i>			1.186	0.013					
<i>WW10-105-1b</i>			1.208	0.012					
WW10-113-7	0.930	0.004	1.190	0.010					20.7
<i>WW10-113-7a</i>			1.194	0.012					
<i>WW10-113-7b</i>			1.185	0.014					
WW10-118-1	0.860	0.004	1.203	0.013	166	1.4	1.53	0.029	74.1
WW10-125-1	1.038	0.005	1.127	0.012	30.344	0.3	1.38	0.02	12.0
WW10-126-7	0.819	0.004	1.176	0.012	189.42	2.6	1.53	0.026	110.3
WW10-132-1	0.885	0.004	1.108	0.013	57.23	1.1	1.87	0.041	22.6
<i>WW10-132-1a</i>			1.105	0.017					
<i>WW10-132-1b</i>			1.112	0.018					
WW10-141-1	0.975	0.005	1.145	0.015	95.4	1.0	1.73	0.118	35.3
WW10-144-4	0.892	0.004	1.129	0.012	31.785	1.0	1.15	0.039	18.1
WW10-145-1	0.803	0.004	1.094	0.011	89.8	0.7	1.32	0.093	75.3
<i>WW10-145-1a</i>			1.083	0.013					
<i>WW10-145-1b</i>			1.106	0.015					

Chapter 4:
Rare earth elements in melt inclusions from the western Galapagos Spreading Center: Evidence for deep melting beneath a plume-influenced intermediate spreading rate ridge

Chris J. Russo¹, David W. Graham¹ and Adam Kent²

¹ College of Oceanic and Atmospheric Sciences, Oregon State University, Corvallis, OR

² Geosciences Department, Oregon State University, Corvallis, OR

4.1 Abstract

Rare earth element (REE), Ba, Sr, Zr and Y concentrations in 74 melt inclusion from 8 basalts recovered along the western Galapagos Spreading Center (GSC) were determined by laser ablation ICP-MS. Similar to glass compositions from this region, all melt inclusions can be classified as either enriched (EMORB), transitional (TMORB) or normal (NMORB) on the basis of K_2O concentrations and K/Ti ratios. Melt inclusions closely mimic associated glasses but with a larger compositional range. Melt inclusions from the easternmost portion of the region were entirely EMORB, while melt inclusions from the westernmost portion of the region were dominantly NMORB. The most diverse melt inclusions were found in samples from the central portion of the study region where basalt chemistry and axial structure have previously been described as transitional.

Forward modeling of the REE concentrations is in agreement with deep derivation of an enriched 'plume' signature along the portion of the ridge axis where the Galapagos hotspot has the greatest influence on crustal structure and axial morphology. Modeling of REE variations supports the derivation of NMORBs along the GSC from a depleted mantle source by moderate degrees of melting (average $F \sim 9\%$ with maximum $F \sim 20\%$) of spinel lherzolite at constant melt productivities of 0.3-0.4%/km. The EMORB melt inclusion compositions are generated by mixing of small degree melts of spinel lherzolite (1.2 to 3.6%) with small degree melts of garnet lherzolite ($\leq 2.5\%$). If melt productivities are an order of magnitude lower in the garnet stability field (as suggested from other studies of the effect of elevated H_2O in the MORB mantle) then melting depths extend ~ 35 to 60 km into the garnet stability field and suggest melt column height of ≤ 120 km along the GSC nearest the Galapagos hotspot.

There is a limited range of melt inclusion compositions in both EMORB and

NMORB samples. Melting processes and source enrichment appear to be closely tied to the morphologic and structural variations along the GSC, producing distinct chemical ‘end-members’ or groups. The most strongly plume influenced compositions appear to be the most deeply derived, and combined with the lack of depleted compositions in this sample type, support a deep, strong lateral flow of hotspot-derived mantle toward the GSC (Harpp and White, 2001).

4.2 Introduction

Mid-ocean ridge segments situated over, or near, mantle plumes are characterized by morphologic and geochemical gradients attributed to the addition of heat and material to the ‘normal’ asthenosphere beneath the ridge system by the plume source (Schilling, 1991; Ito and Lin, 1995). Hotspot-influenced mid-ocean ridges, on one hand, typically have enriched trace element signatures (such as high $(La/Sm)_n$ values) which may be indicative of small degrees of melting, while on the other hand also have shallow axial depths associated with greater crustal thickness and increased melt production. The western Galapagos Spreading Center (GSC) between 98° and 91° W is a well-studied example of a hotspot-influenced mid-ocean ridge spreading center whose along-axis variations in bathymetry and gravity (Ito and Lin, 1995), axial morphology (Canales et al., 1997, 2002; Sinton et al., 2003) and in the trace element and isotopic composition of erupted MORBs (Schilling et al., 1976, 1982, 2003; Fisk et al., 1982; Verma and Schilling, 1982; Detrick et al., 2002) are well known. Detailed study of the western GSC (west of the large transform at 90.7°W) has revealed that the geophysical and geochemical variations along this portion of ridge axis are correlated at local scales, and reveal that the nearby Galapagos hotspot influences the ridge axis both structurally and chemically. Collectively these existing characterizations provide an ideal backdrop on which to explore what, if any, relationship exists between the

chemical diversity of ridge axis lavas and the morphologic structure of the ridge, such as crustal thickness.

Melt inclusions are thought to represent partial melts trapped prior to complete mixing and homogenization of mantle-derived melts, thereby offering a unique window into the process of melt generation (Watson, 1976; Falloon and Green, 1986; Sobolev and Shimizu, 1993; Sinton et al., 1993). In particular, the analysis of melt inclusions may help elucidate the origin of the diversity sampled in erupted MORB (i.e. N-MORB, T-MORB and E-MORB) if discrete differences in trace element ratios are preserved that otherwise would be lost in the mixing and dilution of volumetrically small batches of melt.

Melt inclusions trapped in olivine and plagioclase phenocrysts from along the well characterized western GSC have been analyzed for a suite of major, minor and trace element concentrations in an effort to 1) better characterize the diversity of melts generated along the axial depth gradient away from the hotspot; 2) investigate how the melt inclusion compositions relate to their host lava compositions; and 3) evaluate possible links between the enriched component of these lavas and the depth at which they are generated.

4.3 Background

4.3.1 General tectonic overview

The Galapagos mantle plume is a long-lived feature whose oldest activity is recorded in the ~93 Ma lavas of the Caribbean Plateau (Duncan and Hargraves, 1984). During the period from ~25 Ma to as recently as 5 Ma the Galapagos plume was centered beneath the paleo-GSC, resulting in the formation of the Cocos and Carnegie Ridges (Hey et al., 1977). Since ~5 Ma the GSC has migrated northward to its current location north of the Galapagos archipelago, where it forms the plate boundary

between the Cocos Plate to the north and the Nazca Plate to the south (Figure 1). The current configuration of the GSC allows for the clear distinction into two sections 1) the eastern and 2) the western GSC, that are separated from one another by the large, ~100-km-long Galapagos Transform, located near 90°50'W (Schilling et al., 2003; Sinton et al., 2003; Christie et al., 2005).

4.3.2 The Galapagos Archipelago and Plateau

South of the Galapagos Transform lie the ten volcanic islands of the Galapagos Archipelago which are situated along the east-west trending Galapagos Plateau. The western extent of the plateau is marked by the island Fernandina which lies above the probable location of the current plume center (White et al., 1993; Graham et al., 1993; Kurz and Geist, 1999). Coeval volcanism is widely dispersed across the platform but the small areal extent of the Galapagos Islands indicates the plume is relatively weak, and as a result, the underlying mantle plume is sheared 'downstream' to the east by asthenospheric flow associated with the relatively rapid eastward migration of the Nazca Plate (>60 mm/yr; White et al., 1993; Harpp and White, 2001; Christie et al., 2005). Shearing of the plume in this configuration is believed to account for an unusual 'horseshoe' geochemical pattern of basalts erupted on the plateau; lavas erupted from seamounts and islands near the northern, southern and western edges of the plateau have enriched, OIB-like geochemical characteristics, while lavas erupted near the central and eastern part of the plateau have more MORB-like, depleted, geochemical characteristics (White and Hofmann, 1978; Geist et al., 1988; White et al., 1993; Graham et al., 1993; Harpp, 1995; Sinton et al., 1996; Kurz and Geist, 1999; Harpp and White, 2001).

As a result of the northward migration of the ridge axis, a 'wedge' of younger, thinner, and thus, weaker lithosphere is found between the northern extent of the

plateau and the ridge axis (Feighner and Richards, 1995; Harpp and Geist, 2002). To the northwest of the plateau the trace of a sharp transition between this thin young crust and the thicker older crust is marked by the Wolf-Darwin lineament, a seamount/island chain trending northwest from the margin of the plateau toward the western GSC (White et al., 1993). Just east of the Wolf-Darwin lineament, three other northwest trending seamount lineations are apparent in bathymetric maps extending from near the western GSC towards the island of Pinta (Figure 1; Sinton et al., 2003). Geochemical and age constraints on these lineaments suggest they do not represent a temporal record of plume-ridge interaction, but instead are controlled by lithospheric extensional faults associated with the 90°50'W transform fault (Feighner and Richards, 1994; Harpp and Geist, 2002, Harpp et al. 2003; Sinton et al., 2003). This diverse and complicated distribution of geochemical characteristics has led investigators to argue for a heterogeneous plume consisting of two (Schilling et al., 2003) or three (White et al., 1993; Harpp and White, 2001) enriched mantle components mixed with a depleted component, presumably the shallow asthenosphere MORB source.

4.3.3 The western Galapagos Spreading Center

The western GSC extends to the west from the 90°50'W transform fault to ~102°W near where it intersects the Galapagos microplate (Sinton et al., 2003). On the coarsest scale the western GSC can be divided into three regions comprising the Eastern, Middle and Western Provinces (Sinton et al, 2003). Over this ~800 km long stretch of mid-ocean ridge the axial depth shoals from ~3500 m deep at 97.7°W to <1700 m depth at 91.4°W. Coincident with this change in axial depth is a minor change in spreading rate from ~45 mm/yr in the west to ~56 mm/yr in the east, and a morphologic change from axial valley morphology in the west to an axial high

morphology in the east (Detrick et al., 2002; Sinton et al., 2003). It is estimated that of the ~1700 m change in axial depth, ~700 m is accounted for directly by influence of the 'hotspot swell', while the remaining change is accounted for by the changes in ridge axis morphology (Canales et al., 2002) and associated magma production. Detailed seismic work conducted as part of the G-Prime experiment (Galapagos Plume-Ridge Interaction Multidisciplinary Experiment) revealed that in addition to the change in spreading rate and morphology, crustal thickness also increases toward the hotspot, from 5.6 ± 0.2 km at 97°W to ~7.9 km at 91.5°W (Detrick et al., 2002). Additionally, the significant increase in crustal thickness east of 94°W suggests the primary effect of the hotspot on melt productivity beneath the western GSC is confined to within about 400 km of the plume center (Detrick et al., 2002).

The Eastern Province extends from the $90^\circ 50'$ W transform fault to the propagating rift tip near $93^\circ 15'$ W (Detrick et al., 2002; Sinton et al., 2003). This portion of the GSC maintains a roughly constant axial depth of ~1800 m, with axial high morphology, a relatively shallow magma lens (~1.4-2.3 km), and the thickest crustal construction (~7.9 km thick east of 92.7°W , Detrick et al., 2002). Lavas erupted along this portion of the GSC are EMORB with high K/Ti, lower Mg#, and high incompatible trace element ratios and concentrations. These lavas have been interpreted as reflecting the composition of parental magmas supplying the ridge axis that are likely to have experienced relatively limited crystal fractionation (Schilling et al., 1982, 2003; Verma and Schilling, 1982; Detrick et al., 2002; Sinton et al., 2003; Cushman et al., 2004).

The Middle Province extends from west of the $93^\circ 15'$ W propagating rift tip to its termination at the $95^\circ 30'$ W propagating rift tip, the focus of numerous concentrated studies over the past 2+ decades (Hey et al., 1980; Christie and Sinton, 1986; Hey et al., 1989; Hey et al., 1992). Morphologically the Middle Province is considered transitional, lacking an obvious axial valley or a well-defined axial high

(Sinton et al., 2003). Compared to the Eastern Province, the Middle Province is characterized by thinner crust (6-7 km thick), and although an axial magma lens is imaged below the eastern portion of this province, it resides at greater depth in the crust (2.5-4.3 km depth) than in the Eastern Province (Detrick et al., 2002), likely the result of a decreased rate of magma supply in the Middle Province relative to the Eastern Province (Sinton et al., 2003). Lavas erupted along the Middle Province are dominantly transitional basalts (Cushman et al., 2004), with trace element ratios and abundances intermediate between the more enriched samples erupted within the Eastern Province and typical NMORB usually characterized by strong trace element depletion.

The Western Province extends from the 95°30'W propagating rift tip to ~98°W, the edge of the G-PRIME study area (Detrick et al., 2002; Sinton et al., 2003). Morphologically the Western Province ridge axis has axial depths >3000 m, with the axis lying in approximately 10 km wide by 800 m deep valleys. This portion of the ridge axis also has the thinnest crust (~5.6-6 km) and lacks the presence of an axial magma lens (Detrick et al., 2002). Within the axial valleys are numerous seamounts, apparently randomly distributed and ranging from 50 m to 500 m tall (Behn et al., 2004). Lavas erupted in the Western Province are dominantly NMORB, with relatively lower incompatible element ratios and concentrations (Cushman et al., 2004) and REE patterns having moderate LREE depletions.

4.3.4 Hydrous melting along the western GSC

The systematic variation in axial morphology, crustal thickness and MORB geochemistry along the western GSC indicate that there is a strong link between these observable/measurable features and melt generation at depth in the mantle. Another intriguing observation resulting from the G-PRIME experiment is a regional,

eastward, reduction in near-axis seamount population density from $234 \pm 14 \times 10^{-3}$ km^{-2} in the west to $54 \pm 10 \times 10^{-3}$ km^{-2} in the east (Behn et al., 2004). The decrease in seamount population density coincides with a change in lava flow morphology from pillow dominated in regions densely populated by seamounts to more lobate/sheet-like morphologies in regions that are sparsely populated. Combined these observations suggest a change in volcanic style from point-source-fed eruptions in densely populated regions to fissure-fed eruptions in sparsely populated regions, ultimately reflecting an increase in effusion rate as the GSC approaches the Galapagos hotspot (Behn et al., 2004).

Intuitively, the combination of increased crustal thickness, effusion rate, and decreased axial depth in the eastern portion of the western GSC suggests larger degrees of melting should also be expected. However, the observed major and minor element variations of G-PRIME basalt glasses provide a contrary viewpoint when initially taken at face value (Detrick et al., 2002; Cushman et al., 2004). Glasses from the Eastern Province, despite being erupted in the region with the thickest crust, have major element characteristics (e.g. high Al_2O_3 , low SiO_2 and $\text{CaO}/\text{Al}_2\text{O}_3$) with the strongest signature of low degrees of melting (Cushman et al., 2004). The apparent disparity in regions of thick crust with small extents of melting led to the suggestion that the along-axis gradient in K/Ti and H_2O , from enriched compositions in the east to depleted compositions in the west, results from the increased importance of hydrous melting closer to the hotspot (Cushman et al., 2004). The hydrous melting model predicts that the increased presence of water in the peridotite source region depresses the mantle solidus temperature, and this in turn extends the depth over which melting occurs (Plank and Langmuir, 1992). However, because melt production (i.e. the percent of melt produced per km of decompression once a package of mantle crosses its solidus) is lower in the hydrous zone, the average extent of melting is also lower, and the hydrous zone contributes a higher proportion of incompatible elements to the

magma. Because this zone is envisioned to be present at depths beneath the anhydrous zone, its contribution is considered additional. In this view, when melts are eventually aggregated prior to eruption they become mixtures of the low extent melts from the hydrous zone and higher extents of melting from the anhydrous zone, which leads to a lower average extent of melting despite the fact that more melt has been produced (Cushman et al, 2004) and greater crustal thickness and shallower axial depths are present (Asimow and Langmuir, 2002).

4.4 Methods

Approximately 0.4 to 0.5 kg of moderately to sparsely-phyric basaltic whole rock was crushed in a hammer mill and sieved into two useable size fractions (0.25-0.5 mm and 0.5-1.0 mm). After crushing and sieving, samples were cleaned by repeated washings in millipore water using an ultrasonic bath. This processes was repeated until 'cloudiness' in the water was no longer observed and the samples were then dried in an ~40°C oven. Plagioclase and olivine phenocrysts were hand picked under a binocular microscope to maximize the proportion of phenocrysts with amply large melt inclusions. Hand picked phenocrysts were then mounted in 1/4" O.D. stainless steel tubing using mixed epoxy. Phenocrysts and melt inclusions were then exposed and identified using a petrologic microscope under reflected light before a fine polish was achieved using a cloth wheel and 2 µm alumina grit. After polishing the 1/4" plugs were cleaned, once again, in an ultrasonic bath and set into 1" stainless steel rounds and digitally photographed under transmitted and reflective light.

Major element oxides of SiO₂, Al₂O₃, P₂O₅, K₂O, CaO, MnO, Cr₂O₃, FeO, Na₂O, MgO and TiO₂ were analyzed by electron microprobe (EMP; Cameca SX 100) in the College of Oceanic and Atmospheric Sciences (COAS) at Oregon State University (OSU). All analyses were conducted using a 5-10 µm diameter electron

beam, with a 15 kv acceleration voltage, and 30 nA beam current.

Trace element analyses of melt inclusions were conducted using a Merchantek 213 nm quintupled Nd:YAG UV laser coupled to a VG instruments Excell quadrupole inductively coupled mass spectrometer (LA-ICP-MS) in the W.M. Keck Collaboratory for Plasma Spectrometry within COAS at OSU. The sample cell configuration on this unit has been designed to hold a standard 1" microprobe round in the center with enough additional space to either side to hold modified thin section mounts containing standard reference materials. The sample is isolated in a helium atmosphere and helium gas is used to carry the ablated particulates through Tygon tubing to the mass spectrometer. The helium gas (with transported particulates) is mixed with argon gas within the torch-box housing using a small nylon-T, and is then introduced to the ICP torch. Beam diameters varied between 55 and 80 μm depending on inclusion size and a laser repetition rate of 3 Hz was used for all analyses.

Analyses began with a 45 second background reading followed by a 45 second acquisition period. The data was generated in peak hopping mode using a single point per peak, with 10 ms dwell time and 5 ms settling time on each analyte (Ca, Ti, Sr, Y, Zr, Ba, La, Ce, Pr, Nd, Sm, Eu, Gd, Tb, Dy, Er and Yb). Under these conditions individual acquisitions typically lead to between 30 and 45 second long signal plateaus resulting in ~ 0.75 to 1.25 seconds of count time per analyte. Typical count rates were; > 3000 cps for the LREE (La, Ce and Pr), 900 cps for Nd, and 350-600 cps at the MREE and HREE (Sm, Eu, Gd, Tb, Dy, Er and Yb), values typically 30-50 times the limit of detection.

Sample concentrations were determined using USGS quenched basalt standard BCR-2G with ^{43}Ca as an internal standard. An inherent challenge with melt inclusion analyses is the inability, due to the destructive nature of the technique, to replicate analyses of the inclusions. The precision, accuracy and reproducibility of the trace element analyses by LA-ICP-MS were therefore evaluated through the repeated

analysis of USGS quenched basalt standards BHVO-2G and BIR-2G. Blocks of 5 analyses on each of these standard glasses were conducted at the start and end of each analytical session using the same settings and analysis procedure used to analyze the melt inclusions. Accepted values for the concentrations in these standard glasses bracket those determined for the melt inclusions analyzed as part of this study. A total of 30 analyses were conducted on BHVO-2G and 28 were conducted on BIR-2G (Table 1; Figure 2).

Three additional samples analyzed during a preliminary stage of this project are also included (samples 34D-1, 63D-1 and 83D-1). Melt inclusions in these samples were analyzed using similar techniques to those described above with the following important differences; 1) samples were analyzed from doubly polished 100 μm thick-sections, and 2) the trace element analyte list did not include Tb. Although this sample preparation technique has the added advantage of preserving the petrographic relationships between host phenocrysts and inclusions, as well as host rocks and phenocrysts, it ultimately proved to expose insufficiently few inclusions at the sample surface. In this sense, the previously described techniques allowed for the maximum number of inclusions to be exposed for analysis during a single analytic session, which we determined to be the most important factor given that the main goal of this study was to investigate melt diversity in these samples.

4.5 Results

4.5.1 Sample descriptions and host geochemistry

Melt inclusions contained within eight samples from along the western GSC were analyzed in this study, two each from within the detailed seismic boxes Gala 1 (samples 84D-4 and 88D-1) and Gala 2 (samples 58D-2 and 63D-1), one from detailed seismic box Gala 3 (sample 17D-4) and one each from the region between

Gala 2 and Gala 3 (sample 38D-2) and Gala 1 and Gala 2 (sample 83D-1, Canales et al., 2002; Detrick et al., 2002). In terms of their glass compositions, samples 63D-1, 83D-1, 84D-4 and 88D-1 are NMORB compositions ($K/Ti < 0.9$), samples 34D-1, 38D-2 and 58D-2 are TMORB compositions (K/Ti between 0.9 and ~ 0.15) and sample 17D-4 is an EMORB ($K/Ti > 0.15$ and $K_2O > 0.20$, Cushman et al., 2004). In terms of crystallinity, samples 38D-2, 58D-2 and 84D-4 contain $>10\%$ crystals, with sample 58D-2 containing $>15\%$ crystals (Behn et al., 2004). Samples 17D-4 and 88D-1 represent two of the least crystalline samples with crystal counts $<5\%$. In terms of enrichment, 17D-4 has the highest fractionation corrected (oxide weight percents corrected for crystal fractionation to $MgO = 8.0$) TiO_2 , Al_2O_3 , and Na_2O and the lowest FeO , SiO_2 and CaO/Al_2O_3 values, thereby defining the location on-axis with the greatest plume influence (Cushman et al., 2004).

The inclusions in this study were not re-homogenized by heating prior to analysis, so their major element compositions have been variably affected by post-entrapment modification, either by further crystallization due to cooling or through diffusive interaction with their host minerals. However, because laser ablation effectively removes all material from within the inclusion, this technique is capable of giving accurate results for trace element concentrations without rehomogenization provided a suitable internal standard (such as Ca) is chosen, i.e. an element not significantly affected by post-entrapment precipitation on the host walls (Halter et al., 2002; Pettke et al., 2004).

A total of 74 melt inclusion analyses are reported in this study; 60 are from the 5 samples from which grains were separated and 14 were analyzed *in situ* from the 100 μm thick sections. An additional 10 samples were analyzed and rejected on the basis of insufficient count rates to produce coherent results (< 150 total counts at middle to heavy rare earth element masses). A majority of the inclusions were hosted in olivine (48) with the remainder (26) hosted in plagioclase. In two samples, 17D-4

and 34D-1, only melt inclusions from olivine phenocrysts were analyzed (23 total). In sample 38D-2, 7 inclusions were hosted in olivine phenocrysts and 3 were hosted in plagioclase. In sample 58D-2, 5 inclusions were hosted in olivine and 9 were hosted in plagioclase. Melt inclusions analyzed in the remaining samples (63D-1, 83D-1, 84D-4 and 88D-1) were hosted equally in olivine and plagioclase (2 of 4, 2 of 5, 4 of 9 and 5 of 9 olivine hosted, respectively). In terms of enrichment groups, a majority of individual melt inclusions can be classified in the same group as their host glasses (as reported in Cushman et al., 2004). For example, 17 melt inclusions were analyzed in sample 17D-4, all of which are EMORB based on their K/Ti and K_2O contents. A total of 10 inclusions were analyzed in sample 38D-2. Based on their K/Ti and K_2O contents, 4 inclusions in this sample are EMORB, 4 are TMORB and 2 are NMORB. Sample 38D-2 is the only sample from which inclusions were distributed amongst all three enrichment groups. Four inclusions were analyzed from 34D-1, all of which are TMORB based on their K/Ti and K_2O contents. The remaining 5 samples have mixed inclusions that are either TMORB or NMORB, however, in all of these samples the majority of inclusions follow the enrichment classification of their host glass. For example, sample 88D-1 has a NMORB host glass composition, and 8 of 9 inclusions analyzed in this sample also have NMORB compositions (Figure 3).

4.5.2 Trace element variation by enrichment groups

The trace element data for all 74 inclusions analyzed as part of this study are reported in Table 2. Generally speaking, the enrichment groups defined using K/Ti and K_2O form distinct groups in terms of trace element characterization, however these distinctions are not entirely self consistent. In particular it is much harder, if not impossible, to define a boundary between NMORB and TMORB compositions using the same melt inclusion analyses on all incompatible trace element diagrams

(Figure 4). Given the diversity of inclusions sampled from 38D-2, two melt inclusions from this sample have been selected as defining the approximate boundaries between EMORB-TMORB and TMORB-NMORB. The transition from EMORB to TMORB is best represented by the concentrations of 38D-2 MI#7 (e.g. La = 6.93), and the transition from TMORB to NMORB by 38D-2 MI#9 (e.g. La = 2.49; Figure 4).

By far the greatest enrichment is observed in Sr, Ba and La concentrations, with EMORB values ranging up to 413, 149, and 16.2 $\mu\text{g/g}$, respectively. Values for Sr, Ba and La in TMORB melt inclusions range between 62-114, 12-59, and 2.5-7.5 $\mu\text{g/g}$, respectively. The most depleted inclusion analyzed in this study is from sample 88D-1 (MI#2) with Sr, Ba and La concentrations of 84, 4.1 and 0.9 $\mu\text{g/g}$, respectively. The data trend for NMORB switches from having the lowest concentrations at a given La concentration for Ba to higher values at a given La concentration for Sr (Figure 4), consistent with the predicted compatibilities of Ba, La and Sr in basaltic systems (i.e., with relative K_D 's following the compatibility sequence Ba < La < Sr).

In terms of the remaining trace elements measured in this study, especially for the elements that are compatible in garnet (i.e. Tb, Y, Yb), the enriched inclusions from sample 17D-4 generally have concentrations no higher than TMORB and NMORB from the GSC, and also have small concentration ranges. For example, Y concentrations in EMORB melt inclusions from 17D-4 range from 28-47 $\mu\text{g/g}$, compared to the range in Y concentration observed in TMORB (58D-2) and NMORB (84D-4), which have ranges of 18-78 $\mu\text{g/g}$, and 18-49 $\mu\text{g/g}$, respectively.

There is a clear distinction between inclusions with EMORB versus NMORB glass compositions. Along the western GSC, the enriched inclusions only occur in two samples (17D-4 and 38D-2) and these are from lavas located where the ridge axis morphology is strongly influenced by the Galapagos hotspot. Conversely, all melt inclusions in NMORB lavas are dominantly NMORB as well. Melt inclusions from samples east of the 93°15'W propagating rift tip and melt inclusions from samples

west of the 95°30'W propagating rift tip define separate trends on variation diagrams (e.g. Figure 4). Sample 58D-2 from near the 95°30'W propagating rift tip contains a 'bi-modal' population of melt inclusions, some of which plot along the trend with the more enriched samples from east of the 93°15'W propagator, while others plot along the trend defined by samples from west of the 95°30'W propagator (Figure 4). Although the melt inclusions contained in samples from east of the 93°15'W propagator trend towards more enriched values, the inclusions in sample 17D-4 appear to derive from a substantially more enriched mantle source. From this perspective, melt inclusions from samples 34D-1, 38D-2 and 58D-2 (Middle Group) appear as though they may derive from mixtures of highly enriched plume influenced melt (as sampled by 17D-4, in the Eastern Group) with more depleted normal MORB melt (as sampled by 63D-1, 83D-1, 84D-4 and 88D-1, from the Western Group).

4.6 Discussion

4.6.1 Hydrous melting and the depth of melt initiation

A deep hydrous melting zone explains the paradox of western GSC MORB being associated with the thickest ocean crust despite having major element compositions that suggest their derivation from small degrees of melting (Fisk et al., 1982; Fisk, 1986; Detrick et al., 2002; Cushman et al., 2004). The hydrous melting model suggests this paradox can be readily resolved by the 'addition' of a hydrous melting field below that of the normal anhydrous melting field capable of producing NMORB compositions. Melt production in the hydrous zone is substantially lower than in the overlying anhydrous melting zone (Asimow et al., 2004), and as a result melt extraction in the hydrous zone is only expected to produce small melt fractions (i.e. 2-3%; Hirschmann et al., 1999).

Consistent with these predictions, Cushman et al. (2004) determined a range

of variables, including mantle upwelling rate, melt productivity and melting interval (depth over which melting occurs) that were suitable to reproduce the observed $\text{Na}_{8,0}$ (fractionation corrected Na_2O contents) and crustal thickness variations along the western GSC. The hydrous melting model suggests that variations in crustal thickness and basalt glass composition are accounted for by a slight enrichment in highly incompatible element concentrations in the plume influenced mantle source, and an increase in temperature ($< 20^\circ \text{C}$), coupled with an increased upwelling rate in the hydrous melting region (1.5 to 3.5 times that of the upwelling rate in the anhydrous zone, typically believed to match the half spreading rate of the ridge system (Cushman et al., 2004)). Additional constraints were placed on; 1) the depth interval over which melting occurs (~ 80 km for GSC NMORB and up to 120 km for EMORB), 2) the difference in melt productivity between the anhydrous and hydrous melting zones (an order of magnitude difference, from $\sim 0.4\%/ \text{km}$ (anhydrous) to $\sim 0.04\%/ \text{km}$ (hydrous)), and 3) a mean degree of melting for GSC EMORB (2-6.5%; Cushman et al., 2004).

The results of the hydrous melting model predict that the depth of melt initiation is greater beneath the eastern, plume-influenced portion of the western GSC compared to the NMORB dominated westernmost portion of the GSC, a consequence of which could be the expansion of the melting region to depths at which garnet is stable in lherzolite assemblages (i.e. at depths > 60 to 80 km; McKenzie and O'Nions, 1991). Rare earth element (REE) composition of a melt can be particularly diagnostic of source mineralogy and degree of melting; REE are large ion lithophile elements whose behavior has been well characterized and their partition coefficients in major mantle minerals are well known (Salters and Stracke, 2004). Mantle assemblages containing the mineral garnet strongly affect the relationship between light REE (LREE) and heavy REE (HREE) elements, due to the high partition coefficients of the HREE in garnet. In the next section, forward models of spinel lherzolite and garnet lherzolite melting are used to test the influence of varying source mineralogy on REE

element concentrations, and on LREE/MREE and MREE/HREE ratios.

4.6.2 Aggregated, non-modal, fractional melting of spinel lherzolite and garnet lherzolite lithologies

The model starting assemblages, bulk partition coefficients, and source compositions are summarized in Table 3. Because the main objective of these calculations is to determine the influence of source mineralogy on sample enrichment, the initial chemical compositions have been held constant for both source lithologies and assumed to be the depleted mantle composition of Salters and Stracke (2004). The equation used to derive the melting curves on Figures 5 and 6 are the aggregated non-modal fractional melting equation of Shaw (1970):

$$[x_i] = [x_o] (1/D_o) (1 - ((P F)/D_o))^{(1/P - 1)}$$

where x_i is the concentration in the liquid, x_o is the concentration in the source, D_o is the bulk partition coefficient, F is the degree of melting and P is the proportion each phase contributes to the melt. The results of these calculations suggest that the GSC NMORB are generated by ~9 to 20% melting of a spinel lherzolite source. These values are similar to those of Cushman et al. (2004) for melt productivities between 0.26 and 0.45 %/km and an anhydrous melting column between ~45 and 60 km in length. A small contribution of melt generated in the garnet stability field as small (< 1%) non-modal instantaneous fractional melts cannot be ruled out. However, such a contribution is not resolvable in the results presented in Figure 5. The possibility that very small degree fractional melts generated in the garnet field may contribute to NMORB compositions is suggested by the results presented in Figure 6, where a few of the more depleted melt inclusions with relatively low $(La/Yb)_n$ plot at relative

high $(\text{Tb/Yb})_n$ values. However, when the REE concentrations are also considered it appears that such a contribution is an artifact of the difficulties in making very precise and accurate measurements at the low Tb concentration levels of these inclusions (Figure 7).

Melt inclusions in sample 17D-4 are unique in that they are far more enriched in the highly incompatible elements, while having slightly less variable HREE concentrations compared to inclusions from TMORB and NMORB host lavas. This characteristic has led to generally elevated LREE/MREE and MREE/HREE ratios in sample 17D-4. The aggregated melting model (Figures 5 and 6) suggests that inclusions from sample 17D-4 may have been produced by sub-equal amounts of melting in the garnet and spinel lherzolite field. The degree of melting in each field varies slightly depending on the choice of REE ratios used. In general, the melt inclusion REE concentrations and REE ratios in 17D-4 can be produced by mixing melts from the spinel field (having degrees of melting between 1.2% and 3.6%) with melts from the garnet lherzolite field (generated by 1.4% to 2.5% melting). If these deeper garnet melts are predominantly derived from the hydrous melting zone (with melt productivity of $\sim 0.04\%/km$) then the hydrous melting zone must extend between 35 and 63 km below that of the anhydrous zone. These estimates are in good agreement with values between 28 and 58 km predicted by the hydrous melting model, and producing 1.1% to 1.7% of melt (Cushman et al., 2004). Assuming constant productivity of $0.3\%/km$ in the spinel lherzolite (anhydrous) field and $0.04\%/km$ in the garnet lherzolite (hydrous) field, the similar degrees of melting generated in the spinel and garnet fields suggest upwelling rates are between ~ 5 and 8 times higher through the garnet (hydrous) field compared to the spinel (anhydrous) field, values somewhat higher than the maximum value predicted by Cushman et al. (2004) of 3.5. However, given the constant composition of the source material for both of these calculated melt curves, these values are similar to those required by the hydrous melting model

without source enrichment (Cushman et al., 2004).

One fairly surprising result of this melt inclusion investigation is the absence of NMORB (or TMORB) compositions in the 17D-4 melt inclusions. This is very different than what is observed for lavas to the west, which show a gradual progression towards NMORB-dominated inclusions. One potential explanation for the lack of intermediate and more depleted compositions in sample 17D-4 extends from considering the GSC melt inclusion compositions within the context of the range of basalt glass compositions from the Wolf-Darwin Lineament (WDL) seamounts (Harpp and White, 2001).

Melt inclusion data and WDL glass compositions normalized to a depleted western GSC glass sample (80D) are plotted in Figure 7. The WDL glass compositions clearly fall along a trend between the 17D-4 melt inclusion compositions and the melt inclusion compositions that describe the NMORB component along the GSC farther to the west. If the EMORB inclusions from 17D-4 represent melts generated at greater depths relative to the NMORB compositions sampled farther to the west, as suggested by the REE modeling, the absence of NMORB compositions in 17D-4 and overall enriched composition of the host lava suggest that larger degree melts generated at shallower depths in the mantle are absent in this lava. One possible explanation for the apparent absence of more depleted melts in sample 17D-4 involves the complex tectonic structure separating thicker, older lithosphere west of the WDL and younger, thinner lithosphere east of the WDL, between it and the Galapagos Transform, providing a pathway for the preferential removal of the more depleted relatively shallow melts produced in this region. This mechanism was previously suggested by Harpp and Geist (2002) who suggest the formation of the WDL occurs as the result of extension, oriented at oblique angles to the ridge axis, originating in response to the intersection of the GSC with the 90°50' W transform. In their model, extension in this region promotes local mantle upwelling and permits melt ascent off-

axis where, in a normal setting, it would not ordinarily occur. Here, it is suggested that this extension results in a preferential removal of more depleted melts generated at relatively shallow depths in the mantle that in a more normal ridge setting might be focused to the ridge axis. By effectively removing these relatively shallow melts they are no longer focused to the ridge axis and are therefore not available to mix with and dilute the more enriched melts generated at greater depths below the ridge axis. In this view, both the more depleted relatively shallow melts, and the more enriched deeper melts contribute to the construction of the lithosphere in this region, but as a result of the tectonic setting may be dispersed locally in such a way that allows deep, small degree, enriched melts to be delivered along the easternmost portion of the ridge axis in this region.

4.7 Conclusions

- 1) Melt inclusions analyzed in GSC basalts show greater chemical diversity compared to their host basalt glasses along the western GSC. However, the average melt inclusion compositions resemble those of their respective host basalt.
- 2) Melt inclusions in NMORB host lavas generally show less diversity than melt inclusions hosted in EMORB and TMORB lavas. Production of EMORB and NMORB lavas along the western GSC may represent 'end-member' cases for the depth of melting along the ridge axis.
- 3) NMORB melt inclusions cluster along crystal fractionation trends, suggesting that these melts are more readily homogenized and cooled. This is consistent with their eruption along a portion of the ridge axis where crystallinity is observed to be higher (Detrick et al. 2002).
- 4) REE element modeling indicates EMORB melts are generated from

smaller degrees of melting generated at greater depths. The degrees of melting inferred from these forward models agree well with the degrees of melting predicted by the hydrous melting model of Cushman et al. (2004).

- 5) Melt inclusions analyzed from sample 17D-4 suggest a relatively large (up to 50%) component of melt generated from great depths (≥ 60 km). Furthermore, the absence of intermediate or depleted melt inclusion compositions nearest the hotspot suggest that these melts efficiently reach the ridge axis without significant mingling with melts generated at shallower depths in the region.

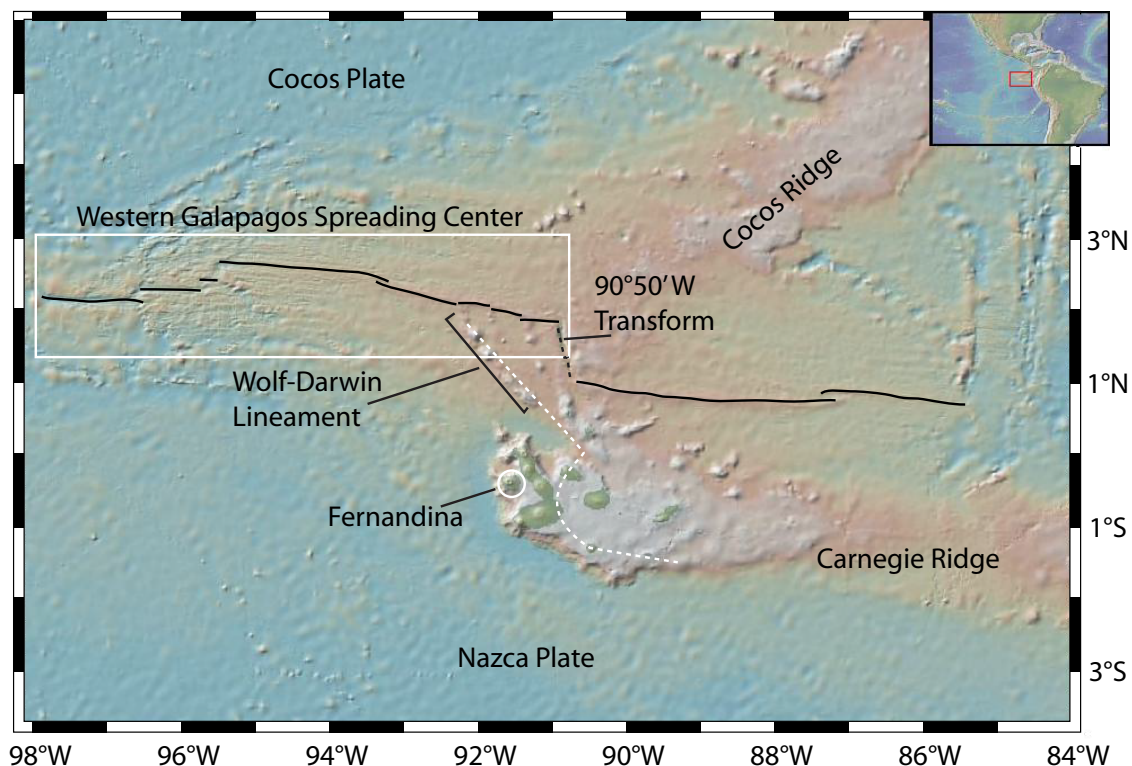


Figure 4-1. Regional map of the eastern equatorial Pacific near the Galapagos Islands. The thin black line depicts the ridge axis east and west of the 90°50' W Galapagos Transform (GT, dashed black line). The Galapagos Spreading Center (GSC) divides the Cocos Plate to the North from the Nazca Plate to the South. The extent of the western GSC is highlighted by the white box and extends westward from the GT out towards ~98°W. The Wolf –Darwin lineament (WDL) is depicted by the bracketed black line and extends to the northwest from the Galapagos Platform towards the western GSC, where it intersects near 92°W. The dashed white line trending dominantly NW-SE across the Galapagos Plateau marks the trace of the transition between thicker, older crust to the west from thinner, younger crust to the east (White et al., 1993). Other highlighted features included; 1) the island of Fernandina, which represents the current surface expression of the plume and 2) the Cocos and Carnegie Ridges representing the dominant plate motions of the Cocos and Nazca Plates, respectively since ~5 Ma when the plume source was centered on the ridge axis.

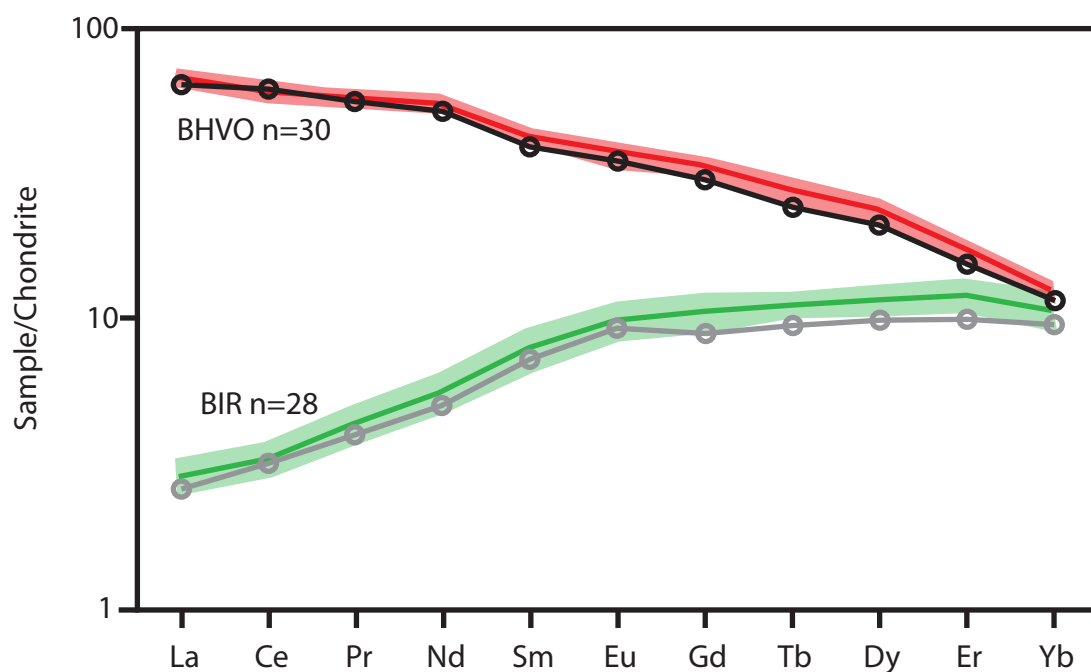


Figure 4-2. Chondrite normalized values for USGS fused glass basalt standards BHVO-2G and BIR-2G. Rare earth element diagram for the analytes measured in this study. Black and grey circles are accepted values for these USGS standards. Solid red and green lines are average values for these standard glasses determined during the course of this study. The red and green envelopes are ± 1 standard deviation on that average. BHVO-2G represents a compilation of 30 analyses and BIR-2G represents 28 analyses.

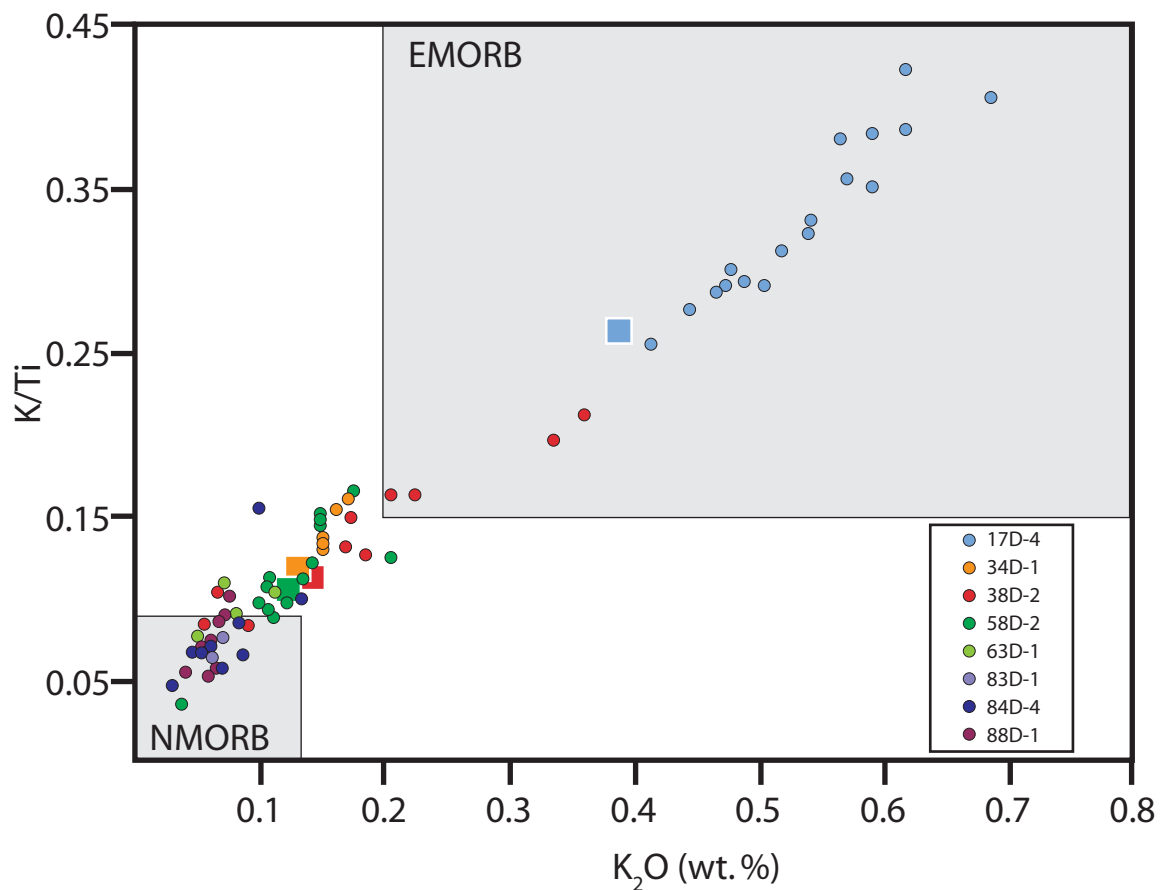


Figure 4-3. Enrichment groups for analyzed melt inclusions from the western GSC. Diagram plots K_2O (weight percent potassium oxide) versus K/Ti (moles K over moles Ti) for all 74 inclusions analyzed in this study. Large darker grey box in the upper right hand portion of the diagram defines the EMORB field ($K_2O > 0.2$ and $K/Ti > 0.15$, as defined by Cushman et al., 2004). Lighter grey box defines the field for NMORB ($K_2O < 0.09$, Cushman et al., 2004). Large colored squares represent values determined for each host glass as reported in Cushman et al., 2004. Melt inclusions generally cluster near the values of their host glass. Sample 17D-4 (light blue circles) are generally more enriched than their host glass, while inclusions from sample 38D-2 (red circles) have the greatest diversity, ranging from NMORB to EMORB.

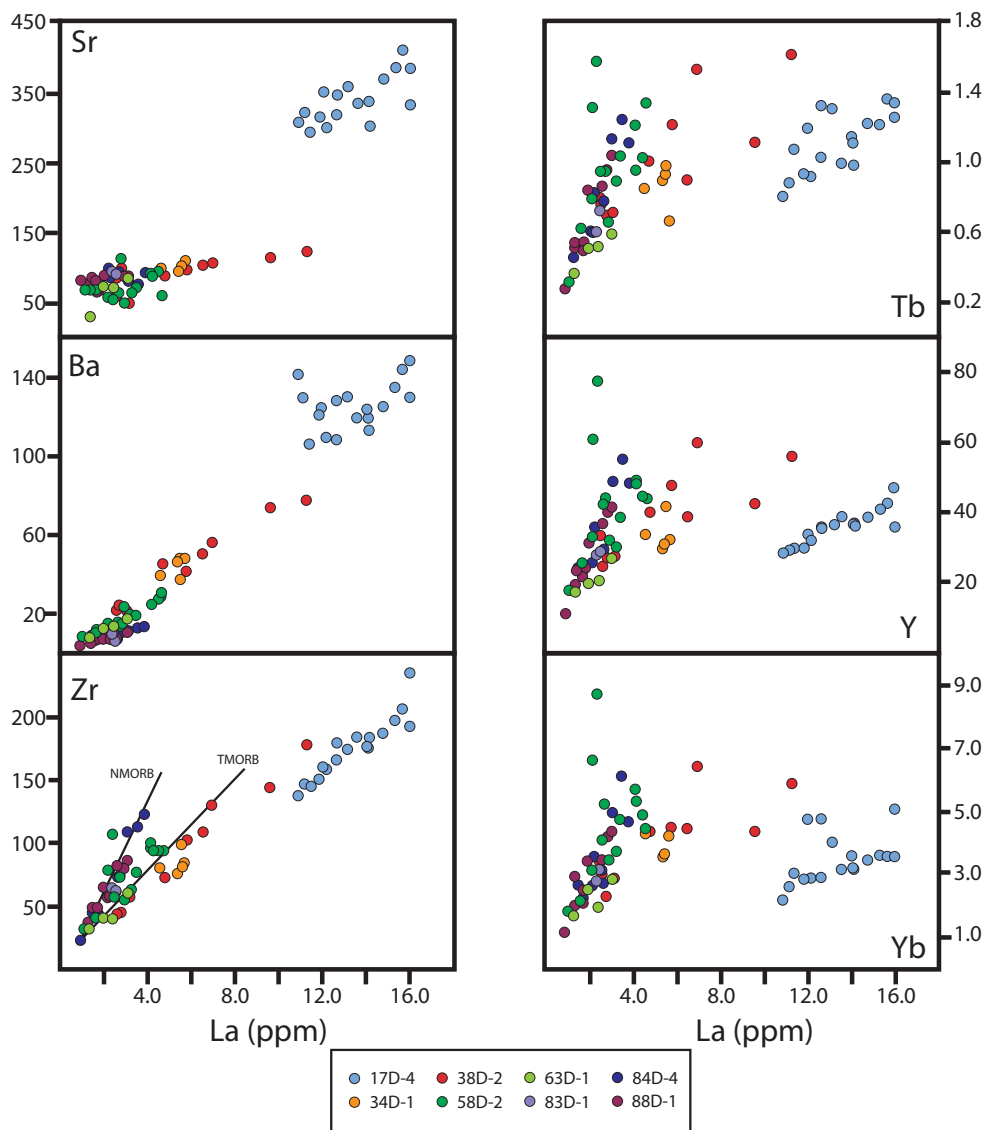


Figure 4-4. Trace element variation diagrams. Selected trace element concentrations (in $\mu\text{g/g}$) plotted against La concentrations (also in $\mu\text{g/g}$). Notice the clear enrichment of Sr in the most enriched (plume influenced) inclusions from 17D-4 (light blue circles). The NMORB trend is defined by the different shades of purple and is generally consistent with variable degrees of crystal fractionation. In mid-ocean ridge systems crystal fractionation is expected to raise incompatible element concentrations without producing large changes in incompatible element ratios. Notice the tendency for inclusions from the westernmost T-MORB sample 58D-2 (dark green circles) to be divergent along both the NMORB trend and the less well defined TMORB trend shown by the intermediate character of inclusions from samples 34D-1 and 38D-2 (orange and red circles, respectively). The rotation observed in the most enriched inclusions (light blue circles) from co-varying trace element concentrations at Zr to relatively uniform Yb concentrations at variable La concentrations is consistent with these samples production from relatively smaller degrees of melting.

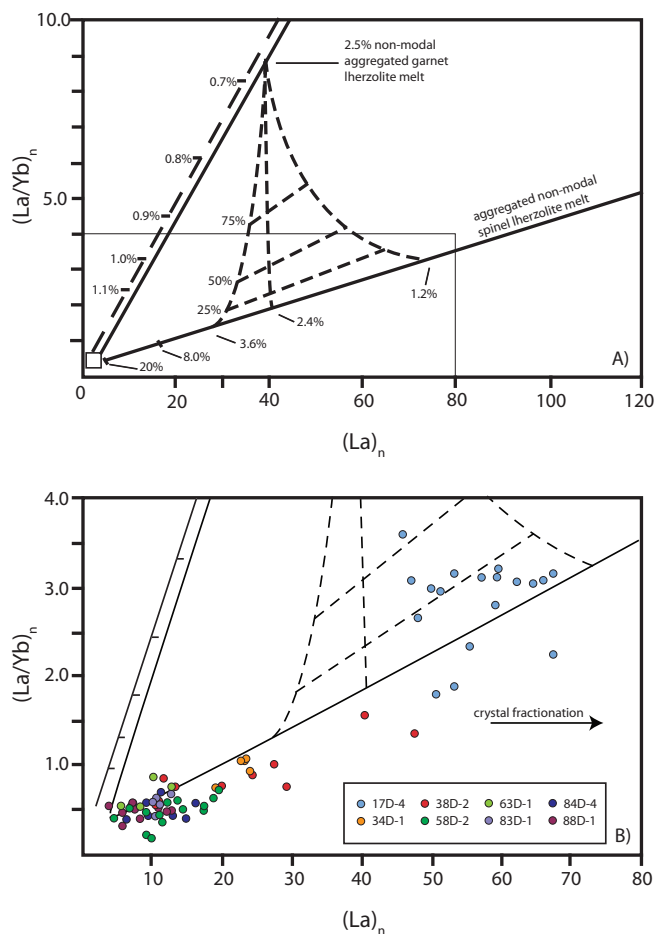


Figure 4-5. $(La/Yb)_n$ versus $(La)_n$. A) Results of the non-modal aggregated melt calculations for spinel lherzolite and garnet lherzolite assemblages (solid lines). The large dashed line running near vertically along the left side of the diagram represents instantaneous non-modal fractional melts of the same garnet lherzolite assemblage used in the aggregated model. Dashed grid shows mixing between melts produced by varying degrees of spinel lherzolite melt mixed with a 2.5% aggregated non-modal fractional melt of garnet lherzolite. Open square in the lower left hand corner is the depleted mantle composition of Salters and Stracke (2004), used as the source in these calculations. The box marked by the thin black line defines the portion of the diagram enlarged in B) Analyzed melt inclusion compositions plotted on top of the calculated compositions discussed in (A). The arrow on the right demonstrates the general direction at which crystal fractionation proceeds. The enriched melt inclusions from sample 17D-4 (light blue circles) are the only samples that plot well above the curve generated for spinel lherzolite melting, suggesting that as much as one-half of the melt generation occurred in the garnet lherzolite field. All values on both diagrams are normalized to the chondrite values from Sun and McDonough (1989). Partition coefficients used in the model calculations are from Salters and Stracke (2004), 2.0 GPa coefficients were used in the spinel lherzolite melting calculations and the 3.0 GPa coefficients were used in the garnet lherzolite melting calculations, see text for details

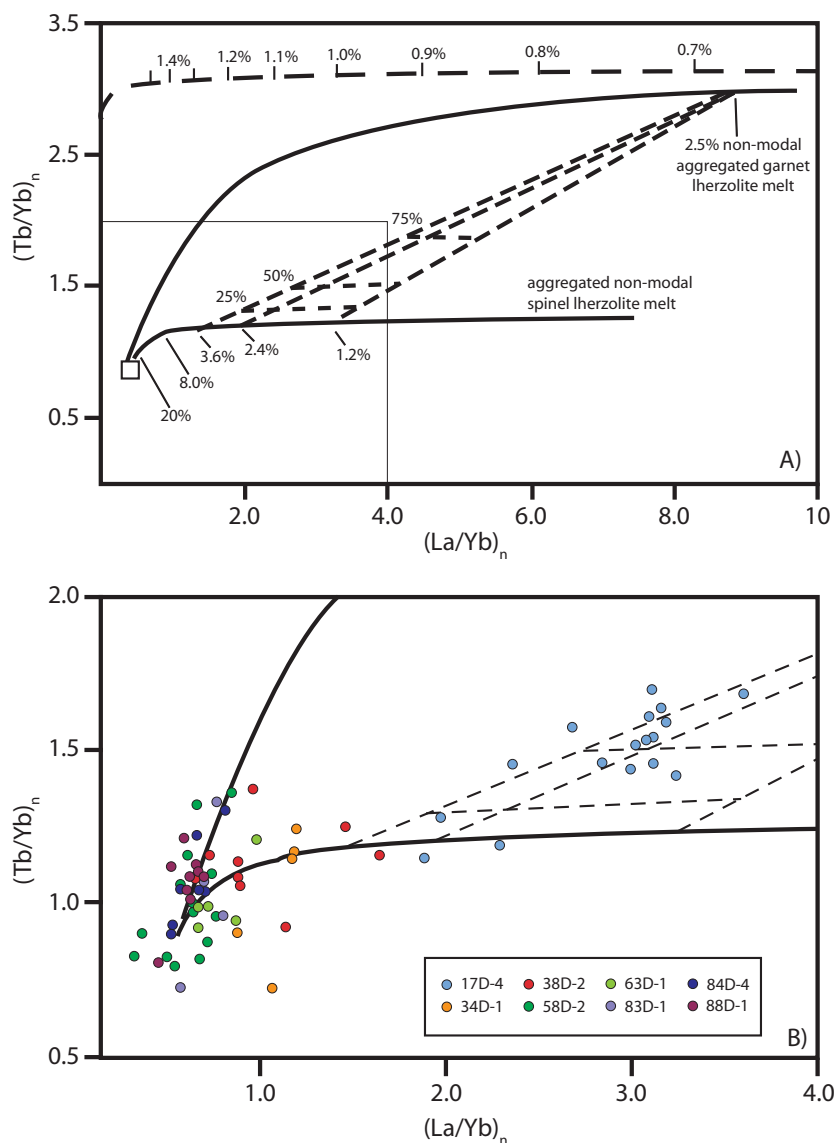


Figure 4-6. $(Tb/Yb)_n$ versus $(La/Yb)_n$. A) Results of the non-modal aggregated melt calculations for spinel lherzolite and garnet lherzolite assemblages. All lines and symbols are the same as in Figure 5. B) Analyzed melt inclusion compositions plotted on top of the calculated compositions. Again the enriched inclusions from sample 17D-4 (light blue circles) stand apart from the remainder of the inclusions as being the only samples consistently plotting along mixing arrays between garnet and spinel lherzolite melts. There is some suggestion on the left side of the diagram that even NMORB inclusions may have some contribution from small amounts of instantaneous fractional melts generated in the garnet peridotite field, but the resolution is poor at these depleted compositions and the results are inconsistent with inferences based on Figure 5. All values on both diagrams are normalized to the chondrite values from Sun and McDonough, 1989.

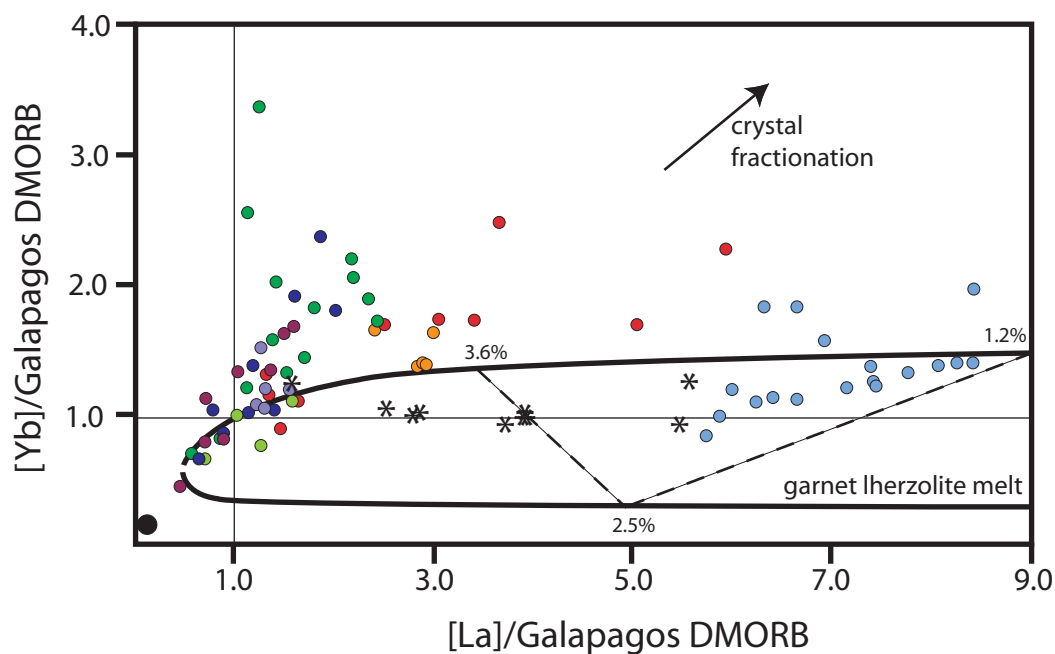


Figure 4-7. Normalized La and Yb concentrations of western GSC melt inclusions. All concentrations were normalized to those of 80D-1, a depleted MORB from the westernmost GSC with the lowest [REE]. Melting curves and melt inclusion data normalized to a depleted host glass from the westernmost portion of the western GSC. Melting trajectories, and mixing curves are the same as in Figures 5 and 6. The arrow in the upper right portion of the diagram depicts the general direction of crystal fractionation. A majority of the melt inclusions from west of the $93^{\circ}15'W$ propagating rift tip plot along a trend similar to that predicted for crystal fractionation. The black stars are for lavas from the Wolf-Darwin Lineament (WDL; Harpp and White, 2001) and form an array between the enriched melt inclusions from 17D-4 and the NMORB component (80D-1) depicted by the crossing thin black lines. Note that the WDL basalts lie in appropriate positions to be parental compositions to the relatively highly crystallized samples 34D-1 and 38D-2.

Table 1 - Results for USGS standard glasses								
	BIR	+/-		accepted	BHVO	+/-		accepted
	$\mu\text{g/g}$	1σ	(%)		$\mu\text{g/g}$	1σ	(%)	
Sr	114	4	3.9	110	405	4	1.1	389
Y	18.0	1.8	9.8	16.0	29.5	2.2	7.4	26.0
Zr	16.3	1.7	10.5	15.5	186	12	6.7	172
Ba	6.73	0.84	12.4	7.00	127	6	4.9	129
La	0.67	0.09	12.7	0.62	16.0	0.7	4.4	15.3
Ce	1.98	0.25	12.8	1.95	36.8	2.2	5.9	37.9
Pr	0.41	0.06	13.9	0.38	5.40	0.24	4.5	5.34
Nd	2.59	0.39	14.9	2.37	25.4	1.2	4.9	24.4
Sm	1.19	0.19	15.9	1.12	6.48	0.27	4.1	6.03
Eu	0.57	0.08	13.8	0.54	2.13	0.16	7.5	2.04
Gd	2.16	0.31	14.4	1.85	6.79	0.39	5.8	6.23
Tb	0.41	0.04	9.7	0.36	1.02	0.07	6.9	0.90
Dy	2.92	0.33	11.3	2.51	5.91	0.41	7.0	5.31
Er	1.97	0.25	12.6	1.66	2.80	0.20	7.2	2.55
Yb	1.80	0.24	13.1	1.65	2.07	0.12	5.9	1.96
<i>n</i> =	28				30			

all values are in $\mu\text{g/g}$ and an average values measured during the duration of the study

n is the number of analyses included in the average value

1σ is the standard deviation of *n* number of analyses

accepted values are isotope dilution values from Kent (unpublished data)

Table 2- Sample locations, axial depth and melt inclusion enrichment diversity

Sample	Lat (°N)	Long (°E)	Axial depth (m)	Geographic Group	MI Enrichment Groups
17D-4	2°04.2'	91°48.0'	1762	Eastern	E
34D-1	2°17.4'	93°00.6'	2167	Eastern	T
38D-2	2°21.4'	93°16.1'	2293	Eastern	E,T,N
58D-2	2°31.6'	94°20.9'	2457	Middle	T,N
63D-1	2°35.5'	94°44.7'	2655	Middle	T,N
83D-1	2°08.1'	96°49.0'	2957	Western	N
84D-4	2°08.2'	96°52.5'	3042	Western	N,T
88D-1	2°08.4'	97°11.5'	3229	Western	N,T

MI enrichment refers to the enrichment groups observed in melt inclusions from each sample. E= EMORB, T = TMORB and N= NMORB, group types are listed in order of the number of observed enrichment type in that sample, for example E,T indicates the largest population was EMORB followed by TMORB

Table 3 Trace element results for individual melt inclusions

	17D-4									
	MI#1		MI#2		MI#3		MI#4		MI#5	
	55		55		55		55		55	
	OI									
Sr	354	1.5	349	5.9	361	1.4	295	1.5	317	5.2
Y	33.6	0.65	35.3	0.91	36.5	0.95	29.6	0.46	29.7	0.55
Zr	160	1.5	168	4.3	175	2.9	145	1.9	153	3.0
Ba	125	1.2	128	2.4	130	1.9	106	0.9	121	1.4
La	12.0	0.24	12.6	0.41	13.2	0.16	11.4	0.13	11.9	0.23
Ce	27.0	0.26	29.4	0.32	30.8	0.59	26.4	0.14	30.2	0.20
Pr	4.33	0.085	4.51	0.069	4.70	0.042	3.83	0.036	4.11	0.017
Nd	22.3	0.30	22.6	0.46	24.2	0.55	19.0	0.34	18.7	0.49
Sm	5.99	0.176	6.17	0.220	6.46	0.092	5.18	0.179	4.66	0.198
Eu	2.37	0.171	2.41	0.106	2.27	0.137	1.86	0.053	1.90	0.098
Gd	8.61	0.209	8.50	0.328	8.06	0.593	5.47	0.365	5.09	0.158
Tb	1.19	0.067	1.33	0.033	1.30	0.059	1.07	0.009	0.95	0.036
Dy	7.97	0.133	7.62	0.324	7.65	0.251	6.11	0.178	5.84	0.210
Er	4.26	0.173	4.71	0.404	4.31	0.256	3.94	0.080	2.99	0.078
Yb	4.73	0.334	4.74	0.213	4.07	0.139	3.09	0.107	2.83	0.077
Zr/Y	4.77		4.76		4.81		4.91		5.13	
Zr/Ba	1.29		1.31		1.35		1.37		1.26	
La/Sm	2.01		2.05		2.04		2.20		2.54	
La/Yb	2.54		2.67		3.23		3.69		4.19	
Tb/Yb	0.25		0.28		0.32		0.35		0.33	

all concentrations are in mg/g

errors are 1 standard deviation from the individual analysis of the analyte ratioed to ⁴³Ca

Table 3 (continued)

	17D-4									
	MI#6		MI#7		MI#8		MI#9		MI#10	
	80		80		80		55		80	
	OI									
Sr	325	3.4	309	3.3	304	4.3	321	3.8	388	4.9
Y	29.1	0.43	28.3	0.96	37.2	1.53	36.1	1.27	36.4	0.78
Zr	149	2.3	140	4.8	185	7.3	181	4.6	193	3.9
Ba	130	2.3	142	1.5	114	5.2	109	2.0	148	3.0
La	11.2	0.19	10.9	0.26	14.1	0.42	12.6	0.19	16.0	0.18
Ce	34.5	0.44	41.3	1.24	31.6	0.76	27.7	0.33	40.1	0.32
Pr	3.95	0.104	4.15	0.115	4.43	0.051	3.98	0.057	5.56	0.115
Nd	17.5	0.29	17.0	0.64	20.2	0.39	18.8	0.24	25.5	0.72
Sm	4.65	0.258	4.08	0.218	5.38	0.122	4.99	0.132	5.93	0.391
Eu	1.53	0.069	1.50	0.025	1.78	0.062	1.73	0.061	2.24	0.038
Gd	4.91	0.184	4.73	0.414	5.85	0.232	5.73	0.235	7.63	0.491
Tb	0.88	0.026	0.80	0.064	0.98	0.034	1.04	0.028	1.27	0.067
Dy	4.93	0.159	4.60	0.399	5.78	0.146	5.92	0.169	7.47	0.213
Er	3.02	0.209	2.72	0.219	3.58	0.130	3.27	0.100	4.71	0.263
Yb	2.59	0.093	2.16	0.036	3.14	0.152	2.88	0.107	3.62	0.168
Zr/Y	5.11		4.94		4.97		5.01		5.30	
Zr/Ba	1.14		0.99		1.63		1.67		1.30	
La/Sm	2.41		2.67		2.63		2.53		2.70	
La/Yb	4.32		5.04		4.50		4.39		4.43	
Tb/Yb	0.34		0.37		0.31		0.36		0.35	

Table 3 (continued)

	17D-4 MI#11		17D-4 MI#12		17D-4 MI#13		17D-4 MI#14		17D-4 MI#15	
	80		55		55		55		55	
	OI									
Sr	340	2.7	335	2.1	414	6.0	387	5.2	340	3.9
Y	37.0	0.54	47.1	0.43	42.5	0.47	40.9	0.76	36.1	0.62
Zr	179	3.0	237	1.7	207	1.9	199	1.6	176	2.8
Ba	124	0.9	131	1.3	144	1.8	135	2.0	120	2.9
La	14.0	0.25	16.0	0.23	15.7	0.28	15.3	0.31	14.1	0.21
Ce	32.2	0.39	37.0	0.56	38.5	0.48	37.3	0.26	32.9	1.15
Pr	4.50	0.048	5.03	0.141	5.32	0.116	5.05	0.107	4.50	0.183
Nd	22.1	0.60	23.8	0.58	25.5	1.06	24.7	0.47	20.8	0.97
Sm	5.59	0.198	7.54	0.400	7.32	0.833	6.59	0.644	6.27	0.188
Eu	2.08	0.060	2.20	0.075	2.32	0.108	2.15	0.131	1.92	0.141
Gd	7.23	0.213	7.32	0.711	6.96	0.700	7.53	0.730	7.39	0.742
Tb	1.14	0.042	1.34	0.045	1.36	0.088	1.21	0.039	1.11	0.045
Dy	7.04	0.303	8.25	0.292	7.58	0.486	7.30	0.437	7.17	0.393
Er	4.06	0.091	4.46	0.098	4.21	0.323	4.14	0.092	3.74	0.380
Yb	3.57	0.110	5.13	0.197	3.63	0.328	3.59	0.334	3.26	0.300
Zr/Y	4.82		5.03		4.86		4.87		4.86	
Zr/Ba	1.44		1.81		1.43		1.48		1.46	
La/Sm	2.51		2.12		2.14		2.33		2.25	
La/Yb	3.94		3.12		4.32		4.27		4.33	
Tb/Yb	0.32		0.26		0.38		0.34		0.34	

Table 3 (continued)

	17D-4		17D-4		17D-4		38D-2		38D-2	
	MI#16		MI#18		MI#19		MI#1		MI#2	
	55	80	80	80	55	55	55	55	55	55
	OI									
Sr	338	7.0	372	2.0	303	1.8	126	1.9	117	4.2
Y	38.7	0.59	38.5	1.20	31.9	0.70	56.2	0.73	42.8	2.57
Zr	186	2.8	187	2.9	158	2.6	178	3.5	145	8.6
Ba	119	3.1	125	0.4	109	1.7	77.7	1.46	74.1	3.83
La	13.6	0.58	14.8	0.18	12.2	0.23	11.3	0.21	9.59	0.752
Ce	31.1	0.74	34.8	0.41	28.7	0.22	26.8	0.444	24.0	1.42
Pr	4.43	0.107	4.99	0.070	4.07	0.028	3.91	0.181	3.36	0.161
Nd	19.2	0.91	22.3	0.29	19.1	0.45	20.2	0.87	17.9	1.46
Sm	5.36	0.490	5.29	0.200	5.23	0.187	6.57	0.171	5.03	0.655
Eu	1.66	0.180	2.09	0.053	1.78	0.048	2.21	0.147	1.65	0.211
Gd	6.74	0.655	7.04	0.196	5.66	0.186	9.08	0.349	7.62	1.051
Tb	1.01	0.065	1.22	0.069	0.93	0.057	1.62	0.056	1.12	0.078
Dy	7.16	0.338	6.50	0.253	5.81	0.233	9.24	0.376	6.89	0.616
Er	3.72	0.404	4.03	0.187	3.20	0.140	6.53	0.284	5.03	0.358
Yb	3.14	0.206	3.44	0.195	2.93	0.130	5.89	0.228	4.38	0.147
Zr/Y	4.81		4.86		4.94		3.18		3.39	
Zr/Ba	1.56		1.49		1.44		2.30		1.96	
La/Sm	2.53		2.79		2.33		1.72		1.91	
La/Yb	4.33		4.30		4.15		1.91		2.19	
Tb/Yb	0.32		0.36		0.32		0.27		0.25	

Table 3 (continued)

	38D-2									
	MI#3		MI#4		MI#5		MI#6		MI#7	
	55		55		80		55		55	
	OI									
Sr	88.7	3.54	100	5.5	99.2	0.80	51.3	3.58	109	5.0
Y	24.8	1.74	27.0	1.14	47.6	0.89	27.6	1.15	60.1	6.55
Zr	44.7	2.18	45.9	2.47	103	1.9	58.2	4.13	131	6.7
Ba	22.2	0.51	24.1	1.46	41.6	1.05	21.4	1.80	56.5	2.73
La	2.56	0.096	2.77	0.451	5.78	0.181	3.11	0.258	6.93	0.537
Ce	7.27	0.114	6.75	0.512	14.8	0.31	7.90	0.751	18.9	1.56
Pr	1.23	0.092	1.25	0.119	2.53	0.108	1.22	0.118	2.99	0.199
Nd	5.82	0.523	6.46	0.370	12.0	0.31	6.79	0.671	17.2	1.23
Sm	2.23	0.417	3.29	1.302	4.15	0.400	2.94	0.355	4.50	0.635
Eu	1.14	0.125	1.08	0.126	1.58	0.093	0.78	0.074	1.74	0.100
Gd	3.78	0.213	4.50	0.645	7.07	0.595	3.56	0.302	9.25	1.208
Tb	0.76	0.069	0.70	0.139	1.22	0.063	0.72	0.024	1.54	0.189
Dy	4.48	0.501	4.11	0.410	8.02	0.246	4.54	0.386	9.74	0.743
Er	3.20	0.163	3.06	0.429	5.05	0.140	2.74	0.257	7.14	1.012
Yb	2.98	0.236	2.32	0.227	4.50	0.180	2.87	0.100	6.45	0.873
Zr/Y	1.80		1.70		2.17		2.11		2.18	
Zr/Ba	2.01		1.90		2.48		2.73		2.31	
La/Sm	1.15		0.84		1.39		1.06		1.54	
La/Yb	0.86		1.19		1.29		1.08		1.07	
Tb/Yb	0.25		0.30		0.27		0.25		0.24	

Table 3 (continued)

	38D-2		38D-2		38D-2		58D-2		58D-2	
	MI#8		MI#9		MI#10		MI#1		MI#2	
	80		80		55		55		55	
	plag		plag		plag		Ol		Ol	
Sr	90.1	1.68	62.0	0.53	105	6.6	96.5	1.78	92.4	1.26
Y	40.4	1.07	33.7	1.81	38.9	1.69	44.7	0.65	49.1	1.29
Zr	73.4	1.83	63.0	3.41	109	9.2	93.6	1.75	100	2.8
Ba	45.2	1.67	13.5	1.57	50.5	4.82	27.8	0.79	24.9	1.10
La	4.76	0.241	2.49	0.155	6.48	0.534	4.45	0.305	4.12	0.148
Ce	13.8	0.47	6.69	0.502	20.9	2.69	11.3	0.28	10.7	0.18
Pr	2.05	0.100	1.20	0.091	2.89	0.315	1.76	0.097	1.82	0.086
Nd	11.0	0.10	6.68	0.492	13.0	1.34	10.8	0.33	10.6	0.83
Sm	4.15	0.107	2.71	0.107	3.84	0.425	3.70	0.206	4.17	0.443
Eu	1.31	0.022	0.94	0.055	1.34	0.089	1.18	0.075	1.43	0.104
Gd	5.00	0.084	4.29	0.079	4.63	0.318	5.44	0.612	5.13	0.172
Tb	1.01	0.044	0.80	0.045	0.90	0.035	1.03	0.095	1.22	0.060
Dy	6.56	0.165	5.21	0.193	5.84	0.300	7.47	0.170	8.03	0.925
Er	4.38	0.198	3.59	0.215	3.97	0.178	5.36	0.394	5.57	0.445
Yb	4.37	0.134	3.39	0.216	4.47	0.484	4.92	0.115	5.72	0.399
Zr/Y	1.82		1.87		2.81		2.10		2.04	
Zr/Ba	1.63		4.67		2.17		3.37		4.03	
La/Sm	1.15		0.92		1.69		1.20		0.99	
La/Yb	1.09		0.74		1.45		0.90		0.72	
Tb/Yb	0.23		0.24		0.20		0.21		0.21	

Table 3 (continued)

	58D-2									
	MI#3		MI#4		MI#5		MI#6		MI#7	
	55		55		80		55		80	
	Ol		Ol		Ol		plag		plag	
Sr	89.3	2.20	72.8	1.05	116	0.7	51.2	1.30	64.4	0.75
Y	48.4	2.54	38.7	0.76	44.0	1.13	32.2	0.30	42.4	0.32
Zr	96.7	4.17	77.3	0.78	73.0	0.35	56.1	0.59	73.0	0.25
Ba	24.9	0.46	19.8	0.17	13.9	0.08	23.7	0.88	15.5	0.07
La	4.15	0.178	3.42	0.203	2.71	0.052	2.89	0.091	2.61	0.029
Ce	10.0	0.27	8.35	0.254	7.96	0.265	7.11	0.153	7.36	0.121
Pr	1.68	0.038	1.48	0.040	1.36	0.001	1.20	0.038	1.28	0.051
Nd	9.22	0.997	8.29	0.182	7.55	0.414	6.22	0.205	7.91	0.032
Sm	3.80	0.629	3.34	0.606	3.03	0.007	2.46	0.057	3.34	0.062
Eu	1.15	0.191	1.03	0.080	1.22	0.019	0.96	0.059	1.16	0.036
Gd	6.46	0.079	4.72	0.482	4.53	0.238	4.19	0.256	5.23	0.061
Tb	0.96	0.186	1.04	0.096	0.95	0.013	0.66	0.034	0.95	0.013
Dy	8.38	0.320	7.13	0.283	6.93	0.102	5.36	0.176	6.76	0.215
Er	5.55	0.391	4.41	0.304	4.64	0.162	3.47	0.228	4.65	0.109
Yb	5.36	0.470	4.74	0.271	5.24	0.097	3.44	0.122	4.09	0.112
Zr/Y	2.00		2.00		1.66		1.74		1.72	
Zr/Ba	3.89		3.91		5.25		2.37		4.71	
La/Sm	1.09		1.02		0.89		1.18		0.78	
La/Yb	0.77		0.72		0.52		0.84		0.64	
Tb/Yb	0.18		0.22		0.18		0.19		0.23	

Table 3 (continued)

	58D-2									
	MI#8		MI#9		MI#10		MI#11		MI#13	
	80		55		80		80		80	
	plag									
Sr	60.6	0.03	56.9	2.19	70.1	0.75	60.6	0.33	70.2	1.21
Y	61.1	0.29	77.6	3.08	17.9	0.36	33.2	0.36	25.5	1.18
Zr	78.7	0.41	108	4.5	33.4	0.52	57.9	0.43	43.1	1.80
Ba	14.5	0.25	16.3	0.48	7.80	0.390	13.8	0.28	11.5	0.11
La	2.15	0.039	2.35	0.092	1.07	0.052	2.14	0.030	1.63	0.061
Ce	6.97	0.052	7.79	0.365	3.83	0.068	6.85	0.058	5.29	0.206
Pr	1.36	0.042	1.40	0.077	0.66	0.010	1.19	0.036	0.92	0.049
Nd	7.85	0.223	9.48	0.088	4.09	0.030	6.91	0.195	5.12	0.060
Sm	3.80	0.237	4.58	0.267	1.52	0.085	2.73	0.057	1.83	0.033
Eu	1.17	0.070	1.26	0.080	0.57	0.008	1.09	0.010	0.84	0.031
Gd	6.73	0.264	7.91	0.257	2.23	0.063	3.99	0.249	3.57	0.102
Tb	1.31	0.023	1.58	0.134	0.32	0.003	0.79	0.009	0.63	0.015
Dy	9.62	0.281	11.7	0.41	2.77	0.217	5.20	0.205	4.17	0.011
Er	6.65	0.086	9.02	0.140	1.66	0.015	3.64	0.110	2.58	0.172
Yb	6.65	0.007	8.76	0.128	1.83	0.045	3.13	0.093	2.16	0.294
Zr/Y	1.29		1.39		1.86		1.74		1.69	
Zr/Ba	5.42		6.61		4.28		4.19		3.74	
La/Sm	0.57		0.51		0.71		0.78		0.89	
La/Yb	0.32		0.27		0.59		0.68		0.76	
Tb/Yb	0.20		0.18		0.17		0.25		0.29	

Table 3 (continued)

	58D-2		58D-2		84D-4		84D-4		84D-4	
	MI#14		MI#15		MI#1		MI#2		MI#3	
	55		55		80		55		80	
	plag		plag		Ol		Ol		Ol	
Sr	67.2	0.30	61.4	1.44	94.0	5.58	78.7	6.79	96.5	0.15
Y	30.3	0.22	43.9	0.51	29.6	0.11	24.5	0.05	48.5	0.31
Zr	63.8	0.30	94.1	2.09	75.0	0.94	49.0	0.50	124	0.7
Ba	20.1	0.77	30.9	1.74	10.3	0.09	8.22	0.486	13.6	0.32
La	3.23	0.114	4.62	0.303	2.66	0.040	1.50	0.122	3.84	0.136
Ce	8.97	0.452	12.7	0.62	9.26	0.118	5.87	0.178	10.8	0.058
Pr	1.61	0.057	2.02	0.077	1.64	0.062	1.16	0.012	2.15	0.010
Nd	8.48	0.968	10.8	0.22	8.56	0.362	5.43	0.020	11.8	0.15
Sm	3.73	0.619	4.69	0.168	3.20	0.280	1.80	0.099	4.20	0.093
Eu	1.02	0.086	1.36	0.095	1.24	0.023	0.82	0.068	1.53	0.033
Gd	4.78	0.247	7.46	0.330	4.39	0.222	3.00	0.354	6.11	0.420
Tb	0.90	0.011	1.34	0.113	0.78	0.035	0.53	0.052	1.12	0.034
Dy	6.35	0.407	8.30	0.213	5.19	0.385	3.82	0.039	7.79	0.123
Er	4.05	0.326	5.39	0.350	3.29	0.244	2.80	0.463	4.74	0.158
Yb	3.74	0.180	4.47	0.159	2.72	0.144	2.68	0.305	4.68	0.246
Zr/Y	2.10		2.14		2.53		2.00		2.55	
Zr/Ba	3.18		3.05		7.31		5.97		9.07	
La/Sm	0.87		0.99		0.83		0.83		0.91	
La/Yb	0.86		1.03		0.98		0.56		0.82	
Tb/Yb	0.24		0.30		0.29		0.20		0.24	

Table 3 (continued)

	84D-4									
	MI#4		MI#5		MI#7		MI#8		MI#10	
	80		80		55		80		80	
	Ol		plag		plag		plag		plag	
Sr	102	14.5	88.3	0.68	73.4	10.71	81.8	2.87	83.6	1.36
Y	25.9	0.28	36.1	0.15	17.8	0.48	23.6	0.73	49.2	0.05
Zr	57.7	0.78	59.0	0.17	37.2	0.50	49.2	1.39	110	0.3
Ba	8.14	0.222	10.9	0.31	8.71	0.062	8.28	0.235	11.3	0.39
La	2.17	0.018	2.24	0.025	1.30	0.103	1.71	0.058	3.06	0.095
Ce	6.41	0.127	7.82	0.152	4.22	0.190	4.97	0.224	8.91	0.060
Pr	1.10	0.052	1.37	0.038	0.92	0.019	0.92	0.026	1.70	0.078
Nd	6.78	0.238	8.28	0.178	4.03	0.436	5.19	0.172	10.3	0.54
Sm	2.15	0.204	3.24	0.026	1.77	0.237	1.96	0.250	3.85	0.305
Eu	0.95	0.031	1.18	0.028	0.74	0.035	0.85	0.036	1.21	0.049
Gd	3.23	0.194	4.71	0.309	2.44	0.170	2.82	0.112	5.85	0.124
Tb	0.60	0.006	0.83	0.018	0.46	0.016	0.50	0.004	1.14	0.046
Dy	4.29	0.150	5.83	0.179	3.03	0.128	3.65	0.098	8.10	0.193
Er	2.97	0.040	3.72	0.171	1.64	0.013	2.50	0.061	5.10	0.224
Yb	2.65	0.030	3.58	0.113	1.71	0.095	2.21	0.182	4.97	0.060
Zr/Y	2.23		1.64		2.09		2.09		2.24	
Zr/Ba	7.09		5.43		4.27		5.94		9.72	
La/Sm	1.01		0.69		0.73		0.87		0.80	
La/Yb	0.82		0.62		0.76		0.77		0.62	
Tb/Yb	0.23		0.23		0.27		0.23		0.23	

Table 3 (continued)

	84D-4		88D-1		88D-1		88D-1		88D-1	
	MI#11		MI#1		MI#2		MI#3		MI#4	
	55		55		80		55		80	
	plag		Ol		plag		plag		Ol	
Sr	78.5	5.61	90.2	1.37	84.1	0.02	80.6	1.15	89.4	0.16
Y	55.4	1.05	31.6	0.40	11.0	0.95	19.3	1.50	40.4	1.86
Zr	114	1.0	65.4	3.61	23.6	2.17	40.5	3.61	80.6	2.98
Ba	13.1	0.69	7.07	0.133	4.07	0.001	6.14	0.559	10.6	0.078
La	3.52	0.084	1.95	0.091	0.89	0.028	1.35	0.084	2.86	0.073
Ce	9.98	0.180	5.78	0.403	2.48	0.179	4.21	0.320	8.77	0.050
Pr	1.92	0.008	1.08	0.079	0.46	0.048	0.82	0.139	1.57	0.002
Nd	11.1	0.60	5.37	0.774	2.68	0.282	4.40	0.296	8.75	0.200
Sm	3.76	0.002	2.34	0.624	0.96	0.008	1.37	0.123	3.15	0.012
Eu	1.24	0.026	0.99	0.165	0.50	0.020	0.57	0.025	1.26	0.028
Gd	5.91	0.489	4.11	0.380	1.46	0.079	2.27	0.021	4.85	0.062
Tb	1.25	0.020	0.84	0.170	0.28	0.002	0.54	0.049	0.96	0.033
Dy	8.35	0.084	4.65	0.560	2.07	0.021	3.19	0.252	6.47	0.350
Er	5.95	0.139	3.55	0.343	1.32	0.081	2.09	0.115	4.32	0.313
Yb	6.15	0.248	3.45	0.528	1.16	0.191	2.04	0.246	4.22	0.050
Zr/Y	2.05		2.07		2.14		2.09		1.99	
Zr/Ba	8.68		9.25		5.79		6.59		7.59	
La/Sm	0.94		0.83		0.93		0.98		0.91	
La/Yb	0.57		0.57		0.77		0.66		0.68	
Tb/Yb	0.20		0.24		0.24		0.27		0.23	

Table 3 (continued)

	88D-1									
	MI#5		MI#6		MI#7		MI#8		MI#9	
	80		55		55		80		55	
	Ol		Ol		Ol		plag		plag	
Sr	88.3	0.15	96.6	0.30	88.1	1.05	69.1	0.63	69.1	0.87
Y	41.8	1.58	37.0	0.42	23.7	0.31	21.3	0.22	24.2	0.08
Zr	87.3	4.11	82.8	0.72	45.5	1.24	42.8	0.84	47.5	1.00
Ba	11.8	0.215	7.19	0.113	5.55	0.213	9.22	0.076	8.69	0.125
La	3.03	0.051	2.59	0.112	1.36	0.084	1.70	0.055	1.77	0.029
Ce	9.37	0.221	7.95	0.170	6.28	0.282	5.99	0.093	5.62	0.124
Pr	1.77	0.075	1.49	0.047	0.96	0.098	1.02	0.005	0.94	0.053
Nd	9.90	0.469	8.72	0.361	5.92	0.045	5.81	0.204	5.22	0.183
Sm	3.30	0.197	3.08	0.041	2.30	0.453	1.92	0.051	1.56	0.078
Eu	1.32	0.034	1.36	0.197	0.77	0.072	0.83	0.059	0.76	0.101
Gd	5.61	0.283	5.27	0.390	2.95	0.251	2.69	0.170	3.12	0.164
Tb	1.04	0.073	0.86	0.104	0.52	0.038	0.50	0.010	0.55	0.032
Dy	6.48	0.073	6.11	0.302	3.88	0.142	3.50	0.073	3.69	0.145
Er	4.35	0.227	3.62	0.260	2.88	0.218	2.35	0.071	2.34	0.060
Yb	4.36	0.157	3.48	0.073	2.94	0.280	2.09	0.127	2.49	0.125
Zr/Y	2.09		2.24		1.92		2.01		1.96	
Zr/Ba	7.39		11.53		8.20		4.65		5.47	
La/Sm	0.92		0.84		0.59		0.88		1.14	
La/Yb	0.70		0.74		0.46		0.81		0.71	
Tb/Yb	0.24		0.25		0.18		0.24		0.22	

Table 4- Parameters used in forward melt models

Modal abundances								
	olivine	orthopyroxene	clinopyroxene	spinel	garnet			
spinel lherzolite	0.5	0.3	0.15	0.05	0			
garnet lherzolite	0.5	0.3	0.12	0	0.08			
Partition coefficients -spinel lherzolite								
Element	ol/liq	opx/liq	cpx/liq	sp/liq	Bulk D (sp)	P (sp)	Source	F=9%
La	0.0005	0.0031	0.03	0	0.0056	0.0188	0.234	2.60
Ce	0.0005	0.004	0.08	<i>0.0005</i>	0.0133	0.0490	0.772	8.58
Sr	0.00004	0.0007	0.091	0	0.0137	0.0545	9.8	109
Nd	0.00042	0.012	0.088	<i>0.0008</i>	0.0168	0.0561	0.713	7.91
Zr	0.00131	0.021	0.18575	<i>0.05</i>	0.0371	0.1198	7.94	83.2
Sm	0.0011	0.02	0.299	<i>0.0009</i>	0.0508	0.1844	0.27	2.65
Eu	0.00805	0.053	0.3245	<i>0.0009</i>	0.0678	0.2098	0.107	0.94
Ti	0.015	0.086	0.35	<i>0.1</i>	0.0903	0.2406	798	6030
Gd	0.0011	0.065	0.35	0	0.0716	0.2282	0.395	3.39
Tb	0.0019	0.038	0.375	<i>0.00075</i>	0.0678	0.2351	0.075	0.66
Dy	0.0027	0.011	0.4	<i>0.0015</i>	0.0639	0.2420	0.531	4.85
Ho	0.00785	0.028	0.41	<i>0.00225</i>	0.0731	0.2534	0.122	1.05
Er	0.013	0.045	0.42	<i>0.003</i>	0.0822	0.2647	0.371	2.99
Yb	0.02	0.08	0.45	<i>0.0045</i>	0.1006	0.2935	0.401	2.88
Partition coefficients -garnet lherzolite								
Element	ol/liq	opx/liq	cpx/liq	gar/liq	Bulk D (gar)	P (gar)	Source	F=1.7%
La	0.0005	0.004	0.015	0.0007	0.0033	0.0060	0.234	13.7
Ce	0.0005	0.004	0.038	0.017	0.0074	0.0200	0.772	41.1
Sr	0.00004	0.0007	0.091	0.0007	0.0110	0.0315	9.8	458
Nd	0.00042	0.012	0.0884	0.064	0.0198	0.0559	0.713	24.6
Zr	0.00076	0.018	0.1142	0.232	0.0394	0.1283	7.94	167
Sm	0.0011	0.02	0.1509	0.23	0.0443	0.1404	0.27	5.17
Eu	0.00805	0.053	0.14545	0.415	0.0730	0.2133	0.107	1.34
Ti	0.015	0.086	0.14	0.6	0.1017	0.2863	798	7390
Gd	0.0011	0.065	0.16	1.2	0.1433	0.5117	0.395	2.68
Tb	0.0019	0.065	0.165	1.2	0.1443	0.5135	0.075	0.51
Dy	0.0027	0.065	0.17	2	0.2150	0.8136	0.531	2.45
Ho	0.00785	0.065	0.175	2.5	0.2618	1.0024	0.122	0.47
Er	0.013	0.065	0.18	3	0.3085	1.1913	0.371	1.21
Yb	0.02	0.08	0.25	5.5	0.5427	2.1504	0.401	0.75

Partition coefficients are from Salters and Stracke (2004), 2.0 GPa for spinel lherzolite assemblage and 3.0 GPa for garnet lherzolite assemblage. Values in italics are from Johnson et al. (1990). F=9% and F=1.7% are calculated melt compositions for at the listed % of melting for spinel lherzolite and garnet lherzolite, respectively. P is the non-modal melt factor.

Chapter 5:
General Conclusions

Chris J. Russo

5.1 Summary

This thesis presents a detailed look at the crustal accretionary process along intermediate spreading ridges using a variety of geochemical techniques to investigate how this process varies temporally and geographically. Specifically, the projects in this thesis addressed how crustal accretion in these systems varied in response to 1) ocean basin growth, 2) regional mantle temperature gradients in a passive environment and 3) the presence of additional thermal and material input. In addition, as a result of the previous isotopic characterization of these regions, collectively these studies have allowed for the investigation of the role mantle heterogeneity plays in the melting process.

In Chapter 2, major and trace element analyses were used as a tool to infer relative differences between melting during the period from 28 to 14 Ma near the modern day eastern boundary of the Australian-Antarctic Discordance (AAD). The AAD is today, and has been since at least ~ 28 Ma, the location of an isotopic boundary between 'Pacific-type' and 'Indian-type' mantle (Christie et al., 2004). In the modern day AAD the boundary between Pacific and Indian mantle types coincides with an abrupt change in axial morphology, a relationship that naturally questions the role source heterogeneity (as defined by the isotopic variability) plays in creating this abrupt morphologic change. The major and trace element results presented in Chapter 2 are consistent with lavas erupted across the region, during the period from 28 to 14 Ma, having been derived by higher degrees of melting originating from greater depths. This change in major and trace element composition is observed despite equivalent isotopic variability during the 28 to 14 Ma period compared to the modern AAD. This observation argues against mantle heterogeneity driving the abrupt morphologic change coincident with the isotopic boundary in the modern AAD. Alternatively, the larger degrees of melting from greater mean depths are interpreted to have resulted

from enhanced upwelling and mantle melting driven by the closer proximity of the thick continental keel to the ridge axis during earlier times.

Chapter 3 presents, U-series disequilibria results for 16 MORB glasses from the SEIR. These measurements greatly expand the amount of existing data from this region (previously only 2 other samples had been analyzed, Bourdon et al., 1996a). These data span a range in $(^{230}\text{Th}/^{232}\text{Th})$ versus $(^{238}\text{U}/^{232}\text{Th})$ space equivalent to ~70% of the entire observed global range, supporting the use of the SEIR as a regional scale analog to the global mid-ocean ridge system. Despite the large range in and excellent correlation ($R^2=0.91$) between $(^{230}\text{Th}/^{232}\text{Th})$ and $(^{238}\text{U}/^{232}\text{Th})$ a simple along-axis relationship between $(^{230}\text{Th}/^{238}\text{U})$ and axial depth is not observed, as would be expected in terms of the ‘global’ trend suggested by Bourdon et al. (1996a). Significant insight into the melting process is gained by combining the U-series results with detailed bathymetric data from the region, and these results are consistent the shallowest axial lavas being produced in an environment with higher mantle porosity, possibly accompanied by higher melting rates. These results are also consistent with the intermediate and deep axial lavas generally following the relationship predicted by the Bourdon et al. (1996) model. Combined these two approaches (regional characterization and morphological characterization) to evaluating U-series data are consistent with transitions in morphology along intermediate spreading rate ridges being very sensitive to small changes in mantle temperature, upwelling rate, and residual porosity. This response occurs over short spatial scales and in a threshold fashion, consistent with geophysical observations along intermediate spreading rate ridges (Chen, 1996, 2000; Baran et al., 2005). Additionally, measured $^{232}\text{Th}/^{238}\text{U}$ (κ) values converge with $^{232}\text{Th}/^{238}\text{U}$ values inferred from Pb isotopes (κ_{pb}). This observation suggests a recent introduction of an old mantle heterogeneity that has experienced less Th and U fractionation throughout its history compared to the depleted upper mantle.

In Chapter 4, trace element concentrations in melt inclusions are reported for a suite of lavas erupted along the western Galapagos Spreading Center (GSC). These data show greater chemical diversity compared to their host basalt glasses, while the average melt inclusion compositions generally resemble those of their respective host basalt. This result supports melt inclusions representing small isolated ‘batches’ of melt that have not yet been mixed and homogenized, a process not directly resolvable through analysis of host basalt glasses. Melt inclusions from NMORB host lavas were found to be less diverse than those from EMORB and TMORB compositions. TMORB compositions are generated by mixing of melts from different ‘end-member’ processes which dominate in the generation of EMORB and NMORB melt production. Rare earth element (REE) modeling indicates NMORB compositions can be generated by ~9% aggregated non-modal fractional melting generated entirely in the spinel lherzolite stability field. EMORB compositions are most consistent with smaller degrees of melting (~2%) generated in both the spinel lherzolite and garnet lherzolite stability fields that are subsequently mixed. These models suggest that in the case of EMORB generation as much as 50% of the melt production may occur in the garnet stability field. These results provide an initial framework from which more detailed models that consider additional variables such as dynamic upwelling and isotopic compositions can be based.

Collectively, the results presented in this thesis demonstrate that the geochemical signatures of MORB erupted along intermediate spreading rate ridges, like axial morphology, are highly sensitive to, and reflect systematically, slight variations in the melt generation process. The results of this study further substantiate that mantle heterogeneity, while of fundamental importance, is not solely responsible for the geochemical and morphologic variations observed along intermediate rate spreading ridges. Rather, the geochemical and morphologic variations along intermediate rate spreading ridges can only be accurately characterized through a

complete and integrated consideration of geophysical, geochemical and geological observations.

Bibliography

- Albarede, F.; 1998, Time-dependent models of U-Th-He and K-Ar evolution and the layering of mantle convection, *Chemical Geology*, 145, pp. 413-429.
- Albarede, F., R.D. van der Hilst; 2002, Zoned mantle convection, *Philosophical Transactions of the Royal Society*, 360, pp. 2569-2592.
- Allegre, C.J., D.L. Turcotte; 1986, Implications of a two-component marble-cake mantle, *Nature*, 323, pp. 123-127.
- Allegre, C.J., M. Condomines; 1982, Basalt genesis and mantle structure studied through Th isotopic geochemistry, *Nature*, 299, no. 5878, pp. 21-24.
- Allegre, C.J.; 2002, The evolution of mantle mixing, *Philosophical Transaction of the Royal Society of London*, 360, pp. 2411-2431.
- Allegre, C.J., E. Lewin; 1995, Isotopic systems and stirring times of the Earth's mantle, *Earth and Planetary Science Letters*, 136, pp. 629-646.
- Arndt, N.T., S.L. Goldstein; 1989, An open boundary between lower continental crust and mantle: its role in crust formation and crustal recycling, *Tectonophysics*, 161, pp. 201-212.
- Asmerom, Y.; 1999, Th-U fractionation and mantle structure, *Earth and Planetary Science Letters*, 166, pp. 163-175.
- Baran, J.M., J.R. Cochran, S.M. Carbotte, M.R. Nedimovic; 2005, Variations in upper crustal structure due to variable mantle temperature along the Southeast Indian Ridge, *Geochemistry, Geophysics, Geosystems*, 6, no. 11, Q11002, doi:10.1029/2005GC000943.
- Beattie, P.; 1993, Uranium-thorium disequilibria and partitioning on melting of garnet peridotite, *Nature*, 363, pp. 63-65.
- Ben Othman, D., C.J. Allegre; 1990, U-Th isotopic systematics at 13°N east Pacific Ridge segment, *Earth and Planetary Science Letters*, 98, pp. 129-137.
- Bourdon, B., A. Zindler, T. Elliott, C.H. Langmuir; 1996a, Constraints on mantle melting at mid-ocean ridges from global ^{238}U - ^{230}Th disequilibrium data, *Nature*, 384, pp. 231-235.
- Bourdon, B., C.H. Langmuir, A. Zindler; 1996b, Ridge-hotspot interaction along the Mid-Atlantic Ridge between 37°30' and 40°30'N: the U-Th disequilibrium evidence, *Earth and Planetary Science Letters*, 142, pp. 175-189.

- Bourdon, B., N.M. Ribe, A. Stracke, A.E. Saal, S.P. Turner; 2006, Insights into the dynamics of mantle plumes from uranium-series geochemistry, *Nature*, 444, pp. 713-717.
- Burnard, P., D. Graham, K. Farley; 2004 Fractionation of noble gases (He, Ar) during MORB mantle melting: a case study on the Southeast Indian Ridge, *Earth and Planetary Science Letters*.
- Canales, J.P., Ito, G., Detrick, R.S., Sinton, J.; 2002, Crustal thickness along the western Galapagos Spreading Center and the compensation of The Galapagos hotspot, *Earth and Planetary Science Letters*, 203, pp. 311-327.
- Cande, S.C., J.C. Mutter; 1982, A revised identification of the oldest seafloor spreading anomalies between Australia and Antarctica, *Earth and Planetary Science Letters*, 58, pp. 151-160.
- Carbotte, S.M., C. Small, and K. Donnelly; 2004, The influence of ridge migration on the magmatic segmentation of mid-ocean ridges, *Nature*, 429, pp. 743-746.
- Chabaux, F., C.J. Allegre; 1994, ^{238}U - ^{230}Th - ^{226}Ra disequilibria in volcanics: A new insight into melting conditions, *Earth and Planetary Science Letters*, 126, pp. 61-74.
- Chase, C.G.; 1981, Oceanic Island Pb: Two-Stage Histories and Mantle Evolution, *Earth and Planetary Science Letters*, 52, pp. 277-284.
- Chen, Y.J.; 2000, Dependence of crustal accretion and ridge-axis topography on spreading rate, mantle temperature, and hydrothermal cooling, in Dilek, U., Moores, E.M., Elthon, D., and Nicoloas, A., eds., *Ophiolites and Oceanic Crust: New Insights from Field Studies and the Ocean Drilling Program: Boulder, Colorado, Geological Society of America Special Paper 349*, pp. 161-179.
- Chen, Y.J.; 1996, Dynamics of the Mid-ocean Ridge Plate Boundary: Recent Observations and Theory, *PAGEOPH*, 146, no. 3/4, pp. 621-648.
- Christie, D.M. and Sinton, J.M.; 1986, Major element constraints on melting, differentiation and mixing of magmas from the Galapagos 95°5W propagating rift system, *Contributions to Mineralogy and Petrology*, 94, pp. 274-288.
- Christie, D.M., Pyle, D.G., Pedersen, R.B., Miller, D.J.; 2004, Leg 187 synthesis: evolution of the Australian Antarctic Discordance, the Australian Antarctic Depth anomaly, and the Indian/Pacific mantle isotopic boundary, In Pedersen, R.B., Christie, D.M., Miller, D.J., (eds.), *Proceedings of the Ocean Drilling Program, Scientific Results, 187*, pp. 1-41.
- Christie, D.M., West, B.P., Pyle, D.G. and Hanan, B.B.; 1998, Chaotic topography, mantle flow and mantle migration in the Australian-Antarctic discordance, *Nature*, 394, pp. 637-644.

- Cochran, J.R., Sempere, J-C, SEIR Scientific Team; 1997, The Southeast Indian Ridge between 88°E and 118°E: Gravity anomalies and crustal accretion at intermediate spreading rates, *Journal of Geophysical Research*, 102, pp. 15,463-15,487.
- Condomines, C., O. Sigmarsson; 2000, ^{238}U - ^{230}Th disequilibria and mantle melting processes: a discussion, *Chemical Geology*, 162, pp. 95-104.
- Condomines, M., Ch. Hemond, C.J. Allegre; 1988, U-Th-Ra radioactive disequilibria and magmatic processes, *Earth and Planetary Science Letters*, 90, pp. 243-262.
- Condomines, M., P. Morand, C.J. Allegre; 1981, ^{230}Th - ^{238}U radioactive disequilibria in tholeiites from the FAMOUS zone (Mid-Atlantic Ridge, 36°50'N): Th and Sr isotopic geochemistry, *Earth and Planetary Science Letters*, 55, pp. 247-256.
- Constantin, M., R. Hekinian, D. Bideau, R. Hebert; 1996, Construction of the oceanic lithosphere by magmatic intrusions: Petrological evidence from plutonic rocks formed along the fast-spreading East Pacific Rise, *Geology*, 24, no. 8, pp. 731-734.
- Cooper, K.M., S.J. Goldstein, K.W.W. Sims, M.T. Murrell; 2003, Uranium-series chronology of Gorda Ridge volcanism: new evidence from the 1996 eruption, *Earth and Planetary Science Letters*, 206, pp. 459-475.
- Cushman, B., Sinton, J., Ito, G., Dixon, J.E.; 2004, Glass compositions, plume-ridge interaction, and hydrous melting along the Galapagos Spreading Center, 90.5°W to 98°W, *Geochemistry, Geophysics, Geosystems*, 5, doi:10.1029/2004GC000709.
- Detrick, R.S., Sinton, J.M., Ito, G., Canales, J.P., Behn, M., Blacic, T., Cushman, B., Dixon, J.E., Graham, D.W., Mahoney, J.J.; 2002, Correlated geophysical, geochemical, and volcanological manifestations of plume-ridge interaction along the Galapagos Spreading Center, *Geochemistry, Geophysics, Geosystems*, 3, doi:10.1029/2002GC000350.
- Donnelly, K.E., S.L. Goldstein, C.H. Langmuir, M. Spiegelman; 2004, Origin of enriched ocean ridge basalts and implications for mantle dynamics, *Earth and Planetary Science Letters*, 226, pp. 347-366
- Dosso, L., H. Bougault, C. Langmuir, C. Bollinger, O. Bonnier, J. Etoubleau; 1999, The age and distribution of mantle heterogeneity along the Mid-Atlantic Ridge (31-41°N), *Earth and Planetary Science Letters*, 170, pp. 269-286.
- Douglas-Priebe, L.M.; 1998 Geochemical and petrogenetic effects of the interaction of the Southeast Indian Ridge and the Amsterdam-St.Paul hotspot, M.S. thesis, Oregon State University, Corvallis.

- Dupre, B., C.J. Allègre; 1983 Pb-Sr isotope variation in Indian Ocean basalts and mixing phenomena; *Nature*, 303, pp. 142-146.
- Elliott, T., Zindler, A., Bourdon, B.; 1999, Exploring the kappa conundrum: the role of recycling in the lead isotope evolution of the mantle, *Earth and Planetary Science Letters*, 169, pp. 129-145.
- Elliott, T.; 1997, Fractionation of U and Th during mantle melting: a reprise, *Chemical Geology*, 139, pp. 165-183.
- Elthon, D., D.K. Ross, J.K. Meen; 1995, Compositional variations of basaltic glasses from the Mid-Cayman Rise spreading center; *Journal of Geophysical Research*, 100, pp. 12,497-12,512.
- Freighner, M.A., and M.A. Richards; 1994, Lithospheric structure and compensation mechanisms of the Galapagos Archipelago, *Journal of Geophysical Research*, 99, pp. 6711-6729.
- Fisk, M.R., A.E. Bence, J.G. Schilling; 1982, Major element chemistry of Galapagos Rift Zone magmas and their phenocrysts, *Earth and Planetary Science Letters*, 61, pp. 171-189.
- Forsyth, D.W., R.L. Ehrenbard, S. Chapin; 1987, Anomalous upper mantle beneath the Australian-Antarctic Discordance; *Earth and Planetary Science Letters*, 84, pp.471-478.
- Fretzdorff, S., K.M. Haase, P.T. Leat, R.A. Livermore, C.-D. Garbe-Schonberg, J. Fietzke, P. Stoffers; 2003, ^{230}Th - ^{238}U disequilibrium in East Scotia backarc basalts: Implications for slab contributions, *Geology*, 31, no. 8, pp. 693-696.
- Fretzdorff, S., R.A. Livermore, C.W. Devey, P.T. Leat, P. Stoffers; 2002 Petrogenesis of the Back-arc East Scotia Ridge, South Atlantic Ocean; *Journal of Petrology*, 43, pp. 1435-1467.
- Galer, S.J.G., R.K. O'Nions; 1986, Magmagenesis and the mapping of chemical and isotopic variations in the mantle, *Chemical Geology*, 56, pp. 45-61.
- Galer, S.J.G., R.K. O'Nions; 1985, Residence time of thorium, uranium and lead in the mantle with implications for mantle convection, *Nature*, 316, no. 6031, pp. 778-782.
- Galer, S.J.G., S.L. Goldstein; Early mantle differentiation and its thermal consequences, *Geochimica et Cosmochimica Acta*, 55, pp. 227-239.

- Gast, P.W.; 1969, The Isotopic Composition of Lead from St. Helena and Ascension Islands, *Earth and Planetary Science Letters*, 5, pp. 353-359.
- Geli, L.; accepted 2007, The thermal regime of the South-East Indian Ridge between 88°E and 140°E: Remarks on the Subsidence of the Ridge Flanks, *Journal of Geophysical research*, 2006JB004578R.
- Gill, J., M. Condomines; 1992, Short-Lived Radioactivity and Magma Genesis; *Science*, 257, pp. 1368-1376.
- Goff, J.A., Y. Ma, A. Shah, J.R. Cochran, J.-C. Sempere; 1997, Stochastic analysis of seafloor morphology on the flank of the Southeast Indian Ridge: the influence of ridge morphology on the formation of abyssal hills, *Journal of Geophysical Research*, 102, B7, pp. 15,521-15,534.
- Goldstein, S.J., M.T. Murrell, D.R. Janecky, J.R. Delaney, D.A. Calgue; 1992, Geochronology and petrogenesis of MORB from the Juan de Fuca and Gorda ridges by ^{238}U - ^{230}Th disequilibrium, *Earth and Planetary Science Letters*, 109, pp. 255-272.
- Graham, D.W., D.M. Christie, K.S. Harpp, J.E. Lupton; 1993, Mantle Plume Helium in Submarine Basalts from the Galapagos Platform, *Science*, 262, no. 5142, pp. 2023-2026.
- Graham, D.W., J. Blichert-Toft, C.J. Russo, K.H. Rubin, F. Albarede; 2006, Cryptic striations in the upper mantle revealed by hafnium isotopes in southeast Indian ridge basalts, *Nature*, 440, no. 9, pp. 199-202.
- Graham, D.W., J.E. Lupton, F.J. Spera, D.M. Christie; Upper-mantle dynamics revealed by helium isotope variations along the southeast Indian ridge, *Nature*, 409, 2001, pp. 701-703.
- Graham, D.W., K.T.M. Johnson, L. Douglas-Priebe, J.E. Lupton; 1999, Hotspot-ridge interaction along the Southeast Indian Ridge near Amsterdam and St. Paul islands: helium isotope evidence, *Earth and Planetary Science Letters*, 167, pp. 297-310.
- Gurnis, M., R.D. Müller, L. Moresi; 1998, Cretaceous vertical motion of Australia and the Australian-Antarctic Discordance; *Science*, 279, pp. 1499-1504.
- Gurnis, M., R.D., Müller; 2003, Origin of the Australian-Antarctic Discordance from an ancient slab and mantle wedge; In Hills, R.R. and Müller, R.D. (Eds.), *Evolution and Dynamics of the Australian Plate*, Special Paper of the Geological Society of America, 372, pp. 417-429.

- Hanan, B.B., Blichert-Toft, J., Pyle, D.G., Christie, D.M.; 2004, Contrasting origins of the upper mantle revealed by hafnium and lead isotopes from the Southeast Indian Ridge, *Nature*, 432, pp. 91-94.
- Hanson, G.N.; 1977, Geochemical evolution of the suboceanic mantle, *Journal of the Geological Society of London*, 134, pp. 2365-253.
- Harpp K.S., W.M. White; Tracing a mantle plume: Isotopic and trace element variations of Galapagos seamounts, *Geochemistry, Geophysics, Geosystems*, 2, 2001.
- Harpp, K.S., and D. Geist; 2002, Wolf-Darwin lineament and plume-ridge interaction in northern Galapagos, *Geochemistry, Geophysics, Geosystems*, 3, doi:10.10292000GC000370.
- Harpp, K.S., K.R. Wirth and D.J. Korich, 2003, Northern Galapagos Province: Hotspot induced, near ridge volcanism at Genovesa Island, *Geology*, 30, pp. 399-402.
- Hart, S.R.; 1984, A large-scale isotope anomaly in the Southern Hemisphere mantle, *Nature*, 309, pp. 753-757.
- Hekinian, R., G. Thompson, G. Bideau; 1989, Axial and Off-Axial Heterogeneity of Basaltic Rocks From the East Pacific Rise at 12°35'N-12°51'N and 11°26'N-11°30'N, *Journal of Geophysical Research*, 94, no. B12, pp. 17,437-17,463.
- Hey, R.N., J.M. Sinton, M.C. Kleinrock, R.N. Yonover, K.C. Macdonald, S.P. Miller, R.C. Searle, D.M. Christie, T.M. Atwater, N.H. Sleep, H.P. Johnson, C.A. Neal; 1992, ALVIN Investigation of an Active Propagating Rift System, Galapagos, 95.5°W, *Marine Geophysical Research*, 14, pp. 207-226.
- Hey, R.N., Sinton, J.M., F.K. Duennebieer; 1989, Propagating rifts and spreading centers, in Winterer, E.L., Hussong, D.M. and Decker, R.W. eds, *The Eastern Pacific Ocean and Hawaii*: Boulder, CO, Geological Society of America.
- Hirschmann, M.M., E.M. Stolper; 1996, A possible role for garnet pyroxenite in the origin of the 'garnet signature' in MORB, *Contributions to Mineralogy and Petrology*, 124, pp. 185-208.
- Hofmann, A.W.; 1988, Chemical differentiation of the Earth: the relationship between mantle continental crust and oceanic crust, *Earth and Planetary Science Letters*, 90, pp. 297-314.
- Hofmann, A.W.; 1997, Mantle geochemistry: the message from oceanic volcanism, *Nature*, 385, pp. 219-229.

- Hofmann, A.W.; 2003, Sampling Mantle Heterogeneity through Oceanic Basalts: Isotopes and Trace Elements, *Treatise On Geochemistry*, 2, pp. 61-101.
- Ito, G., J. Lin, C.W. Gable; 1997, Interaction of mantle plumes and migrating mid-ocean ridges: Implications for the Galapagos plume-ridge system, *Journal of Geophysical Research*, 102, no. B7, pp. 15,403-15,417.
- Ito, G.T., J. Lin; 1995, Mantle temperature anomalies along the present and paleoaxes of the Galapagos spreading center as inferred from gravity analyses, *Journal of Geophysical Research*, 100, no. B3, pp. 3733-3745.
- Janney, P.E., A.P. Le Roex, R.W. Carlson; 2005, Hafnium Isotope and Trace Element Constraints on the Nature of Mantle Heterogeneity beneath the Central Southwest Indian Ridge (13°E to 47°E), *Journal of Petrology*, 46, no. 12, pp. 2427-2464.
- Johnson, K.T.M., H.J.B. Dick, N. Shimizu; 1990 Melting in the oceanic upper mantle: an ion microprobe study of diopsides in abyssal peridotites, *Journal of Geophysical Research*, 95, pp. 2661-2678.
- Kelemen, P.B., G. Hirth, N. Shimizu, M. Spiegelman, H.J.B. Dick; 1997, A review of melt migration processes in the adiabatically upwelling mantle beneath oceanic spreading ridges, *Philosophical Transactions of the Royal Society of London*, 355, pp. 283-318.
- Kempton, P.D., Pierce, J.A., Barry, T.L., Langmuir, C.H., Christie, D.M.; 2002 Sr-Nd-Pb-Hf isotope results from ODP Leg 187: Evidence for mantle dynamics of the Australian-Antarctic discordance and origin of the Indian MORB source, *Geochemistry, Geophysics, Geosystems*, 3.
- Kigoshi, K.; 1967, Ionium dating of igneous rocks, *Science*, 156, pp. 932-934.
- Klein, E.M., and Langmuir, C.H.; 1987, Global Correlations of Ocean Ridge Basalt Chemistry with Axial Depth and Crustal Thickness, *Journal of Geophysical Research*, 92, pp. 8089-8115.
- Klein, E.M., C.H. Langmuir, A. Zindler, H. Staudigel, B. Hamelin; 1988, Isotope evidence of a mantle convection boundary at the Australian-Antarctic Discordance, *Nature*, 333, pp. 623-629.
- Klein, E.M., C.H. Langmuir; 1989 Local Versus Global Variations in Ocean Ridge Basalt Composition: A Reply; *Journal of Geophysical Research*, 94, pp. 4241-4252.
- Kokfelt, T.F., C. Lundstrom, K. Hoernle, F. Hauff, R. Werner; 2005, Plume-ridge interaction studied at the Galapagos spreading center: Evidence from ^{226}Ra - ^{230}Th - ^{238}U and ^{231}Pa - ^{235}U isotopic disequilibria, *Earth and Planetary Science Letters*, 234, pp. 165-187.

- Kurz, M.D., D.J. Geist; 1999, Dynamics of the Galapagos hotspot from helium isotope geochemistry, *Geochimica Cosmochimica Acta*, 63, pp. 4139-4156.
- Landwehr, D., J. Blundy, E.M. Chamorro-Perez, E. Hill, B. Wood; 2001, U-series disequilibria generated by partial melting of spinel lherzolite, *Earth and Planetary Science Letters*, 188, pp. 329-348.
- Langmuir, C.H. and Bender, A.E.; 1984, The geochemistry of oceanic basalts in the vicinity of transform faults: Observations and implications, *Earth and Planetary Science Letters*, 69, 107-127.
- Langmuir, C.H. and others; 1977, Petrogenesis of basalts from the FAMOUS area: Mid-Atlantic Ridge, *Earth and Planetary Science Letters*, 36, pp. 133-156.
- Langmuir, C.H., Klein, E.M., Plank, T., 1992, Petrology systematics of mid-ocean ridge basalts: constraints on melt generation beneath ocean ridges, In: Phipps Morgan, J., Blackman, D.K., Sinton, J.M., (eds.) *Mantle Flow and Melt Generation at Mid-Ocean Ridges*, Geophysical Monograph, American Geophysical Union, 71, pp. 183-280.
- LaTourrette, T.Z.; Kennedy, A.K.; Wasserburg, G.J., 1993, Thorium-Uranium Fractionation by Garnet: Evidence for a Deep Source and Rapid Rise of Oceanic Basalts, *Science*, 261, pp. 739-742.
- Lin, S.-C., L.-Y. Chiao, B.-Y. Kuo; 2002, Dynamic interaction of cold anomalies with the mid-ocean ridge flow field and its implications for the Australian-Antarctic Discordance; *Earth and Planetary Science Letters*, 203, pp. 925-935.
- Lundstrom, C.C., J. Gill, Q. Williams, B.B. Hanan; 1998b, Investigating solid mantle upwelling beneath mid-ocean ridges using U-series disequilibria. II. A local study at 33°S Mid-Atlantic Ridge, *Earth and Planetary Science Letters*, 157, pp. 167-181.
- Lundstrom, C.C., J. Gill, Q. Williams, M.R. Perfit; 1995, Mantle Melting and Basalt Extraction by Equilibrium Porous Flow, *Science*, 270, no. 5244, pp. 1958-1961.
- Lundstrom, C.C., J. Gill, Q. Williams; 2000, A geochemically consistent hypothesis for MORB generation, *Chemical Geology*, 162, pp. 105-126.
- Lundstrom, C.C., Q. Williams, J.B. Gill; 1998a, Investigating solid mantle upwelling rates beneath mid-ocean ridges using U-series disequilibria, 1: a global approach, *Earth and Planetary Science Letters*, 157, pp. 151-165.

- Ma, Y. and Cochran, J.R., 1996, Transitions in axial morphology along the Southeast Indian Ridge, *Journal of Geophysical Research*, 101, pp. 15,849-15,866.
- MacDougall, J.D., 1995, Using Short-lived U and Th Series Isotopes to Investigate Volcanic Processes, *Annual Reviews of Earth and Planetary Science Letters*, 23, pp. 143-167.
- Mahoney, J.J., J.H. Natland, W.M. White, R. Poreda, S.H. Bloomer, R.L. Fisher, A.N. Baxter; 1989, Isotopic and geochemical provinces of the western Indian Ocean spreading centers, *Journal of Geophysical Research*, 94, pp. 4033-4052.
- Mahoney, J.J., A.P. le Roex, Z. Peng, R.L. Fisher, J.H. Natland; 1992, Western limits of the Indian MORB mantle and the origin of low $^{206}\text{Pb}/^{204}\text{Pb}$ MORB: Isotope systematics of the central Southwest Indian Ridge (17°-50°E), *Journal of Geophysical Research*, 97, pp. 19,771-19,790.
- Mahoney, J.J., D.W. Graham, D.M. Christie, K.T.M. Johnson, L.S. Hall, D.L. Vonderhaar; 2002, Between a Hotspot and a Cold Spot: Isotopic Variation in the Southeast Indian Ridge Asthenosphere, 86°E-118°E, *Journal of Petrology*, 43, no. 7, pp. 1155-1176.
- Marks, K.M., J.M. Stock, K.J. Quinn; 1999, Evolution of the Australian-Antarctic discordance since Miocene time; *Journal of Geophysical Research*, 104, pp. 4967-4981.
- Marks, K.M., P.R. Vogt, S.A. Hall; 1990, Residual Depth Anomalies and the Origin of the Australian-Antarctic Discordance Zone; *Journal of Geophysical Research*, 95, pp. 17,325-17,337.
- McKenzie, D., and Bickle, M.J.; 1988, The volume and composition of melt generated by extension of the lithosphere; *Journal of Petrology*, 29, pp. 625-679.
- McKenzie, D.; 1985, ^{230}Th - ^{238}U disequilibrium and the melting processes beneath ridge axes, *Earth and Planetary Science Letters*, 72, pp. 149-157.
- McKenzie, D.; 2000, Constraints on melt generation and transport from U-series activity ratios, *Chemical Geology*, 162, pp. 81-94.
- Meyzen, C. M., J. N. Ludden, E. Humler, B. Luais, M. J. Toplis, C. Me´vel, and M. Storey; 2005, New insights into the origin and distribution of the DUPAL isotope anomaly in the Indian Ocean mantle from MORB of the Southwest Indian Ridge, *Geochem. Geophys. Geosyst.*, 6, Q11K11, doi:10.1029/2005GC000979.
- Meyzen, C.M., Toplis, M.J., Humler, E., Ludden, J.N., Mevel, C.; 2003, A discontinuity in mantle compositions beneath the southwest Indian ridge, *Nature*, 421, pp. 731-733.

- Michael, P.J. and Cornell, W.C.; 1998, Influences of spreading rate and magma supply on crystallization and assimilation beneath mid-ocean ridges: evidence from chlorine and major element chemistry of mid-ocean ridge basalts, *Journal of Geophysical Research*, 103, 18,325-18,356.
- Mukasa, S.B., Shervais, J.W., Wilshire, H.G., Nielson, J.E.; 1991, Intrinsic Nd, Pb, and Sr Isotopic Heterogeneities Exhibited by the Lherz Alpine Peridotite Massif, French Pyrenees, *Journal of Petrology*, Special Lherzolite Issue, pp. 117-134.
- Newman, S., R.C. Finkel, J.D. Macdougall; 1984, Comparison of ^{230}Th - ^{238}U disequilibrium systematics in lavas from three hot spot regions: Hawaii, Prince Edward and Samoa, *Geochimica et Cosmochimica Acta*, 48, pp. 315-324.
- Niu, Y. and Hekinian, R.; 1997, Spreading-rate dependence of the extent of mantle melting beneath ocean ridges, *Nature*, 385, pp. 326-329.
- O'Nions, R.K., D. McKenzie; 1993, Estimates of Mantle Thorium/Uranium Ratios from Th, U and Pb Isotope Abundances in Basaltic Melts, *Philosophical Transactions*, 342, no. 1663, Melting and Melt Movement in the Earth, pp. 65-77.
- O'Nions, R.K., D.P. McKenzie; 1988, Melting and continent generation, *Earth and Planetary Science Letters*, 90, pp. 449-456.
- O'Nions, R.K., Pankhurst, R.J., Gronvold, K.; 1976, Nature and development of basalt magma sources beneath Iceland and the Reykjanes Ridge, *Journal of Petrology*, 17, 315-338.
- Palmer, J., J.-C. Sempéré, D.M. Christie, J. Phipps-Morgan; 1993, Morphology and tectonics of the Australian-Antarctic Discordance between 123°E and 128°E, *Marine Geophysical Research*, 15, 121-151.
- Paul, D., W.M. White, D. Turcotte; 2002, Modelling the isotopic evolution of the Earth, *Philosophical Transactions of the Royal Society of London*, 360, pp. 2433-2474.
- Paul, D., W.M. White, D.L. Turcotte; 2003, Constraints on the $^{232}\text{Th}/^{238}\text{U}$ ratio (κ) of the continental crust, *Geochemistry Geophysics Geosystems*, 4, no. 12.
- Peate, D.W., C.J. Hawkesworth, P.W. van Calsteren, R.N. Taylor, B.J. Murton; 2001, ^{238}U - ^{230}Th constraints on mantle upwelling and plume-ridge interaction along the Reykjanes Ridge, *Earth and Planetary Science Letters*, 187, pp. 259-272.
- Peate, D.W., C.J. Hawkesworth; 2005, U-Series Disequilibria: Insights into Mantle Melting and the Timescales of Magma Differentiation, *Reviews of Geophysics*, 43, pp. 43.

- Pertermann, M., M.M. Hirschmann; 2003a, Partial melting experiments on a MORB-like pyroxenite between 2 and 3 GPa: Constraints on the presence of pyroxenite in basalt source regions from solidus location and melting rate, *Journal of Geophysical Research*, 108, no. B2, doi:10.1029/2000JB000118.
- Pertermann, M., M.M. Hirschmann; 2003b, Anhydrous Partial Melting Experiments on MORB-like Eclogite: Phase Relations, Phase Compositions and Mineral-Melt Partitioning of Major Elements at 2-3 GPa, *Journal of Petrology*, 44, no. 12, pp. 2173-2201.
- Pettke, T., W.E. Halter, J.D. Webster, M. Aigner-Torres, C.A. Heinrich; 2004, Accurate quantification of melt inclusion chemistry by LA-ICPMS: a comparison with EMP and SIMS and advantages and possible limitations of these methods, *Lithos*, 78, pp. 333-361.
- Phipps Morgan, J., Y.J. Chen; 1993, Dependence of ridge-axis morphology on magma supply and spreading rate, *Nature*, 364, pp. 706-708.
- Pietruszka, A.J., E.H. Hauri, R.W. Carlson, M.O. Garcia; 2006, Remelting of recently depleted mantle within the Hawaiian plume inferred from the ^{226}Ra - ^{230}Th - ^{238}U disequilibria of Pu'u 'O'o eruption lavas, *Earth and Planetary Science Letters*, 244, pp. 155-169.
- Pietruszka, A.J., K.H. Rubin, M.O. Garcia; 2001, ^{226}Ra - ^{230}Th - ^{238}U disequilibria of historical Kilauea lavas (1790-1982) and the dynamics of mantle melting within the Hawaiian plume, *Earth and Planetary Science Letters*, 186, pp. 15-31.
- Prinzhofer, A., E. Lewin, C.J. Allegre; 1989, Stochastic melting of the marble cake mantle: evidence from local study of the East Pacific Rise at 12°50'N, *Earth and Planetary Science Letters*, 92, pp. 189-206.
- Pyle, D.G., D.M. Christie, J.J. Mahoney, R.A. Duncan; 1995, Geochemistry and geochronology of ancient southeast Indian and southwest Pacific seafloor; *Journal of Geophysical Research*, 100, pp. 22,261-22,282.
- Pyle, D.G., D.M. Christie, J.J. Mahoney; Resolving an isotopic boundary within the Australian-Antarctic Discordance; *Earth and Planetary Science Letters*, 112, 1992, pp. 161-178.
- Pyle, D.G.; 1994, Geochemistry of mid-ocean-ridge basalt within and surrounding the Australian-Antarctic Discordance; Ph.D. dissertation, Oregon State University, Corvallis.

- Rehkamper, M., A.W. Hofmann; 1993, Recycled ocean crust and sediment in Indian Ocean MORB, *Earth and Planetary Science Letters*, 147, pp. 93-106.
- Reynolds, J.R., C.H. Langmuir; 1997, Petrological systematics of the Mid-Atlantic Ridge south of Kane: Implications for ocean crust formation; *Journal of Geophysical Research*, 102, pp. 14,915-14,946.
- Ritzwoller, M.H., N.M. Shapiro, G.M. Leahy; 2003, The Australian-Antarctic mantle anomaly as the principal cause of the Australian-Antarctic Discordance, *Journal of Geophysical Research*, 108, doi: 10.1029/2003JB002522.
- Royer, J.-Y., D.T. Sandwell; 1989, Evolution of the eastern Indian Ocean since the Late Cretaceous: Constraints from Geosat altimetry, *Journal of Geophysical Research*, 94, 13,755-13,782.
- Rubin, K.H., I. van der Zander, M.C. Smith, E.C. Bergmanis; 2005, Minimum speed limit for ocean ridge magmatism from ^{210}Pb - ^{226}Ra - ^{230}Th disequilibria, *Nature*, vol 437, no. 22, pp. 534-538.
- Rubin, K.H., J.D. Macdougall; 1992, Th-Sr isotopic relationships in MORB, *Earth and Planetary Science Letters*, 114, pp. 149-157.
- Rubin, K.H.; 2001, Analysis of $^{232}\text{Th}/^{230}\text{Th}$ in volcanic rocks: a comparison of thermal ionization mass spectrometry and other methodologies, *Chemical Geology*, 175, pp. 723-750.
- Saal, A.E., S.R. Hart, N. Shimizu, E.H. Hauri, G.D. Layne; 1998, Pb isotopic variability in melt inclusions from oceanic island basalts, Polynesia, *Science*, 282, pp. 1481-1484.
- Salters, V.J.M., A. Stracke; 2004, Composition of the depleted mantle, *Geochemistry, Geophysics, Geosystems*, 5, doi: 10.1029/2003GC000597.
- Salters, V.J.M., S.R. Hart; 1989, The hafnium paradox and the role of garnet in the source of mid-ocean-ridge basalts, *Nature*, 342, no. 6248, pp. 420-422.
- Salters, V.J.M.; 1996, The generation of mid-ocean ridge basalts from the Hf and Nd isotope perspective, *Earth and Planetary Science Letters*, 141, pp. 109-123.
- Schilling, J.-G.; 1973, Iceland mantle plume: geochemical evidence along Reykjanes Ridge, *Nature*, 242, pp. 565-571.
- Schilling, J.-G., R.N. Anderson, P. Vogt; 1976, Rare earth, Fe and Ti variations along the Galapagos Spreading Center and their relationship to the Galapagos Mantle Plume, *Nature*, 261, pp. 108-113.

- Schilling, J.-G., R.H. Kingsley, J.D. Devine; 1982, Galapagos Hot Spot-Spreading Center System 1. Spatial Petrological and Geochemical Variations (83°W-101°W), *Journal of Geophysical Research*, 87, pp. 5593-5610.
- Schilling, J.-G., C. Ruppel, A.N. Davis, B. McCully, S.A. Tighe, R.H. Kingsley, J. Lin; 1995, Thermal structure of the mantle beneath the equatorial Mid-Atlantic Ridge: Inferences from the spatial variation of dredged basalt glass compositions, *Journal of Geophysical Research*, 100, pp. 10,057-10,076.
- Schilling, J.-G., D. Fontignie, J. Blichert-Toft, R. Kingsley, U. Tomza; 2003, Pb-Hf-Nd-Sr isotope variations along the Galapagos Spreading Center (101°-83°W): Constraints on the dispersal of the Galapagos mantle plume, *Geochemistry, Geophysics, Geosystems*, 4, no. 10.
- Schouten, H., H.J.B. Dick, K.D. Klitgord; 1987, Migration of mid-ocean-ridge volcanic segments; *Nature*, 326, pp. 835-839.
- Sempéré, J.-C., B.P. West, L. Geli; 1996, The Southeast Indian Ridge between 127°E and 134°40'E: contrasts in segmentation characteristics and implication for crustal accretion, In C.J. Macleod, P.A. Tyler, C.L. Walker (Eds.), *Tectonic, Magmatic, Hydrothermal and Biological Segmentation of Mid-Ocean Ridges*, Geological Society Special Publication, 118, pp. 1-15.
- Sempéré, J.-C., J. Palmer, D.M. Christie, J. Phipps-Morgan, A.N. Shor; 1991, The Australian-Antarctic Discordance, *Geology*, 19, pp. 429-432.
- Shaw, D.M.; 1970, Trace element fractionation during anatexis, *Geochimica et Cosmochimica Acta*, 34, pp. 237-243.
- Sigmarsson, O., S. Carn, J.C. Carracedo; 1998, Systematics of U-series nuclides in primitive lavas from the 1730-36 eruption of Lanzarote, Canary Islands, and implications for the role of garnet pyroxenites during oceanic basalt formations, *Earth and Planetary Science Letters*, 162, pp. 137-151.
- Sims, K.W.W., D.J. DePaolo, M.T. Murrell, W.S. Baldrige, S.J. Goldstein, D.A. Clague; 1995, Mechanisms of Magma Generation Beneath Hawaii and Mid-Ocean Ridges: Uranium/Thorium and Samarium/Neodymium Isotopic Evidence, *Science*, 267, no. 5197, pp. 508-512.
- Sims, K.W.W., S.J. Goldstein, J., Blichert-Toft, M.R. Perfit, P. Kelemen, D.J. Fornari, P. Michael, M.T. Murrell, S.R. Hart, D.J. DePaolo, G. Layne, L. Ball, M. Jull, J. Bender; 2002, Chemical and isotopic constraints on the generation and transport of magma beneath the East Pacific Rise, *Geochimica et Cosmochimica Acta*, 66, no. 19, pp. 3481-3504.

- Sinton, C.W., D.M. Christie, V.L. Coombs, R.L. Nielsen, M.R. Fisk; 1993, Near-primary melt inclusions in anorthite phenocrysts from the Galapagos Platform, *Earth and Planetary Science Letters*, 119, no. 4, pp. 527-538.
- Sinton, J., R. Detrick, J.P. Canales, G. Ito, M. Behn; 2003, Morphology and segmentation of the western Galapagos Spreading Center, 90.5°-98°W: Plume-ridge interaction at an intermediate spreading ridge, *Geochemistry, Geophysics, Geosystems*, 4, doi:10.1029/2003GC000609.
- Small, C., J.R. Cochran, J.-C., Sempere, D. Christie; 1999, The structure and segmentation of the Southeast Indian Ridge, *Marine Geology*, 161, pp. 1-12.
- Sobolev, A.V.; 1996, Melt inclusions in minerals as a source of principle petrological information, *Petrology*, 4, pp. 209-220.
- Sobolev, A.V., N. Shimizu; 1993, Ultra-depleted primary melt included in an olivine from the Mid-Atlantic Ridge, *Nature*, 363, pp. 151-154.
- Stracke, A., A. Zindler, V.J.M. Salters, D. McKenzie, K. Gronvold; 2003, The dynamics of melting beneath Theistareykir, northern Iceland, *Geochemistry Geophysics Geosystems*, 4, no. 10, 8513, doi:10.1029/2002GC000347.
- Stracke, A., B. Bourdon, D. McKenzie; 2006, Melt extraction in Earth's mantle: Constraints from U-Th-Pa-Ra studies in oceanic basalts, *Earth and Planetary Science Letters*, 244, pp. 97-112.
- Stracke, A., V.J.M. Salters, K.W.W. Sims; 1999, Assessing the Presence of Garnet-Pyroxenite in the Mantle Sources of Basalts Through Combined Hafnium-Neodymium-Thorium Isotope Systematics, *Geochemistry Geophysics Geosystems*, 1.
- Sun, S.-S., W.F. McDonough; 1989, Chemical and isotopic systematics of oceanic basalts: Implications for mantle composition and processes, in *Migmatism in the Ocean Basin*, edited by A.D. Saunders and M.D. Norry, Geological Society of America Special Publications, London, 42, pp. 313-345.
- Tatsumoto, M.; 1978, Isotopic Composition of Lead in oceanic basalts and its implication to mantle evolution, *Earth and Planetary Science Letters*, 38, pp. 63-87.
- Tatsumoto, M., R.J. Knight, C.J. Allegre; 1973, Time differences in the formation of meteorites as determined from the ratio of lead-207 to lead-206, *Science*, 180, pp. 1279-1283.
- Tepley, F.J., C.C. Lundstrom, K.W.W. Sims, R. Hekinian; 2004, U-series disequilibria in MORB from the Garrett Transform and implications for mantle melting, *Earth and Planetary Science Letters*, 223, pp. 79-97.

- Tikku, A.A., S.C. Cande; 1999, The oldest magnetic anomalies in the Australian-Antarctic Basin: Are they isochrones?; *Journal of Geophysical Research*, 104, pp. 661-677.
- Tolstoy, M., A. J. Harding, J. A. Orcutt, and J. Phipps Morgan; 1995, Crustal thickness at the Australian Antarctic Discordance and neighboring Southeast Indian Ridge, *Eos Trans. AGU*, 76(46), Fall Meet. Suppl., F570.
- Turcotte, D.L., D. Paul, W.M. White; 2001, Thorium-uranium systematics require layered mantle convection, *Journal of Geophysical Research*, 106, B7, pp. 4265-4276.
- Turner, S., C. Hawkesworth, N. Rogers, P. King; 1997, U-Th isotope disequilibria and ocean island basalt generation in the Azores, *Chemical Geology*, 139, pp. 145-164.
- Turner, S., J. Blundy, B. Wood, M. Hole; 2000, Large ^{230}Th -excesses in basalts produced by partial melting of spinel lherzolite, *Chemical Geology*, 162, pp. 127-136.
- Veevers, J.J., S.L. Eittreim; 1988, Reconstruction of Antarctica and Australia at breakup (95 ± 5 Ma) and before rifting (160 Ma), *Australian Journal of Earth Science*, 35, pp. 355-362.
- Veevers, J.J.; 1982, Australian-Antarctic depression from the mid-ocean ridge to adjacent continents, *Nature*, 295, pp. 315-317.
- Verma, S.P., J.-G. Schilling; 1982, Galapagos hot spot-spreading center system $^{87}\text{Sr}/^{86}\text{Sr}$ and large ion lithophile element variations (85°W - 101°W), *Journal of Geophysical Research*, 87, no. B13, pp. 10,838-10,856.
- Vlastelic, I., E. Lewin, T. Staudacher; 2006, Th/U and other geochemical evidence for the Reunion plume sampling a less differentiated mantle domain, *Earth and Planetary Science Letters*.
- Vogt, P.R., N.Z. Cherkis, G.A. Morgan; 1983, Project Investigator-1. Evolution of the Australian-Antarctic Discordance deduced from a detailed aeromagnetic study; In Oliver, R.L., P.R. James, J.B. Jago (Eds.), *Antarctic Earth Science, International Symposium*, 4, 608-613.
- Weissel, J.K., D.E. Hayes; 1971, Asymmetric seafloor spreading south of Australia, *Nature*, 231, pp. 518-522.
- Weissel, J.K., D.E. Hayes; 1972, Magnetic anomalies I the southeast Indian Ocean, in *Antarctic Oceanology II: The Australian-New Zealand Sector, Antarctic Research Series*, 19, edited by D.E. Hayes, pp. 165-196, AGU, Washington D.C..

- Weissel, J.K., D.E. Hayes; 1974, The Australian-Antarctic Discordance: New results and implications, *Journal of Geophysical Research*, 79, pp. 2579-2587.
- West, B.P., J.-C. Sempéré, D.G. Pyle, J. Phipps-Morgan, D.M. Christie; 1994, Evidence for variable upper mantle temperature and crustal thickness in and near the Australian-Antarctic Discordance, *Earth and Planetary Science Letters*, 128, pp. 135-153.
- West, B.P., W.S.D. Wilcock, J.-C. Sempéré; 1997, Three-dimensional structure of asthenospheric flow beneath the Southeast Indian Ridge, *Journal of Geophysical Research*, 102, pp. 7783-7802.
- White, W.; 1985, Sources of oceanic basalts: Radiogenic isotopic evidence, *Geology*, 13, pp. 115-118.
- White, W.M.; 1993, $^{238}\text{U}/^{204}\text{Pb}$ in MORB and open system evolution of the depleted mantle, *Earth and Planetary Science Letters*, 115, pp. 211-226.
- Williams, R.W., J.B. Gill; 1989, Effects of partial melting on the uranium decay series, *Geochimica et Cosmochimica Acta*, 53, pp. 1607-1619.
- Wood, D.A.; 1979, A variably veined suboceanic upper mantle – Genetic significance for mid-ocean ridge basalts from geochemical evidence, *Geology*, 7, pp. 499-503.
- Wood, D.A.; 1979, Dynamic partial melting: its application to the petrogenesis of basalts erupted in Iceland, the Faeroe Islands, the Isle of Skye (Scotland) and the Troodos Massif (Cyprus), *Geochimica et Cosmochimica Acta*, 43, pp. 1031-1046.
- Zindler, A., H. Staudigel, R. Batiza; 1984, Isotope and trace element geochemistry of young Pacific seamounts: implications for the scale of upper mantle heterogeneity, *Earth and Planetary Science Letters*, 70, pp. 175-195.
- Zindler, A., S.R. Hart, F. Frey; 1979, Nd and Sr isotope ratios and rare earth element abundances in Reykjanes Peninsula basalts evidence from mantle heterogeneity beneath Iceland, *Earth and Planetary Science Letters*, 45, pp. 249-262.
- Zou, H., A. Zindler, Y. Niu; 2002, Constraints on Melt Movement Beneath the East Pacific Rise from ^{230}Th - ^{238}U Disequilibrium; *Science*, 295, pp. 107-110.
- Zou, H., A. Zindler; 2000, Theoretical studies of ^{238}U - ^{230}Th - ^{226}Ra and ^{235}U - ^{231}Pa disequilibria in young lavas produced by mantle melting, *Geochimica et Cosmochimica Acta*, 64, no. 10, pp. 1809-1817.